UNIVERSITY OF SOUTHERN QUEENSLAND

Faculty of Health, Engineering and Sciences
School of Mechanical and Electrical Engineering

Experimental and Numerical Study of MILD Combustion in an Open-End Furnace with Exhaust Gas Recirculation using Methane and Biogas

A Dissertation Submitted by

Muhamad Mat Noor, B.Eng.(Hons), M.Sc.(Mech. Eng.)

For the Award of

Doctor of Philosophy

2015

Abstract

The world's energy demand by 2042 is estimated at about 18 billion tons of oil equivalent with 80 % fulfilled by the combustion of fossil fuel. Combustion is predicted to be the most important way of generating energy to cater for these energy needs. The need to address energy sustainability (fuel depletion) and environmental pollution (emission) has led to an increased interest in energy efficiency improvement. Combustion technologies with higher thermal efficiency and biogas (renewable) fuels are possible long-term solutions. The Moderate or Intense Low oxygen Dilution (MILD) combustion technology can play a significant role to produce higher thermal efficiency and reduce emissions. MILD combustion has achieved great success, however it needs further fundamental study due to the current limited research on open-end furnaces.

In this study, an open-end furnace with an enclosure wall was used to capture the exhaust gas and utilised it as Exhaust Gas Recirculation (EGR). The EGR recirculates a portion of exhaust gas back to the combustion chamber to dilute the oxygen before the oxidant is mixed with the fuel and increases the reactant temperature. This setup is an open-end furnace because it allows a portion of the exhaust gas to flow out and be utilised as external EGR. In the case of a closed furnace, the exhaust gas is recirculated internally to dilute the reactants and increase their temperature. The wall thickness for the open-end furnace is very thin compared to the closed furnace which normally has a thick wall. The development and operating cost for the open-end furnace is cheaper than the closed furnace but the external EGR structure is an additional installation for the open-end furnace. The main objectives of this thesis are to conduct numerical modelling using Computational Fluid Dynamics (CFD) to design and develop the furnace, to develop and fabricate the new open-end furnace combustion chamber and to optimise the furnace performance to achieve MILD combustion.

The numerical modelling for the MILD combustion using CFD has been extensively conducted on different burners and different scale furnaces. In this study, the three-dimensional CFD model was utilised to develop and optimise the furnace. The Reynolds–Averaged Navier–Stokes (RANS) equations were solved using realisable k–ε turbulent models which has been shown by others to be a reasonably accurate model to predict the combustion temperatures and combustion products. In this research, the results of the simulation slightly over-predict the flame temperatures by about 2 % compared to the experimental results. The non-premixed, partially premixed and premixed combustion with chemical equilibrium and non-adiabatic energy treatment for the thermo-chemical database were used. The Discrete Ordinates (DO) model was used to solve the radiative transfer equation for a finite number of discrete solid angles in the Cartesian coordinate system. The Weighted Sum of Gray Gas Model (WSGGM) was used for the absorption coefficient. The method of meshing was tetrahedrons patch conforming with advanced sizing function of proximity and curvature. The active assembly, fine span angle centre and fine relevance centre setting were used for all grids. All the governing equations were solved using the second order upwind discretisation scheme for higher accuracy of the calculation. The pressure-velocity coupling scheme with a least-squares cell-based gradient was used and presto was used as the pressure discretisation scheme. The early stage of the combustion chamber development started with a CFD simulation of a basic enclosed wall and top open combustion chamber. After analysing the results, two external EGR pipes were added. Then two more EGR pipes were added to make a total of four EGR pipes. The final model was improved with regard to the pipe size and the top part of the chamber design to ensure it collected an appropriate amount of the exhaust gas. This model was later used for the experimental and numerical modelling.

The laboratory scale combustion chamber (total volume of 0.33 m^3 and thermal intensity of 18.8 $\mathrm{kW/m^3}$ atm) was developed and fabricated. In this study, the air and fuel supply system was also developed especially for this furnace operation. The parameters for the experimental study were the fuel compositions and the equivalence ratio. The experimental data was collected with 42 thermocouples (R-type and K-type), a gas analyser, an oxygen sensor and pressure transducers. The EGR flow rates were determined based on the pressures and temperatures in the EGR pipes. A National Instruments compact data acquisition system was used with analogue to digital converter modules and controlled by Labview software. Experimental tests were conducted where the secondary air supply was heated and non-heated while the reactants were varied to produce non-premixed, partially premixed and premixed flames. Methane fuel ignited more quickly than biogas due to its higher calorific value and lower self-ignition temperatures. The combination of heated secondary air with partially premixed fuel was the quickest to ignite. The combustion chamber, EGR and exhaust temperatures and the exhaust gas species were experimentally studied for the various equivalence ratios. The flame temperature for the biogas is lower than methane due to the lower calorific value of the fuel. Both methane and biogas flames produced very low $\mathrm{NO_x}$ (2 ppm) for all flow rates whereas for carbon monoxide, biogas produced almost zero once the flame became steady.

The numerical modelling for the partially-premixed methane and biogas using the same geometry and conditions as the experimental work is conducted and the flame temperatures are 1,499 K and 1,368 K respectively. These can be compared to the experimental flame temperatures for methane and biogas which are 1,483 K and 1,358 K respectively. The numerical modelling over-predicts by 1.13 % and 0.73 % respectively, which is good agreement. The exhaust gas species (CO_2, H_2O, O_2 and NO_x) were analysed at the exhaust pipe and the downstream of the EGR pipes. Both methane and biogas flames are lean. The combustion is completed with zero unburned hydrocarbons detected and excess oxygen was recorded for both the exhaust pipe and the downstream of the EGR pipes. At the downstream end of the EGR pipes, the excess oxygen is much higher due to the fresh supply of secondary air diluting the exhaust gas as expected. The NO_x emissions for methane and biogas are very low (< 3 ppm) for both locations. The numerical sensitivity test was conducted to study the effect of the chamber wall temperature boundary condition on the flame temperature. The results show that the flame temperature is very sensitive to the combustion chamber wall boundary conditions. It concluded that biogas has advantages over methane due to lower peak temperature making the combustion chamber and burner last longer and be more economical to operate. More numerical modelling was conducted for the experimental furnace geometry; when appropriate oxygen dilution (3–13 %) and the preheated oxidant were applied, the model could achieve the MILD regime. The limitation of the developed experimental furnace was discussed where it required a minimum of 0.1 MW/m^3 atm thermal density to achieve and sustain MILD combustion.

Further simulations were conducted using the same furnace geometry except a bluff-body air-fuel nozzle to successfully achieve MILD combustion. The oxygen mole fraction is diluted between 3 % and 13 % and the oxidant supply is preheated to achieve the overall reactant temperature above the fuel self-ignition temperature. The average and maximum chamber temperatures were almost identical at 3 % inlet oxygen mole fraction. The chamber temperature uniformity ratio was $\leq 20\,\%$ when the oxygen mole fractions were $\leq 13\,\%$. The conventional flame was produced (the uniformity ratio of the chamber's temperature was $> 20\,\%$) when the oxygen mole fraction reached $> 14\%$.

A new open-end furnace was designed, fabricated and tested experimentally as well as numerically. The open-end furnace with the enclosed chamber numerically operated in the MILD combustion regime for both the industrial burner and the bluff-body burner. These results can be utilised by the heating industry and also for further studies by combustion researchers. It is recommended that future work to extend this study be carried out experimentally and numerically. The further studies can be undertaken using different fuel compositions, a new gas burner, higher secondary air preheating temperatures and a modified combustion chamber.

Certification of Dissertation

I certify that the ideas, designs and experimental work, results, analyses and conclusions set out in this dissertation are entirely my own effort, except where otherwise indicated and acknowledged.

I further certify that the work is original and has not been previously submitted for assessment in any other course or institution, except where specifically stated. [3ex]

Muhamad Mat Noor, B.Eng.(Hons), M.Sc.(Mech. Eng.)

U1013680

Signature of Candidate

Date

ENDORSEMENT

Supervisory Team

Dr. Andrew P. Wandel Signature of Principal Supervisor	Professor Dr. Talal Yusaf Signature of Associated Supervisor
Date	Date

Dedication

Thee my Lord to be satisfied
To my father: Haji Mat Noor Adam
To my mother: Hajjah Che Thom Haji Yaacob
To my wife: Puan Daswati Haji Ghazali
To my kids: Muhammad Nur Amiruddin, Nurul Ain Nafisah,
Nurin Aisyah, Nurina Amni and Nurin Aqila
To my brothers : Sanusi, Azmi, Shaifol, Zamani,
Abdul Rahman and Abdul Rahim
To my sisters : Noriah and Suzarmaini

Acknowledgements

In the name of Allah, Most Gracious, Most Merciful

I would like to express my gratitude and sincere thanks to my supervisors Dr. Andrew P. Wandel and Professor Dr. Talal Yusaf for their guidance, support and encouragement throughout my study. I also have grateful appreciation to them for giving me the opportunity to do my work on this research project. I would like to thank The Ministry of Education (Malaysia) for the provision of my financial assistance (scholarship) and Universiti Malaysia Pahang for the approval of my study leave and family financial support.

I would like also to acknowledge the great contributions by Dr. Paul Baker, Dr. Richard Landers, Dr. A. Aziz Hairuddin, Dr. A. Saddam Hussein, Dr. K. Saleh, Terry Byrne, Dean Beliveau and Juanita Ryan. They supported me in many ways and provided helpful discussion during this project. I am grateful to the USQ Mechanical Workshop, Chris Galligan and Brian Aston for the discussion and development to complete the combustion chamber. Not forgetting thanks for the gas supply installation by Air Liquide and the gas fitters, P. Alwyard and H.M. Harry, for testing and commissioning the gas supply and combustion ignition and safety systems. Also enormous thanks to Mrs. Weide Wandel for proof-reading of this thesis.

A special thank you goes to my colleagues and friends in the USQ Combustion Group, USQ Computational Engineering and Science Research Centre and UMP Combustion Group (Professor Dr. M.M. Rahman and Dr. K. Kadirgama) for their fruitful discussions, friendship and help. My sincere thanks to my lovely wife, G. Daswati, for the help to accomplish this thesis. I acknowledge my sincere indebtedness and gratitude to my parents and families for their prayers, sacrifices and moral support given to me. Special thanks to my thesis examination's committee members for their comments and suggestions which were crucial for the successful completion of this thesis.

Muhamad Mat Noor, B.Eng.(Hons), M.Sc.(Mech. Eng.)

University of Southern Queensland
March 2015

List of Publications and Presentations

Journal Articles

Noor MM, Wandel AP, Yusaf T, 2014, Air Fuel Ratio for the Mixture of Biogas and Hydrogen on Non-Premixed MILD Combustion, Int. J. Automot. Mech. Eng., 10, 2144-2154, (Scopus SNIP: 2.10).

Noor MM, Wandel AP, Yusaf T, 2014, The Simulation of Biogas Combustion in MILD Burner, J. Mech. Eng. Sci., 6(1), 995-1013.

Noor MM, Wandel AP, Yusaf T, 2014, Effect of Air-Fuel Ratio on Temperature Distribution and Pollutants for Biogas MILD Combustion, Int. J. Automot. Mech. Eng., 10, 1980-1992, (Scopus SNIP: 2.10).

Noor MM, Wandel AP, Yusaf T, 2013, MILD Combustion: The Future for Lean and Clean Combustion Technology, Int. Rev. Mech. Eng. 8(1), 251-257, (SNIP: 0.64).

Noor MM, Wandel AP, Yusaf T, 2013, Design and Development of MILD Combustion Burner, J. Mech. Eng. Sci., 5(1), 668-681.

Noor MM, Wandel AP, Yusaf T, 2012, A Review of MILD Combustion and Open Furnace Design Consideration, Int. J. Automot. Mech. Eng., 6(1), 730-754, (Scopus SNIP: 2.10).

Noor MM, Hairuddin AA, Wandel AP, Yusaf T, 2012, Modelling of Non-Premixed Turbulent Combustion of Hydrogen using Conditional Moment Closure Method, IOP: Mat. Sci. Eng., 36, 012036, 1-17, (Scopus SNIP: 0.15).

Conference Papers

Noor MM, Wandel AP, Yusaf T, 2013, Numerical Study of Oxygen Dilution and Temperature Distribution of Biogas Combustion in Bluff-Body MILD Burner, Australian Combust. Symp., 6-8 Nov, UWA, Perth, Australia, ACS13-57, 299-303.

Noor MM, Wandel AP, Yusaf T, 2013, The Analysis of Recirculation Zone and Ignition Position of Non-Premixed Bluff-Body for Biogas MILD Combustion, Int. Conf. Mech. Eng. Research, 1-3 Jul, Malaysia, P245, 1-10.

Noor MM, Wandel AP, Yusaf T, 2013, Discretization of Three Dimensional Non-uniform Grid Conditional Moment Closure Elliptic Equation using Finite Different Method, Malaysian PG Conf., 4-5 July, Sydney, Australia, MPC13-07, 48-60.

Yusaf T, Noor MM, Wandel AP, 2013, MILD Combustion: The Future for Lean and Clean Combustion, 2nd Int. Conf. of Mech. Eng. Research, 1-3 Jul, Malaysia, ICMER13-K03, 1-15.(Keynote Paper)

Noor MM, Wandel AP, Yusaf T, 2012, A Preliminary Study of Control Parameters for Open Furnace MILD Combustion using CFD, 2nd Malaysian PG Conf., 7-9 Jul, Bond University, Gold Coast, Australia, MPC12-16, 46-60.

Noor MM, Wandel AP, Yusaf T, 2012, The Modelling of the Effect of Air Fuel Ratio on Unburned Hydrocarbons for MILD Combustion, 2nd Malaysian PG Conf., 7-9 Jul, Bond University, Gold Coast, Australia, MPC12-27, 159-163.

Noor MM, Wandel AP, Yusaf T, 2012, Numerical Investigation of Influence of Air and Fuel Dilution for Open Furnace MILD Combustion Burner, Southern Reg. Eng. Conf., Engineers Australia, 1-2 Sept, USQ, Australia, SREC12-02.

Noor MM, Yusaf T, Wandel AP, 2011, Study of Random Particle Interactions for Analysis of Diffusion Lengths in Turbulent Combustion Modelling, Australian Combust. Symp., 29 Nov - 1 Dec, Uni. of Newcastle, Australia, ACS11-36, 66-69.

Noor MM, Hairuddin AA, Wandel AP, Yusaf T, 2011, Implementation of Conditional Moment Closure using Taylor Expansion and Finite Different Method, 1st Int. Conf. of Mech. Eng. Res., 5-7 Dec, Malaysia, ICMER11-151, 1-12.

Contents

List of Figures

List of Tables

Acronyms & Abbreviations

AD : Anaerobic digestion
ADC : Analogue to digital conversion
ALS : Australian laboratory service
ANOVA : Analysis of variance
AVC : Atmospheric Vent Combustion
BOD : Biological oxygen demand
BR : Blockage ratio
CCS : Carbon capture and storage
CDC : Colourless distributed combustion
CFD : Computational fluid dynamics
CMC : Conditional moment closure
CO : Carbon monoxide
CO_2 : Carbon dioxide
COD : Chemical oxygen demand
EC : Electrical conductivity
EGR : Exhaust gas recirculation
FIR : Fuel induced recirculation
FOG : Fat, oil and grease
GHG : Greenhouse gas
GUI : Graphic user interface
HC : Hydrocarbon
HCCI : Homogeneous charge compression ignition
HHV : Higher heating value
HiTAC : High temperature air combustion
HPC : High performance computing
HTOC : High temperature combustion
IEA : International Energy Agency
IRZ : Inner recirculation zone
ISA : Instrument Society of America
JHC : Jet in hot co-flow
LDA : Laser Doppler Anemometry
LRS : Laser Rayleigh Scattering
LCV : Low calorific value
LES : Large eddy simulation
LHV : Lower heating value

LSD	:	Least significant difference
MFB	:	Mass fraction burn
MILD	:	Moderate or intense low oxygen dilution
MMC	:	Multiple mapping conditioning
MWTPs	:	Municipal waste water treatment plants
NI	:	National Instrument
NH_3-N	:	Ammonia as nitrogen
NO	:	Nitric oxide
NO_2	:	Nitrogen dioxide
NO_x	:	Nitrogen oxides
N_2O	:	Nitrous oxide
NPF	:	Non-premixed flame
OH	:	Hydroxyl
ORZ	:	Outer recirculation zone
ORP	:	Oxidation-reduction potential
PAH	:	Polycyclic aromatic hydrocarbons
PCA	:	Principal component analysis
PDE	:	Partial differential equation
PDF	:	Probability density function
PF	:	Premixed flame
PPF	:	Partially premixed flame
PM	:	Particulate matter
RH	:	Relative humidity
RME	:	Rapeseed ethyl ester
RoHR	:	Rate of heat release
RANS	:	Reynolds-averaged Navier-Stokes
SDE	:	Stochastic differential equation
SI	:	Spark ignition
SO_x	:	Sulphur oxides
SOC	:	Start of combustion
SPDL	:	Stochastic particle diffusion length
TKN	:	Total Kjeldahl nitrogen
TSS	:	Total concentration of suspended (non-soluble) solids
Tc	:	Chamber temperature
T_{in}	:	Inlet temperature
T_{si}	:	Self-ignition temperature
UCL	:	Upper calorific value
UHC	:	Unburned hydrocarbons
UV	:	Ultra violet
VFA	:	Volatile fatty acids
fps	:	frame per second

Nomenclature

R : gas constant
T : temperature
U : internal energy
V : volume
W : chemical source term
Y : mass fraction
Z : mixture fraction (a conserved scalar)
A_n : air nozzle outer diameter
C_p : specific heat at constant pressure
D_a : air nozzle outer diameter
D_b : bluff-body diameter
D_i : air/fuel nozzle inner diameter
F_n : fuel nozzle outer diameter
R_d : internal dilution ratio
R_{tu} : Temperature uniformity ratio
K_v : dilution ratio
T_r : temperature of the reactants
T_c : chamber temperature
T_{in} : inlet temperature
T_{si} : self-ignition temperature
d : fuel nozzle inner diameter
k : turbulent kinetic energy
$\dot{q}$: heat release rate
$\dot{m}$: mass flow rate
n : total number of species
σ : standard deviation
p_c : chamber pressure
t : time
: timescale
u : velocity
v : specific volume
: physical velocity
$\dot{v}$: volume flow rate
x, y : physical location
α : chemical species
δt : time interval

μ : mean
ν : kinematic viscosity
ρ : density or mean fluid density
$\dot{\omega}$: chemical reaction rate
ε : turbulent kinetic energy dissipation rate

Chapter 1

Introduction

This chapter consists of the background to the study, alternative fuel for furnace combustion, rationale of the study, research objectives and scope of the dissertation.

1.1 Background

Sustainability of energy supplies is becoming more important because of concern over the depletion of fossil fuel reserves. With the current supply and demand, the fossil fuel could be depleted by 2042 (Shafiee and Topal, 2009). The production of energy through the combustion process represents the main source of energy supply for the next 50 years (Yusaf et al., 2013). Figure 1.1 shows that combustion of fossil fuels is projected to fulfil about 80 % of these energy needs. The human race is facing a major problem due to depletion of energy supplies and environmental pollution (Yusaf et al., 2013). The demand for energy is dramatically increasing due to the growth of the world's population and substantial economic development in some parts of the world such as South East Asia, China and India. Combustion pollution is linked to the increase of the earth's temperature (Figure 1.2), unstable weather, increase in ocean levels and ice melting in the North and South Poles (NRC, 2010). Some of the major challenges are to provide efficient energy and limit Greenhouse-Gas (GHG) emissions. Any improvement in the combustion process will impact the community significantly by reducing costs and pollution. The research and scientific communities are ready to accept these challenges for the future of mankind. The more efficient use of fuel with low GHG emissions and Carbon Capture and Storage (CCS) might be effective ways to gradually reduce GHG emissions (Orr, 2005; IEA, 2006). In 2000, IEA (2002) and Kevin et al. (2005) reported that CO_2 contributed 77 % of greenhouse gas emissions with combustion accounting for 27 %, making it a major contributor to global climate change.

A major concern is whether the total pollution can be reduced from current levels when the rate of energy consumption will increase. In order to counter

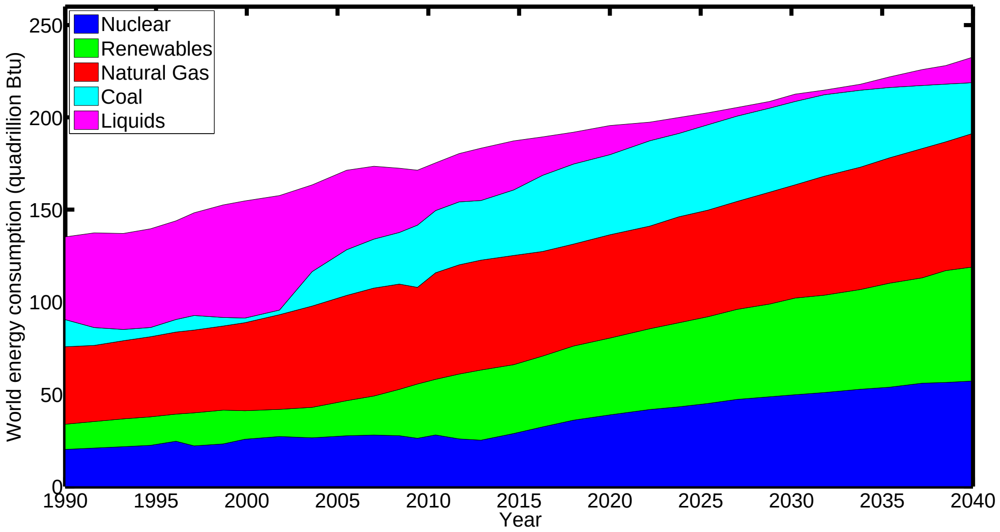

Figure 1.1: The history and prediction of world energy consumption (USEIA, 2013).

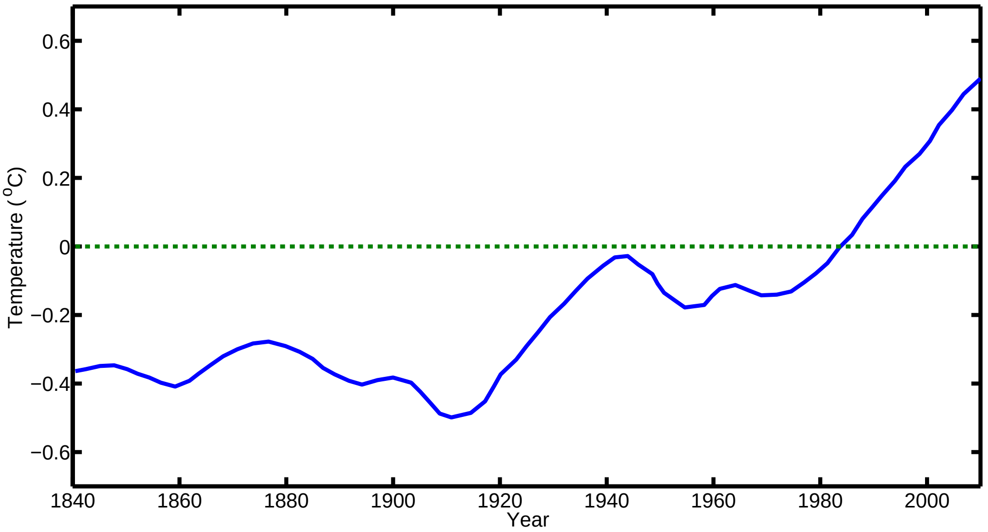

Figure 1.2: The history and prediction of unwanted increase of earth's temperature (Maczulak, 2010).

this issue, the improvement of combustion efficiency with lower emissions has led researchers to have more interest in new combustion technology (Smith and Fox, 2007; Merci et al., 2007). One of the methods of improving combustion efficiency is to preheat the reactants using hot flue gases. However, preheating the combustion air generally increases the flame temperature, which results in more formation of thermal NO_x. Note that if the temperature is below 1,450 K, the amount of NO_x is still very low because the formation of thermal NO_x gradually increases when the temperature of combustion reaches 1,500 K (Scheele et al., 2008; AET, 2012).

A new combustion technology has been invented that is able to contribute to the increase of combustion efficiency and reduction of combustion emissions. In 1989, during combustion experiments with a self-recuperative burner, Wünning (1991) observed a surprising phenomenon. He found that at furnace temperatures of 1,000°C and about 650°C air preheat temperature, no flame could be seen and no UV-signal could be detected. The fuel was completely burnt and the CO was below 1 ppm in the exhaust. The NO_x emissions were almost zero with smooth and stable combustion. Wünning (1991) called that condition "Flameless Oxidation" or FLOX (Wünning and Wünning, 1997; Milani and Wünning, 2007). This new combustion technology was also named Moderate or Intense Low Oxygen Dilution (MILD) combustion (Dally et al., 2002; Cavaliere and de Joannon, 2004). Researchers from Japan (Katsuki and Hasegawa, 1998; Tsuji et al., 2003) found that High-Temperature Air Combustion (HiTAC) is nearly the same as MILD combustion, while operating at higher temperatures. Colourless Distributed Combustion (CDC) (Arghode and Gupta, 2011*a*; Arghode and Gupta, 2013) is based on HiTAC except that the combustion intensity is much higher and the residence times are much shorter.

1.2 Alternative Fuels for Furnace Combustion

Biogas is a Lower Calorific Value (LCV) fuel that is produced from the biodegradation (anaerobic digestion) of organic materials of biological origin (biomass) in anoxic environments, such as swamps, wetlands, sediments, and in the rumen of ruminant animals. Generally biogas consists of about 60 % methane, 35 % carbon dioxide and 4.5 % nitrogen (by volume) and small amounts of some other gases. Biogas is an attractive alternative to replace the dependence on fossil fuels due to its extensive potential applications (Ashrafi et al., 2008; Muradov et al., 2008; Tsolakis et al., 2011; Rafiq and Hustad, 2011). In the last decade, the significance of renewable fuels as an alternative has increased due to dwindling supplies of conventional energy sources and rising oil prices (Ersahin et al., 2011). The exhaust emissions from combustion of fossil fuel is also an issue with regard to global warming. Moreover, the fossil fuel itself is toxic and may cause long-term adverse effects to the aquatic environment when an oil-spill incident from a fuel tanker occurs, or waste oil is deliberately dumped into oceans, rivers or lakes. Experimental studies have found that the Polycyclic Aromatic Hydrocarbons (PAH) contained in diesel may induce skin, lung and possibly urinary bladder cancer (Mastrangelo et al., 1996; BP, 1998). Therefore, research on new alternative fuels is very important in order to overcome these problems.

Biofuel is one of the most important renewable energy resources (Hussen, 2014), being produced from locally-available feedstocks. In Australia, the major sources are piggeries (Maraseni and Maroulis, 2008) and sugar cane (Simpson et al., 2012; Salter et al., 2013). In America, soy beans are used while in Europe rapeseed is used (Mamat, 2009; Santilena, 2012). Microalgae is one of the recently found good source of biofuel (Hussen, 2014). Najafi et al. (2011) and Allwayzy et al. (2014) summarised that microalgae has great potential as a sustainable biofuel resource. The main benefit of biofuel is that it is carbon neutral. Some researchers claim that engines running on biofuel produce more CO_2 compared to those running on conventional fuels, but if the analysis includes the carbon cycle, the use of biogas actually emits less CO_2 to the atmosphere. The advantages of biofuel have been reported by many researchers as renewable energy, non-toxic, biodegradable and sulphur free (Labeckas and Slavinskas, 2006; Bozbas, 2008).

Biogas consists of about 60 % methane, 40 % carbon dioxide and other gases. To utilise biogas in a laboratory combustion experiment, synthetic biogas was created. This was due to the need for consistency of the biogas composition and the ready availability of methane and carbon dioxide in the gas cylinders. In order to create practical synthetic biogas, a mixture of 60 % methane and 40 % carbon dioxide was used for the laboratory experiments in this thesis. This ratio of biogas was also used by a number of other researchers (Pomeroy, 2008; Colorado et al., 2010; Salunkhe et al., 2012; Keramiotis and Founti, 2013). Using energy balance to calculate the combustion efficiency, biogas provides 2 % lower efficiencies compared to natural gas (Colorado et al., 2010). This condition is compensated for by reducing greenhouse gases when using biogas as a fuel. Colorado et al. (2009) showed that the MILD combustion regime can be achieved with different fuel compositions.

1.3 Rationale of the Study

Combustion is still a dominant process for world energy production. A cleaner and more efficient combustion process is demanded by the combustion industries due to fuel depletion and environmental quality issues. These two challenges for the combustion community are to reduce the combustion pollution and the dependency on fossil fuel. One of the significant factors for the cost of energy is the efficiency of the combustion process. The aim of this study is to improve the quality of combustion for future energy efficiency. MILD Combustion seems to be one of the future techniques for lean and clean combustion technology (Yusaf et al., 2013). The benefits of MILD combustion are already well known and include reduced NO_x and increased thermal efficiency (Tsuji et al., 2003; Dally et al., 2004; Cavaliere and de Joannon, 2004; de Joannon et al., 2012). MILD combustion has generated great interest for many applications such as furnace ovens for final and raw material processing. The cost of final products to end customers will include the cost of the products or raw materials heating processes. This final product cost will increase if the furnace fabrication and operation cost is increased.

In order to gain the benefits of MILD combustion, further research is required, especially on open-end systems. The open-end furnace is believe to have cheaper development and operating costs compared to the closed-end furnace. As its name suggests the open-end furnace is open at one end with enclosed walls to capture and utilise the heat from the flame. Enclosure walls are also used to capture the exhaust gas to be utilised as Exhaust Gas Recirculation (EGR). This configuration is considered an open-end furnace due to the opening at the top of the furnace. This opening will allow a proportion of exhaust gas to flow out.

This study utilises the MILD combustion technique in an open-end furnace using biogas and methane. This study differs from existing research by using an open-end burner where the products mix with the reactants outside the furnace, whereas previous work on closed furnaces has recirculated the products to mix with the reactants inside the furnace. The experimental work is coupled with Computational Fluid Dynamics (CFD) to design and develop the open-end furnace. Through the combination of the study parameters (preheating the reactants using EGR to dilute the oxygen in the fresh air supply, high reactant jet velocity and preheating the air supply), turbulent mixing of the reactant and optimisation of MILD combustion in an open-end furnace can be achieved. EGR reduces $\mathrm{NO_x}$ emissions through the reduction of the flame temperature (Turns, 2006), increases ignition delay, increases heat capacity of the air and fuel mixing and dilutes the oxygen with inert gas components (Pierpont et al., 1995). A more detailed explanation on EGR can be found in many books and technical papers (Baltasar et al., 1997; Heywood, 1988; Smith and Bartley, 2000; Minamoto et al., 2013)

The main purpose of EGR is to dilute fresh air with exhaust gas and therefore reduce the peak combustion temperature to reduce the amount of $\mathrm{NO_x}$ (Abd-Alla et al., 2001; Hountalas et al., 2008). Nathan et al. (1992) and Parham et al. (2000) reported that by controlling the mixing through their precessing gas jet, a simultaneous reduction in $\mathrm{NO_x}$ emissions between 30–50 % and an increase in heat transfer rate from 2–10 % were achieved. Recently Colorado et al. (2009) studied MILD combustion using biogas (methane diluted with inert gases) and reported that $\mathrm{NO_x}$ and soot emissions were reduced but CO emission was increased. This was caused by using a high fuel dilution and low co-flow oxygen level. Besides this, it was believed that the overall benefits and advantages of biogas are much higher than the disadvantages (Rajendran et al., 2012).

1.4 Research Objectives

The overall aim of this research is to develop a numerical model and design a reliable laboratory-scale experimental setup which can both be used to investigate the possibility of open-furnace MILD combustion. This research project consists of numerical simulations and experimental work. The main objectives are:

(i) Design and optimise the three-dimensional open-end furnace with a partially premixed burner.

(ii) Develop, construct and commission the open-end furnace, gas supply control system and high accuracy in-furnace measurement system.

(iii) Perform experiments with a range of parameters for temperature profiles and exhaust gas emissions using methane and biogas fuel.

(iv) Validate the numerical simulations using the experimental data.

(v) Optimise the parameters by using CFD to achieve MILD combustion.

1.5 Scope of the Study

This thesis studies the open-end furnace MILD combustion. The main purpose is the experimental and numerical analysis of combustion performance and pollution emission of a methane and biogas as an alternative fuel. Therefore, the thesis topics are categorised as introduction to MILD combustion, CFD simulation to design and develop an open-end furnace and the experimental work. Further simulations were carried out to study other nozzle designs and parameters.

1.6 Organisation of the Thesis

This thesis consists of seven chapters including the introduction. The background and rationale of the study, the alternative fuels considered and the scope of the study are briefly introduced in this chapter. The rest of the chapters describe the fundamentals of MILD combustion, the development of the furnace, the computational modelling and the experimental work as follows.

Chapter 2 reviews the fundamentals of MILD combustion and topics covered in the study. The literature review includes computational, empirical and experimental solutions to the study. Further reviews in this chapter are the overview of exhaust gas recirculation, heat exchanger, bluff-body, biogas, methane and exhaust gas emissions such as nitrogen oxide.

Chapter 3 presents the numerical modelling and three-dimensional CFD simulations. This chapter also describes the setup of the model geometry, boundary conditions and solver selection to predict the combustion behaviour of the MILD combustion burner. The burner and combustion chamber design is discussed step by step from the first draft to the final model, ready for fabrication.

Chapter 4 presents the furnace development and fabrication, ignition system and experimental apparatus. The experimental data is used to validate the numerical model. The experimental setup consists of combustion chamber, burner, reactant supply and measurement instrumentation. The last part of this chapter describes the experimental operating procedures, equipment calibration and experimental parameters.

Chapter 5 contains the results and discussion, including the performance and emissions for the methane and biogas fuel. The experimental results are then compared to and validated with the numerical models.

Chapter 6 is about results and discussion for further CFD modelling. A bluff-body nozzle is numerically studied and the results include the temperature distributions and the combustion product analysis.

Chapter 7 covers the conclusions and limitations of the presented work. This chapter also includes the recommendations for future investigations into MILD combustion and this experimental test rig.

Chapter 2

Literature Review

This chapter presents an introduction to MILD combustion. The modelling of MILD combustion is also described. In addition, the chapter discusses the studies on MILD combustion design requirements such as oxygen dilution and reactant preheating. The combustion quality and emissions produced from the experiment of the MILD combustion is the third part discussed in this chapter. The chapter also covers the properties of a methane and biogas mixture as an alternative fuel.

2.1 Introduction

The earliest concept of MILD combustion came from the excess enthalpy combustion technique (Weinberg, 1971; Lloyd and Weinberg, 1974). The early research and development of MILD combustion came from Germany (Wünning and Wünning, 1997; Plessing et al., 1998), Japan (Katsuki and Hasegawa, 1998; Yuan and Naruse, 1999; Tsuji et al., 2003) and Australia (Dally et al., 2002; Szegö et al., 2003; Christo and Dally, 2005). When MILD combustion commences, the furnace will be bright and transparent (Wünning and Wünning, 1997; Tsuji et al., 2003). MILD combustion takes place at reduced temperature (1,100–1,600 K) and is characterized by minor temperature fluctuations and a flat thermal field (Dally et al., 2004). Figure 2.1 shows a comparison between MILD and high-temperature combustion (Cavaliere and de Joannon, 2004). The heat from the exhaust gas was utilised to preheat the reactant (Arrieta and Amell, 2014). The oxidiser co-flow also can be used to preheat and dilute the fuel stream (Sepman et al., 2013). The temperature of the reactant must be higher than the mixture self-ignition temperature (Table 2.1).

The recirculation of hot flue gas to preheat the reactants and simultaneously dilute the oxygen is a key concept of MILD combustion (Tsuji et al., 2003; Roiha et al., 2014; Huang et al., 2014). The maximum temperature increase due to the combustion is lower than the mixture self-ignition temperature (Cavaliere and de Joannon, 2004). Recent applications of MILD combustion have been in

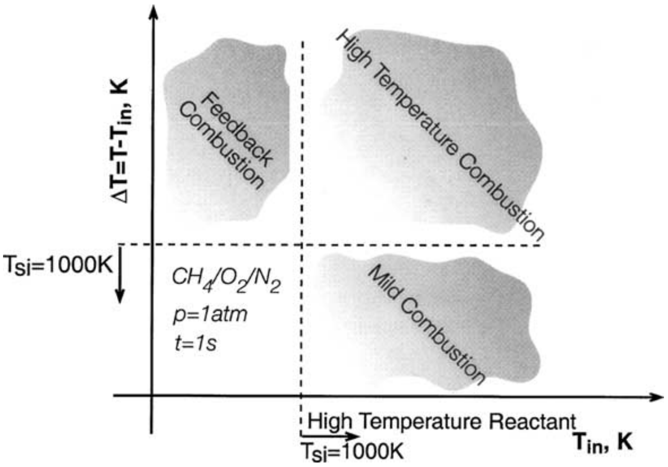

Figure 2.1: Combustion modes for a methane/oxygen/nitrogen mixture (Cavaliere and de Joannon, 2004).

Table 2.1: Summary of different combustion modes (Cavaliere and de Joannon, 2004).

Combustion mode	**Inlet conditions**	**Working conditions**
MILD combustion	$T_{in} > T_{si}$	$\Delta T < T_{si}$
High Temperature Air Combustion (HiTAC)	$T_{in} > T_{si}$	$\Delta T > T_{si}$
Feedback combustion	$T_{in} < T_{si}$	$\Delta T > T_{si}$

the research and development of gas turbines (Duwig et al., 2008; Arghode and Gupta, 2011*a*), micro gas turbines (Cameretti et al., 2013), gasification systems (Tang et al., 2010), dried sludge combustion (Shim et al., 2014) and pressurised combustion (Mingming et al., 2014). A variety of other fuels have also recently been researched such as sawdust (Dally et al., 2010), light oil (Li et al., 2014), natural gas (Abuelnuor et al., 2013), biogas (Hosseini and Wahid, 2013) and pulverised coal (Vascellari et al., 2014; Weidmann et al., 2014).

The main difference between conventional and MILD combustion is the temperature distributions and oxygen mole fraction. The temperature uniformity ratio (R_{tu}) is the ratio of the highest to average temperature divided by the average temperature and used to describe the uniformity of the gas temperature field inside the furnace (Liu and Zheng, 2013). The temperature uniformity ratio was calculated as $R_{tu} = (T_{max} - T_{avg}) / T_{avg}$. Figure 2.2 shows the comparison of the temperature contour for conventional combustion (Figure 2.2(a)) and MILD combustion (Figure 2.2(b)). The temperature distribution for conventional combustion is between 100 and 1,100°C and the average chamber temperature is 500°C. The chamber's temperature uniformity ratio for the conventional combustion is 120 %. That uniformity ratio shows the temperature distribution is non-uniform. The lower the uniformity ratio, the lower the temperature gradient in the combustion chamber. If the uniformity ratio is zero, that shows there is

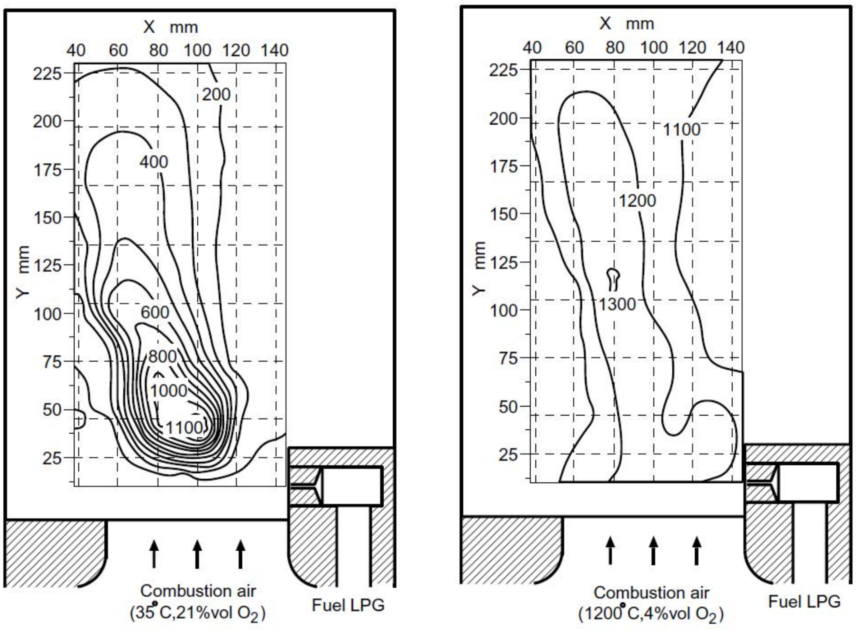

(a) (b)

Figure 2.2: Combustion temperature distribution (a) conventional combustion: with room temperature oxidant containing 21 % oxygen mole fraction (b) MILD combustion: with preheated oxidant containing 4 % oxygen mole fraction (Tsuji et al., 2003).

no temperature gradient in the combustion chamber. The temperature distribution for MILD combustion (Figure 2.2(b)) is between 1,000 and 1,300°C, and the average of the chamber temperature is 1,083°C. The chamber's temperature uniformity ratio is 20 % which shows the chamber's temperature was uniformly distributed.

To achieve MILD combustion, the air supply has to be preheated (Wünning, 1991; Dally et al., 2004). Many researchers claim that regenerative heating or preheating is an important element in MILD combustion applications, which may add some complexity when retrofitting systems. However, previous studies have shown that preheating is not required in the case of a closed furnace (Derudi et al., 2007*c*; Szegö et al., 2007; Szegö et al., 2008). This is due to the reactants being preheated by the internal EGR if the furnace is closed.

2.1.1 MILD Combustion

Industrial burners need a stable and efficient flame for an economical and safe heating process. On an industrial scale, diffusion or non-premixed combustion is commonly used due to its controllability and safety (Tsuji et al., 2003; Peters, 2004). Bluff-body burners can offer a stable burner as required. There are many different shapes and geometries such as cone, cylinder, vee gutter, disc and sphere. The geometry will affect the reactant recirculation zone just above the air-fuel nozzle where the air and fuel mixing process occurs. MILD combustion has been proven to produce clean and efficient combustion. This combustion mode can be useful in gas turbine applications due to low maximum temperatures (close to the air inlet temperature), low noise level, good flame stability and low pollution emissions. In contrast, the problems related to large-scale application of MILD gas turbines are the characteristic combustion timescale relative to the chemical timescale (the ignition delay time) and the preheating of the fresh reactants (ultralean, superdiluted, highly preheated). MILD combustion is commonly described by many researchers in different ways (Tsuji et al., 2003; Cavaliere and de Joannon, 2004; Noor et al., 2012*a*; Li et al., 2011; Zou et al., 2014) and can be summarised as follows:

(i) The important conditions to establish MILD combustion are: local oxygen concentration is less than 5 to 10 % and local temperature in the reaction zone is greater than fuel auto-ignition.

(ii) The requirements to achieve MILD combustion: high preheat temperature of oxidant supply and adequate mixing of the reactant via high velocity of fuel and oxidant inlet (within the turbulent flow regime) or other means.

(iii) The key technology to sustain MILD combustion is strong entrainments of high temperature exhaust gas used to dilute oxygen mole fraction in oxidant supply.

(iv) The temperature field in the combustion chamber or enclosure must be uniformly distributed with the chamber's temperature uniformity ratio being less than 20 %.

(v) Recycling the waste heat of exhaust gas will increase the thermal efficiency of MILD combustion by 30 % and reduce the NO_x emissions by more than 90 % when comparing the same level of air preheating temperature (1,300 K) with conventional and MILD combustion (Tsuji et al., 2003).

Furnace efficiency is defined as the ratio of heat received by the heated material to thermal energy supplied to the furnace through the combusted fuel and air heater. Furnace lean and clean operation is very critical since two-thirds of the heating factory energy budget is due to the fuel cost (Thomas, 2011). Combustion thermal efficiency in the furnace can be improved by recycling the exhaust gases (Tsuji et al., 2003; Peng et al., 2011). Greater understanding of flame structure is necessary to widen the application range of MILD combustion (Medwell et al., 2007) especially for the open-end furnace (Noor et al., 2012*b*). The open-end furnace is the furnace with the opening on the top side to exhaust the flue gas. In the current experiment, four external EGR pipes have their entrances contained within the top opening. Both the entrances of the EGR pipes and the top opening have a special design with a conical shape and the entrance of the top opening slightly lower than the four EGR pipes' entrance. This design was selected to ensure the flue gases are collected and flow into the four EGR pipes.

The EGR pipes will recirculate some of the flue gas back into the chamber through the bottom of the furnace. This design was selected because the EGR will be mixed with the fresh air supply to dilute the oxygen mole fraction in the fresh air supply. The main difference between the closed furnace and the open-end furnace are: the closed furnace comes with a small exhaust opening that will allow a small volume of flue gas to exit and the open-end furnace has a big opening to allow a higher volume of flue gas to exit from the combustion chamber. Then for the closed furnace, because there is only a small flue gas exit from the combustion chamber, the flue gas will be recirculated internally, mixed and diluted the reactant. Whereas for the open-end furnace, the flue gas is recirculated externally, mixed and diluted by the oxidant before it is mixed and diluted the reactant.

Recent studies on low calorific value fuels used in MILD combustion show that low NO_x emissions were achieved due to the low combustion temperature (Colorado et al., 2010; Danon et al., 2010). The fundamental parameters of MILD combustion are the average combustion chamber temperature (T_c), dilution ratio (K_v), and jet velocity (Derudi et al., 2007*a*). K_v is a key parameter for the MILD combustion working conditions. Several other researchers (Wünning and Wünning, 1997; Cavigiolo et al., 2003; Dally et al., 2008; Galletti et al., 2009) defined dilution ratio as the ratio between the recycled exhausts and the incoming air and fuel flow rates. MILD combustion has many advantages, such as producing very high thermal efficiencies and low emissions of NO_x. It produces a uniform temperature distribution, excellent combustion stability and has been considered one of the new-generation, clean and efficient combustion technologies. It has great potential to be implemented in many industrial applications.

Figure 2.3 shows a comparison of MILD and conventional combustion. The central jet with the bluff body in the burner block within the MILD combustion furnace operates on natural gas with 10 kW of heat input for conventional flame of natural gas (Figure 2.3(a)) and MILD combustion (Figure 2.3(b)). The flame that attached to the centre jets of the bluff-body (Figure 2.3(a)) became invisible when the combustion started to switch from conventional mode to MILD mode. When the MILD mode was achieved, the heated coflow is not used because it is no longer necessary. Similarly the central jet with the bluff body in the burner block within the MILD combustion furnace operates on sawdust with 10 kW of heat input for conventional flame of natural gas (Figure 2.3(c)) and MILD combustion (Figure 2.3(d)). The photographs taken from a side window close to the bottom of the furnace show the typical sawdust combustion with air as the carrier gas. For the conventional mode, the multiple intermittent flame sheets exist, near to the centerline fuel jet exit, while in MILD mode, the flame does not have a visible flame sheet: the combustion is distributed through the chamber.

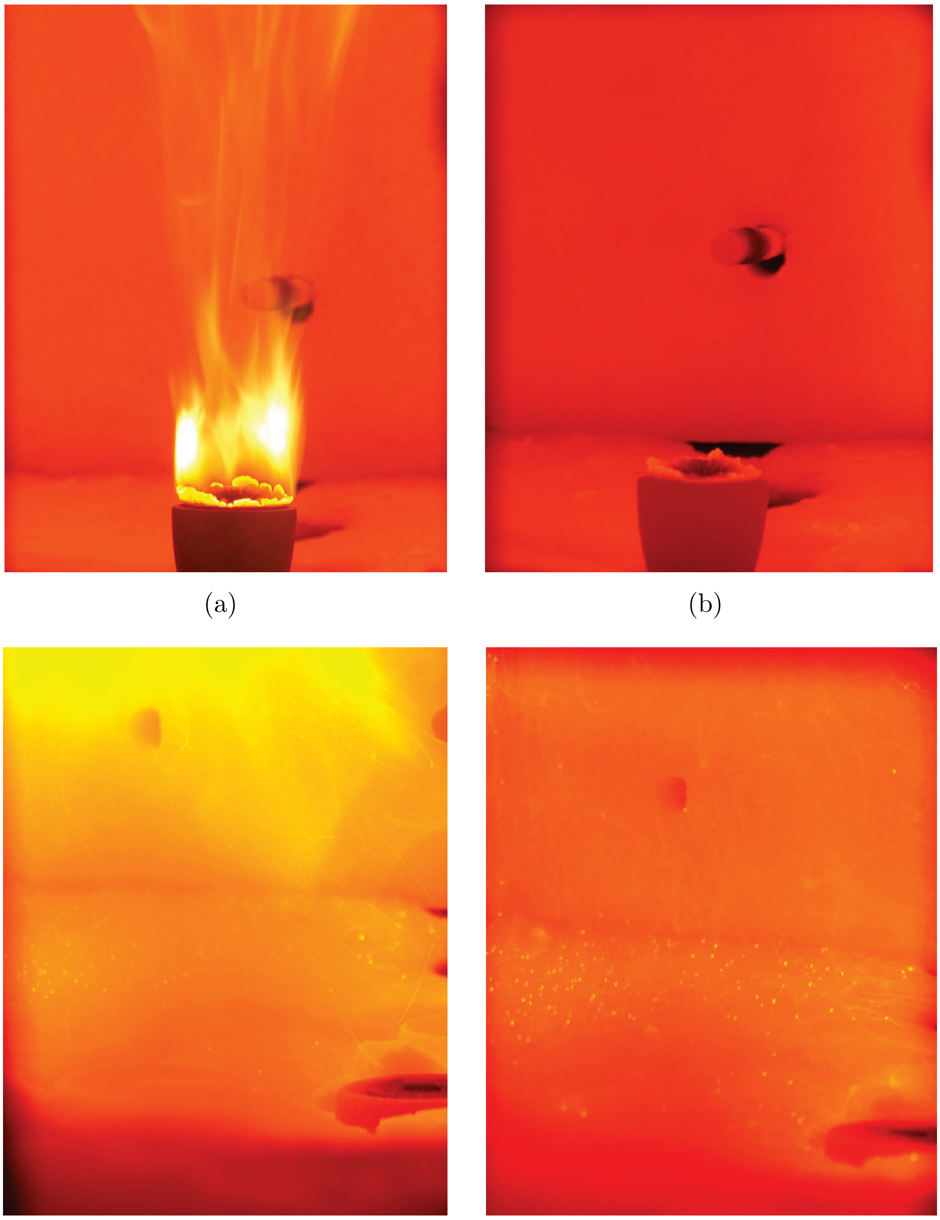

(a) (b)

(c) (d)

Figure 2.3: MILD and Conventional combustion with 10 kW of heat input for (a) conventional flame of natural gas (b) MILD combustion of natural gas (c) conventional combustion of sawdust (d) MILD combustion of sawdust (Dally et al., 2010).

2.1.2 Comparison of MILD and Conventional Combustion

MILD combustion is greatly different from normal combustion mainly because of the low oxygen concentration and the mixture temperature being higher than the fuel autoignition point (Li et al., 2011; Abuelnuor et al., 2014). The oxygen mole fraction must be in the range of 3 to 13 % to achieve MILD combustion. The air supply needs to be heated by using a recuperator or regenerator to absorb waste heat from the flue gas. The preheating was not required when the furnace was almost fully closed with a very small exhaust outlet. If the furnace with the open end or large exhaust pipe was used, the internal pre-heating did not occur because the hot flue gas easily escape through the large exhaust pipe. A recuperator can preheat the air to 1,000 K while the regenerator can heat the combustion air to about 1,600 K (Tsuji et al., 2003). The temperature difference can be seen in Figure 2.4 as a comparison of MILD and normal combustion.

Recently Parente et al. (2011) studied the MILD combustion regime using a methodology based on Principal Component Analysis (PCA), investigating the main features for the characterisation process. PCA can effectively identify low-dimensional representations of the CH_4/H_2 experimental dataset. Figure 2.5 illustrates the flame region for MILD and conventional combustion based on the [OH] contours. Significantly, both the reacting and non-reacting zones for the MILD case are bigger compared to the conventional case. The advantages of MILD combustion are already reaching industry: Danon (2011) reported an increase in demand for expertise on the implementation of MILD combustion, especially for large-scale furnaces equipped with multiple burners. MILD combustion was achieved experimentally (Dally et al., 2008; Li et al., 2010; Mi et al., 2010) and numerically (Awosope et al., 2006; Galletti et al., 2009; Szegö, 2010) in premixed and partially-premixed combustion modes. For the furnace combustion, simultaneous increase of the radiant heat transfer and reduced NO_x emissions is possible with careful control of the fuel and air mixing (Mullinger and Jenkins, 2008). Nakamura et al. (1993) and Weber (2001) experimentally studied several pilot-scale furnaces equipped with heat exchangers. They demonstrated that the port angles and locations will affect the heat transfer.

2.1.3 Furnaces

A furnace is a device used for high-temperature heating. There are two ways to utilise the heat from the furnace. Material can be directly heated in the furnace or by the use of other means like fluid flowing through a pipe and heated by

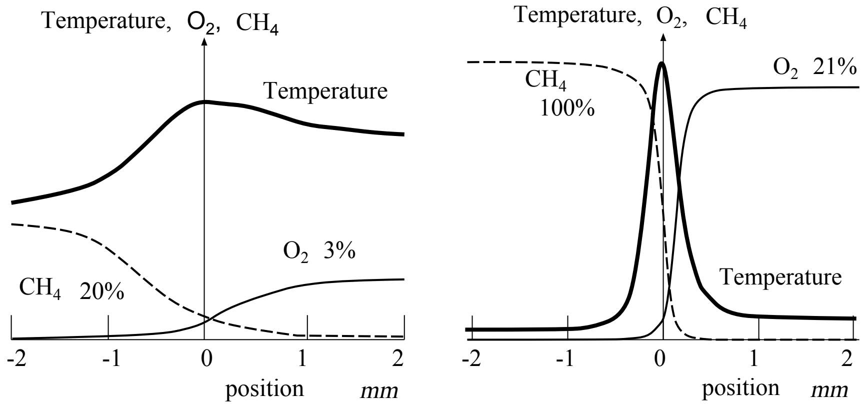

(a) MILD combustion (b) Conventional combustion

Figure 2.4: The temperature and mass fraction for flame front (Tsuji et al., 2003).

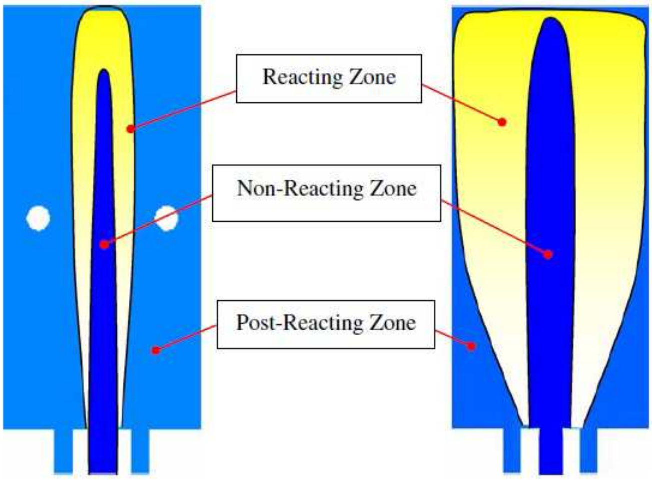

Figure 2.5: Closed furnace reacting zone for conventional (left) and MILD combustion (right) (Fei and Mi, 2011).

the furnace and then utilising the hot fluid for material heating. For the type of furnace where flue gases directly contact the materials, the type of fuel is a critical issue. This is due to some materials being intolerant of sulphur or particulate matter. Most of the industrial furnaces are open-end furnaces with the opening on the top side to exhaust the flue gas (Figure 2.6(c)). The open-end furnace with a chimney is also called Atmospheric Vent Combustion (AVC).Furnaces with this system are the least expensive to install.

The use of an open-end furnace operating in MILD combustion mode is investigated in this research. The open-end furnace is open at one end with enclosed walls to capture and utilise the heat from the flame. Enclosure walls are also used to capture the exhaust gas to be utilised as Exhaust Gas Recirculation (EGR). This configuration is considered an open-end furnace due to the opening at the top of the furnace. Generally, the setup for an open-end furnace is cheaper than for a closed furnace because the latter needs a thick and solid wall. However, open-end furnaces have additional complexity because of their requirement for preheating (Noor et al., 2012*a*). Oldenhof et al. (2011) commented that studying flameless combustion in an open and unconfined setup might give valuable insights. The combination of open-end furnace, oxidant preheating and the effect of air-fuel mixing (Oldenhof et al., 2011) need to be fully addressed. To the best of the author's knowledge, there is no reported data about MILD combustion in open-end furnace applications.

2.2 Biogas Composition and Properties

Biogas and natural gas are promising alternative fuels to meet strict pollution emission regulations in many countries. In 2001, natural gas met about 25 % of the energy needs for the United States (USEIA, 2011). In 2006, almost 24 million cubic metres of biogas were used as vehicle fuel in Sweden, which is equivalent

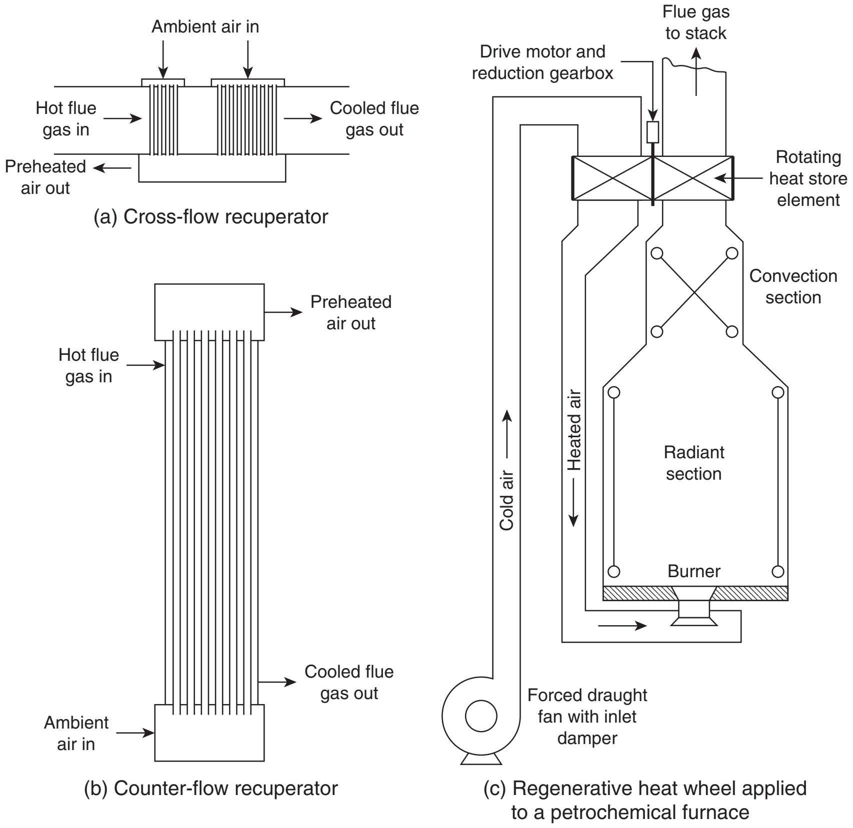

(a) Cross-flow recuperator

(b) Counter-flow recuperator

(c) Regenerative heat wheel applied to a petrochemical furnace

Figure 2.6: Industrial furnaces with opening on the top (Mullinger and Jenkins, 2008).

to 26 million litres of petrol (Clementson, 2007). Figure 2.7 shows the Swedish biogas production and consumption for vehicles. Biogas energy conversion at Danish communal biogas plants use an engine-generator to produce electricity. The efficiency of the plant with regard to generated electricity is 35 to 40 % and heat is 45 to 50 % and about 15 % is loss (Nielsen, 2009). Table 2.2 shows the combustion properties of natural gas and biogas. Natural gas and biogas consist of about 90 % and 60 % hydrocarbon respectively. This property means natural gas has a higher calorific value than biogas. Biogas, biodiesel and bioethanol are all biofuels and most of the biofuels are derived from biomass. Biofuels are very attractive alternative fuels which have a promising future as a substitute for conventional fuel (Hussen, 2014). The production of biofuels is normally based upon locally-available feedstocks including soybean, rapeseed, jatropha seed, palm oil, sunflower, cottonseed, tallow (animal fat) or even waste cooking oil.

Carbon dioxide (CO_2) is currently the primary concern for green-house gases, global warming and its consequences (Volks, 2008). When fuels are combusted, CO_2 will be released as a waste by-product. Biogas produced from biomass uses CO_2 in the photosynthesis stage, hence it will reduce the CO_2 in the atmosphere. Figure 2.8 shows the CO_2 cycle for biogas/biofuels. Typically, biogas consists of methane, nitrogen and carbon dioxide with other minor impurities

(Speight, 2008). It can be burned in gas engines and turbines for power generation, reformed to produce hydrogen (Purwanto and Akiyama, 2006), or used as an automotive fuel (Borjesson and Mattiasson, 2008). The main chemical compounds in biogas are methane (comprising 55% to 70 %) and carbon dioxide (30 to 45 %), while oxygen and nitrogen are below 2 % each and ammonia, hydrogen and hydrogen sulphide are less than 1 % each. Biogas extracted from decaying organic matter has various compositions and properties depending on feedstock types, digestion systems, temperature, retention time, etc. Table 2.3 presents an average biogas composition.

(a) production tank (b) used for vehicle

Figure 2.7: One of the Swedish biogas tanks and vehicle refuelling (Clementson, 2007).

Table 2.2: Combustion properties of natural gas and biogas (Gonzalez et al., 2009).

Properties	**Natural gas**	**Biogas**
Air theoretical volume, V_a (m^3)	9.44	5.71
Lower calorific value, LCV (MJ/kg)	44.1	26.9
Upper calorific value, UCV (MJ/kg)	54.2	33.3
Relative density, ρ_r	0.57	0.94
Dew temperature, T_R(°C)	59.09	57.66

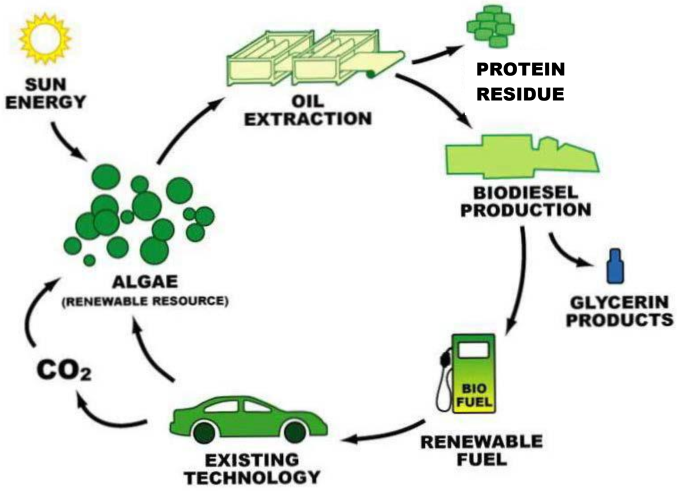

Figure 2.8: Life cycle of carbon dioxide and biofuels (Cheng and Wang, 2013).

Table 2.3: Biogas composition (Clementson, 2007; Seadi et al., 2008; Nielsen, 2009; Balat and Balat, 2009).

Compound	**Volume (%)**
Methane (CH_4)	50-75
Carbon dioxide (CO_2)	25-45
Water vapour (H_2O)	1–7
Oxygen (O_2)	< 2
Nitrogen (N_2)	< 2
Ammonia (NH_3)	< 1
Hydrogen (H_2)	< 1
Hydrogen sulphide (H_2S)	< 1

Methane is the main component of natural gas and biogas and is the most abundant organic compound on earth. Internal combustion engines run on natural gas can operate at lean burn and stoichiometric conditions with different combustion and emission characteristics. Table 2.4 shows the differences in natural gas composition between some countries. These are only representative values for each country, and vary between different geographic areas. Natural gas or pure methane are commonly used for industrial burners. Considering biogas with the standard methane content of 50 %, the heating value is 21 MJ/Nm^3, the density is 1.22 kg/Nm^3 and the mass is similar to air at 1.29 kg/Nm^3 (Seadi et al., 2008). The use of gas is predicted to continue to replace coal for electricity generation as it is a cleaner fuel producing lower greenhouse gases. Coal usage is predicted to increase by 50 %, whereas gas is expected to increase by 88 % (Scragg, 2009).

The lower the methane content, the lower the heating value for the biogas. Table 2.5 shows a comparison of energy balance for biogas (with 60 % methane and 40 % carbon dioxide) and natural gas (with 97 % methane). The summary was made for a furnace that operates in flameless mode with biogas or natural gas, and conventional mode with natural gas. The supply of thermal energy was constant at about 21 kW for both combustion modes. The energy calculated includes all the input to the combustion chambers which are fuel, air through the cooling tubes and air that will be preheated by the regenerative honeycombs.

The efficiency for the combustion with conventional mode is only 41.4 % whereas for biogas and natural gas in MILD mode it is 68 % and 70 % respectively. The energy balance was used to calculate the combustion efficiency. MILD combustion furnace fuel with biogas provides 2 % lower efficiencies compared to natural gas (Colorado et al., 2010).This condition is compensated for by reducing greenhouse gases when using biogas as a fuel. These results indicate that the flameless combustion regime can be achieved with different fuel compositions.

Table 2.4: The difference in natural gas composition for Australia, Greece, Sweden, United States and Malaysia (Kong and Reitz, 2002; Olsson et al., 2002; Papagiannakis and Hountalas, 2004; Jonathan, 2006; Ramli, 2009; GM, 2011; Hairuddin et al., 2014).

Component	**Percentage volume**				
	Australia	**Greece**	**Sweden**	**US**	**Malaysia**
Methane (CH_4)	90.00	98.00	87.58	91.10	92.74
Ethane (C_2H_6)	4.00	0.60	6.54	4.70	4.07
Propane (C_3H_8)	1.70	0.20	3.12	1.70	0.77
Butane (C_4H_{10})	0.40	0.20	1.04	1.40	0.14
Higher HC (C_xH_y)	0.19	0.10	0.19	-	-
Carbon dioxide (CO_2)	2.70	0.10	0.31	0.50	1.83
Nitrogen (N_2)	1.00	0.80	1.22	0.60	0.45

Table 2.5: Biogas and natural gas energy balance (Colorado et al., 2010).

Combustion mode (fuel)	**Flameless (biogas)**	**Flameless (natural gas)**	**Conventional (natural gas)**
Energy input (fuel, combustion and cooling air), (kW)	21.13	21.31	21.02
Energy losses through wall, (kW)	3.00	3.07	3.20
Energy removed by cooling tubes, (kW)	14.39	14.99	8.71
Energy at chimney output, (kW)	2.72	1.39	8.25
Energy of the combustion products after the regenerative system, (kW)	1.01	1.36	0
Efficiency, (%)	68.0	70.0	41.4

2.3 MILD Combustion Modelling

The modelling of MILD combustion has been successfully carried out by many researchers (Mardani et al., 2011; Evans et al., 2013; Afarin and Tabejamaat, 2013). The earliest CFD modelling for MILD (HiTAC) technology originated from the Japanese heating industry where a few researchers (Ishii et al., 1997; Zhang et al., 1997; Hini et al., 1998) conducted simulations on the NO_x formation for the experimental continuous slab reheating furnace. In this study, MILD combustion will be experimentally and numerically studied using an open-end furnace. MILD combustion is a relatively new field that has many unresolved issues that require further attention and consideration (Dally et al., 2010). MILD combustion technology has started to be commercialised but is still not well adopted in most of the furnace industry. Thus it is very important to conduct substantial fundamental and applied research to improve combustion performance and efficiency (Cavaliere et al., 2008; Danon, 2011; Parente et al., 2011). The fuel-air mixing in MILD combustion is becoming one of the interesting studies (Tsuji et al., 2003). This is due to the effect of air-fuel mixing turbulence to the achieving MILD state. Precise prediction of turbulent mixing is important in modelling the turbulent combustion because it has a large effect on the flow field and turbulence-chemistry interaction (Shabanian et al., 2011). The reactants' jet velocity and their angles are the main parameters affecting the quality of the air-fuel mixture (Galletti et al., 2007).

2.3.1 Turbulent Flows

Almost all flows in nature, industrial processes and practical engineering applications are turbulent flows (Wilcox, 1994). Turbulent flows are very complex because they are rotational, fully three dimensional and time-dependent where the flows characterised by the fluctuating of velocity fields. Some researchers have defined the properties for turbulent flow. Stewart (1969) wrote a practical definition with various commonly accepted properties of turbulence. Similarly, Tennekes and Lumley (1972) noted the distinguishing properties of turbulence to be: large Reynolds, irregularity, diffusivity, three-dimensional vorticity fluctuations and large dissipation rates. This approach is continued by Pope (2000). The main characteristic of MILD combustion is strong coupling between turbulence and chemistry (Parente et al., 2008), occurring at similar timescales (Plessing et al., 1998), thus the turbulence-chemistry interactions should be treated with finite-rate approaches. The level of homogeneity of the mixing field (de Joannon et al., 2010) and slower reaction rates make the accurate modelling of this combustion regime challenging (Aminian et al., 2011), especially for the heat release rate and NO_x formation, thus a fundamental study on the mixing quality is required.

2.3.2 Reynolds Number

Prior to Pope (2000), Frisch (1995) also emphasized the influence and importance of Reynolds Numbers to turbulence phenomena. Libby (1996) give a wide range of data for velocity fluctuations to distinguish the turbulence from "unsteady laminar flow". Researchers continue to effectively and efficiently model and experiment the turbulence phenomena for better application, especially in combustion. Osborne Reynolds (1842–1912) used a ratio of forces, inertial to viscous, to characterize the flow and it is called the Reynolds Number (Re).

$$Re = \frac{\rho V D}{\mu} = \frac{V D}{\nu} \tag{2.1}$$

where V is flow velocity and D is the flow wetted perimeter. The jet Reynolds Number is the number used to define the turbulent flows at the burner fuel or air inlet. For non-premixed combustion, there are a few types of modelling methods for the mixing process: probability density function (PDF) based model (Pope, 1985; Haworth, 2010), flamelet model (Peters, 1984), fast chemistry limit model (Bilger, 1980) and mapping closure model (Pope, 1991). Besides those models, there are a few other developments such as conditional moment closure (CMC) (Klimenko and Bilger, 1999) and Multiple Mapping Conditioning (MMC) by Klimenko and Pope (2003), with further developments (Wandel and Klimenko, 2005; Wandel, 2013) for the mixing process.

The flame stability is one of the important issues in lean combustion, yet not much research has been done (and published) in this area for MILD combustion (Szegö, 2010). One of the main parameters for flame stability is turbulent flows. Flame stability is closely related to a good dilution ratio and the control of the oxidation process. These conditions are closely related to the mixing process which requires turbulent mixing in order to achieve a stable flame. A stable flame will avoid the flame being lifted and blown-off (which results in flame extinction). Figure 2.9 shows the flame with the exposure time of the photograph and the relative luminosity of each flame. MILD combustion mostly occurs under turbulent conditions. Studies on the effect of turbulent mixing on chemical kinetic showed that turbulent mixing intensity plays an important role in achieving a MILD state (Katsuki and Hasegawa, 1998; Hamdi and Hmaeid, 2012; Abtahizadeh, 2014).

2.4 MILD Combustion Design

Flame stabilisation is an important issue in order to design MILD burners with flexible fuels such as syngas (synthetic gas). The experimental setup for a MILD burner successfully achieved the MILD regime for earlier research groups such as the Wünning group (Wünning and Wünning, 1997; Wünning, 2005), the Dally group (Szegö et al., 2003; Dally et al., 2010), Rota group (Derudi et al., 2007*a*; Derudi and Rota, 2011) and the Katsuki group (Katsuki and Hasegawa, 1998; Hasegawa et al., 2002). Images of the Adelaide and Milano furnaces can be seen

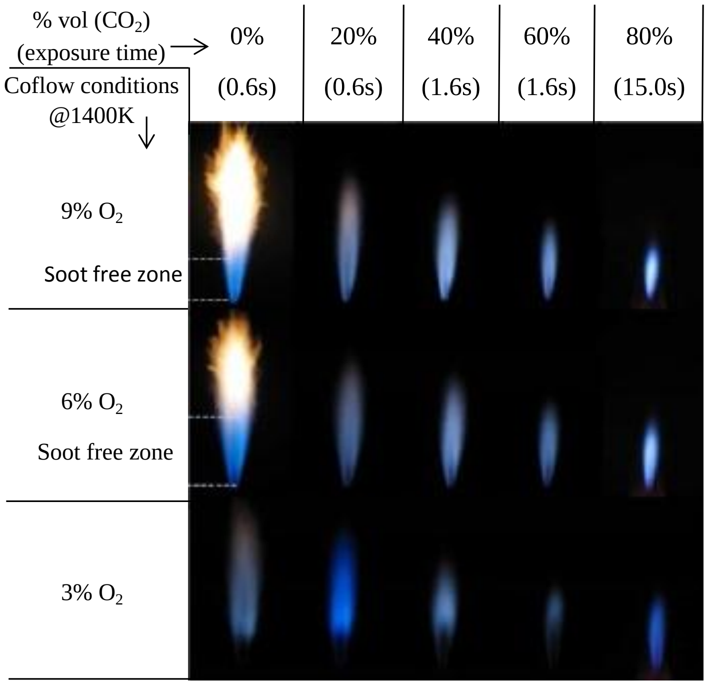

Figure 2.9: Photograph of the flame with the exposure time and the relative luminosity of each flame (Colorado et al., 2009).

in Figure 2.10. The Centre for Advanced Gas Combustion Technology (CAGCT) and the Canadian Gas Research Institute (CGRI) developed an ultra-low NO_x burner for use with natural gas and air (Sobiesiak et al., 1998). Fleck et al. (2000) in their experimental work tested this furnace under a wide range of operating conditions.

2.4.1 Oxidant Dilution

Oxygen dilution is one of the key factors necessary to achieve the MILD regime. The MILD combustion regime is plotted in Figure 2.11 with respect to the dilution ratio and temperature (Wünning and Wünning, 1997). It shows that there are four main regimes: a clean MILD combustion region, where MILD is easily sustained without any significant emissions; an unstable flame region; a conventional (normal) flame combustion region and a no-combustion or extinction zone. The more usual representations (Wünning and Wünning, 1997; Cavigiolo et al., 2003) identify different regimes of stable and unstable flame combustion and a flameless oxidation region. Figure 2.12 indicates that the MILD combustion range for oxygen dilution is about 3 to 13 % and the reactant temperature is above the self-ignition temperature.

EGR was utilised to dilute and preheat the oxidant, Wünning and Wünning (1997) formulated the dilution ratio (K_v) with EGR as:

$$K_v = \frac{M_E}{(M_F + M_A)} = \frac{(M_T - M_F - M_A)}{(M_F + M_A)} \tag{2.2}$$

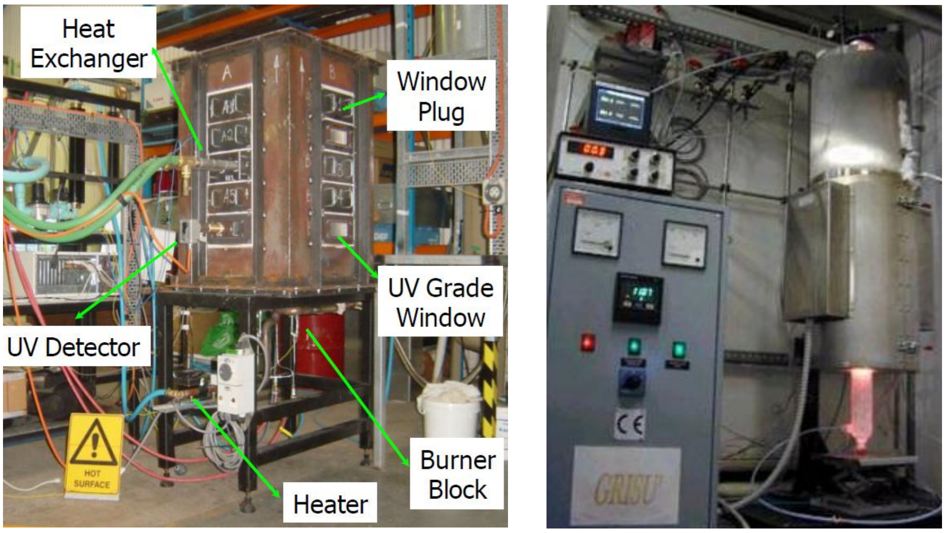

(a) (b)

Figure 2.10: Experimental setup for MILD combustion fully closed burner a) University of Adelaide, Australia (Szegö et al., 2008), b) Politecnico di Milano, Italy (Derudi and Rota, 2011).

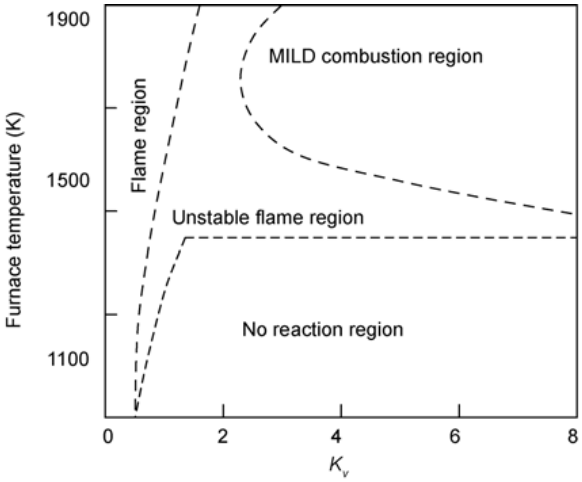

Figure 2.11: The relationship between furnace temperature and dilution ratio (Wünning and Wünning, 1997).

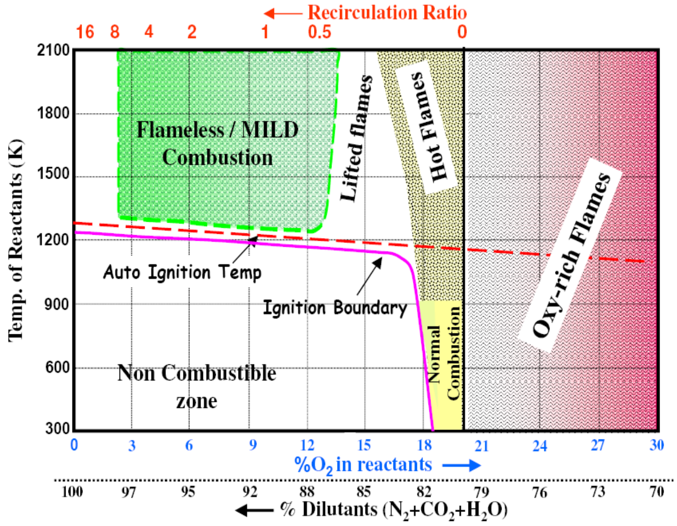

Figure 2.12: Schematic regime diagram for methane-air JHC flames (Rao, 2010).

The total mass flow rate, M_T is calculated by adding up the EGR mass flow rate, M_E, fuel mass flow rate, M_F and fresh air mass flow rate, M_A. The dilution ratio and temperature inside the combustion chamber are to be measured when combustion achieves steady state. The equivalence of mass and volume flow rates is for constant-density processes. The minimum dilution ratio is 2.5 (Wünning and Wünning, 1997).

2.4.2 Reactants Preheating

In diffusion or non-premixed combustion, to reduce waste and flue gas release to atmosphere, heat from the flue gas can be recirculated by preheating the supply air with exhaust heat from the burned products. Lloyd and Weinberg (1975) reported that using the heat recirculation to preheat the mixture can attain stable combustion with a lean combustion mixture and expand the flammability limits of the combustion.

2.4.2.1 Heat Exchanger

Regenerators and recuperators are heat exchange systems that recover heat. The temperature of combustion air in an adiabatic system can theoretically be raised to almost the same temperature as the exhaust stream by regenerative heat exchangers. From their analysis, Li et al. (2011) concluded that the regenerative heat exchanger system for MILD combustion has great advantages of energy savings and low NO_x emissions. Figure 2.13 shows the comparison between normal combustion, heat recirculating using a recuperator, and a regenerator used in MILD combustion. Regenerators cycle the heat through heat sinks. The heat from the primary medium is first stored in a heat sink and later regenerated from that heat sink by the secondary medium. The recuperators cycle the heat through a high-temperature metallic heat exchanger and both media are separated by a wall through which heat is transferred directly. In both cases, heat from flue gas

Table 2.6: Comparison for air-fuel combustion with and without recuperator (Joachim, 2012).

Properties	With recuperator	Without recuperator
Enthalpy in steel, kWh/t	200	200
Flue gas enthalphy, kWh/t	155	290
Flue gas temperature, °C	850	1200
Air preheating, °C	450	20
Thermal efficiency (%)	60	42
Energy need, kWh/t	365	500

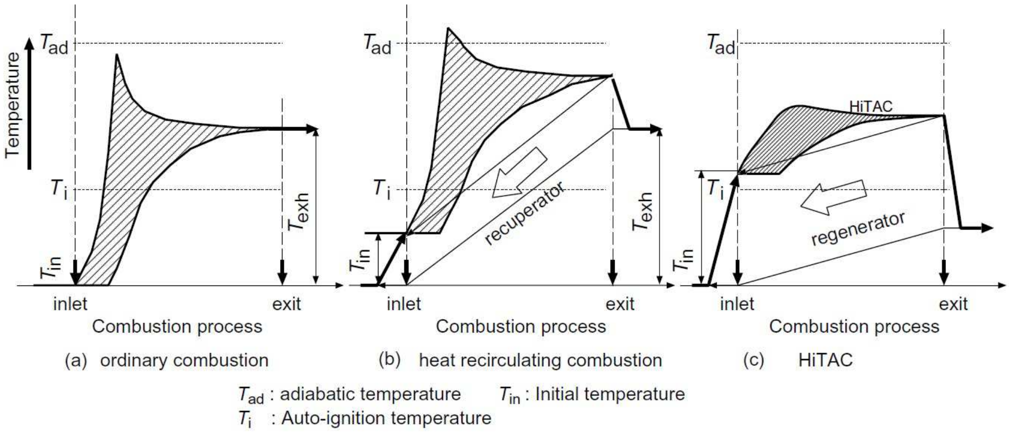

Figure 2.13: The comparison between a recuperator and a regenerator (Tsuji et al., 2003).

was used to preheat the air supply to the combustion. The comparison for the combustion with and without recuperators can be seen in Table 2.6. The combustion with the recuperator shows higher thermal efficiency with lower energy input and lower heat loss through exhaust gas.

Figure 2.6 shows an industrial regenerative combustion system for high-temperature air combustion with a heat recirculating method. One of the better regenerator designs is the honeycomb type (Tsuji et al., 2003). The recirculation of hot combustion products increases the reactant temperature. An ensemble of inlet variables and boundary conditions that determine which single or multiple processes exist within a reactor can be used to characterise the reactor and its operation (Cavaliere et al., 2008).

2.4.2.2 Exhaust Gas Recirculation

The thermal efficiency of furnaces and other heating equipment such as kilns, ovens and heaters is the ratio of heat received by the target material and heat supplied to the heating equipment. A large amount of the heat is wasted in the form of flue gases and a small amount through wall loss, opening loss, stored heat and cooling water loss. The design, operation and maintenance of the heating equipment are the key factors for these losses. Exhaust gas recirculation (EGR) is one of the methods to recover these losses. EGR behaves differently to heat regenerators. EGR works by recirculating a portion of the exhaust gas back to the combustion chamber. The main purpose of EGR is that the oxygen in the combustion chamber will be diluted by the hot flue gas and the mixture will be heated directly. The volume of hot flue gas to inject back into the system depends on the level of oxygen dilution needed. EGR with MILD combustion was used (Katsuki and Hasegawa, 1998; Cavaliere and de Joannon, 2004) as a solution to avoid NO_x and soot formation.

The control parameter is the heating required by the furnace, which determines the required dilution ratio. A thermocouple was used to measure the heat produced by the flame. The comparison of the combustion with and without exhaust gas recirculation was measured and analysed. This data was used for the efficiency improvement. Figure 2.14 shows a comparison of the combustion with and without EGR. The furnace in Figure 2.14(a) is running without a regenerator (EGR) and 654 BTU of heat is lost through flue gas. The difference for Figure 2.14(b) is the furnace running with the regenerator (EGR) and from 654 BTU of heat in the flue gas, only 133 BTU is lost to the atmosphere. Some 521 BTU of the heat is returned to the system through the use of the regenerator. For the same amount of fuel input, the system produced 37.4 % efficiency for the system without EGR and 72.4 % for the system with EGR. The vent damper blade acts as a control valve at the furnace stack. The vent damper blade was used to control the outflow from the furnace and the percentage of the opening size determined the percentage of the EGR. The EGR and the fresh air mixing determine the dilution ratio of the system. The total flue gas leaving the system must be equal to the quantity of fresh air and fuel supply.

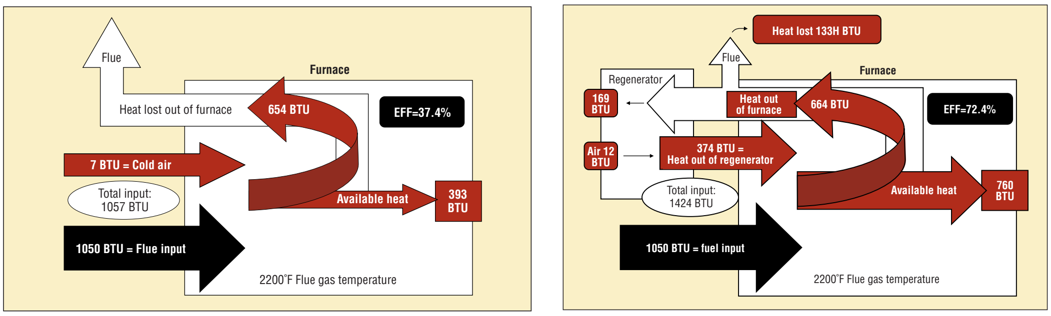

(a) 21 %

(b) 8 %

Figure 2.14: Efficiency of the heating system (a) without EGR (b) with EGR (Kraus and Barraclough, 2012).

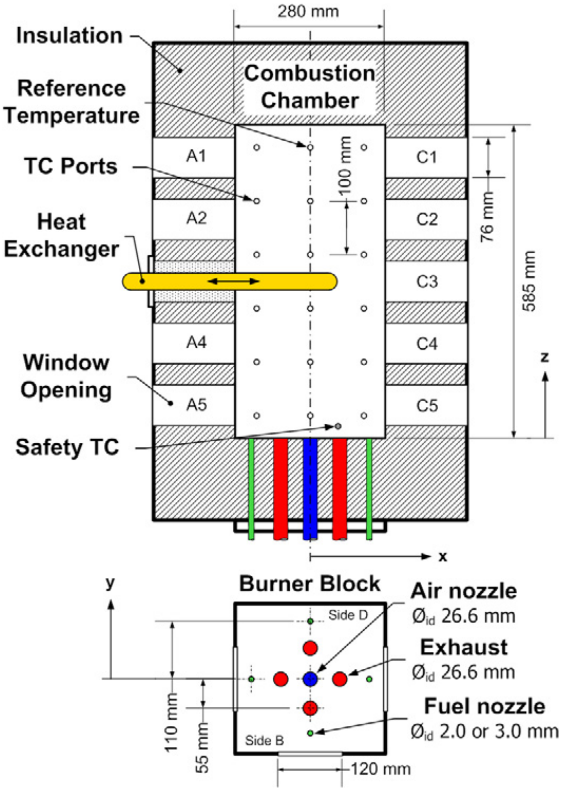

Figure 2.15: MILD combustion furnace and parallel jet burner system (Szegö et al., 2009).

2.5 MILD Combustion Experiment

Part of the MILD combustion experimental work was carried out to validate part of the simulation results. Most of the experiments that were carried out were using premixed and non-premixed combustion with a closed furnace. The premixed combustion mode is when the fuel and oxidant are mixed prior to the nozzle exit. The non-premixed mode is when the fuel and oxidant are injected to the enclosed furnace through different ports and mixing and combustion proceed inside the chamber. Nathan et al. (1992) and Parham et al. (2000) reported that by controlling the mixing through their precessing gas jet, a simultaneous reduction in NO_x emissions by 30 to 50 % and an increase in heat transfer by 2 to 10 % were achieved. Szegö et al. (2008) used a furnace with 20 kW supplied by the fuel and 3.3 kW from the preheated air (Figure 2.15). This closed furnace used parallel air and fuel jets with one central air nozzle, four fuel jets and four exhausts. All the nozzles are located on the bottom of the furnace. This MILD combustion setup has produced data in various experiments including fuel tests flame tests, NO_x tests, and heat exchanger tests (Maruta et al., 2000; Mörtberg et al., 2006; de Joannon et al., 2010).

Figure 2.16 shows a picture of a small size high-intensity Colourless Distributed Combustion (CDC) combustor with premixed and non-premixed combustion modes. The combustor was operated with air preheat temperatures of 300 K and 600 K with very low emissions. The NO_x emission can be reduced effectively by means of low-oxygen concentration combustion (Suzukawa et al., 1997; Fuse et al., 2002). The recirculation flue gases are entrained with the combustion air and fuel before combustion occurs to limit the peak temperature. This behaviour only occurred when the exhaust gases were recirculated: an adiabatic internal recirculation does not affect the adiabatic flame temperature but only the oxygen dilution. As a result, thermal NO_x is suppressed. The lower the oxygen concentrations, the lower the flame temperature (Lee and Choi, 2009). The lower the flame temperature, the lower the NO_x formation.

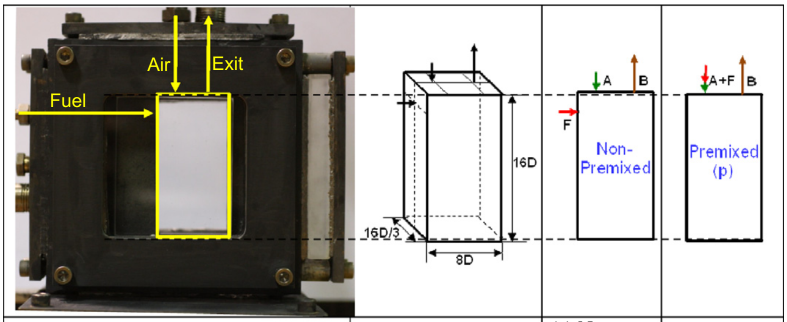

(a) CDC combustor (b) Schematic (c) Non-premixed (d) Premixed

Figure 2.16: High intensity CDC combustor (Arghode and Gupta, 2013).

There are two main modes for MILD industrial applications: a one-flame system (self-regenerative burner) and a two-flame system (Figure 2.17). Both of them are composed of at least two regenerators. The fuel is continuously supplied and switching occurs for heat storing and releasing between the two regenerators. A pair of burners for the two-flame system operate alternately and the flow path for air ejection in each burner is filled with ceramic regenerators. When one of the burners is in combustion mode, the other one will recover energy from exhaust gases and function as the regenerator (Choi and Katsuki, 2001; Zhenjun et al., 2010). The oxygen concentration and the temperature of the preheated air will affect the MILD flame as shown in Figure 2.18. The flame generally becomes less visible when the oxygen level decreases to 2 % (Gupta et al., 1999).

The dilution ratio (K_v) and the chamber ambient temperature must be controlled to achieve MILD combustion. The minimum dilution ratio to achieve MILD combustion is 2.5 (Wünning and Wünning, 1997). The temperature of the steady state combustion must comply with the temperature of the working condition, as in Table 2.1. The MILD combustion key control strategies are based on the heating requirement of the furnace. Based on the heating requirement, the dilution ratio and fresh air supply will be controlled. EGR, fresh air and fuel supply are controlled based on the dilution ratio required. Fuel consumption is the key to measuring the efficiency of the system. Thermocouples were used to measure the heat produced by the flame. The comparison of the combustion with and without exhaust gas recirculation was measured and analysed.

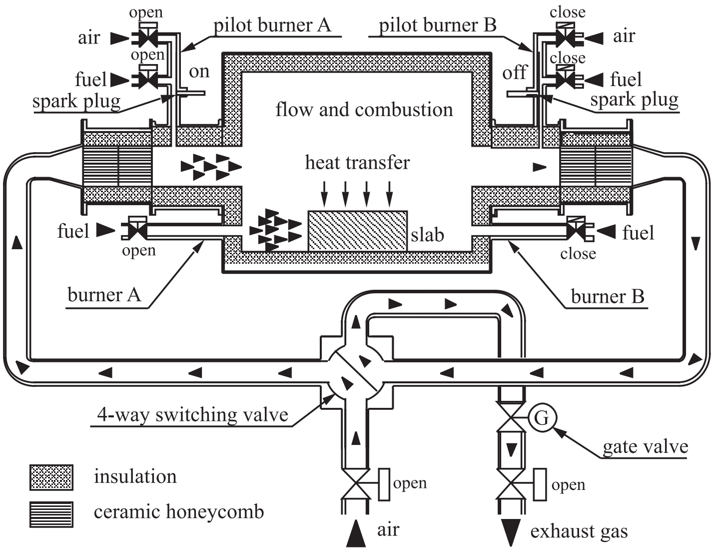

(a) Two-flame regenerative burning system

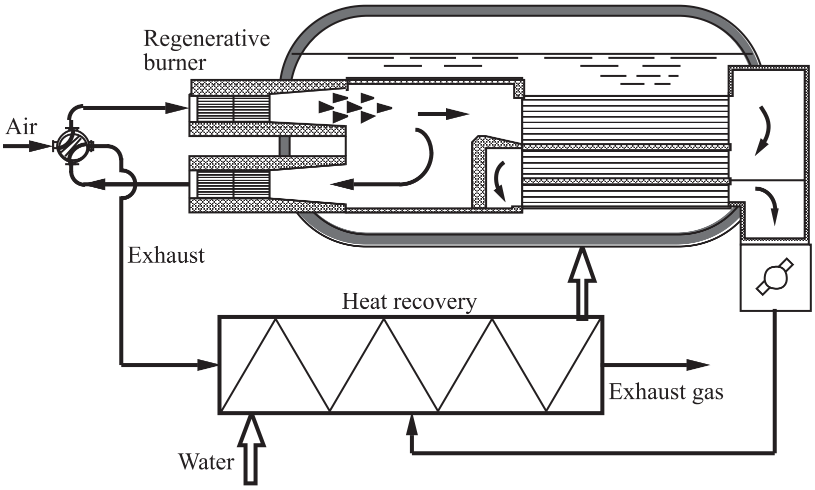

(b) Single-flame regenerative burning system

Figure 2.17: Schematic of two-flame and one-flame type regenerative burning systems (Choi and Katsuki, 2001).

(a) 21 % O_2 (b) 8 % O_2 (c) 2 % O_2

Figure 2.18: Combustion air temperature of 1,100°C (Gupta et al., 1999).

The dilution ratio was controlled by the opening of the vent damper. The vent damper at the furnace stack was used to control the outflow from the furnace and the percentage of the opening size determined the percentage of the EGR. The EGR and the fresh air mixing determined the dilution ratio of the system. The total flue gas exiting the system must be equal to the quantity of the fresh air supply.

2.5.1 Lambda

The mixture composition, indicated by lambda (λ) [the Air-Fuel Ratio (AFR) divided by the stoichiometric AFR], is an important parameter for the combustion process. The stoichiometric AFR is the ratio of air required to complete the combustion of the fuel. Low λ will result in unburned hydrocarbons (UHC) that harm the environment and are a waste of energy resources. High λ will result in possibility of flame extinction due to insufficient fuel or too high excess air combustion. For methane combustion, the process involves a highly heterogeneous mixture with λ values ranging from about 0.5 to 1.5. (Iorio, 2014). The effect of AFR on the combustion efficiency has been studied for MILD combustion (Kumar et al., 2005). The results show that the performance of combustion is very sensitive to λ, with optimum efficiency near stoichiometry. The industrial heating community always uses lean combustion, which reduces the fuel cost and unwanted UHC gases that are released to the atmosphere, but if MILD combustion were used instead of conventional flames, operation closer to stoichiometric conditions, with the corresponding increase in efficiency, would be viable.

2.5.2 Exhaust Emission

The emissions from combustion have a significant effect upon air pollution. The main pollutants emitted from combustion are nitrogen oxides, unburned hydrocarbon, carbon monoxide, sulphur oxides and particulate matter (Heywood, 1988; Turns, 2000). Of these five pollutants, only nitrogen oxides, unburned hydrocarbon and carbon monoxide were discussed due to their relevance to a MILD combustion system operating in an enclosed system with gaseous fuels (Szegö, 2010). MILD combustion does not affect the formation of sulphur oxides. Colorado et al. (2010) used biogas and natural gas in their experiment with a non bluff-body closed MILD burner. The results show that the combustion with biogas emits a lower amount of nitrogen oxides (NO_x) and O_2 and a higher amount of CO and CO_2 as compared to natural gas (Table 2.7). Generally, emissions produced by both biogas and natural gas were very low and similar during the MILD combustion mode. For NO_x, biogas and natural gas produce 2 ppm and 3 ppm respectively. The same trend applies for CO and O_2 which the difference is very small. Biogas produced higher levels of CO_2 due to the biogas itself containing a higher amount of CO_2 compared to natural gas.

Table 2.7: Exhaust pollutant from flameless combustion (Colorado et al., 2010).

Pollutant	**Natural gas**	**Biogas**
Carbon monoxide (ppm)	15	16
Nitrogen oxide (ppm)	3	2
Carbon dioxide (%vol)	9.8	14.2
Oxygen (%vol)	3.4	3.1

Table 2.8: Pollutant from fossil fuel combustion (kg of pollutant per 10^9 kJ of energy input) (USEIA, 1999).

Pollutant	**Natural gas**	**Oil**	**Coal**
Carbon dioxide	273,780	383,760	486,720
Carbon monoxide	94	77	487
Nitrogen oxide	215	1,048	1,069
Sulphur dioxide	2.34	2,625	6,063
Particulate	16.4	197	6,420
Mercury	0.00	0.016	0.037

Tsuji et al. (2003) reported that when using a regenerator to recycle the waste heat of exhaust gases, the NO_x emissions reduce by 50 %, while thermal efficiency increases by 30 %. Dally et al. (2010) in their experiment for MILD combustion using sawdust, showed that the optimal equivalence ratio to reduce both CO and NO_x emissions was in the range of 0.71 to 0.75 for CO_2 as sawdust carrier gas and at 0.75 for N_2 as the carrier gas. Table 2.8 shows the comparison for pollutants produced by natural gas, oil and coal. It can be clearly seen that the natural gas is much cleaner than oil and coal.

2.5.2.1 Unburned Hydrocarbons

Hydrocarbon pollutant emissions are the result of incomplete combustion of the hydrocarbon fuel. Hydrocarbon fuels are categorised based on their chemical compositions such as paraffin (alkanes), olefins (alkenes), acetylenes (alkynes), or cyclic hydrocarbons (Bohac and Assanis, 2001). The air-fuel equivalence ratio, commonly indicated by λ is used to translate the air-fuel ratio to the stoichiometric air-fuel ratio. Completed combustion at stoichiometric combustion is where the combustion was at λ equal to 1.0. The MILD combustion produced UHC when λ less than 1.0 was used due to rich fuel condition. Too lean a mixture with an air-fuel ratio more than 20:1 also gives potential sources of UHC (Griffiths and Barnard, 1985). Too much excess air or oxygen concentrations that are too low may cause partial oxidation and fuel pyrolysis.

The quenching process (such as cold stream) gives a possibility for UHC (Turns, 2000). Therefore, the mixing pattern and burner configuration also play an important role to ensure complete combustions. Normally bluff-body plays an important role to help the proper mixing process. Heywood (1988) reported that

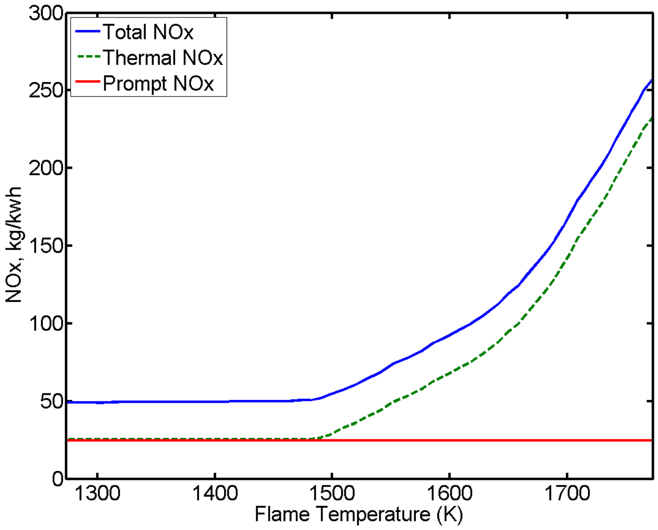

Figure 2.19: Formation of NO_x (Scheele et al., 2008).

generally in many combustion devices, λ plays important role in the amount of UHC and CO emissions produced. UHC is sensitive to burner temperature, where it decreases as the temperature increases.

2.5.2.2 Oxides of Nitrogen

The most relevant oxides of nitrogen (generally called NO_x) are nitric oxide (NO) and nitrogen dioxide (NO_2) (Heywood, 1988). Nitrous oxide (N_2O), on the other hand, generally comes from natural sources and is not produced by the combustion process. NO_x is one of the most hazardous pollutants due to its contribution to acid rain, ozone depletion and photochemical smog formation. NO_x is also one of the regulated air pollutants and is stringently controlled by most countries through air and environmental pollutant regulations. Bowman (1992) reported that more than 90 % of the NO_x is NO which comes from the oxidation of nitrogen at high temperature combustion. The NO formation drastically increased when the combustion temperature reached 1,600 K or higher. This can be seen in Figure 2.19. Hence most of the NO_x control strategies are to lower the peak temperature, keep the residence time short and lower the oxygen concentrations in the high-temperature zone (Wünning and Wünning, 1997). In all combustion processes, the majority of NO_x formations are thermal NO_x, prompt NO_x and fuel NO_x (Heywood, 1988; USEPA, 1999; Kutz, 2006).

Thermal NO_x, also known as the Zeldovich mechanism. Thermal NO_x is mainly dependent on the temperature of the combustion flame and essentially independent of the completeness of combustion. The concentration of thermal NO_x is controlled by the nitrogen and oxygen molar concentrations and the temperature of combustion. Combustion at temperatures well below 1,500 K forms much smaller concentrations of thermal NO_x. The thermal NO_x route is highly dependent on the combustion temperature. The formation of thermal NO_x can be defined through the extended Zeldovich mechanism (Glassman and Yelter, 2008).

$$\begin{aligned} O + N_2 &\leftrightharpoons NO + N \qquad (2.3) \\ N + O_2 &\leftrightharpoons NO + O \qquad (2.4) \\ N + OH &\leftrightharpoons NO + H \qquad (2.5) \end{aligned}$$

Prompt NO_x also known as the Fenimore mechanism. The key to prompt NO_x is rich combustion. Prompt NO_x is formed from molecular nitrogen in the air combining with fuel in fuel-rich conditions which exist, to some extent, in all combustion. This nitrogen is then oxidised along with the fuel and becomes NO_x during combustion, just like fuel NO_x. The abundance of prompt NO_x is disputed by the various researchers - probably because they are either considering fuels intrinsically containing very large or very small amounts of nitrogen, or are considering burners that are intended to either have or not have fuel-rich regions in the flame. For the Fenimore mechanism, the NO_x formation can be described as the following chemical reaction (Bowman, 1992):

$$\begin{aligned} HCN + O &\leftrightharpoons NCO + H \qquad (2.6) \\ NCO + H &\leftrightharpoons NH + CO \qquad (2.7) \\ NH + (H, OH) &\leftrightharpoons N + (H_2, H_2O) \qquad (2.8) \\ N + OH &\leftrightharpoons NO + H \qquad (2.9) \\ N + O_2 &\leftrightharpoons NO + O \qquad (2.10) \end{aligned}$$

Under the MILD regime, the numerical results show that the Fenimore mechanism was the NO_x dominant product (Lee and Choi, 2009; Abtahizadeh, 2014). This is in agreement with the experimental work by Sepman et al. (2011) and Dally et al. (2002). Sepman et al. (2011) measured the NO_x in an axisymmetric laminar-jet-in-hot-coflow burner which showed that the NO_x formation in a MILD flame is less than 2 ppm.

Fuel NO_x or fuel mechanism is the least important NO_x. Fuel NO_x originates from fuels containing nitrogen such as certain coals (solid fuel) and oil (liquid fuel) which typically contain 0.32% nitrogen by weight. An oxidation of the already-ionised nitrogen contained in the fuel will produce fuel NO_x. During the combustion process, the nitrogen bound in the solid or liquid fuel is released as a free radical and ultimately forms free N_2, or NO. The chemical reaction process is complex where the reaction schemes typically consider in the order of 50 intermediate species and hundreds of separate reversible reactions. In general during the process, the volatile fuel nitrogen is evolved mainly as HCN (and NH_3). The HCN reacts with O and OH (free radical species) to form CN, NCO, HNCO and some other intermediates. The chemical reaction of these intermediates then reacts with H to produce NH and NH_2. The most successful method to minimise fuel NO_x is by burning the fuel by staged combustion. This involves the delaying

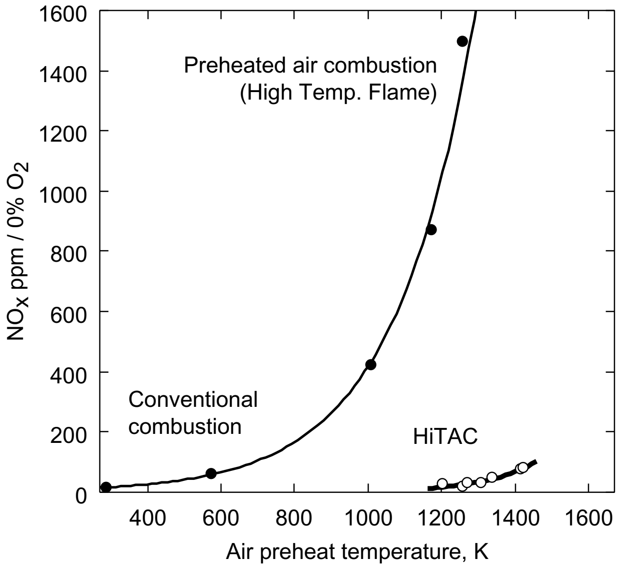

Figure 2.20: Preheated air temperature on NO_x emission (Tsuji et al., 2003).

of the mixing process between the fuel gas and air. For fuel mechanism, the NO_x formation is characterised by the chemical reactions below.

$$O + N_2 + M \leftrightharpoons N_2O + M \tag{2.11}$$

$$H + N_2O \leftrightharpoons NO + NH \tag{2.12}$$

$$O + N_2O \leftrightharpoons 2NO \tag{2.13}$$

Fuel NO_x is not shown in Figure 2.19 since it is not dependent on temperature but fuel type. Conversely prompt NO_x is independent of temperature. The thermal NO_x is highly dependent on temperature where it is consistently low below 1,500 K and starts to increase above 1,500 K.

The influence of air temperature on NO_x emissions for conventional and MILD combustion mode is shown in Figure 2.20. For conventional combustion mode, an exponential increase of NO_x emission when the air preheating temperature increase. When the preheated air higher than the fuel auto-ignition temperature (about 1,150 K), the MILD combustion mode can be seen with ultra-low NO_x emission produced. Comparing both mode, the difference is the concentration of oxygen mole fraction in the reaction zone where local combustion reactions take place. For MILD combustion mode, very low oxygen mole fraction in air supply suppress the formation of NO_x due to lack of oxygen to react with available nitrogen. It reduced more than 90 % when comparing the same level of air preheating temperature (1,300 K) for conventional and MILD combustion.

2.5.2.3 Carbon Monoxide

Incomplete combustion will produce pollutant emissions including carbon monoxide (CO) and UHC. Due to its severe effect to the health and possible life threatening hazard to the high concentration inhalers, carbon monoxide is labelled as a highly toxic gas. Raub (1999) reported that carbon monoxide will prevent the cells and tissues from oxygenation by creating the blood carboxyhaemoglobin. Westbrook and Dryer (1984) summarised and simplified the oxidation process to form CO_2 as:

$$\mathrm{C_xH_yO_z} + \frac{1}{2}\left(\mathrm{x} + \frac{\mathrm{y}}{2} - \mathrm{z}\right)\mathrm{O_2} \rightarrow \mathrm{xCO} + \frac{\mathrm{y}}{2}\mathrm{H_2O} \tag{2.14}$$

$$\mathrm{CO} + \frac{1}{2}\mathrm{O_2} \rightarrow \mathrm{CO_2} \tag{2.15}$$

In Equation (2.14), the carbon partially oxidises to become CO and it needs more energy to form CO_2 (Equation 2.15) to form a complete combustion by-product. Incomplete combustion will only oxidise for step 1 and not react for step 2. This shows that CO is produced when there is insufficient oxygen or reaction time during high temperature to completed the oxidation of carbon to CO_2. Rich fuel combustion is also likely to produce high levels of CO due to high hydrocarbons with low oxygen. This condition needs to be avoided in order to reduce CO in flue gas.

2.5.2.4 Carbon Dioxide

Carbon dioxide is a product of complete combustion. The combustion of methane and oxygen can be written in a stoichiometric combustion equation as shown in Equation 2.16. The main properties of carbon dioxide are colourless gas and odourless at low concentration and sharp and acidic at high concentration.

$$\mathrm{CH_4} + 2\mathrm{O_2} \rightarrow \mathrm{CO_2} + 2\mathrm{H_2O} \tag{2.16}$$

Carbon dioxide is a greenhouse gas and the combustion of carbon-based fuels from the industrial revolution until now has rapidly increased the concentration of carbon dioxide in the atmosphere. This higher atmospheric carbon dioxide has led to the global warming phenomenon. In order to reduce and mitigate the impact of carbon dioxide, currently there are a few actions being undertaken. The actions are increase the low carbon energy sources, increase the biogas or biofuel which is a good carbon cycle and the carbon capture and storage (CCS) to reduce the release of carbon dioxide to the atmosphere.

2.6 Summary

In much of the literature, MILD combustion has been proven to be a good technique over other emission-curbing combustion technologies. Recently, many numerical and experimental studies, from laboratory scale to industrial applications, have been performed on MILD combustion. In this literature study, the general and detailed evolution of MILD combustion is discussed. The improvement of MILD combustion is not just to increase the efficiency, but also helpful to improve combustion quality in order to meet the requirements of more stringent emission rules and legislation. From the literature review, it can be seen that there is limited research available on open MILD combustion systems, with particularly on the biogas as a fuel. The literature review presented in this chapter indicates that experimental work on MILD combustion is very important to study the possibility and efficiency of a furnace using biogas as a fuel. This is very significant for open-top industrial burners, which are used in most of the heating and curing processes in production and assembly factories. The MILD combustor is designed to fulfil the requirement of industrial burners by having a high efficiency and low exhaust gas emissions. Therefore, a further numerical and experimental investigation into this combustion regime will be carried out in this thesis. Some researchers have successfully used a closed furnace without EGR to achieve MILD combustion but other researchers used experimental and simulation techniques to investigate the combustion and EGR behaviour on MILD combustion.

Chapter 3

Computational Fluid Dynamics Modelling

This chapter discusses the simulation and experimental setup designed using Computational Fluid Dynamics (CFD) before the experimental work commenced. The introduction and theory of CFD are also summarised at the beginning of the chapter. Section 3.3 deals with the setup of the model geometry, boundary conditions and solver selection to predict the combustion behaviour of the MILD combustion burner. Section 3.4 deals with designing the experimental setup.

3.1 Introduction

The application of computer simulations to improve many complex engineering processes has rapidly expanded in line with the computer's development over the last few decade. CFD was simultaneously advanced for simulation of the laboratory and industrial-scale engineering problems. CFD was started in the 1950s, stimulated by the advent of high-performance computer systems. CFD offers reliable predictions of the effect of various parameters on combustion performance. The results of modelling can be viewed quickly and easily, compared to the time and cost required by the equivalent experimental work. Simulations frequently present information on physical quantities that are quite difficult to measure.

CFD has been extensively used for fluid flow, combustion and heat transfer as well as to explore and design engineering hardware (Baukal et al., 2001; Davidson, 2002) including combustion chambers. It is also increasingly being used for the optimisation of gas burners (Scharler and Obernberger, 2000), industrial gas furnaces (Dally et al., 2004; Riahi et al., 2012) and coal combustion (Calchetti et al., 2007; Saha et al., 2013). CFD may help in optimising burners' performances through parameters such as injection nozzles, fuel and oxidant mixing and flue gas recirculation.

The objective of the modelling is to predict and analyse the flow and combustion behaviour before the experimental work takes place. This is to reduce trial and error in the design and development stage. This study focused on the different parameter settings and burner head design of the combustion process. The CFD results were later validated against the combustion experimental results. The CFD commercial software package ANSYS Fluent 14.5 was used and run on a High Performance Computing (HPC) computer at The University of Southern Queensland. The computations have been carried out using four processors of a 30-node Sun X2200 load sharing server. Each node has 16 GB of RAM and 2 quad-core 2.7 GHz CPUs with an AMD Opteron processor (USQ, 2012).

CFD modelling often gives the desired result when numerically solving many engineering problems (Rahimi et al., 2006; Mollica et al., 2010; Rashmi et al., 2011). Numerical results alone are not fundamentally strong without validation by experimental work. Different scales of MILD combustion setup have been simulated using CFD software over the past few decades (Danon, 2011). In this project, CFD modelling was used to design the geometry that can achieve MILD combustion. The parameters involved in the modelling were air and fuel supply volume flow rates (which influence λ), exhaust opening size and fuel properties.

3.2 Governing Equations

The governing equations for fluid flow modelling are the continuity equation (or mass conservation equation), momentum conservation equation (Navier–Stokes equation) and energy equation (Ferziger and Peric, 1999). In combustion modelling, the fluid flow modelling is coupled with the chemical reaction equation. The fluid properties such as density, viscosity, specific heat, thermal conductivity, molecular diffusivity and radiation have to be given as a function of the stated variables.

3.2.1 Mass Conservation Equation

The continuity equation is a mass balance equation and overall mass in the system is conserved. The general form of continuity equation or the conservation of mass equation is:

$$\frac{\partial \rho}{\partial t} + \nabla.(\rho \upsilon) = 0 \tag{3.1}$$

where ρ is the fluid density and υ is the average flow velocity.

3.2.2 Momentum Conservation Equation

The Navier-Stokes equation is the momentum conservation equation and can be written as:

$$\frac{\partial \left(\rho \upsilon_i\right)}{\partial t} + \frac{\partial \left(\rho \upsilon_i \upsilon_j\right)}{\partial x_j} = -\frac{\partial p}{\partial x_i} + \frac{\partial \tau_{ij}}{\partial x_j} + \rho g + F_i \tag{3.2}$$

where p is the static pressure, ρg is the gravitational force and F_i is other forces. The viscous stress tensor is:

$$\tau_{ij} = \mu \left(\frac{\partial \upsilon_i}{\partial x_j} + \frac{\partial \upsilon_j}{\partial x_i} \right) - \frac{2}{3} \mu \delta_{ij} \left(\frac{\partial \upsilon_k}{\partial x_k} \right) \tag{3.3}$$

where μ is the molecular viscosity and δ_{ij} is the Kronecker δ.

3.2.3 Combustion Species Equation

The governing equation is how the process is written in mathematical forms in terms of related qualities like temperature, pressure, density and viscosity. For gas combustion, the governing equations are summarised below (Williams, 1985). Species:

$$\begin{aligned} \frac{\partial(\rho y_\alpha)}{\partial t} + \nabla . (\rho u y_\alpha) &= -\nabla . (J_i^\alpha) + \rho W_\alpha \\ \alpha &= 1, 2, ... n_s \end{aligned} \tag{3.4}$$

The molecular diffusive flux term (J_i^α) can be approximated by the gradient-diffusion model (Boussinesq model).

$$J_i^\alpha = \rho D_\alpha \frac{\partial y_\alpha}{\partial x_i} = -\frac{\mu}{Sc_\alpha} \frac{\partial y_\alpha}{\partial x_i} \tag{3.5}$$

where D_α is the molecular diffusivity of the species α. The Schmidt number (Sc_α) and Lewis number (Le_α) are:

$$Sc_\alpha = \frac{\mu}{\rho D_\alpha} \tag{3.6}$$

$$Le_\alpha = \frac{D}{D_\alpha} = \frac{\lambda}{\rho c_p D_\alpha} \tag{3.7}$$

The relationship between the Lewis number and the Schmidt number can be shown by a combination of Equations (3.6) and (3.7) and summarised below:

$$Sc_\alpha = \frac{\mu}{\rho D Le_\alpha} \tag{3.8}$$

The chemical source term can be calculated using Equation (3.9) and the reaction rate is obtained by using Equation (3.10). The Arrhenius equation (Equation 3.11) is used to determine the reaction rate constant, k.

$$W_\alpha = \frac{w_\alpha}{\rho} \sum_j \nu_{\alpha j} \omega_j \tag{3.9}$$

$$\omega_j = k_{fj} \prod_{\alpha=1}^{n_s} [X_\alpha]^{v'_{\alpha j}} - k_{bj} \prod_{\alpha=1}^{n_s} [X_\alpha]^{v''_{\alpha j}} \tag{3.10}$$

$$k = A T^\beta \exp\left(-\frac{E_a}{RT} \right) \tag{3.11}$$

The rate of progress variable ω_j is the net strength of reaction j in the forward direction and w_α is the mean molecular weight. ρ is the density, E_a is the activation energy and A and β are constants. R is the universal gas constant and T is the temperature. To model the chemical process in the gas phase, during the flow and mixing, the gas composition will change due to the chemical reaction and the detailed chemistry describes the basic reactions at a molecular level. Detailed explanations for this process can be found in Peters (2004); Warnatz et al. (2006) and Glassman and Yelter (2008).

3.2.4 Energy Conservation Equation

The conservation equation for enthalpy can be written as:

$$\frac{\partial(\rho h)}{\partial t} + \frac{\partial(\rho v_i h)}{\partial x_i} = -\frac{\partial \dot{Q}''_i}{\partial x_i} + \tau_{ij}\frac{\partial v_i}{\partial x_j} + \rho v_i F_i + S_h \tag{3.12}$$

where h is the total specific enthalpy (J/kg) and $\dot{Q}''_i$ is the heat flux (W/m^2). When more than one species involved, h can be calculated by:

$$h = \sum_\alpha Y_\alpha h_\alpha \tag{3.13}$$

where Y_α is the mass fraction and h_α is the total enthalpy for species α in the mixture. h_α can be defined as:

$$h_\alpha = h^o_{T_r,\alpha} + \int_{T_r}^{T} C_{p,\alpha}(T)dT \tag{3.14}$$

where h^o is the enthalpy of formation, T_r is the reference temperature and $C_{p,\alpha}(T)$ is the specific heat at constant pressure of species α.

3.2.5 Turbulence Model

There are various models available to solve the turbulent flow. The choice of turbulence model will depend on considerations such as the physics encountered in the flow, the established practice for a specific class of problem, the level of accuracy required, the available computational resources and the amount of time available for the simulation (Fluent, 2012). Therefore, understanding of the specific turbulence problems such as capabilities and limitations of the various options are essential to ensure that the turbulence model chosen is the best.

Most of the CFD simulations for MILD combustion have been based on the Reynolds–Averaged Navier–Stokes (RANS) equations using the standard or realisable k–ε model (Orsino et al., 2001; Christo and Dally, 2005; Danon et al., 2010). The k–ε model developed by Launder and Spalding (1974) is widely used to solve turbulence flow problems. The realisable k–ε turbulence model was developed by Shih et al. (1995) based on the standard k–ε turbulence model. For MILD combustion simulation, there is no evidence from the literature to show any superior performance of the realisable k–ε compared to the standard k–ε model (Verssimo et al., 2012). The realisable k–ε model was the upgraded model to counter the weakness of the standard k–ε model, in terms of predicting round jets, flows with a recirculation region and swirling flows (Wilcox, 1994). Transport equations for the realisable k–ε model are as follows:

$$\begin{aligned}\frac{\partial}{\partial t}(\rho k)+\frac{\partial}{\partial x_j}(\rho k u_j) &= \frac{\partial}{\partial x_j}\left[\left(\mu+\frac{\mu_t}{Pr_k}\right)\frac{\partial k}{\partial x_j}\right]+G_k+G_b-\rho\varepsilon \\ &\quad -Y_M+S_k \qquad (3.15)\\ \frac{\partial}{\partial t}(\rho \varepsilon)+\frac{\partial}{\partial x_j}(\rho \varepsilon u_j) &= \frac{\partial}{\partial x_j}\left[\left(\mu+\frac{\mu_t}{Pr_\varepsilon}\right)\frac{\partial \varepsilon}{\partial x_j}\right]+\rho C_1 S\varepsilon-\rho C_2\frac{\varepsilon^2}{k+\sqrt{v\varepsilon}} \\ &\quad +C_{1\varepsilon}\frac{\varepsilon}{k}C_{3\varepsilon}G_b+S_\varepsilon \qquad (3.16)\end{aligned}$$

where G_k is the generation of turbulent kinetic energy due to the mean velocity gradients, G_b is the generation of turbulent kinetic energy due to buoyancy, Y_M is the contribution of the fluctuating dilatation in compressible turbulence to the overall dissipation rate, Pr_k and Pr_ϵ are the turbulent Prandtl numbers, S_k and S_ε are source terms and C_1, C_2 and C_3 are constants.

Compared to the standard k–ε, the realisable k–ε more accurately predicts the distribution of the dissipation rate of round jets. In this research, the convergence behaviour of realisable k–ε was more stable compared to the standard k–ε model. The model was developed with two additional transport equations to represent the turbulent properties of the flow. The model has been used to solve free shear layer flows with a relatively small pressure gradient (Bardina et al., 1997). The model is good for wall-bounded and internal flows, especially when the mean pressure gradient is small. The accuracy of the calculation made by the k–ε model is well accepted. The flow at the inlet area for air and fuel injecting is mostly turbulent due to the bluff-body burner design. It involves a complicated combination of small-scale and large-scale flow structures such as turbulent shear layers, jets and boundary layers (Devi et al., 2004; Ling and Tun, 2006).

3.3 Modelling Approach

In this study, ANSYS Fluent 14.5 was used to model MILD combustion in the mode of non-premixed combustion. The second-order scheme was used to discretise the governing equations including mass, momentum, energy and species in addition to the turbulence transport and combustion model. The mixture fraction based chemistry models, which play a fundamental role in non-premixed combustion, were used in this work. Lupant et al. (2007) and Mancini et al. (2003) solved a mixture fraction transport equation with a β-function PDF to model the turbulence-chemistry interaction. The equilibrium assumption was used for the thermo-chemical database. Figure 3.1 shows the simulation flow-chart for the numerical analysis.

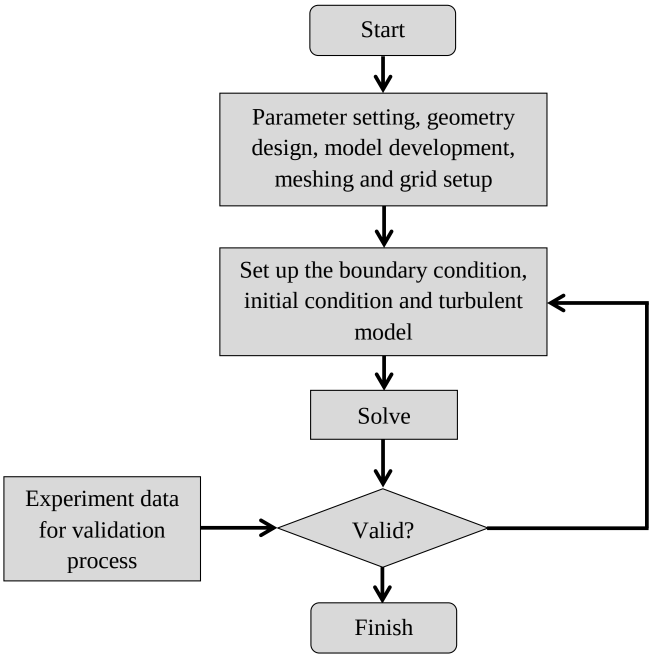

Figure 3.1: Modelling and simulation flow chart.

3.3.1 Combustion

Non-premixed combustion was used by many other researchers for MILD combustion (Dally and Peters, 2002; Medwell et al., 2007; Merci et al., 2007; Colorado et al., 2009; Mardani et al., 2010). In this study, non-premixed combustion with chemical equilibrium and non-adiabatic energy treatment were used. This approach has been specifically developed for the simulation of turbulent diffusion flames with fast chemistry. A number of previous numerical models by other researchers use chemical equilibrium (Orsino et al., 2001; Tobacco et al., 2002; Lupant et al., 2007). Specifically, Lupant et al. (2007) found that the computed fields of temperature in the horizontal plane give good results and the temperatures obtained far downstream and near the walls are correctly estimated. These mean that chemical equilibrium is acceptable to use for the numerical modelling for MILD combustion. However, in MILD combustion the low reactants concentration have a lower heat release rate and lower Damköhler number in comparison with the ordinary combustion regime (Katsuki and Hasegawa, 1998; Plessing et al., 1998). This condition leads to an increase of the chemical timescales and the enhanced turbulence levels reduce the turbulent mixing timescales. This behaviour may cause the fast chemistry to be inferior to the finite-rate chemistry model. The non-adiabatic modelling option includes the radiation and wall heat transfer. The RANS equations together with a realisable k–ε turbulence model (Shih et al., 1995; Saha et al., 2014) are solved. In the current study, 16 species are solved at 56 grid points in the mixture fraction space for a range of enthalpies to yield 24,472 potential compositions in the PDF look-up table.

3.3.2 Radiation Model

The radiation model used in this work is the Discrete Ordinates (DO) model (Chui and Raithby, 1993). The DO radiation model solves the radiative transfer equation for a finite number of discrete solid angles in the Cartesian coordinate system. The DO model is applicable to a wide range of optical thicknesses. Because the optical thickness for MILD flames is not well defined or well known, the DO model is a good selection. The model solves a radiative transfer equation. The absorption coefficient used is the Weighted Sum of Gray Gas Model (WSGGM) (Hottel and Sarofim, 1967; Smith et al., 1982) and used for spray combustion (Choi and Baek, 1996) and gas furnace (Liu et al., 1998). The WSGGM is selected due to it being a reasonable compromise between the oversimplified gray gas model and a complete model.

3.3.3 Boundary Conditions

Boundary conditions have to be carefully specified to minimise errors. The success of CFD simulations strongly depends on the boundary conditions selection (Ganesan et al., 2004). A velocity inlet boundary condition was used at the air and fuel supply pipe. An outlet vent boundary condition was used to define the exhaust outlet on the top of the burner. A no-slip wall boundary was used. A standard wall function was used for the boundary condition for velocity at the combustion chamber wall. The temperature of the wall was set at 300 K and an exhaust fan with zero gauge pressure was used for the exhaust outlet boundary condition. The furnace wall boundary conditions were set at a constant temperature (300 K) to ensure it was a similar condition to the experimental work setup.

3.3.4 Modelling Solutions

All the governing equations were solved using the second order upwind discretisation scheme for higher accuracy of the calculation. For triangular, tetrahedral meshes and more complex meshing, the flow was never aligned with the mesh. Second-order discretisation generally obtained more accurate results compared to the first-order scheme (Fluent, 2010). Double precision was used to reduce floating point errors. The pressure-based solver gives an option to solve the flow problem in either a segregated or coupled manner. In order to have a better relationship between pressure and velocity, the COUPLE method was used for the pressure-velocity coupling scheme with a least-squares cell-based gradient and presto for pressure discretisation scheme. For steady-state flows, the COUPLE method gives a robust, efficient single-phase implementation and good performance compared to the segregated solution schemes (Fluent, 2012). The COUPLE algorithm is necessary for transient flows, especially when large time steps are used or the meshing quality is not good enough.

Because of the iterative nature of the solution methodology, it is necessary to determine when the solution has converged. The residuals are used for this purpose; the absolute values must be less than 0.001 and 0.000001 for the solution to be deemed to have converged. The convergence criteria for the simulation residuals for all the study parameters were set at 10^{-3}. All the residuals achieved this target except for the continuity and mixture fraction variance transport equations, whose residuals were less than 0.002. The final model geometry and boundary conditions are described in Section 3.4.3.

3.4 Simulation for Geometry Design

The design modeller software in ANSYS workbench was used to draw the MILD furnace. The early stage of the combustion chamber development started with a CFD simulation of a basic enclosed combustion chamber as in Figure 3.2(a).

3.4.1 Preliminary Model

The computational work began with normal combustion without EGR to check the combustion of LCV gas (biogas) consisting of 60 % methane and 40 % carbon dioxide by mole fraction (Figure 3.2(a)). The fuel enters the combustion chamber through a 20 mm diameter fuel supply pipe at 5–10 m/s into the combustion chamber. Air was injected at 10–15 m/s through an annulus gas supply pipe downstream of the chamber. The exhaust ducting consists of a vent damper acting as a throttle for the flue gas flow. If the vent damper is totally closed, the flue gas will not flow out of the chamber. The vent damper can be adjusted to control the volume of flue gas flow out from the chamber and flow through into the EGR pipe. More details on the burner and chamber specifications are shown in Table 3.1.

Once the combustion was stable, then two EGR pipes were added to the system to test the combustion with an oxidiser diluted by flue gas through the EGR

Table 3.1: Typical data for furnace and burner in Figure 3.2(c).

Item	**Data**
Fuel	60 % CH_4 + 40 % CO_2 by mole fraction
Oxidiser	Atmospheric air, heated to 800 K
Fuel supply	Round 1,256 mm^2, 5–10 m/s
Air supply	Annulus 5,140 mm^2, 10–15 m/s
Bluff-body diameter	40 mm
Chamber size	Diameter 375 mm, Height 650 mm
EGR	2 EGRs with 386.9 mm^2 each inlet
Mesh method	Tetrahedrons (Patch conforming method)
Elements/nodes	421,172 elements and 92,034 nodes

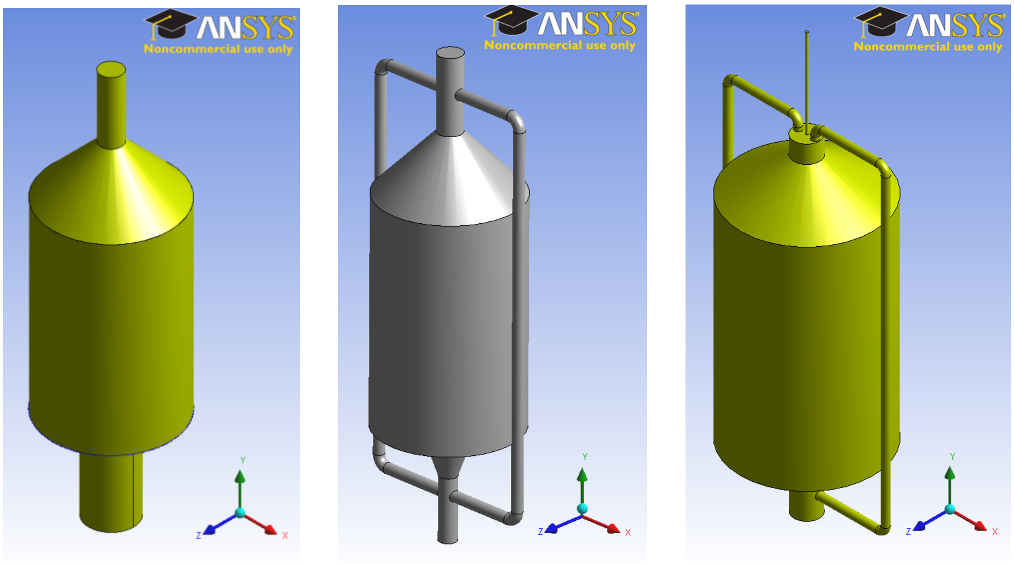

(a) (b) (c)

Figure 3.2: First model of combustion chamber geometry (a) no EGR pipe (b) with 2 EGR pipes (c) with 2 EGR pipes and EGR curved inlet.

(Figures 3.2(b) and 3.2(c)). At the beginning of the simulations (Figure 3.2(b)), the EGR pipe was connected perpendicular and straight to the air supply pipe and exhaust outlet pipe. Then the problem encountered in the simulations was the fluid did not smoothly flow into the EGR pipe. This because to the hot flue gas was flowing straight to the exhaust on the top of the chamber even though the opening of the exhaust is very small. An improvement was made to the inlet of the EGR. The smooth corner to help the fluid flow into the EGR pipe was added (Figure 3.2(c)). The result was encouraging, with the flow showing significant improvement.

3.4.2 Four-EGR Model

The next improvement of the model was made by adding two more EGR pipes to become four EGRs. This new design can be seen in Figure 3.3. The fuel enters the combustion chamber through the fuel supply pipes underneath the apparatus. There are four small fuel supply pipes with a size of 5 mm diameter. The total inlet area is 78.5 mm^2. It is then combined to become one fuel nozzle and enter the combustion chamber. The opening of the fuel nozzle is 24.3 mm^2. The fuel is supplied at 20 to 40 m/s depending on the need for lean or rich combustion.

Fresh air was injected through a 5 mm diameter supply pipe at the side of each EGR pipe to induce the EGR to flow downward. The injected fresh air has to be mixed with the EGR gas. The mixture then flows through four EGR pipes at the downstream part of the apparatus. It is then combined at the mixing cone located below the air nozzle. From this mixing cone, the mixtures enter the combustion chamber through the annulus air nozzle surrounding the fuel nozzle.

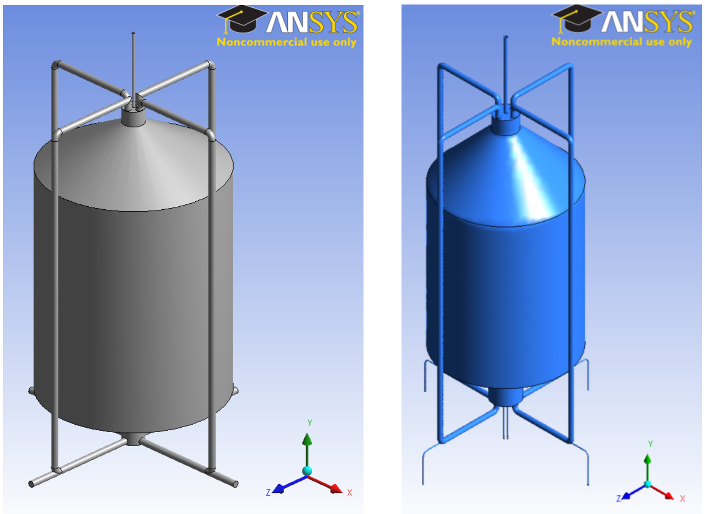

(a) (b)

Figure 3.3: Second model with 4 EGRs, (a) air supply internal diameter is 22 mm, (b) air supply internal diameter is 5 mm.

Table 3.2: Typical data for furnace and burner in Figure 3.3(b).

Item	**Data**
Fuel	60 % CH_4 + 40 % CO_2 by mole fraction
Oxidiser	Atmospheric air, heated to 800 K
Fuel supply	4 × 19.6 mm^2, 20–40 m/s each
Air supply	4 × 19.6 mm^2, 60–120 m/s each
Bluff-body diameter	40 mm
Chamber size	Diameter 600 mm, Height 860 mm
EGR	4 EGRs with 386.9 mm^2 each inlet
Mesh method	Tetrahedrons (Patch conforming method)
Elements/nodes	501,831 elements and 111,975 nodes

The two external EGR pipes in the first model were increased to four pipes. This is to ensure more exhaust gas can be re-circulated through EGR pipes to dilute the O_2 and preheat the oxidant. More detailed burner and chamber specifications are shown in Table 3.2.

After the computational testing and analysis, the bluff-body burner with 24.3 mm^2 fuel inlet and 97.3 mm^2 oxidiser inlets was chosen. The maximum temperature of the combustion is 1540 K which is below the limit of the temperature for the rapid formation of NO_x. The temperature of the combustion zone is 1200 to 1540 K (Figure 3.4). The inside wall temperature is about 750 to 800 K and the EGR flow is about 700 to 750 K. The flow of the EGR is below 5 m/s since the opening of the chamber outlet is 176.6 mm^2. The total supply inlet is 486.8 mm^2 with the ratio of supply inlet to outlet being 2.8:1. In order to increase the EGR flow, this opening can be reduced, thereby increasing the EGR ratio. An EGR ratio of 50 % means half of the flue gas will flow back to the combustion chamber.

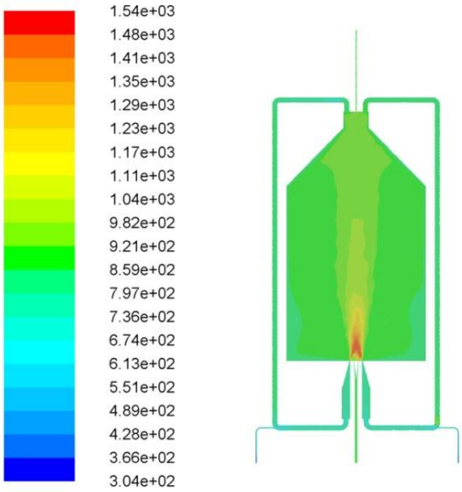

Figure 3.4: Combustion temperature in the chamber for Figure 3.3(b).

The EGR flow is very important to achieve MILD combustion. Flue gas from the EGR will preheat the reactant and dilute the oxygen in the fresh air (Tsuji et al., 2003). The oxygen content in the oxidiser will be reduced from 21 % to the required level. Figure 3.5 shows the velocity magnitude, only showing the range between −5.0 to 5.0 m/s. The flow magnitudes are highest at the centre of the chamber and dramatically reduce to very low speeds far from the centre. These velocity magnitude differences in the flow field will create different pressure gradients which cause the turbulence in the flow field. The turbulent flow will distribute the flame heat throughout the combustion chamber and produce a homogeneous chamber temperature.

There are four air supplies, one at each EGR. Every air supply pipe diameter is 5 mm with 100 m/s air velocity input, which produces total volume flow rate for the air of 7,850 cm^3/s. If air is injected at 100 m/s and the supply pipe diameter is bigger than 5 mm, then the EGR flow will be in the reverse direction. This is due to the volume flow rate being higher than the allowed value for the air nozzle in the combustion chamber. The air will reverse flow through the EGR pipe, which is an unwanted condition. Figure 3.6 shows the EGR flowing in the reverse direction. The EGR should flow from upstream to downstream but this setting make EGR flow in the reverse direction. Each EGR pipe is 379.9 mm^2. The EGR should flow from upstream to downstream and mix with fresh air before combustion occurs in the chamber. Figure 3.7 shows the correct flow of the EGR. This flow can be achieved when the air supply is controlled below 100 m/s for a 5 mm air supply pipe.

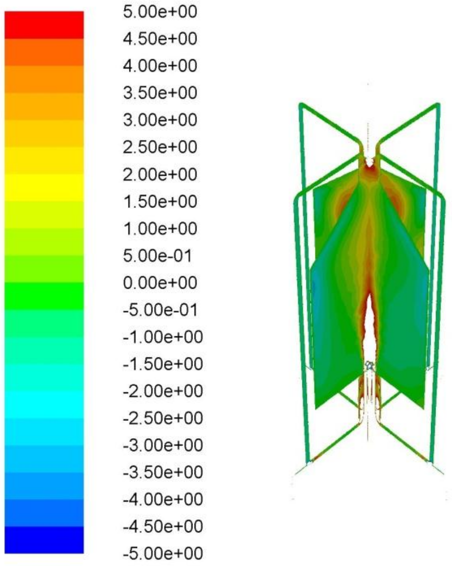

Figure 3.5: Velocity magnitude between −5.0 and 5.0 m/s for Figure 3.3(b) with gas supply at 20 m/s and air supply at 80 m/s.

3.4.3 Final Model

The open furnace MILD combustion was modelled using the ANSYS design modeller and simulated with the size of 2.2 m height and 0.6 m width (Figure 3.8). The injection of air and fuel was designed as a bluff-body to help the air-fuel mixing process. The fuel nozzle was in the middle with a diameter of 1 mm and an annulus air nozzle around the fuel nozzle with an opening size of 1,570 mm^2 (Figure 3.9). The air and fuel supply pipe size ratio for this model is 4:1. The final EGR is shown in Figure 3.8 with 4 EGR pipes and a 108 mm exhaust pipe with a vent damper to control the exhaust opening and closing.

The open furnace model was developed and numerically studied using FLUENT to optimise parameters toward achieving MILD combustion in the chamber. The chamber design was finalised with four EGR pipes and the downward flow for flue gas was achieved. The LCV gas used in the study consists of 60 % methane and 40 % carbon dioxide by mole fraction. From the CFD results, the temperature of the combustion zone is 1200–1500 K and the temperature for the inside wall of the chamber and EGR pipe flow is about 750–800 K. The flow for the EGR is below 5 m/s since the opening for the chamber outlet is relatively big: 15 mm in diameter. This EGR flow rate can be increased by reducing the exhaust flow rate and increasing the EGR pipe diameters from 11 to 50 mm. The final EGR pipes are each 50 mm. More details on the burner specification are shown in Table 3.3. There are two driving forces for EGR: the percentage of vent damper opening for the exhaust, which encourages flow to be redirected into the EGR inlets; and the fresh oxidant supply jet near the end of each EGR pipe (on the side injected into the downstream part of the EGR pipe) which induces flow through the pipes. The

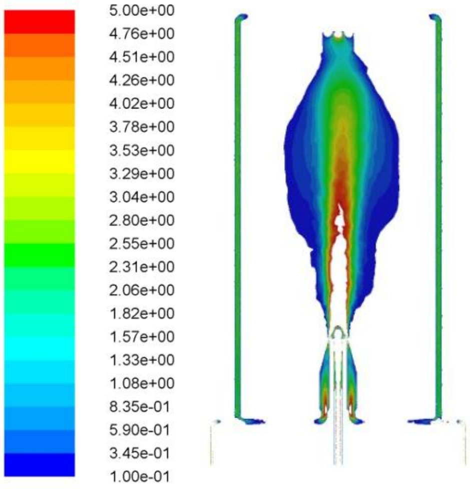

Figure 3.6: Velocity in Y direction between 0.1 and 5.0 m/s for Figure 3.3 (b) with gas supply at 40 m/s and air supply at 120 m/s producing reversed flow in EGR.

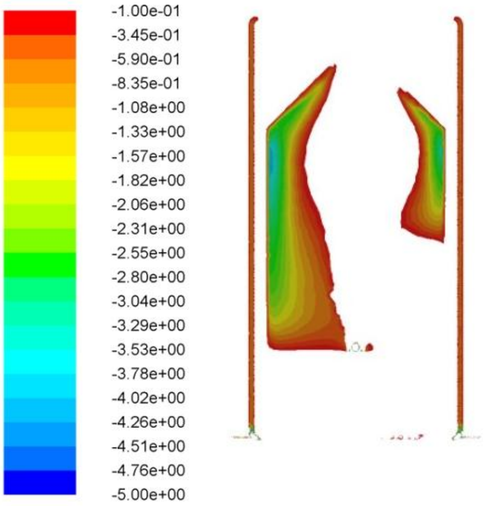

Figure 3.7: Velocity in Y direction between −0.1 and −5.0 m/s for Figure 3.3 (b) with gas supply at 20 m/s and air supply at 80 m/s producing correct flow in EGR.

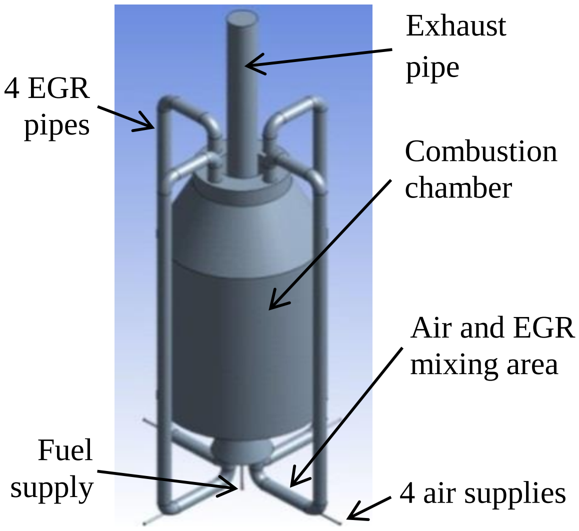

Figure 3.8: The geometry and boundary conditions.

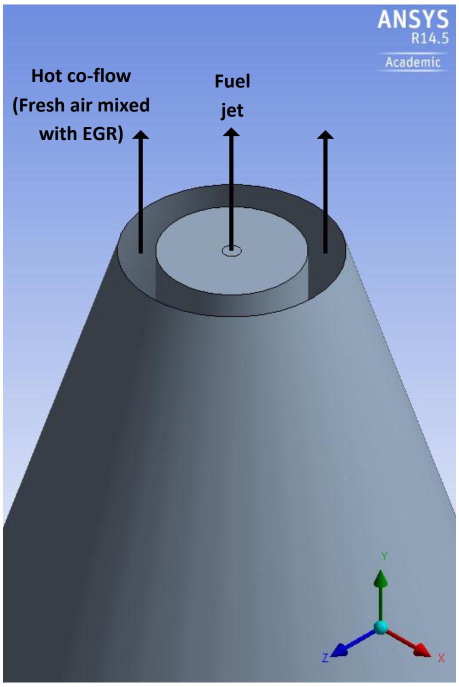

Figure 3.9: Fuel and air nozzle geometry.

flue gas flow through the EGR pipe for the current results is calculated at 35.7 % with the balance (controlled by a butterfly valve) allowed to flow out through the exhaust pipe on top of the burner. If the model is symmetrical, the model can be cut in half (Figure 3.10(b)). The smaller the model, the shorter the modelling time and CPU resources become less intensive which reduces simulation cost.

The CFD commercial software has successfully been used to develop an open furnace for MILD combustion. The simulation of MILD combustion achieved the

Table 3.3: Typical data for furnace and burner in Figure 3.8.

Item	**Data**
Fuel	60 % CH_4 + 40 % CO_2 by mole fraction
Oxidiser	Atmospheric and synthetic air
Fuel supply	1 × 78.5 mm^2, 40–100 m/s
Air supply	4 × 78.5 mm^2 each, 80–150 m/s each
Bluff-body diameter	40 mm
Chamber size	Diameter 600 mm, Height 860 mm
EGR	4 EGRs with 1962 mm^2 each inlet

MILD state. The combustion has to be enclosed to collect the exhaust gas which is utilised to dilute the oxygen in the oxidant stream and, at the same time, increase the oxidant temperature. Four EGR pipes were added so the exhaust gas can be mixed with the fresh supply air. The building and development of the furnace was carried out at the University of Southern Queensland mechanical workshop. The furnace was equipped with three high-temperature glass windows to monitor and record the flame propagation.

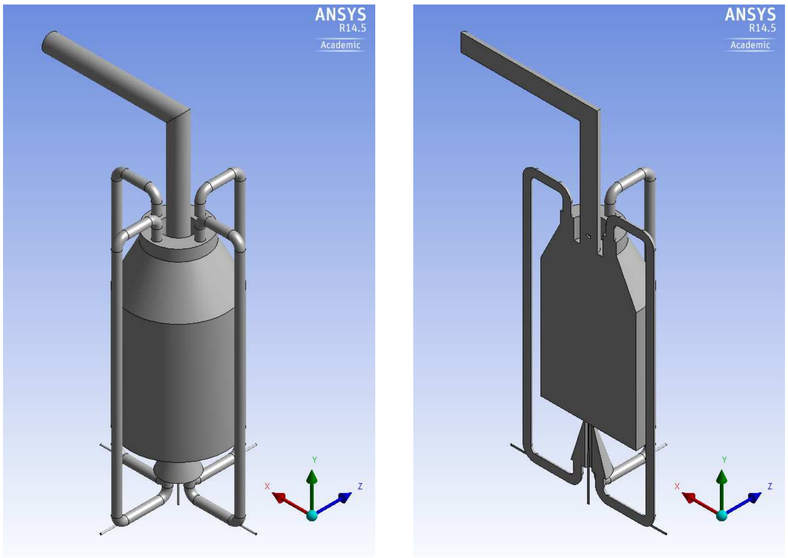

(a) (b)

Figure 3.10: Design modeller for the MILD furnace (a) full model, (b) half model axisymmetric at XY-plane model.

3.5 Mesh Generation

The most critical part of the CFD process is model meshing. The mesh is very important and mesh size is known to influence the accuracy of the simulation results. Meshing will create a grid of cells or elements on which all the desired fluid flow equations are to be solved. The size of the grid will have a significant impact on the computational time and data storage, which together are called the

Table 3.4: Details of mesh settings with elements and nodes count.

Sizing	**Mesh grid A**	**Mesh grid B**	**Mesh grid C**	**Mesh grid D**
Smoothing	High	High	High	High
Transition	Slow	Slow	Slow	Slow
Minimum size	0.50 mm	0.25 mm	0.15 mm	0.10 mm
Maximum size	70.0 mm	40.0 mm	20.0 mm	10.0 mm
Elements count	598,255	687,940	897,703	1,192,425
Nodes count	218,751	247,254	302,299	371,167

"cost of the simulations". The grid also will significantly affect the convergence speed and the solution accuracy. Coarse grids (few cells) will give a high speed of convergence but most likely low accuracy, while fine grids will give a low speed of convergence with high accuracy. Industrial CFD problems normally consist of large numbers of cells, typically several hundred thousand grid cells (Peters, 2004).

The method of meshing chosen here is tetrahedrons patch conforming with advanced sizing function of proximity and curvature. The active assembly, fine span angle centre and fine relevance centre setting were used for all grids. The details of the settings can be seen in Table 3.4. The smallest, average and largest cell sizes were 0.2, 4.9 and 10 mm respectively. The three-dimensional image of the mesh geometry can be seen in Figure 3.11. The grid sizes are non-uniform and a fine mesh was applied in critical regions. Likewise coarser grids were applied to regions where the variations in fluid flow are relatively small and far from the boundary. The mesh element refinement was used at the air supply pipe (Figure 3.12(a)), fuel supply pipe (Figure 3.12(b)), air and fuel nozzles (Figure 3.13(a)) and inlet and vent damper at exhaust flow control (Figure 3.13(b)).

Inflation is very important for the near-wall area or boundary layer mesh. The near-wall was meshed with inflation layers and the nozzle area was meshed with inflation, body of influence and edge sizing techniques. The meshing process must be started with a coarse mesh to check the quality of the statistics. The mesh inflation for the near-wall region was five layers with a growth rate of 20 % and maximum thickness of 2.0 mm. This layer of the element can be seen in Figures 3.12 and 3.13.

3.5.1 Meshing Quality

The required qualities to be checked are the skewness and aspect ratio on the mesh metric and smoothness (change in cell size). The maximum skewness must be below 0.98 (Fluent, 2006) or the solution will be prone to produce divergence errors and will not converge as desired. The overall range of skewness is from zero to one, where the best is zero and worst is one. The skewness value is calculated based on an equilateral or equiangular shape. For equilateral shapes, the skewness is the optimal cell size minus the actual cell size, normalised by the optimal

Figure 3.11: Three-dimensional meshing of geometry.

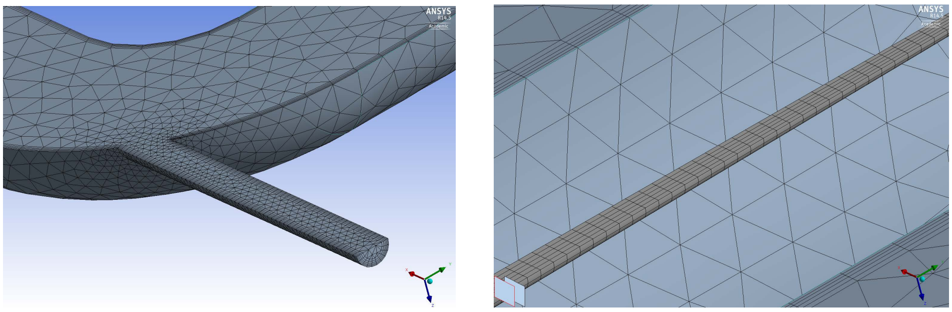

(a) Air supply

(b) Fuel supply

Figure 3.12: Meshing for air and fuel supply pipes.

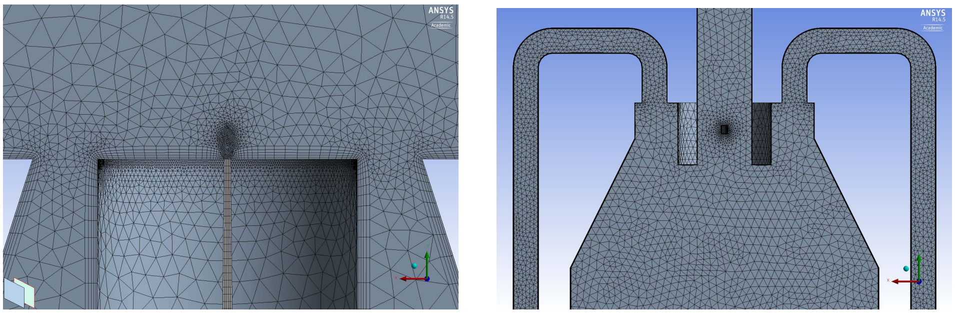

(a) Air and fuel nozzles

(b) Exhaust vent damper

Figure 3.13: Fine meshing for critical areas.

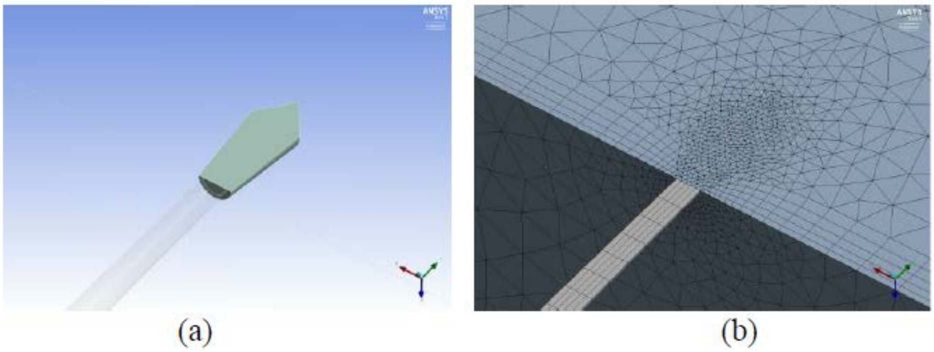

Figure 3.14: Body sizing meshing for body of influence (a) geometry (b) meshing.

cell size. In this simulations the coarse mesh give a maximum skewness of 0.9817, which is higher than the allowable value. Smaller mesh grids are needed to reduce the skewness. When the meshing was finalised with fine grids (mesh grid D), the maximum skewness was lowered to 0.8283. The aspect ratio was calculated by dividing the longest edge length by the shortest edge length. The best aspect ratio is 1.0, which means the cell is uniform. The cell shapes are triangle and quadrilateral for two-dimensional problems and tetrahedron, hexahedron, pyramid wedges and polyhedron for three-dimensional problems. The smoothness or the change in the cell size must be gradual and not more than 20 % change from one cell to the next. If there are cells that jump in size, the smoothness will be very bad and the solution will be hard to converge.

The node and element quantity is very critical since it will affect the final result and the computational time, which is also the computational cost. The higher the meshing element, the better the final result will be, but the longer the computational time to complete the simulation. At this point, the acceptable mesh quality will be the best solution for both an acceptable final result and computational time. For the fuel supply pipe, the size is very small and needs special meshing treatment like sweep method, face sizing and edge sizing. Number of division is selected for the edge sizing technique. The area of the fuel jet mixing with the air jet needs super-fine mesh and this can be done by using the body sizing meshing technique. There are three types of body sizing: element size, sphere of influence and body of influence. For the body of influence, the scope geometry is the whole body selection and the frozen body needs to be drawn in the Design Modeller as in Figure 3.14(a). The mesh result for the body of influence is shown in Figure 3.14(b). The body of influence meshing is very sensitive and if it is necessary to repeat the process, the frozen body must be removed before drawing again. For the fuel pipe before the nozzle, the meshing technique used is mapped face meshing with edge sizing and sweep method. The mesh can be seen in Figure 3.12(b).

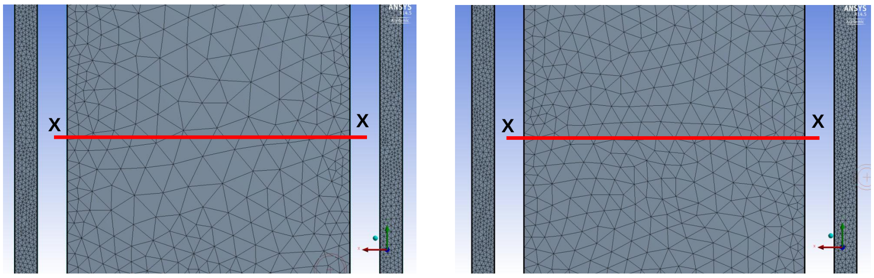

(a) Mesh grid A (b) Mesh grid B

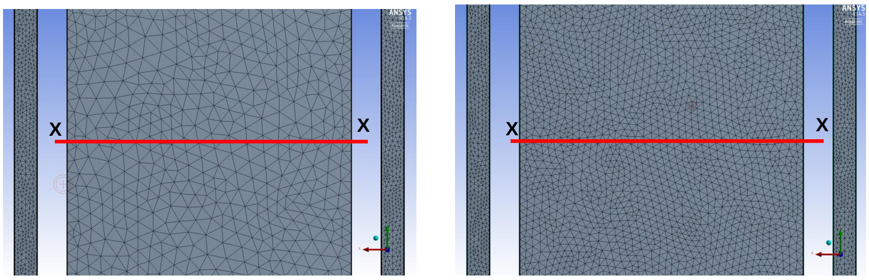

(c) Mesh grid C (d) Mesh grid D

Figure 3.15: Four grids for meshing independence study (cross section X–X is 355 mm above the fuel nozzle).

3.5.2 Meshing Independence Test

In order to simulate and assess the accuracy of the modelling, the grid independence study was done on different mesh settings as listed in Table 3.4. Four different grids (A, B, C and D) were generated to simulate the temperature profiles in the combustion chamber. This method can be used to study the mesh independence test. The same method was used by Wyszynski et al. (2008) and Mamat (2009) in their mesh independence test analysis. The mesh independence test can also be studied by plotting the residuals as a function of the number of elements. The maximum skewness for all grids is below the allowable limit of 0.98. Figure 3.15 shows the different grid sizes. The cross-section of the chamber marked as X–X axis was generated in the model in Figure 3.15 to compare the temperature reading along this line.

The temperature distribution was measured at the middle of the chamber and the result is depicted in Figure 3.16. The result shows that the temperature profile for grid D is smoother and produces a better temperature distribution including near the wall. The temperature difference between the maximum and minimum for each grid can be seen from Figure 3.16 to be 0.47 %, 0.61 %, 0.28 % and 0.28 % for grids A, B, C and D respectively. This shows that grids C and D gave small differences compared to grids A and B. The small temperature profile differences between grids C and D can be seen in the region of 5 mm from the wall. Figure 3.17 shows the combustion chamber contour of average temperatures. The majority of both domains are close to the average temperature of the combustion chamber: for grids C and D the temperature range is 864–866 K and this shows

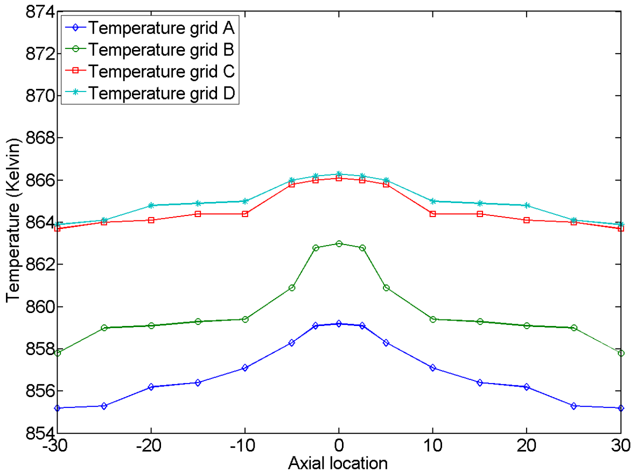

Figure 3.16: Temperature distribution for X–X axis for grids A, B, C and D.

that the temperature was almost identical. From the above results, grid D shows better results, so it was chosen to be used for the rest of the simulation study.

3.6 Location of Spark Ignition

The location of the ignition in the experimental work was very important to ensure the ignition was always successful. Ignition is required to start the flame. Simulations were conducted to locate the best position for the ignition point (Figure 3.18) and therefore informed the experimental design. Figure 3.19(b) shows the flame re-circulation zones on the schematic bluff-body burner diagram. There are three zones in the flame schematic diagram: flame recirculation, flame neck and flame jet zone. The flame recirculation zone was from the flame base up to x/D = 0.50, the flame neck was located at x/D between 0.50 and 2.50 and the flame jet zone was after x/D = 2.50. The fuel and air mean exit velocities are 75 m/s and 5 m/s respectively.

From the analysis of Figure 3.18, it can be seen that two vortices exist in the recirculation zone (Dally et al., 1998). The recirculation zones can be categorised as inner recirculation zone (IRZ) and outer recirculation zone (ORZ), as shown in Figure 3.19(b). The IRZ formed in between the air and fuel jet flows of the bluff-body burner and the ORZ formed outside the annulus air flow. The IRZ was formed due to the bluff-body of the burner and created a swirl flow around the air and fuel nozzles. The IRZ was formed as two circles of different sizes and its centre where the velocity is zero was detected at x/D = 0.25 and r/D = 0.25. These two zones were separated by air co-flow and this phenomenon can be seen in Figures 3.19(b) and 3.18(c).

The recirculation of the mixture of fuel and air was important because that process created the turbulent flow of the mixture which enhanced the mixing

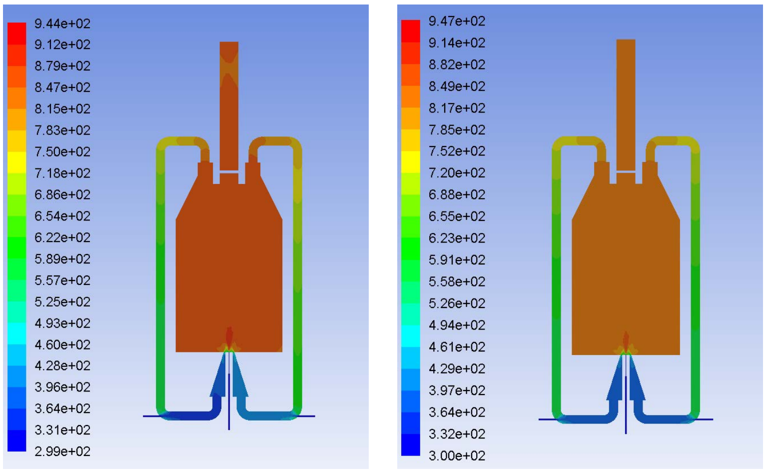

(a) Mesh grid A (b) Mesh grid B

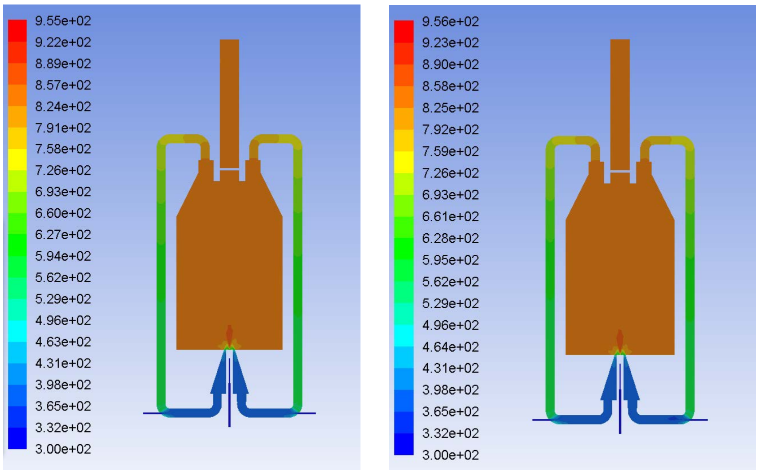

(c) Mesh grid C (d) Mesh grid D

Figure 3.17: Contours of chamber temperature.

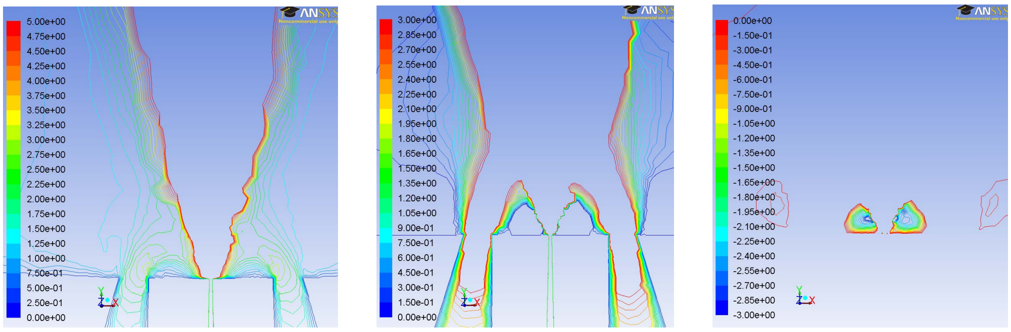

(a) (b) (c)

Figure 3.18: Contour of velocity magnitude (a) total velocity magnitude from 0 to 5.0 m/s (b) contour of Y velocity for 0 to 3.0 m/s, (c) contour of Y velocity for -3.0 to 0 m/s.

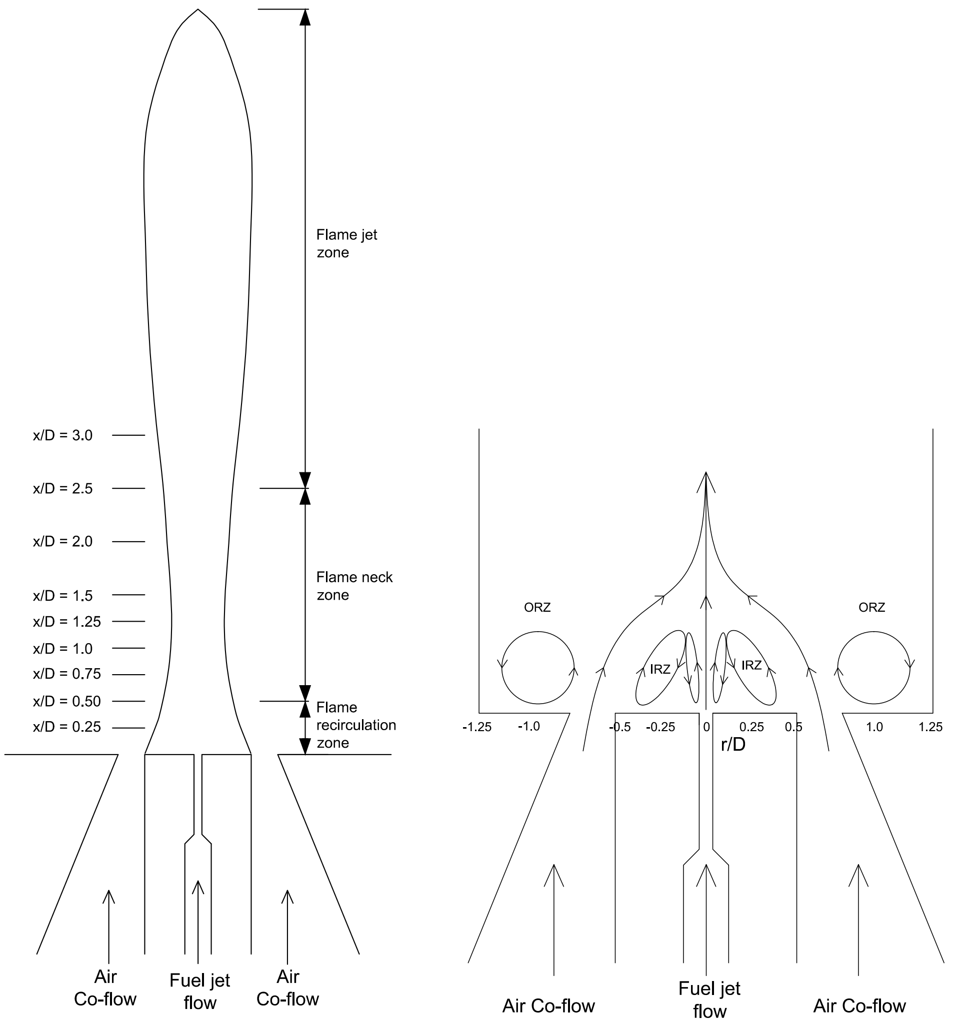

(a) (b)

Figure 3.19: Schematic diagrams for bluff-body burner, a) flame flow field with central fuel jet and annulus air co-flow, b) flow re-circulation zones.

process. The recirculation zone also created the zone centre, of which velocity was almost zero, and created a stable flow profile for stable flame propagation. The intensity of the IRZ is higher than that of the ORZ because the IRZ is the recirculation formed in between the fuel and air jet flows. One cause of the higher intensity is the fuel jet velocity being much higher than the air jet velocity (Figure 3.18(a)). In addition, the IRZ is contained in a small volume within the air jet and has two vortices due to having jets on both sides (Figure 3.19(b)), while the ORZ occupies a bigger volume with a single vortex due to only one side having a jet. Many researchers (Mastorakos, 2009; Triantafyllidis et al., 2009; Neophytou et al., 2012) concluded that the best location for ignition was in the centre of the inner recirculation zone where the recirculation velocity is almost zero. This is important to ensure the spark energy supplied by the tungsten rod was not flushed away, thereby giving sufficient time for the spark energy to ignite the mixture of fuel and oxidant. The development of the ignition system was based

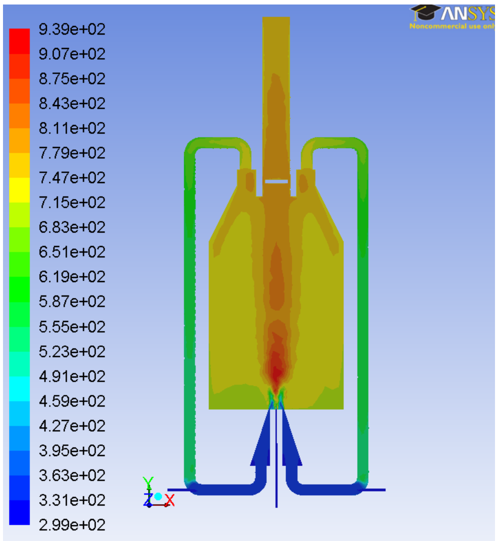

Figure 3.20: Temperature of normal combustion for 3 m/s of methane and 10 m/s of atmospheric air.

on this simulation and more detail about the development and instrumentation is reported in Section 4.2.5.

3.7 Combustion Temperature

The chamber's temperature distribution was discussed for the case of the combustion parameters and furnace geometries as summarised in Table 3.3. The modelling achieved MILD condition because the temperature range was very small and met the MILD regime specifications. The temperature distribution in the chamber was 855–866 K as shown in Figures 3.16 and 3.17. The chamber temperature will not achieve MILD state if the overall inlet and chamber condition are not in the regime favourable to MILD combustion. The chamber temperature for a case that did not achieve MILD combustion is shown in Figure 3.20.

The temperature distribution in the chamber was 620–939 K and the range was outside of the MILD regime specifications due to high excess oxygen supply from the high volume of atmospheric air compared to fuel supply (high air-fuel ratio). This condition will produce normal combustion and not the MILD combustion regime. Figure 3.21 shows that the furnace is open on the top with the streamline flows from air supply pipe to the exhaust opening. Figure 3.21(a) shows the oxidant flows smoothly from the supply inlet to the exhaust opening. This was supported by Figure 3.21(b) that shows the velocity magnitude for the flow. In this case, the combustion products predominantly flow smoothly out from the furnace with very low flow going into the EGR pipe, therefore the requisite preheating of the reactants to produce MILD conditions does not occur.

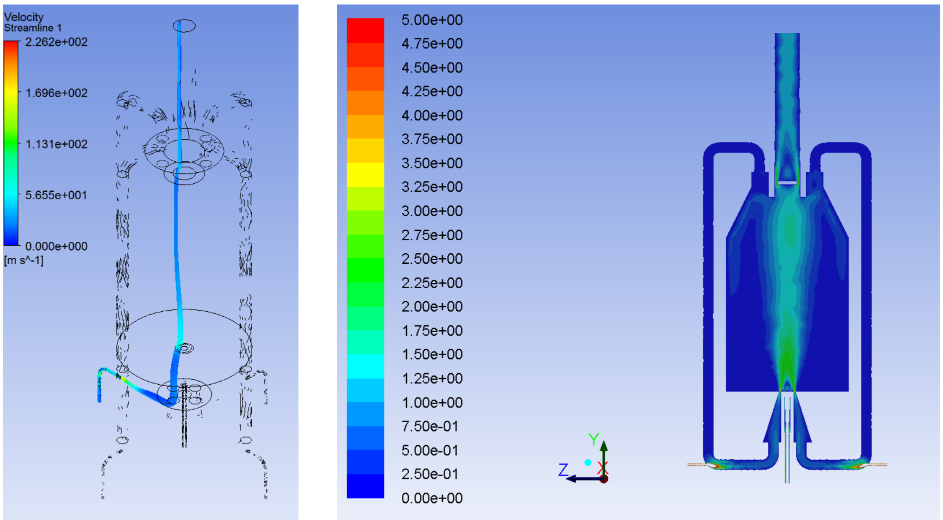

(a) Reactant flow (b) Velocity magnitude

Figure 3.21: The flow inside the combustion chamber for the condition of Figure 3.20.

3.8 Summary

In this chapter, the CFD simulation for the MILD combustion was discussed. All the CFD work was done in three-dimensional simulations. The discussion in this chapter focussed on the chamber design and development. The development of the configuration and parameters underwent a number of iterations to optimise the model and air-fuel supply ratio. The modelling of MILD combustion using CFD has been extensively conducted over the last few decades on different burners and furnace scales (such as laboratory and industrial scales). Most of the furnaces use geometries that are fully closed with a very small opening for exhaust. This design allows the internal recirculation to preheat and dilute the oxygen. This research takes a different strategy of open-top furnace and an external EGR. The study is to evaluate the effect of the external EGR to preheat and dilute the oxygen in oxidant stream and achieve the MILD condition.

Chapter 4

Experimental Methodology

The chapter presents the experimental setup and methodology to validate the numerical model. The experimental test rig consists of a combustion chamber, burner, fuel and oxidant supply system, measurement and instrumentation, which will be described in this chapter. The second phase of this chapter describes the experimental methodology, standard operating procedures and experimental parameters.

4.1 Introduction

The experimental work has been conducted to examine the combustion behaviour, flame characteristics, exhaust gas emissions and chamber temperatures. The oxygen in the secondary inlet is diluted by external EGR. The experimental results have been used to validate the CFD simulation results. A newly developed laboratory-scale open furnace together with a fuel supply and measurement system was use for the experimental work. The experimental work was conducted using methane and biogas to investigate the burner's capability to use LCV gas. The setup of the MILD combustion system consists of a combustion chamber and burner, a fuel and air supply, and a data acquisition system. Cylinders were used for CH_4, CO_2, O_2 and N_2, where CO_2 was blended with CH_4 to produce synthetic biogas, while O_2 and N_2 were mixed to make synthetic air for the oxidant.

4.2 Experimental Setup

The MILD burner can be divided into the combustion chamber, burner, EGR system, exhaust and ignition system. The overall MILD combustion burner experimental setup and its apparatus is presented in Figure 4.1. The combustion chamber was fabricated in-house with a fuel and oxidant supply system (gas control panel). The burner geometry is axisymmetric. The air and fuel supply will be discussed in more detail in Section 4.2.2. The fuel supply either pure methane or methane mixed with carbon dioxide. The burner is capable of operating in premixed, partially-premixed and non-premixed mode by virtue of a control upstream of the burner. The experimental parameters namely air and fuel supply volume flow rate, are considered based on the desired λ and EGR opening amount to dilute oxygen and preheat the reactants. The oxygen in the oxidant supply stream was diluted with the EGR and the reactant temperature increased.

The air and fuel supply velocity at the nozzle is designed to induce proper reactant mixing before the combustion takes place. The primary air is inducted by the fuel stream in the inlet fuel supply, upstream of the burner. At this stage, the fuel jet and primary air turbulent mixing occurred and the mixed reactant flowed through the fuel supply pipe to the burner head where the combustion took place. The burner also has an additional oxidant supplied through the secondary supply pipe. This configuration makes the burner operate in partially premixed combustion mode. The secondary oxidant supply system is presented in Figure 4.2. It has an air, oxygen and nitrogen supply inlet to the mixing plenum. The output from the mixing plenum is split into four, with each supplying an EGR pipe through the side (the secondary oxidant supply). The percentages of the air, oxygen and nitrogen are determined by the required λ value. This secondary oxidant supply

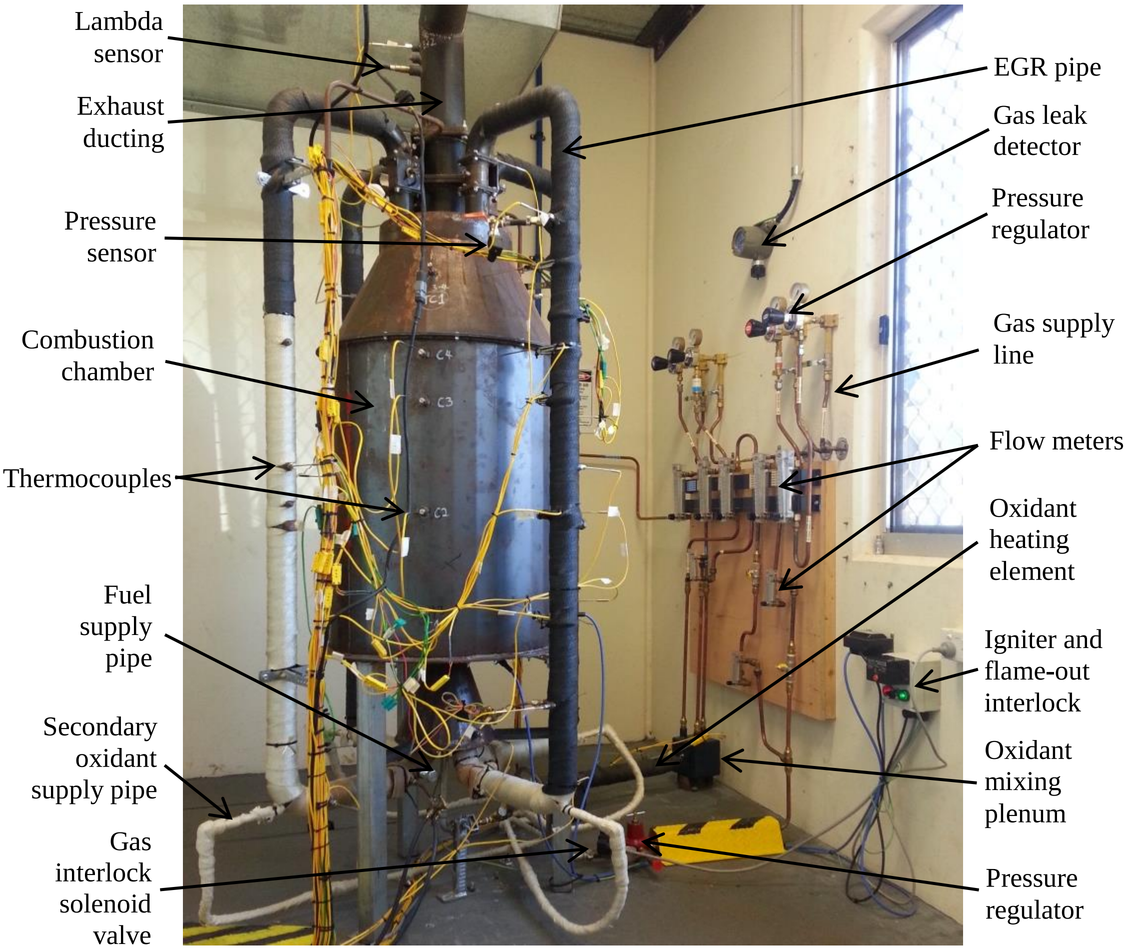

Figure 4.1: Combustion chamber with installed thermocouples, pressure transducers, oxidant and gas supply system, ignition system, and air heating element.

can be preheated by an air heating element that is installed for the oxidant preheating experiments.

In an open burner, the greatest challenge is to achieve the required oxygen dilution conditions. Therefore, the strategy is to dilute oxygen by use of an external EGR technique. The importance of diluting reactants for MILD combustion was supported by Dally and Peters (2007) and Medwell et al. (2008). Dally et al. (2002) concluded that by increasing the oxidant's dilution, it can increase the flame volume and lower the intensity of the reaction. The purpose of the enclosed chamber is to capture the exhaust gas to be used as EGR. The exhaust gas will flow out through the exhaust chimney located at the top of the furnace and controlled by the vent damper (Figure 4.3). The vent damper is made from the same steel as the furnace wall and can withstand temperatures up to about 1,700 K. The setup with an external EGR pipe also allowed the products to be mixed with the reactants outside the combustion chamber. Therefore, this setup is considered to be an open burner. The combustion chamber has been enclosed to ensure the flame has a well-defined boundary wall to avoid additional air entrainment and to maintain a high temperature within the chamber to support MILD combustion. Three clear, high-temperature glass windows were installed to have optical access into the chamber (Figure 4.4). These windows are designed to study the flame behaviour and for image capturing.

The fuel self-ignition temperature for methane is 873 K (Robinson and Smith, 1984) and for biogas is 923 K (Seadi et al., 2008; Nathan et al., 2010). The ignition of biogas is 50 K higher than methane due to the high content of carbon dioxide that acted as the diluent to the fuel. The lower calorific value of the biogas compared to methane makes the biogas fuel harder to ignite. A higher reactant temperature compared to the fuel self-ignition temperature is required to achieve MILD conditions. When this condition is achieved, the combustion will be stable without the possibility of having flame blow-off. The flame is moved toward a MILD combustion regime when the lower oxygen mole fraction is realised and the ambient conditions inside the chamber are at a high enough

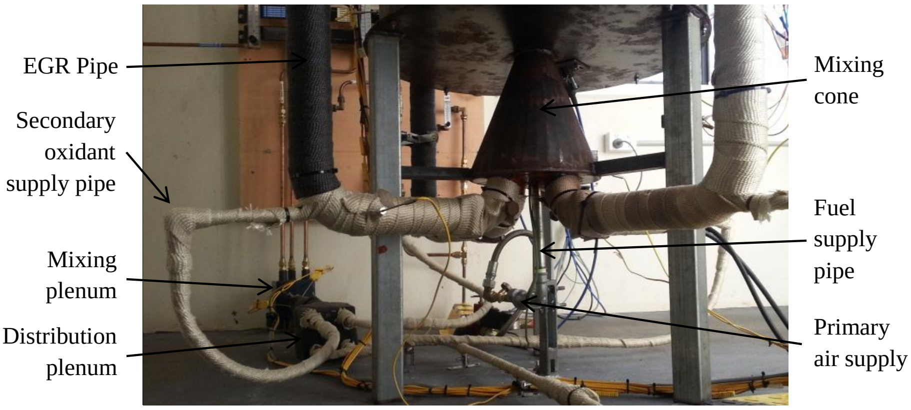

Figure 4.2: Secondary oxidant supply pipe.

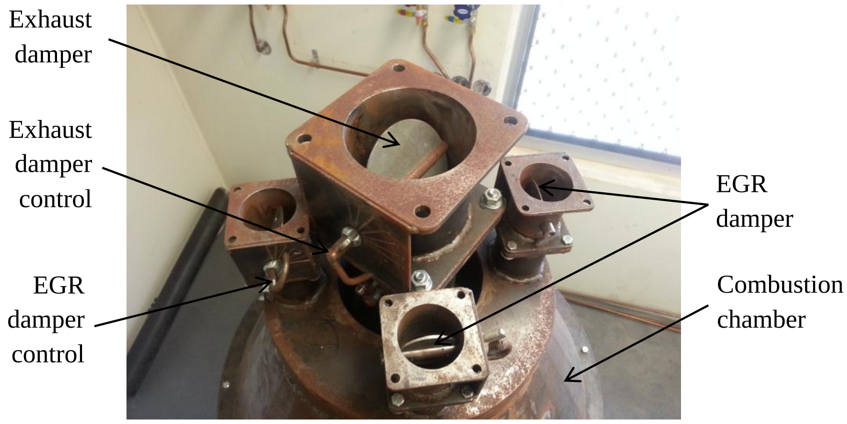

Figure 4.3: Exhaust and EGR vent damper to control exhaust gas flow rate.

temperature to support MILD combustion. Otherwise, if the reactant does not meet the requirement, then either the EGR ratio needs to increase or the fresh air supply needs to be preheated using an external air heater. The preheating of the oxidant supply stream will help the reactant combustion to achieve the MILD regime and reduces the environmental pollutants by keeping the temperature high to ensure the reaction path processes to complete combustion.

4.2.1 Combustion Chamber

The first consideration when designing the combustion chamber is that it must be open at the top, yet enclosed to capture and utilise the exhaust gas. The chamber must be large enough to ensure that the enclosed wall functions as an exhaust gas collector for EGR, but does not function as a closed combustion chamber. The total volume of the combustion chamber is $0.33\,\mathrm{m}^3$. The top opening is to release a percentage of the exhaust gas while recirculating the majority of the exhaust gas to dilute the oxygen in the incoming secondary oxidant supply (atmospheric air or synthetic air which is the mixing of oxygen and nitrogen).

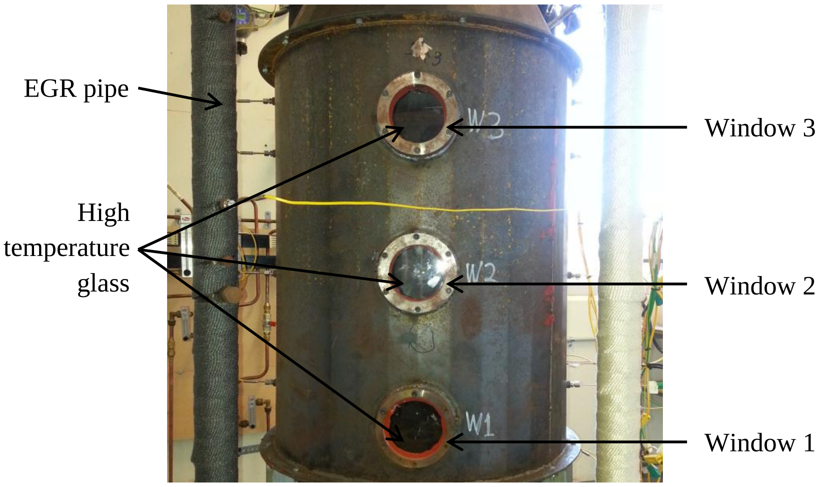

Figure 4.4: Burner observation windows with high temperature quartz glass.

Figure 4.5: Gas control panel with flow meter.

After finalising the pre-design, simulations were undertaken on the ignition location, air-fuel supply ratio and other parametric studies. The MILD combustion parametric study was undertaken using biogas for various combinations of oxidant mole fraction and fuel supply volumes. The gas supply volume flow rate was controlled by flow meters that were mounted on the gas control panel (Figure 4.5). The gas control panel was designed to regulate the flow of each gas and mix these gases downstream. For further detail on the gas control panel, refer to Appendix F.

4.2.2 Gas Burner

The original design of the burner consisted of a 1.0 mm fuel nozzle and surrounding oxidant inlet jet formed by a 40.0 mm diameter bluff-body encircled by a 20 mm annular gap. When attempting to ignite and sustain with a fully non-premixed combustion flame, it was unsuccessful due to poor air-fuel mixing in the reaction region. It was subsequently decided to change the nozzle from 1.0 mm fuel nozzle to a standard commercial premixed air inspirator type gas burner (ASC, 2013) while maintaining the oxidant/EGR annular nozzle. The nozzle was changed to ensure a more positive ignition and stable combustion, which is summarised in Table 4.1.

The standard gas furnace air inspirator type burner model LK15 was used in the experiment (ASC, 2013). The burner has a 7.5 mm inner nozzle diameter,

Table 4.1: Summary of the changes for burner nozzle section.

Item	**Original burner**	**Modified burner**
Fuel nozzle	1.0 mm	7.5 mm
Fuel supply	10 mm	12.7 mm
Re_{fuel}	6,100–11,100	1,800–2,800
Oxidant/EGR nozzle	annular 40/60 mm	annular 27.5/60 mm
Oxidant supply	4 × 10 mm	4 × 10 mm

21.0 mm outer nozzle diameter and 27 mm external nozzle head diameter. The fuel nozzle was selected as it has flame retention by-pass jets set around the inner nozzle for flame stabilization (ASC, 2013). The bypass ports used to re-light the main flame in the event of flame blow-out. The schematic drawing for the industrial retention burner is presented in Figure 4.6. The fuel nozzle for the standard commercial premixed air inspirator type gas burner is presented in Figure 4.7. The location of the fuel nozzle is at the bottom of the schematic diagram as shown in Figure 4.8. The aperture of the gas nozzle at the primary mixing location (near the burner holder) is 0.75 mm. The Reynolds number for the fuel jet is 18,708 when 10.82 L/min fuel is injected through the nozzle, thereby providing a turbulent mixing process of the inlet primary air with the gas stream. The vertical pipe connected to the fuel nozzle to the downstream burner head has a 12.7 mm inner pipe diameter and a 21 mm outer diameter. This burner, also called the half-inch burner, is shown in Figure 4.9.

The maximum burner capacity is 20 MJ/hr for a propane gas supply at the pressure of 100 kPa. When methane is used, the heating capacity is estimated to be 7.8 MJ/hr (2.2 kW). The detailed calculation for the furnace heating capacity can be seen in Appendix A. The burner consists of a burner head (Figure 4.9) and air fuel venturi (Figure 4.10a) for the reactant premixing process. The fuel supply was controlled by the pressure regulator (Figure 4.10b) and the primary air flow rate was controlled by an air inspirator adjustment valve.

4.2.3 Air/Fuel Nozzle

In this study, the air/fuel nozzle at the centre of the burner nozzle with a diameter of 21.0 mm was surrounded by an annular secondary air nozzle with an inner diameter (D_i) of 27 mm and an outer diameter of 60 mm. The air/fuel nozzle is designed to ensure the proper mixing process of the fuel and oxidant by including small recirculation by-pass jets in the mixing zone. The motivation of this design

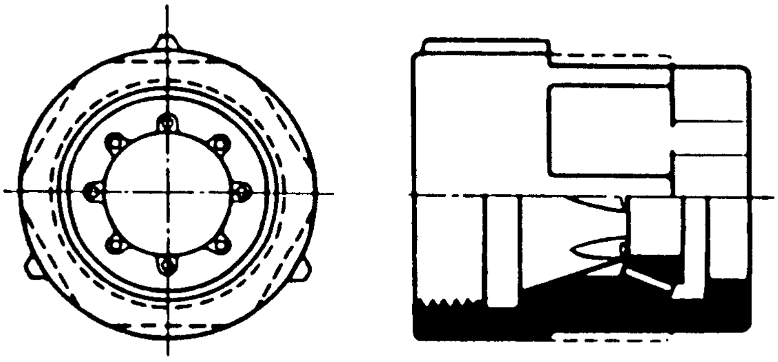

(a) Plan view (b) Side view of bypass ports

Figure 4.6: Industrial premixed burner includes flame retention with air-fuel mixture provided upstream (NAMC, 1952; Turns, 2006).

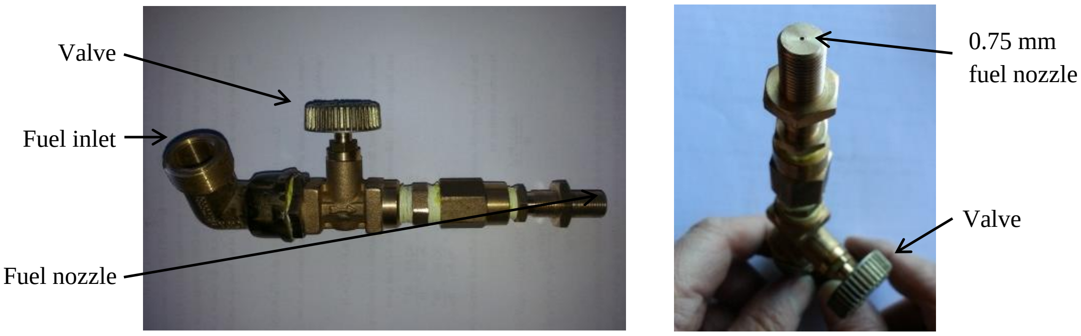

(a) Side view

(b) Top view

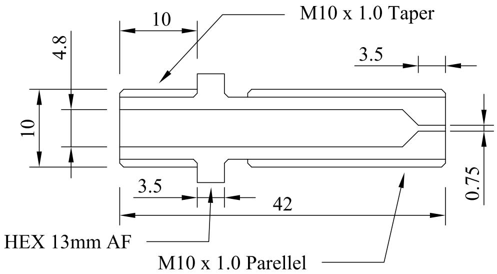

(c) Schematic diagram (all dimensions in mm)

Figure 4.7: The fuel nozzle upstream of air fuel mixing.

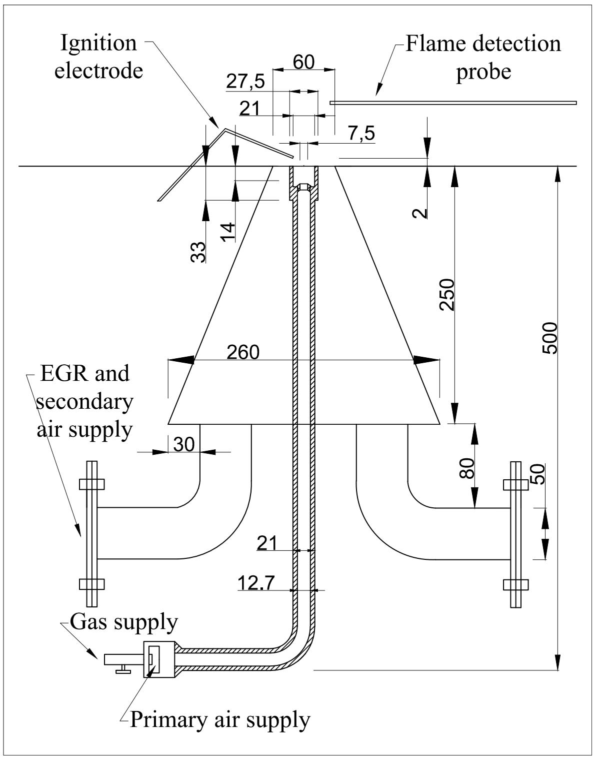

Figure 4.8: Schematic diagram for an air and fuel nozzle for the experimental work (all dimensions in mm).

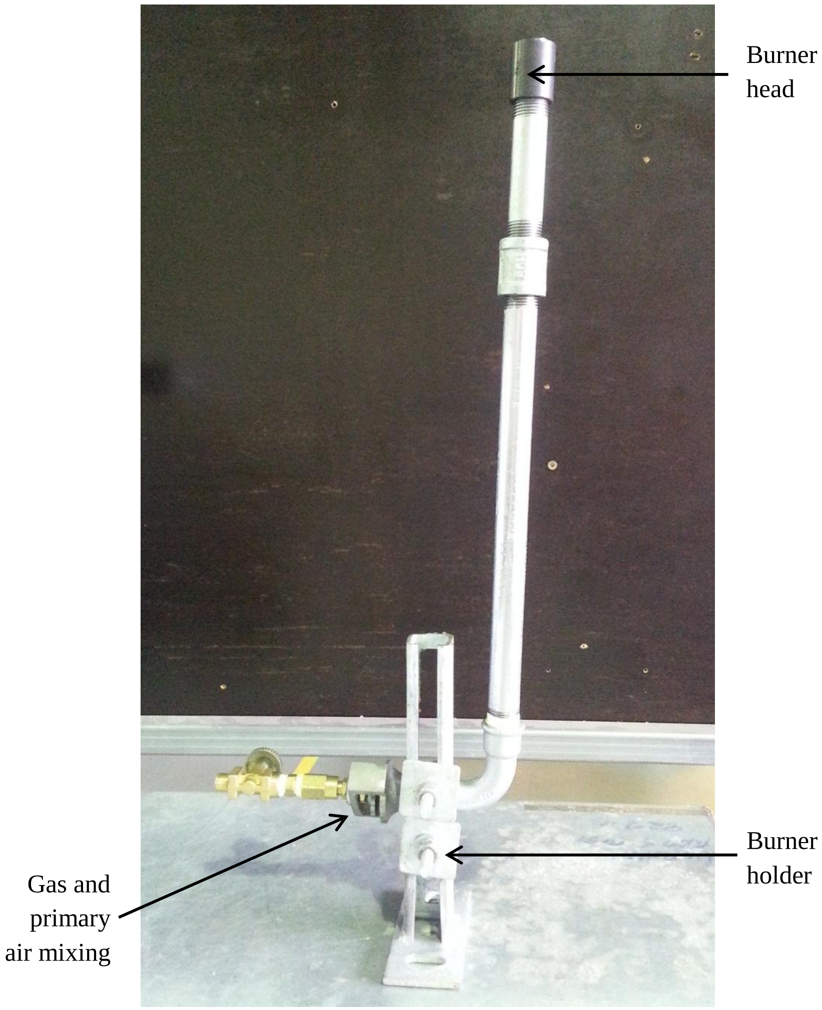

(a) Burner before installation

(b) Installed burner

Figure 4.9: Burner before and after installation in the system.

(a) Gas fuel jet and primary air supply

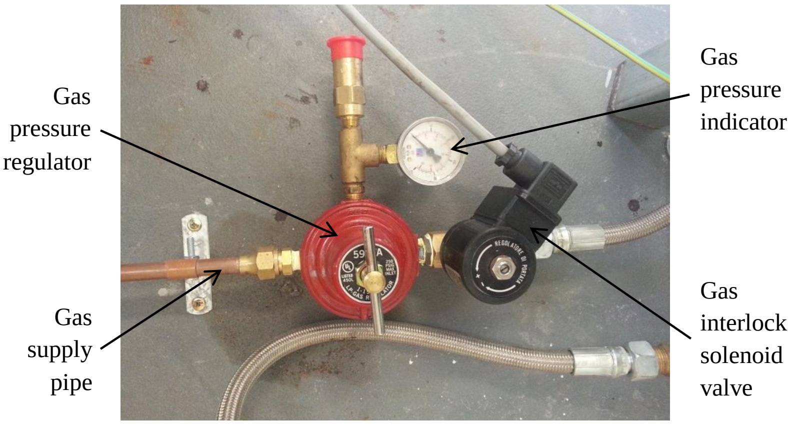

(b) Gas pressure regulator

Figure 4.10: Fuel nozzle and gas supply pressure regulator.

was to ensure a stable flame propagation (Dally et al., 1998). A small recirculation zone of reactant mixing can be achieved at the outer rim of the fuel burner. The schematic diagram for the air/fuel nozzle is shown in Figure 4.8. The volume of primary air supply is manually controlled by the air inspirator adjustment valve. There is zero primary air supply when this valve is completely closed.

Tang et al. (2011) conducted a numerical study to evaluate the effect of the recirculated exhaust gas on the MILD combustion. Their results showed that the recirculated gas effectively reduced the oxygen concentration in the combustion air. An experimental study by Galletti et al. (2007) concluded that reducing the air inlet area increased the jet momentum and enhanced the mixing of the reactants. The increase in the entrainment of the reactant jet and exhaust gas increased the uniformity of the furnace temperature, hence reducing the peak temperature of the reaction, resulting in reduced NO_x emissions.

Effugi et al. (2008) and Derudi et al. (2007*b*) showed that MILD combustion of biogas with a low calorific value can be achieved under the condition of high recirculation rate at $K_v > 5.0$ and high furnace temperatures over 800°C. It has been found that the reactant relative velocity has a strong influence on turbulent mixing to produce complete homogeneity of reactants prior to combustion. This turbulent mixing was affected by the design of the bluff-body nozzle and the homogeneity will effect the combustion temperature.

4.2.4 Exhaust Gas Recirculation System

EGR is one of the key factors for this experimental work and plays an important role in achieving MILD combustion mode. In this burner, the EGR pipes are outside the chamber to study the effect of external EGR to preheat the oxidant and dilute the oxygen mole fraction in the oxidant. The dilution ratio is controlled in the EGR flow using the vent dampers installed on the exhaust pipe and EGR pipes. The percentage of EGR is related to the outflow from the furnace, which is controlled by the percentage of vent damper opening. The volume flow rate of EGR and fresh air was used to determine the dilution ratio of the system. The total exhaust gas out from the system must be equal to the total quantity of fresh air and fuel supplied to the system.

The dilution ratio is measured when the combustion is in steady state and has achieved MILD state. The minimum dilution ratio to achieve MILD combustion was measured at 2.5. The dilution ratio was measured using the mixing of EGR flow rate, secondary air supply flow rate, air fuel supply through the fuel supply pipe and the lambda meter to determine the oxygen content in the exhaust gas. The temperature of MILD steady state combustion should agree with the temperatures found in Table 2.1. The MILD combustion key control strategy is the heating requirement by the furnace. The requirement for the dilution ratio is controlled by controlling the EGR, fresh air and fuel supply stream. Fuel consumption and output energy are the key to measuring the efficiency of the system. Figure 2.14 shows the theoretical comparison of combustion with and without EGR. The same amount of fuel input to the system produce 37.4 % efficiency for the system without EGR and 72.4 % for the system with EGR. This comparison shows that EGR is a very effective factor to reduce the fuel consumption and increase the combustion efficiency.

4.2.5 Ignition System

Ignition is one of the most important elements of combustion. There are two types of ignition processes: auto-ignition and assisted ignition. In the former, the mixture of fuel and oxidant ignite when the temperature of the mixture is higher than the fuel auto ignition point. The auto-ignition point for the fuel with a hot oxidant stream is likely to occur at lean conditions (Echekki and Chen, 2003) and at the location of the most reactive mixture of fuel and oxidant (Mastorakos et al., 1997; Abtahizadeh et al., 2012). For assisted ignition, a heat source (normally from a spark) is applied to the fuel and oxidant mixture. The simple, reliable and low-cost ignition for a gas turbine is through either spark or arc discharge

(Lefebvre and Balla, 2010). Similarly for a gas chamber, spark ignition is the most suitable to ignite the mixture. Ahmed and Mastorakos (2010) found that ignition for non-premixed combustion (diffusion flame) was not well studied and carried out numerical and experimental investigations on the correlation of spark ignition with the local instantaneous mixture fraction in a turbulent non-premixed methane jet.

The location of ignition and the ignition energy is very important for reliable ignition. The simulation study for the ignition location was described in detail in Section 3.6. The spark ignition system used in this experimental work is an inductive ignition system (Techrite AGA6953) to produce a repeatable spark which, together with the transformer Techrite Codice 1820, was used to increase the spark voltage (Techrite, 2014). The flame detection system in this system was controlled by a Siemens Landis Gyr model LGB21 350(A27) (Siemens, 2014). The Siemens Landis control box was installed due to the weak voltage detected (under voltage) when the methane and biogas fuel was ignited. Without this control box, the flame detection system did not detect the flame and shut off the gas supply. The details of the spark ignition system can be seen in Appendix B.

Figure 4.11 shows the overall ignition system including the continuous pulse ignition, which continued for a five-second period, and the gas safety interlock system. The interlock system consists of a flame detection probe that automatically shuts off the supply of fuel if a “flame out” condition is detected. In this study, a 3.0 mm diameter ignition electrode was used with the air gap set at 2.0 mm. The flame detection probe senses the flame and sends the signal to the Techrite ignition box. During the ignition process, the ignition box shuts the gas supply off by closing the solenoid operated gas interlock valve when the mixture fails to ignite and no flame appears within five seconds. The burner requires grounding for the ignition loop circuit. The burner head and the grounding cable for the ignition system can be seen in Figure 4.12.

4.2.6 Gas Supply System

The gases installed for this experimental work were CH_4, CO_2, O_2 and N_2 which were commercially supplied using gas cylinders from Air Liquide Australia. Table 4.2 shows the purity of the gases used in the experiment were between 99.80 % and 99.95 % except for oxygen where the purity was more than 99.50 % (Airliquide, 2012). More details about the gas supply system can be seen in Appendix F. The normal air for the experiment was supplied by an internal air compressor. To ensure the quality of the air supply, the air was filtered by a 0.5 micron filter to remove particulate matter. A water trap was installed to remove the water content in the air. The air was not fully dried but this is assumed not to have any effect on this experiment. Medwell (2007) in his experiment confirmed that the humidity condition did not affect his experimental work.

(a) Overall ignition system

(b) Ignition electrode and flame detection probe

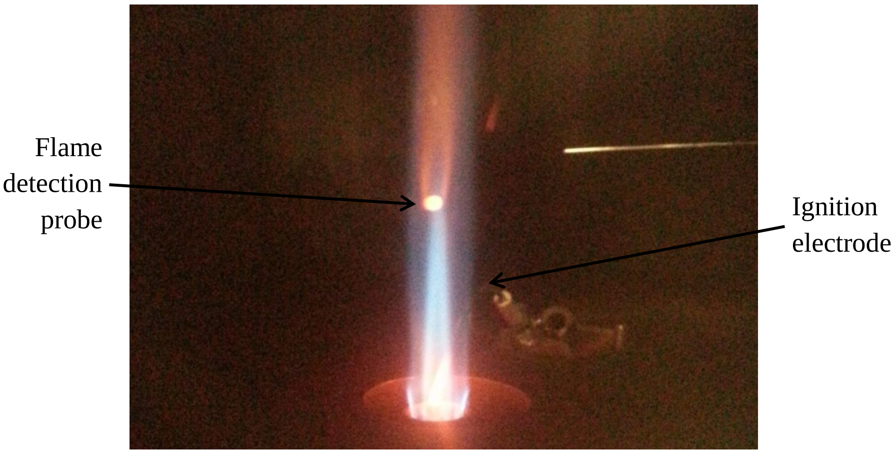

(c) Detection probe with flame

Figure 4.11: Flame safety interlock and ignition system.

Table 4.2: The purity of the supplied gas (Airliquide, 2012).

Gas	**Gas purity**
Methane, CH_4	99.95 %
Oxygen, O_2	99.50 %
Nitrogen, N_2	99.90 %
Carbon dioxide, CO_2	99.80 %

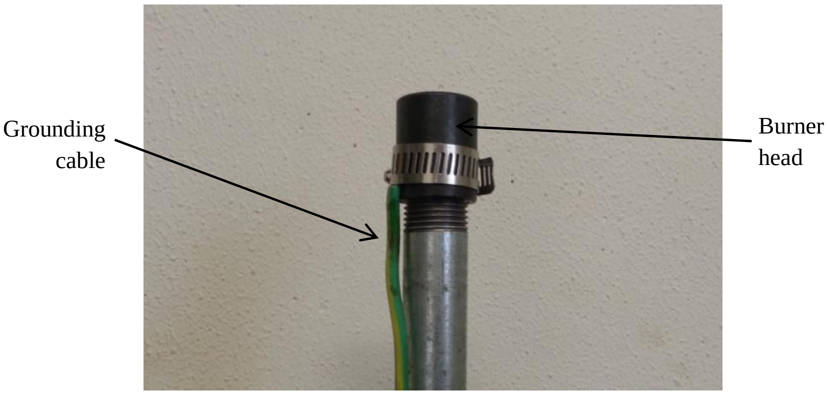

Figure 4.12: Burner head ignition grounding wire.

Table 4.3: Gas density, specific gravity and correction factor to determine the gas flow rate (Dwyer, 2013).

Gas	**Gas density (kg/m^3)**	**Specific gravity**	**Correction factor**
Air	1.205	1.000	1.000
Methane	0.668	0.554	1.343
Oxygen	1.331	1.105	0.951
Nitrogen	1.165	0.967	1.017
Carbon dioxide	1.842	1.529	0.809

There are five supply inlets to the burner: one for fuel and four for oxidant. For the fuel stream, CH_4 and CO_2 are mixed to produce a synthetic mixture of biogas. The flow meters (rotameters) were installed to measure the gas flow rate for each gas line, including compressed air. The flow meters were made by Dwyer Industries. The model used for the CH_4, CO_2 and O_2 was RMA-21-SSV which has a flow rate between 1 and 10 L/min (accuracy: ±4 % of full scale). RMB-55-SSV 19 to 190 L/min (accuracy: ±3 % of full scale) was used for N_2 and compressed air. The gas supply flow meter needs to apply a gas flow rate correction factor due to the flow meter being designed for air. The flow rate factor was calculated based on the gas properties. A summary of the flow rate correction factors can be seen in Table 4.3. The gas correction factor can be calculate by using the equation below.

$$Q_2 = Q_1 \times \sqrt{(1/SG)} \tag{4.1}$$

where Q_2 is the corrected gas flow rate, Q_1 is the flow meter reading flow rate and SG is the specific gravity of the measured gas. The details od the gas correction factor can be found in Appendix F.

The methane and carbon dioxide flow meter measurement has been validated using a manual water displacement method, as shown in Figure 4.13. The gas flow through the pipe displaced the water in the 2.0 L volumetric measuring cylinder and the duration for the water displacement was recorded. The measurement was repeated three times to ensure the accuracy of the measurement. The mea-

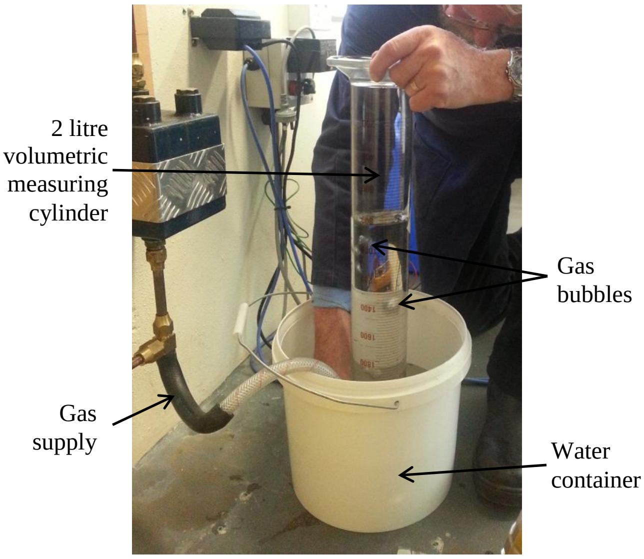

Figure 4.13: The displacement method to measure the carbon dioxide flow rate.

surement is shown in Table 4.4. The flow meters are factory calibrated for air and the correction factor is applied to the other gases used (Dwyer, 2013). At the temperature of 293.15 K and pressure of 101.325 kPa, the specific gravity for methane and carbon dioxide is 0.554 and 1.529 respectively. The correction factor for methane is 1.343, while for carbon dioxide it is 0.809 (Table 4.3). The average for the measurement (Table 4.4) of water displacement for methane and carbon dioxide is 3.85 and 3.97 seconds respectively and the measurement error is 0.7 % and 0.8 % respectively. The flow rate for 15.32 L/min (20 kPa) of methane and carbon dioxide is measured at 16.1 and 26.4 L/min respectively by flow meters and, when the correction factor is applied, the real flow is 21.6 and 21.4 L/min respectively. For air, the average of 3.60 seconds is used to displace 1400 mL of water. This is 23.4 L/min compared to the flow meter reading 23.6 l/min with an error of 1 %.

Table 4.4: Time taken (second) to displace the volume of 1,400 mL of water for 15.32 L/min (20 kPa) of methane and carbon dioxide and 23.6 L/min of air.

Description	**Data 1**	**Data 2**	**Data 3**
Methane	3.85	3.88	3.82
Carbon dioxide	3.95	3.97	3.98
Air	3.60	3.58	3.62

4.2.7 Air Heating Element

The heating element was installed in the oxidant supply pipe line. The secondary air supply was preheated by an air heater Flow Torch 200 (FT200) (Figure 4.14) made by Tutco Farnam (Farnam, 2012). The air was heated in a 50.8 mm internal diameter pipe and has two built-in K-type thermocouples. The heater consists of an open coil spiral-wound element which provides quick heat-up and cool-down cycles with maximum heat transfer. The Flow Torch 200 is capable of operation with airflow of up to 115 SCFM (3,256 L/min), a maximum operating pressure of 120 PSI and maximum output temperature of 673 K. The specifications for the FT200 heater can be seen in Appendix B. The heater and the EGR pipe were wrapped with heat shield exhaust wrapping 302050P (two inches wide) and the copper pipe after the distribution plenum was wrapped using heat-shield exhaust wrapping 301050P (one inch wide) that can withstand maximum heat of 635 K. This is to minimise the heat loss for the heater through the heater wall, the EGR gas through the EGR pipe wall and the heated oxidant through the copper pipe wall. A test was conducted to check the heating element temperature reached a steady condition when the heater was set to maximum. The heating element was set at 673 K with 47.2 L/min of secondary air and the heater temperature is recorded in Figure 4.15. The heating element took 50 seconds to reach the setting temperature and 130 seconds to reach the steady-state temperature.

4.2.8 Exhaust Gas Extraction System

The exhaust gas flows out of the combustion chamber through the installed exhaust gas extraction system. The system consists of an electrical motor acting as an exhaust blower and exhaust ducting which uses the 240 V, 0.72 kW exhaust

(a) Air heating element

(b) Heater control panel

Figure 4.14: Air heating element installation.

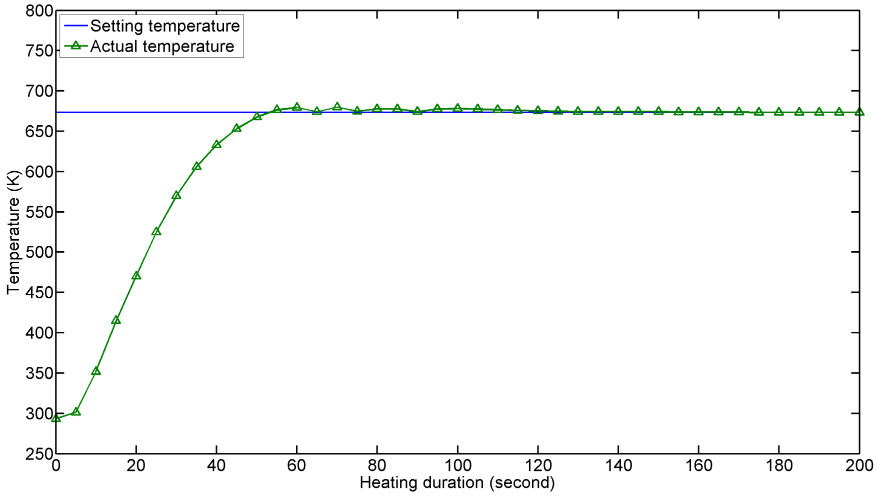

Figure 4.15: The duration of heating element to reach steady maximum temperature.

Table 4.5: Exhaust extraction flow rate measurement using Testo 417 digital anemometer.

Description	**Data 1**	**Data 2**	**Data 3**
Exhaust velocity (m/s)	5.47	5.53	5.51
Exhaust volume flow rate (m^3/s)	0.0501	0.0506	0.0505
Pressure (Pa)	13.50	13.75	13.70

blower AM80ZAA2 made by Lafert Industries. The velocity for the exhaust gas was measured three times and recorded in Table 4.5. The exhaust volume flow rate is 0.0504 m^3/s with suction pressure of 13.7 Pa.

4.3 Experimental Instrumentation

The instrumentation used to measure the experimental data are thermocouples, gas analysers, a lambda sensor, pressure transducers and a digital camera. Except for the digital camera, all the other sensors are connected to the data acquisition system and logged on a computer through a USB link. All the instruments used in the experimental work are described in the following section.

4.3.1 Thermocouples

Thermocouples made by TC Direct (TCDirect, 2012) were used to measure the temperature at 42 different locations including the main chamber, chamber wall, EGR pipe, exhaust pipe, air heater and mixing cone. One thermocouple was used to measure the combustion room ambient temperature (Table 4.6). In this experiment, the laboratory was equipped with a National Instruments compact Data Acquisition (NI cDAQ) system and LabVIEW software (NI, 2012*a*). The temperature was measured using R-type and K-type thermocouples which were

Table 4.6: Location of thermocouples installation.

Location	**Quantity**
Combustion chamber	21
EGR pipe	14
Exhaust pipe	3
Mixing cone	1
Air heating element	2
Room temperature	1
Total	42

Table 4.7: Mean, standard deviation and standard error for sample of K-type thermocouple used.

Sensor no.	**1**	**2**	**3**	**4**	**5**	**6**
Mean	292.8	292.9	292.5	293.0	293.0	293.0
Std Deviation	0.0168	0.0135	0.0832	0.0191	0.0210	0.0223
Std Error	0.0008	0.0007	0.0042	0.0010	0.0011	0.0011

connected to NI modules plugged into the back panel of the NI cDAQ unit.

In the experiments, the R-type thermocouples were used to measure the flame temperature and K-type were for the lower temperature regions such as the preheated air inlet (Tsuji et al., 2003; Verssimo et al., 2012). Thermocouple specifications is presented in Appendix B. Figure 4.16 shows the location of the thermocouples and sensors on the test furnace. The measurement was displayed using a LabVIEW Graphical User Interface (GUI) and recorded in the format of an Excel spreadsheet. The data is collected using an NI cDAQ 9178 chassis with a number of signal conditioning amplifiers and Analogue to Digital Conversion (ADC) modules.

The R-type thermocouples were used for the main chamber temperature measurement since they can withstand temperatures up to 2,040 K. K-type thermocouples that can withstand temperatures up to 1,645 K were used to measure the temperature of the exhaust gas at the exhaust gas pipe on the top of the chamber and the EGR pipe. Sample readings of ambient temperature K-type and R-type thermocouples were taken and are summarised in Tables 4.7 and 4.8 respectively. The thermocouples are subject to reading errors arising from heat losses due to conduction and radiation (Sato et al., 1975; Vishkanta and Menguc, 1987; Heitor and Moreira, 1993). The purpose was to test the thermocouples' reading error. The temperature readings were recorded for ten minutes and analysed statistically. It can be seen that the maximum value of standard error for the K-type and R-type thermocouples are 0.0042 K and 0.0198 K respectively. The result of standard deviation and standard error values indicate that the thermocouple readings are very reliable.

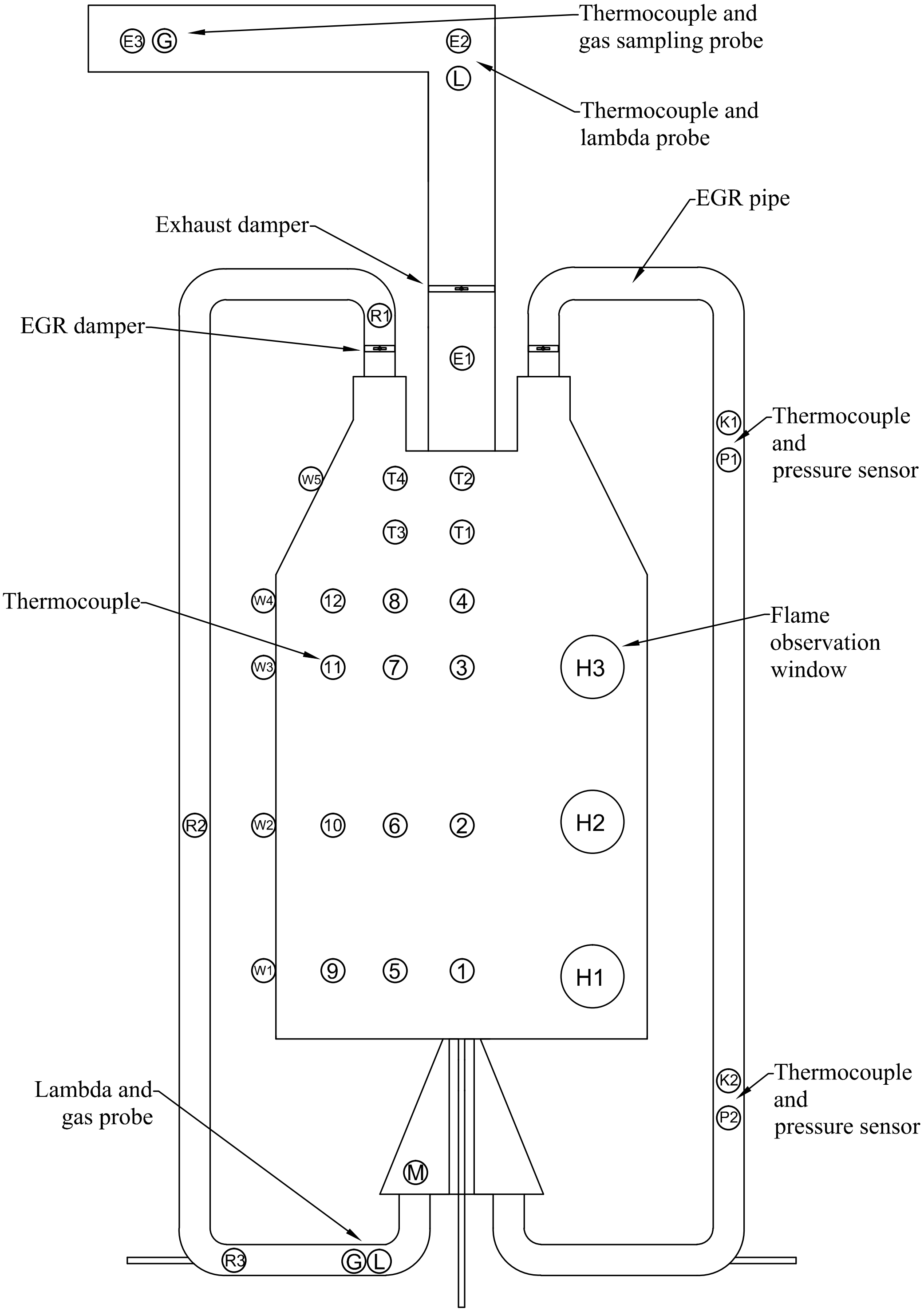

Figure 4.16: The location of measuring sensors: thermocouples, pressure transducers and gas analyser sampling probe. H are observation windows, sensor 1 is R-type thermocouple, sensors 2 to 12,T,W,R,E,M and K are K-type thermocouples, G are gas analysers, L is lambda sensor and P are pressure transducers.

Table 4.8: Mean, standard deviation and standard error for sample of R-type thermocouple used.

Sensor no.	**1**	**2**	**3**	**4**	**5**	**6**
Mean	293.1	292.7	292.6	293.0	292.6	293.2
Std Deviation	0.0643	0.1917	0.1907	0.0637	0.1993	0.3961
Std Error	0.0032	0.0096	0.0095	0.0032	0.0100	0.0198

(a) (b)

Figure 4.17: Gas analyser used to measure exhaust gas compositions. (a) CODA gas analyser. (b) sampling probe.

4.3.2 Gas Analyser

Exhaust gas emissions is one of the most important results from this study. The exhaust gas emissions including combustion by-products has been measured at the exhaust pipe and the EGR pipe using a gas analyser. A CODA gas analyser (Figure 4.17) has been used to measure and record the exhaust gas emissions (CODA, 2012). The gas analyser is equipped with electrochemical sensors for CO, UHC, NO_x, CO_2, O_2 and H_2O (water vapour). This device can accurately measure the following gases: O_2, CO_2, HC, CO and NO_x and is consistent with OIML, EPA and ASM standards (detailed specifications can be found in Appendix B). The gas analyser was connected to a laptop computer to record the data. The gas analyser operating ranges and accuracy are shown in Table 4.9. Prior to the test, the gas analyser was subjected to maintenance and calibration by the manufacturer and daily standard calibrations were undertaken.

Table 4.9: CODA gas analyser measurement accuracy (CODA, 2012).

Gases	**Range**	**Accuracy**	**Accuracy**
CO	0–10 %	±0.02 % abs	±3 %
	10.01–15 %		±5 %
CO_2	0–16 %	±0.3 % abs	±3 %
	16.01–20 %		±5 %
NO_x	0–4000 ppm	±20 ppm abs	±3 %
	4001–5000 ppm		±5 %
O_2	0–25 %	±0.1 % abs	±5 %

The position of the installed exhaust gas sampling probe was guided by European Standards (Directive 1999/96/EC, 1999). The sampling positions are required to be at a location where the temperature of the exhaust gas is not less than 70°C (343 K). For the exhaust gas pipe, the gas was sampled at 1.0 m away from the exhaust exit point (Figure 4.18). This is due to the comparison study of the exhaust gas composition for the exhaust pipe and EGR pipes at the downstream of the EGR pipes. The downstream of the EGR pipes is also far away (about 1.8 m) from the exhaust gas exit point. This was to ensure the chemical reactions were fully completed before the gas composition was measured. For the gas analyser measurement accuracy, refer to Appendix B. The accuracy of the data measurement is between ±3 % and ±5 %, depending on the level of the detected gas measured.

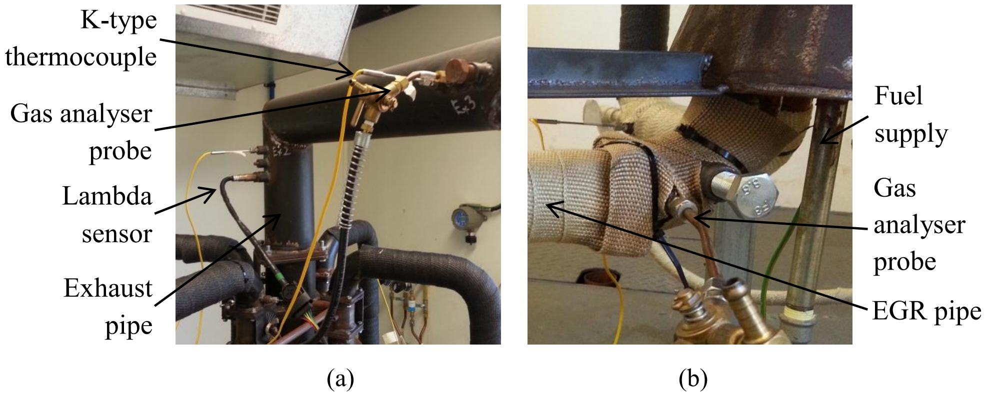

Figure 4.18: Gas analyser sampling location. (a) exhaust gas ducting with thermocouple (left) and exhaust gas sampling (right). (b) EGR pipe with exhaust gas sampling (left) and lambda sensor (right).

4.3.3 Lambda Sensor

Lambda values were measured using a MoTeC Professional Lambda Meter (PLM). The PLM accurately measures the exhaust gas mixture over a wide range of operating conditions, regardless of the type of fuel being used, with a fast response time. The operating range is between $0.7 \leq \lambda \leq 32.0$ with an accuracy of ±1.5 % (MoTeC, 2013). The sensor has been factory calibrated with a trimming resistor embedded in the sensor connector. The oxygen measurement after the mixing process of the EGR and fresh supply oxidant was measured by the lambda sensor. The PLM sensor is shown in Figure 4.19. The actual AFR was calculated from the air flow rate divided by the fuel flow rate. The λ value from the PLM sensor and calculated λ value were found to be in close agreement. Thus, the PLM λ values are considered in this study.

4.3.4 Pressure Transducers

The measurement of the pressure is part of the furnace's normal operating procedures. There are two standard commercial pressure transducers WIKA A10

Figure 4.19: MoTec Profesional Lambda Meter (PLM) sensor and data display (MoTeC, 2013).

(Wika, 2012) at the range of 0 to 1 bar (100 kPa). The published accuracy is 0.25 % installed to measure two pressure points and calculate the flow rate. This technique was used to calculate the EGR flow rate. EGR pipe number four was used to measure the two pressure points and the temperature (Figure 4.20). At both locations, pressure and temperature readings were recorded on the NI data logger. The distance between the two pressure gauges is 1.1 m. The pressure transducers were calibrated to ensure the pressure measurement was accurate. The calibration for pressure transducers was done using a Budenberg 380 dead weight tester and multimeter was used to check the voltage as shown in Figure 4.21.

The calibration process was used to measure the correlation between applied pressure and output voltage. The original output of 4 mA for 0 bar to 20 mA for 1.0 bar has been converted to 1.0 V and 5.0 V respectively by installing 250

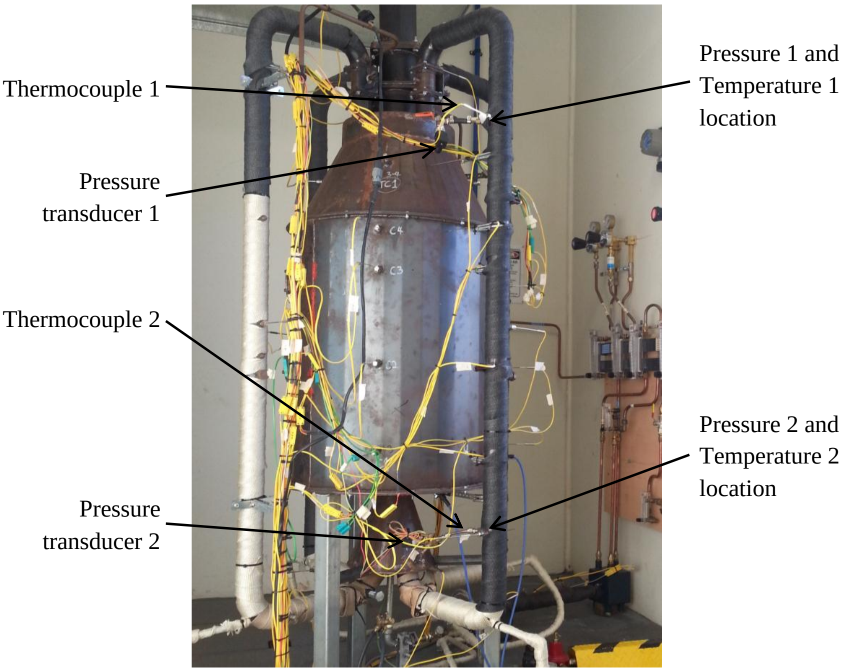

Figure 4.20: The location of two pressure transducers separated by 1.1 m.

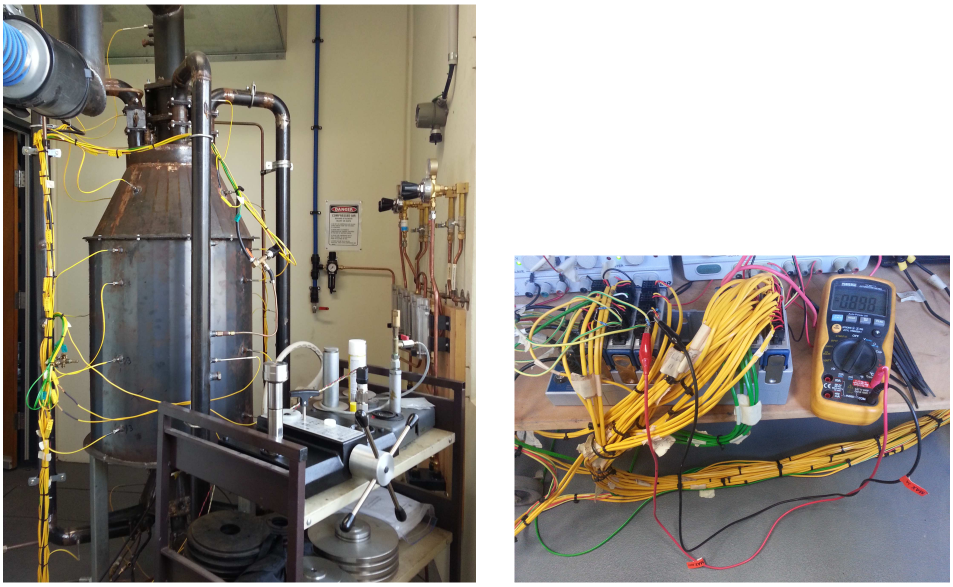

(a) Calibration in progress. (b) Voltage checking by multimeter.

Figure 4.21: Pressure transducer calibration using Budenberg 380 dead weight tester.

Ω resistors. The output was then measured by using a multimeter during the calibration, which is summarised in Table 4.10. The average pressure readings errors are acceptable for both Sensors 1 and 2, which are 0.33 % and 0.27 % respectively. The applied weight and the voltage signal correlation summarised in Equations 4.2 and 4.3 were later used in the LabVIEW scale factor to measure pressure in bars. The correlation between the voltage signal and the pressure is given in Figure 4.22. The values of the coefficient of determination (R^2) for both pressure transducers are 1.0 which shows that the linear relationship between pressure and current is very accurate. For pressure transducer 1:

$$\text{Pressure} = 0.0627(\text{Current}) - 0.2524 \tag{4.2}$$

For pressure transducer 2:

$$\text{Pressure} = 0.0626(\text{Current}) - 0.2517 \tag{4.3}$$

4.3.5 Data Acquisition System

The data acquisition system consists of two computers as the data recorder, interface module and sensors. The first computer was for temperature and pressure

Table 4.10: Pressure transducers calibration.

Pressure	**0 bar**	**0.25 bar**	**0.5 bar**	**0.75 bar**	**1.0 bar**
Sensor 1	4.025 mA	8.034 mA	12.029 mA	16.038 mA	19.973 mA
Sensor 2	4.021 mA	8.029 mA	12.021 mA	16.033 mA	19.983 mA

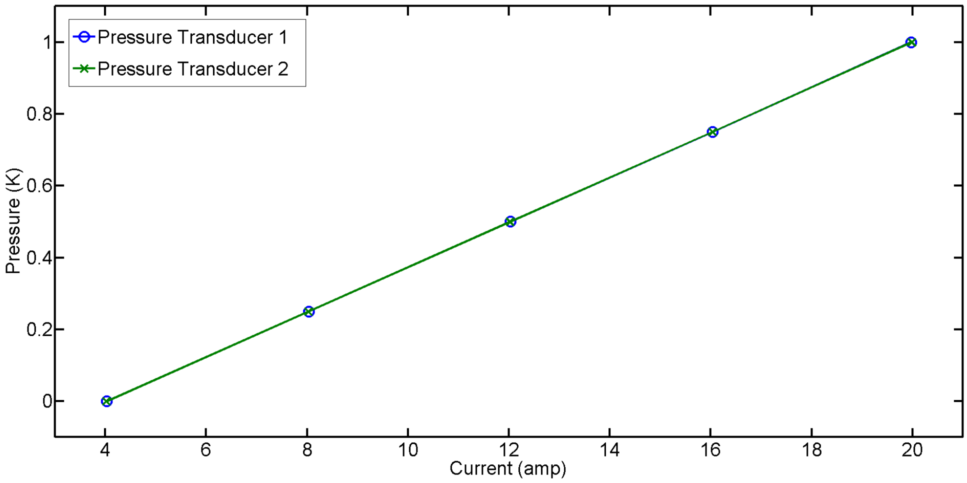

Figure 4.22: The relation of current (ampere) and pressure (bar) for pressure transducer. The pressure transducer range is from 0 to 1.0 bar

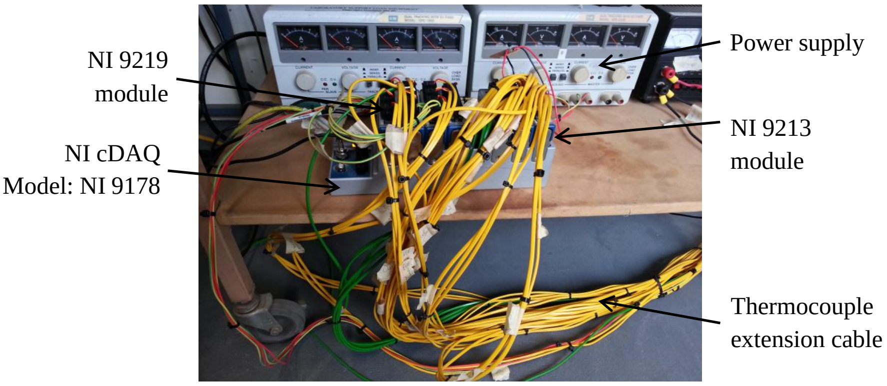

Figure 4.23: Thermocouples and pressure transducers connected to NI cDAQ card.

measurement connected through the National Instrument module (Figure 4.23). The second computer was used to run the CODA gas analyser using compatible software packages provided by the maker. The National Instruments LabVIEW software (NI, 2012*a*) was used to program and record the data from all the thermocouples and pressure transducers. Figure 4.24 shows the LabVIEW graphical user interface to display and record the data. The program was interfaced through the NI cDAQ drivers and NI 9178 module connected through USB to the computer. The NI 9178 module was coupled with two NI 9213 modules and three sets of NI 9219 modules. The LabView circuit diagram can be found in Appendix B.

The temperatures were measured at 42 different locations. Two sets of NI 9213 16-channel thermocouple modules operated at 78 Hz to convert thermocouple readings to digital values (representing the temperature in Kelvin). NI 9213 was specially designed for the temperature module with built-in Cold-Junction Compensation (CJC) and a 24-bit Analogue to Digital Converter (ADC) for up to 0.02°C measurement sensitivity (NI, 2012*b*). Two sets of NI 9219 four-channel universal analogue inputs operating at 100 Hz were used to convert thermocouple

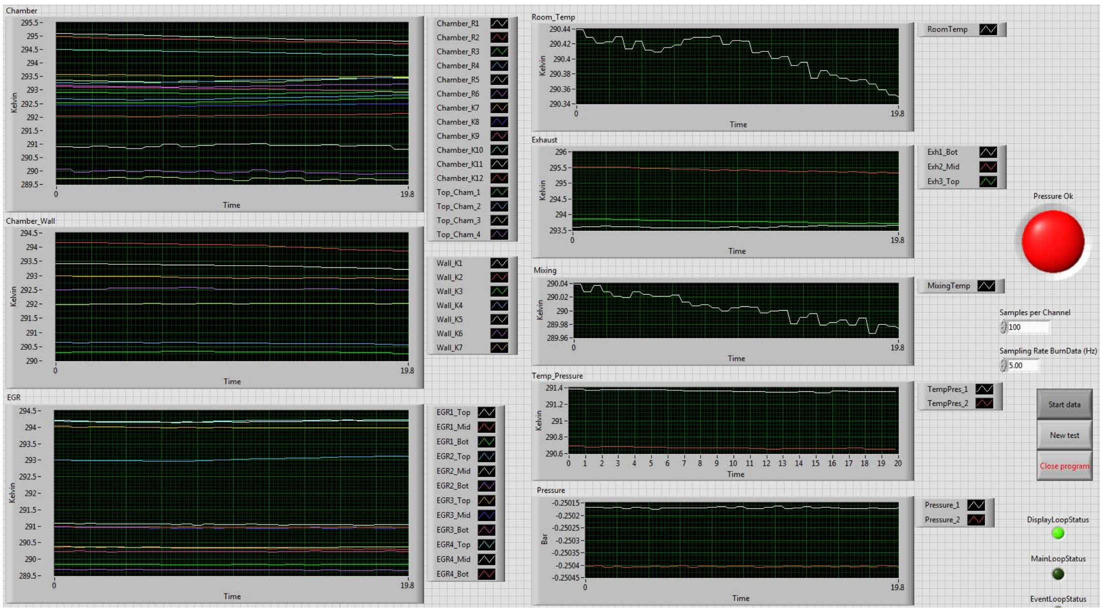

Samples per Channel 100

Sampling Rate BurnData (Hz) 5.00

Figure 4.24: LabVIEW graphical user interface.

readings to digital values representing the temperature in Kelvin. Another set of NI 9219 was used to convert the voltage readings from the WIKA pressure transducer to digital values representing the pressure in bars.

4.3.6 Images Processing Device

A digital camera was used to capture the combustion image and the flame propagation. A Nikon D7100 with Nikon AF-S DX NIKKOR 18-200 mm f3.5-5.6G ED VRII lenses was the digital camera used. The Nikon VRII lens was used because it is specially designed to reduce recorded image and video vibration and noise (Nikon, 2013). The camera detail setting for aperture setting is f3.5, exposure time based on shuttle speed is set to 1/60 second, ISO sensitivity is set automatically for best image quality, when set to automatic setting the ISO was automatically set at low level and white balance setting was set to auto mode to ensure the camera automatically selected the best setting for the best image capturing quality. The video format used was 1,920 × 1,080 at 30 frames per second (fps). The still image and moving video image were captured from the ignition point and also when the flame was stable. The captured images were used to measure the total flame height, flame primary (blue cone flame) and secondary (diffusion flame) combustion zone and flame brush. For the MILD flame, when the flame reaches steady state and becomes invisible to the naked eye, the digital camera can capture the flame luminescence (Oldenhof et al., 2010; Oldenhof et al., 2011). This process is important to determine if the MILD combustion premixed flame is lifted. In normal jet flames, the lift-off height is the axial height of the sharp flame interface. For a MILD flame, to determine lift-off height, a certain threshold level for an averaged quantity is defined. The temperature (Kumar et al., 2007), OH concentration (Cabra et al., 2003; Ertesvag and

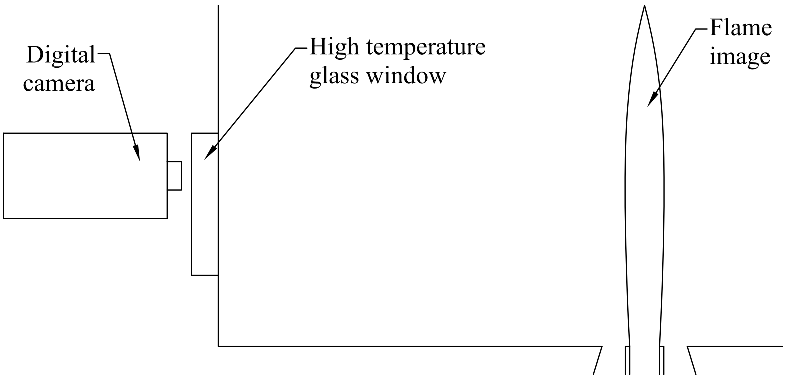

Figure 4.25: Illustration of the camera position and flame image capturing.

Magnussen, 2000) and luminescence (Cabra et al., 2005) were previously used to measure the lift-off height.

The camera position and capturing angle is important to determine the real captured image size. The camera position is perpendicular to the high-temperature glass window and flame image. The same angle of the camera and flame means the images captured are the real size of the flame, as illustrated in Figure 4.25. The images are captured in video mode and the MATLAB image processing solutions toolbox is used to analyse the image (MATLAB, 2014). In the video mode, when the flame reaches steady condition, the static image that represents each case is selected for discussion.

To find the steady flame static image by the image frame in the video mode, a simple MATLAB code was written. The method includes the measurement of the flame size, height and width. The same method is used to analyse the ice accretion (Saleh, 2014) and flame propagation (Heskestad, 1983; Stefan et al., 2012) by the processing of video images using MATLAB software. The method used by the code is described in the following steps:

(i) Load and read each frame of flame propagation from video recorded by digital video camera.

(ii) Identify steady flame for the image capturing. For the case of ignition step by step image, the capturing is started from the ignition spark point (without flame) until the flame is completely ignited and reached steady flame propagation.

(iii) Read the reference for flame height and width for the measurement of sample flame geometry.

(iv) For the static flame image, the flame height and width is measured and recorded for the intended captured frame.

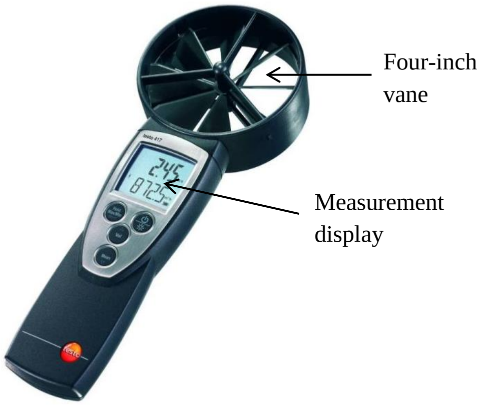

Figure 4.26: Testo 417 used to measure the exhaust gas flow rate (Testo, 2012).

Table 4.11: Testo 417 large vane anemometer specifications (Testo, 2012).

Characteristic	**Value**	**Range**	**Accuracy**
Temperature	°C	0–85°C	±0.5 °C
Flow velocity	m/s	0–20 m/s	±0.1 m/s

(v) Repeat the process for the other flame propagation video at the same video frame number for the same parameter setting and compare the image captured and flame geometry. If the flame is similar, then the image captured and flame geometry is reliable for subsequent discussion.

4.3.7 Digital Anemometer

The digital anemometer was used to measure the exhaust flow rate. A Testo 417 large vane anemometer (Figure 4.26) was used as a small weather station to measure the environmental conditions during the experiment. The specifications of the Testo 417 can be seen in Table 4.11. The ambient temperature and humidity was measured and compared with the data taken by the USQ weather station. A sample report for the USQ weather station can be seen in Appendix B. Exhaust gas suction by the exhaust system was also measured by the anemometer and is summarised in Table 4.5. The average exhaust suction volume flow rate is $0.0504\,\mathrm{m^3/s}$. The pressure was calculated using a dynamic pressure formula which ia $0.5\rho V^2$, where V is the exhaust gas velocity and ρ is the exhaust gas density ($0.9025\,\mathrm{kg/m^3}$).

4.4 Experimental Methodology

Experimental work for the furnace combustion can be conducted on a either laboratory scale (Plessing et al., 1998; Kobayashi et al., 2005; Gupta, 2004) or industrial scale (Fawaz et al., 1994; Weber et al., 2001; Aminian et al., 2012). The laboratory furnace with pilot scale burner described in this study was equipped with premixed, partially-premixed and non-premixed combustion capability. The flame was stabilised by a bluff-body burner to enhance the mixing of fuel and oxidant for the non-premixed combustion and fuel with EGR for the premixed combustion. The experimental work is concentrated on partially-premixed combustion with some experiments on non-premixed and premixed combustion. The Standard Operating Procedure (SOP) for the experimental work including the experimental procedures and methodologies are described in the following section.

Safety is critical to the experimental work in order to comply with the safety requirements, some important measures were undertaken. The safety considerations are: commissioning of test equipment, safety measures, gas detection system, automatic burner safety shut-off system, burner safety cover and experimental room air ventilation. The safety measures applied include the standard operating procedure as pre-start-up procedure, combustion chamber air purging procedure, normal start-up and operating procedure, normal shutdown procedure and emergency shutdown procedure. For details about the safety of the experiment and standard operating procedure, refer to Appendix E.

4.4.1 Test Procedure

The experimental work procedures were carried out to ensure no steps were missing. The check-list of the detailed standard operating procedure and data recording standard were established in order to secure the proper data collections. A brief summary of the main steps of the experimental procedures are listed as follows:

(i) Power ON the combustion room ventilation system, exhaust gas extraction system and carry out the start-up process for the in-furnace measurement system including data acquisition system, ignition system, pressure measurement system and gas analysers. Power ON the oxidant heating element and wait until the temperature reaches the desired level.

(ii) Open the gas supply system from the gas cylinders, gas pressure regulator and ball valve at gas control panel. Set the fuel and oxidant supply volume flow rate by adjusting the flow meters for each gas on the gas control panel.

(iii) Check all the in-furnace measurement systems are ready to collect the data. Start the LabView program (data acquisition system) to start recording the temperature and pressure data collection before starting the ignition system.

(iv) Record the room and environment conditions and then start the ignition system by pressing the ignition ON button. Start the video and image recorder (digital camera or high-speed camera) for the flame behaviour observations.

(v) The flame was ignited 60 seconds after the ignition button is switched ON. If the ignition was not successful, wait for 15 seconds to let the exhaust

Table 4.12: Measured variables unit measurement.

Measured variables	**Unit**	**Measured by**
Temperatures	Kelvin	Thermocouples
Air volume flow rate	L/min	Flow meters
Fuel volume flow rate	L/min	Flow meters
Relative humidity	%	Gas analysers
CO emissions	%	Gas analysers
CO_2 emissions	%	Gas analysers
NO_x emissions	ppm	Gas analysers
O_2	%	Gas analysers
λ	-	Lambda sensors
Pressure	kPa	Pressure transducers

extraction system purge out all the unburned methane in the combustion chamber. Then, re-start the ignition by pressing the ignition ON button.

(vi) Observe the flame behaviour and monitor all the in-furnace measurements to ensure they are at normal recording conditions. Start the data collection immediately for the time-based data monitoring.

(vii) Turn OFF the gas supply when the experiment is completed. Stop all the in-furnace measurement recording after two minutes.

For each parameter setting, the data collection was taken after the burner was allowed to run for 20 minutes after the flame was ignited and the flame had reached steady state. Khalil et al. (2013) and Hasan (2013) in their experimental work applied the same procedure that allowed the MILD burner to run for about 20 minutes before the final data were collected. The combustion emission data reading by the gas analyser was observed to stabilise within three minutes for any change in experimental conditions (Arghode, 2011). For each configuration of parameter settings, the experiments were repeated three times to minimise error and uncertainty. Arghode (2011) estimated the uncertainly in his experiment to be about ±0.5ppm for NO and ±10 % for CO emissions.

The experimental work standard operating procedure are detailed in Appendix E. The experimental work utilises the parameters of fuel compositions and air and fuel supply velocity. The experimental study was carried out for biogas and methane. This experiment was to study the effect of EGR to dilute and preheat the oxidant supply. All the variables were measured and analysed in this study and the employed methods to measure them are summarised in Table 4.12.

4.4.2 Test Conditions

The test conditions are recorded before starting each experimental work in order to avoid the effect of environmental conditions on the experimental result. The environmental conditions that need to be observed include weather, ambient room temperature and humidity. The test room ambient temperature and humidity were measured by a CODA gas analyser. The sample room temperature and environmental conditions is summarised in Table 4.13. The relative humidity was consistent since the experimental work was carried out from the end of Autumn and throughout the Winter season, which is the stable portion of the climate. The weather and the surrounding temperature play an important role for the relative humidity reading since the relative humidity is a measurement of the water vapour content of the air at a given temperature. The continuous room ambient temperature measurement was recorded by the K-type thermocouple simultaneously with the other combustion chamber's temperature measurement. Ambient temperature and humidity were monitored and recorded to ensure the tests performed at relatively similar ambient conditions. This was to avoid either positive or negative effects of the ambient conditions on the experimental results. The average value of the ambient temperature was 295 ± 3 K and the relative humidity was 45 ± 3 %. The experimental room size is 2.2 m wide by 4.8 m long and 3.1 m high and the room ambient temperature was maintained by using a normal room air heater to ensure the environment temperature is 295 ± 3 K for every experiment.

4.5 Biogas Fuel

Biogas is a renewable alternative fuel that has the potential to replace dependency on fossil fuel. Biogas harvesting, production, and utilisation technologies have significantly improved over the last ten years (Michael et al., 2014). Traditionally, biogas fuel has been produced for immediate utilisation as heat energy but currently it is increasingly utilised to generate electricity for waste treatment plants and domestic purposes. The calorific value of biogas is lower than that of natural gas and is variable depending on its chemical composition and physical characteristics. The main composition of biogas is a mixture of methane and carbon dioxide. The ratio of methane to carbon dioxide and other gases depend on the source of the biogas: household waste, waste water treatment plant sludge, agricultural wastes, waste from the food industry and other sources. The composition of biogas varies from 55 % to 65 % methane, 35 % to 45 % carbon dioxide, 0 % to 3 % nitrogen (N_2), 0 % to 2 % oxygen (O_2) and 0 to 1 % each of hydrogen (H_2), hydrogen sulphide (H_2S) and ammonia (NH_3) (Anunputtikul and

Table 4.13: Sample of weather conditions recorded before experimental work started.

Measured variables	**07 May**	**20 May**	**17 June**	**15 July**	**28 Aug**
Test start time	12:00 pm	3:30 pm	4:00 pm	1:30 pm	1:00 pm
Ambient temperatures, K	294.25	293.75	294.55	295.53	295.20
Relative humidity, %	44.8014	44.8013	44.8012	44.8012	44.8012

Rodtong, 2004). Anaerobic digestion is a biological process which makes it possible to degrade organic matter by producing biogas, which is a renewable energy source, and a sludge used as fertiliser (Biogas, 2012). Due to the high content of methane and the possibility of utilising what had previously been considered a waste product, biogas is becoming an attractive source of energy.

4.5.1 Biogas Production

One of the key advantages of using biogas for MILD combustion is the presence of inert gases. The ratio of inert gas in the biogas is about 40%. This effectively pre-dilutes the fuel and reduces the requirements for mixing through dilution with exhaust gases. The experimental biogas collection and quality testing were conducted from abattoir wastewater generated from covered anaerobic ponds. The National Centre for Engineering in Agriculture (NCEA) at USQ engaged with the research project to optimise the production of biogas. The study area is located at Ipswich, South-East Queensland, Australia. The meat processing facility of Churchill Abattoir Pty Ltd weekly slaughters and processes around 3,000 cattle (McCabe and Baillie, 2012). Meat processing produces a high volume of wastewater with a high pollutant load consisting of manure, blood, paunch, fats, oil and greases (Nakhla et al., 2003).

The content of fat, oil and greases in abattoir wastewater has the potential to produce a large volume of methane (Luostarinen et al., 2009). The waste from the abattoir is around 660 tonnes of hot standard carcass weight per week (McCabe et al., 2014) collected and piped to five huge wastewater ponds. Each pond's size is about 50 m long × 20 m wide × 5 m deep. This study was to investigate the abattoir wastewater for the performance and potential of biogas production. The wasterwater was later analysed and treated to optimise the biogas production. The covering technique was used to collect the biogas from each wastewater pond. The image of a covered and uncovered abattoir wastewater pond is shown in Figure 4.27. The wastewater sludge can be seen in Figure 4.28. Biogas from abattoir wastewater can be utilised directly to benefit the abattoir in terms of odour reduction and energy for the production process. A flaring technique can be used to control and reduce the greenhouse gas emissions. Better and more economical usage is to modify the abattoir's existing natural gas boilers and burners to utilise biogas to run a small power plant for electricity supply to abattoir equipment.

The sample measurement and analysis was conducted both on-site and in the laboratory. An on-site analysis was conducted using a Yellow Springs Instrument professional plus field logger for the wastewater temperature, pH, EC and ORP. The laboratory analysis for the abattoir wastewater samples was undertaken by Australian Laboratory Services in Brisbane. The laboratory measurement is COD, BOD, TSS, FOG, ammonia as nitrogen (NH_3–N), total Kjeldahl nitrogen (TKN), alkalinity and volatile fatty acids (VFA) (McCabe et al., 2014).

(a) Uncovered pond (b) Covered pond

Figure 4.27: Abattoir pond for the biogas study (McCabe et al., 2014).

(a) Full pond view (b) Sludge image zoom

Figure 4.28: Sludge at abattoir wastewater pond (McCabe and Baillie, 2012).

For the gas composition analysis, the Geotechnical instruments GA2000 landfill gas analyser was used (GeoTech, 2012). The biogas was analysed for methane, carbon dioxide, oxygen and hydrogen sulphide content. The accuracy for the Geotechnical instruments GA2000 landfill gas analyser is within 98 %. Average on-site biogas composition from covered ponds is presented in Table 4.14.

The methane content in biogas is between 50 % and 75 % by volume (Seadi et al., 2008) but in some cases, it is about 55 % to 65 % (Anunputtikul and Rodtong, 2004). The methane content for the biogas from the abattoir is about 62 % and the carbon dioxide is about 26 % (Table 4.14). It has been recognised that the quality of the biogas depends tremendously on the sources of the biogas itself and

Table 4.14: Average on-site biogas composition from covered pond (McCabe, 2012).

Gas	**CH_4 (%)**	**O_2 (%)**	**CO_2 (%)**	**H_2S (ppm)**	**Others (%)**
Content	62.07	2.69	25.92	925.45	3.17

research is important due to the wide variations in biogas composition. Biogas is one of the key parameters of this study. However, this study was only focusing on synthetic biogas created by the mixing of methane and carbon dioxide. The fuel composition for the experimental work can be seen in Section 4.6.

4.5.2 Biogas Composition

The composition of a gas generated from a digester depends on the substrate of its organic matter load and the feeding rate of the digester (Biogas, 2012). The production of biogas is carried out in the environment in a natural way (e.g. gas of marshes–vegetable and animal matter decomposition where the formation of bubbles at water surface can be observed). In the absence of oxygen (anaerobic digestion), the organic matter is degraded partially by the combined action of several types of micro-organisms. A succession of biological reactions leads to the formation of biogas and sludge. The bacteria which carry out these reactions readily exist in a natural state in liquid manure and anaerobic ecosystems: they develop naturally in a medium without oxygen.

The different sources of biogas production lead to the different specific compositions. Table 4.15 shows the composition of biogas from household waste, waste water treatment plants sludge, agricultural waste and waste of the agrifood industry. Among the sources listed, the highest calorific value of biogas comes from the waste of the agrifood industry which has a methane content of 68 % of biogas resources. Table 4.16 shows that the world-wide consumption of biogas is still low.

4.5.3 Biogas Properties

The energy content of biogas is chemically bound to the percentage of methane content. The properties of biogas vary to some degree depending on their source. Biogas presents interesting physical characteristics compared to natural gas due to the closure of the carbon cycle when it is used for combustion. The carbon

Table 4.15: Biogas composition (Biogas, 2012).

Components	**Household waste**	**Waste water treatment sludge**	**Agricultural wastes**	**Waste of agrifood industry**
CH_4 % vol	55–60	60–75	60–75	68
CO_2 % vol	38–34	33–19	33–19	26
N_2 % vol	5–0	1–0	1–0	1
H_2O % vol (at 40°C)	6	6	6	5
H_2S (mg/m^3)	100–900	1000–4000	3000–10 000	400
NH_3 (mg/m^3)	-	-	50–100	-

Table 4.16: Biogas resources (Biogas, 2012).

World biogas resource	**Produced biogas (TOE/year)**	**Biogas which is consumed (TOE/year)**
Urban and industrial solid waste	750	60–100
Urban and industrial waste water	50	40–50
Agricultural by-products	1000	40–150
Total	1800	140–300
Biogas/worldwide consumption of natural gas	100 %	8–17 %

Table 4.17: Properties of biogas with 55 % to 70 % methane and 30 % to 45 % carbon dioxide (Zicari, 2003; Seadi et al., 2008; Nathan et al., 2010).

Biogas Properties	**Value**
Energy content	6.0–6.5 kWh/m^3
Fuel equivalent	0.60–0.65 L oil per m^3 biogas
Flame speed	0.25 m/s
Explosion limits	6–12 % biogas in air
Research octane number	130
Auto-ignition temperature	620–750°C
Density	0.85–1.0 kg/m^3
Viscosity	$(1.24 - 12.9) \times 10^{-5}$ kg/ms

dioxide produced from the combustion of biogas utilised back by the source of the biogas. Biogas is lighter than air if the amount of CO_2 is not too high and it produces half as many calories in combustion as an equal volume of natural gas (Biogas, 2012). Table 4.17 shows biogas properties. The biogas auto-ignition temperature is higher than that of methane due to the lower calorific value, varying between 893 K and 1,023 K depending on the methane content (Zicari, 2003; Seadi et al., 2008; Nathan et al., 2010). The biogas flame speed is dependent on the composition. The lower the methane content, the lower the flame speed. The physical properties of biogas from household and agri-food industry wastes compared to natural gas are shown in Table 4.18. The calorific value for biogas is 53 % to 67 % of that of natural gas. The density of biogas is much higher due to the higher content of carbon dioxide.

4.6 Experimental Parameters

The parameters for the experiment are air and fuel supply velocity, λ and EGR flow ratio. The fuel for the experiment are biogas and methane, whose compositions are summarised in Table 4.19. The air and fuel supply flow rates depend on the λ value used.

Table 4.18: Biogas physical characteristics compared to natural gas (Ramli, 2009; Biogas, 2012; Hairuddin et al., 2014).

Type of gas	**Biogas 1 Household waste**	**Biogas 2 Agrifood industry**	**Natural gas**
Composition	60 % CH_4 33 % CO_2 1 % N_2 6 % H_2O	68 % CH_4 26 % CO_2 1 % N_2 5 % H_2O	95.4 % CH_4 3.1 % C_2H_6 1.0 % CO_2 0.6 % N_2
UCV (kWh/m^3)	6.6	7.5	11.3
LCV (kWh/m^3)	6.0	6.8	10.3
Density (kg/m^3)	0.93	0.85	0.57

Table 4.19: Fuel composition for the experiment.

Composition	**Methane**	**Carbon dioxide**
Biogas	60 %	40 %
Methane	100 %	0 %

4.6.1 Flow Rate

Table 4.20 shows the gas flow rate used for the experimental work and the CFD simulation. The gas flow rate ranges from 10.82 L/min to 24.20 L/min and 1.02 m/s to 2.30 m/s for the experimental work and numerical work respectively. The secondary air supply was injected through the inlet at each of four EGR pipes. The air temperature was heated by a heating element installed in the supply line to a maximum of 673 K. The inlet volume of the air and fuel was determined by the CFD simulation. Table 4.21 shows the air flow rate used for the experimental work and the CFD simulation. The air flow rate ranged from 80 SCFH (2.0 m/s) to a maximum of 400 SCFH (10.0 m/s). The compressed air pressure was fixed at 500 kPa and the flow rate controlled by the flow meter.

4.6.2 Secondary Air Pre-Heating and EGR

A test was conducted to study the effect of pre-heating the secondary air supply at the flow rate of 11.8 L/min to 47.2 L/min. The secondary air preheating tem-

Table 4.20: The conversion table of fuel supply flow rate for the 12.7 mm fuel supply inlet.

Experimental work		**CFD**
Fuel supply pressure (kPa)	**Gas flow (L/min)**	**Gas flow (m/s)**
10.0	10.82	1.02
30.0	18.70	1.76
50.0	24.20	2.30

Table 4.21: The conversion table of air supply flow rate for the 10.0 mm secondary oxidant supply inlet.

Experimental work	**CFD**
Air flow meter (SCFH)	**Air flow (m/s)**
50	1.25
200	5.0
400	10.0

perature was summarised in Section 5.1.2. The effect of the secondary air supply was studied with EGR and without EGR flow. A total of 16 experiments were performed using 10.8 L/min (10 kPa) of methane as summarised in Table 4.22. The fuel flow rate was kept consistent at 10.8 L/min and the secondary air flow rate was varied. The total heat input is dependent on the fuel flow rate and the secondary air preheating. The equivalence ratios and Reynolds numbers were dependent on the fuel and air flow rates.

4.6.3 Air and Fuel Supply

The experimental parameters are listed in Table 4.23 for methane and biogas premixed and non-premixed combustion. 24 experiments were conducted for methane and biogas. The fuel supply was fixed at 10.82 L/min (10 kPa) for both methane and biogas and the heated secondary air was set as a variable from 11.8 L/min to 70.8 L/min. Higher secondary air was considered compared to the secondary air preheating and EGR study (which used secondary air of 11.8 L/min

Table 4.22: Experimental parameters for pre-heating of the secondary air supply and EGR (secondary air flow rate in L/min).

Exp. No.	**Secondary air (L/min)**	**Secondary air**	**EGR**
P1	11.8	Pre-heat	Yes
P2	23.6		
P3	35.4		
P4	47.2		
P5	11.8	Pre-heat	No
P6	23.6		
P7	35.4		
P8	47.2		
P9	11.8	Not pre-heat	Yes
P10	23.6		
P11	35.4		
P12	47.2		
P13	11.8	Not pre-heat	No
P14	23.6		
P15	35.4		
P16	47.2		

to 47.2 L/min) due to the flame behaviour observed. The air heating element was set to preheat the secondary air to 673 K.

Table 4.23: Experimental parameters for methane and biogas for premixed and non-premixed combustion.

Exp. No.	Secondary air (L/min)	Fuel	Flame type
H1	11.8	Methane	Premixed
H2	23.6		
H3	35.4		
H4	47.2		
H5	59.0		
H6	70.8		
H7	11.8		Non-premixed
H8	23.6		
H9	35.4		
H10	47.2		
H11	59.0		
H12	70.8		
H13	11.8	Biogas	Premixed
H14	23.6		
H15	35.4		
H16	47.2		
H17	59.0		
H18	70.8		
H19	11.8		Non-premixed
H20	23.6		
H21	35.4		
H22	47.2		
H23	59.0		
H24	70.8		

4.7 Experimental Accuracy and Error

The experimental error must be reduced to the minimum possible to ensure the accuracy of the work. The total error can arise from the experimental design, measurement instruments, test conditions, calibrations and data reading (Savariraj et al., 2011). In this work, the experimental readings error measurement has been considered and to reduce the experimental errors, the work was repeated at least three times. The error of each parameter has been considered in the experimental design. Experimental pre-test has been performed and the data was analysed to calculate the standard error and standard deviation. The standard error and standard deviation used to specify the best resolution to obtain high accuracy of the parameters as an example are summarised in Tables 4.7 and 4.8. The sample demonstration of the pre-test conditions, experimental repetitions and calibrations to reduce the error were reported in Sections 4.2.6, 4.3.1, 4.3.4

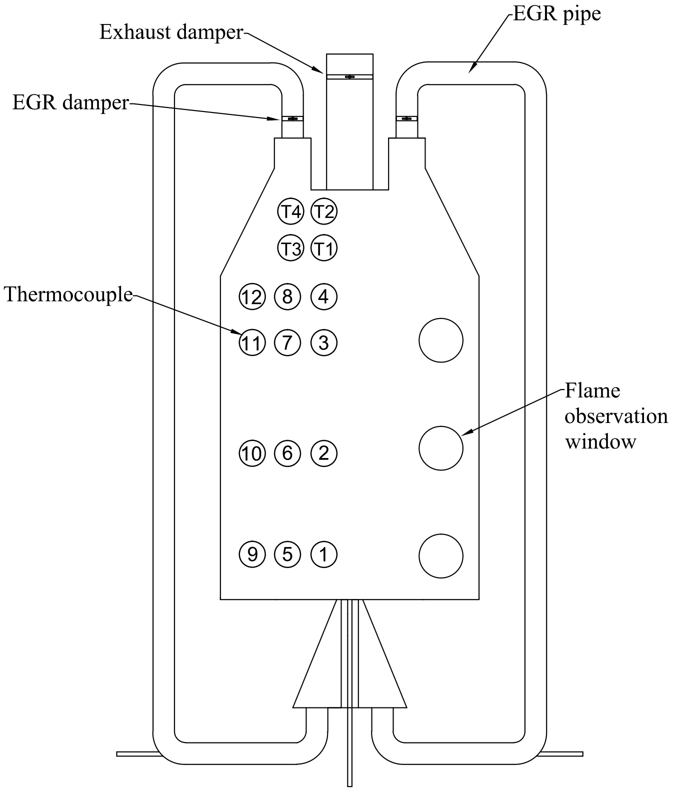

Figure 4.29: The location of K-type thermocouples for early stage experimental work.

and 4.3.7.

4.8 Test Flame Experiments

The experimental testing was repeated three times and the average was reported to obtain reliable measurements. The temperature distribution for the combustion chamber is one of the main data to ensure whether combustion achieved the MILD state. In the early experimental testing, the temperature was recorded at the sensor locations as shown in Figure 4.29.

The thermocouple nearest to the flame was not installed at the centre of the flame and combustion chamber, but 50 mm away. This was because of the thermocouple safety to avoid the over-temperature limit at the beginning of the experiment. The thermocouple installation can be seen in Figure 4.30. Once the temperature of the flame was confirmed to be in the range of 1,450 K to 1,700 K, then the thermocouple was installed at the centre for all further experiments as shown in Figure 4.16. The test for the ignition of the methane fuel is premixed combustion. A sample of the chamber's temperature measurement is shown in Figure 4.31 for 30 seconds of combustion. The methane was injected at 24.2 L/min without a secondary oxidant supply. Figure 4.31 shows that the combustion takes place at 0 to 30 seconds and the chamber temperature increased from ambient tem-

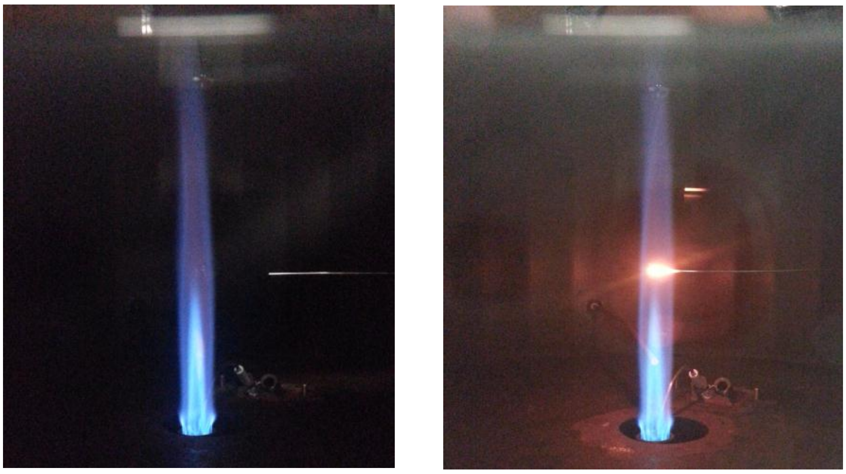

(a) 5 cm from flame centre (b) At the flame centre

Figure 4.30: R-type thermocouple installation for the flame temperature measurement (image size is 270 mm × 315 mm).

perature (298 K) to a maximum of 431.7 K. The chamber temperature required 75 seconds to naturally cool down to the ambient room temperature. The thermocouples measured the temperature at various locations in the chamber, as shown in Figure 4.16.

Figure 4.32 shows the combustion for 24.2 L/min (50 kPa) of methane fuel. A longer duration of fuel supply was applied (420 seconds) and the maximum chamber temperature was 506.5 K at 420 seconds. After 180 seconds the mixture ignited, the chamber's temperature reached nearly peak and started to stabilise with a 0.5% to 1.8% increase in temperature at the 240 seconds time interval. This value is a very small change and was omitted from the analysis. After 420 seconds of combustion, the chamber takes 180 seconds to cool down to ambient temperature. Besides the flame propagation zone, the hottest zone (Figures 4.31 and 4.32) were detected at the top of the chamber area (above the flame propagation and near to the exhaust gas exit point).

4.9 Summary

This experimental work is conducted in order to fulfil the second and third objectives of this thesis. In the current chapter, the combustion chamber experimental apparatus, experimental work procedures, data measurement and operational safety are discussed. The combustion chamber, air and fuel nozzle, exhaust, EGR and ignition system are detailed. The instruments used (data acquisition system, thermocouples, gas analyser, lambda sensor, pressure transducers, digital camera and gas supply system) are discussed. This chapter also summarises the environmental conditions during the experimental work including weather conditions, room ambient temperature and humidity. The experimental methods are

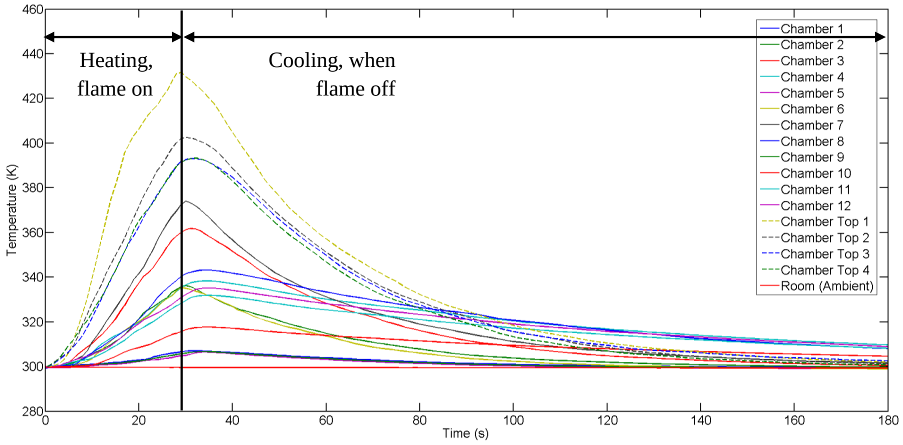

Figure 4.31: Recorded chamber temperature for the combustion of 24.2 L/min of methane supply for the duration of 30 seconds.

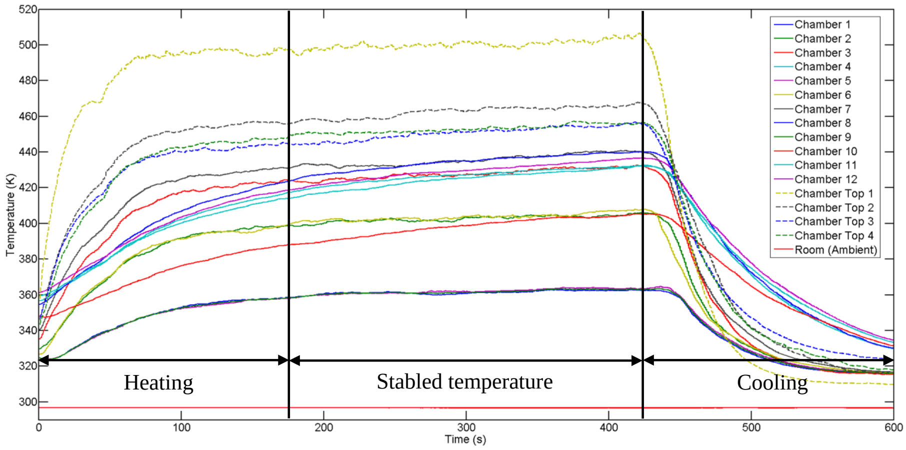

Figure 4.32: Recorded chamber temperature for the combustion of 24.2 L/min of methane supply at the duration of 420 seconds.

discussed and further details of standard operating procedures are summarised in Appendix E. The test procedure includes the measurement of the temperature, pressure, gas compositions and EGR flow rate. The testing parameters of the experiment (fuel compositions, air and fuel supply volume flow rates) were discussed and summarised. The inlet primary air temperature was continuously recorded along with the chamber temperature. The calibration of the pressure transducers and gas flow rate were described and details can be seen in Appendix B. The experimental work was successfully conducted with methane and biogas to validate the numerical work of this project.

Chapter 5

Experimental Results and Discussion

In this chapter, the results obtained from the experimental study are presented. A new laboratory pilot scale combustion chamber was designed, developed and commissioned. The in-furnace measurements for the flame temperature and the combustion product were studied in terms of air/fuel supply, fuel composition, air heater and EGR. At the end of the chapter, the comparison of experimental and numerical studies is discussed.

5.1 Introduction

An experimental work is conducted using methane and biogas as fuel. The detailed schematic diagram of the furnace and burner geometry can be seen in Figure F.1. To achieve the MILD combustion regime, the start-up process needs to preheat the burner and the air-fuel mixture to be higher than the self-ignition temperature (Saha et al., 2014; Abuelnuor et al., 2014). The hot and diluted oxidant from the mixing of the hot supply air and the EGR gas produces MILD combustion. The ambient temperature within the enclosed combustion chamber needs to be higher than the fuel self-ignition temperature. This condition is very important to sustain chemical reactions even in the absence of a flame front (Abuelnuor et al., 2014). There is no modification required to the furnace to change the fuel (methane; biogas) (Colorado et al., 2010). All the combustion in the experimental work did not reach MILD state due to the limitation of low fuel supply. The purpose of the experimental work for this thesis is to validate the numerical modelling work. In this experimental work, various experimental tests were carried out before the experimental validation was started. The various experimental testing are ignition, excess air combustion, methane and biogas flame comparison, non-premixed, partially-premixed and premixed flame, the effect of EGR and secondary air on flame geometry and exhaust gas composition and heated and non-heated secondary air.

5.1.1 Threshold Temperature

The threshold temperature is the minimum ambient enclosed chamber temperature to achieve the MILD combustion regime. In experimental work, before the combustion reached the MILD state, the flame was operated in the conventional regime to preheat the furnace and increase the chamber temperature to achieve the threshold temperature. The threshold temperature for biogas fuel is about 1,173 to 1,223 K in order to achieve the stable MILD combustion regime. Cavigiolo et al. (2003) reported that the threshold for methane is 1,073 to 1,123 K and ethane is 873 to 923 K. In a strong-jet/weak-jet burner when natural gas is used, the average wall temperature needs to reach above 1,013 K in order to sustain the chemical reaction (He et al., 2006). In the present study, the secondary oxidant supply is preheated by an external air heater and an EGR. When the oxygen in the reactant region is diluted to the required level and the threshold temperature in the enclosed chamber is reached, the MILD mode is started. The flame front disappears and flame propagation cannot be observed by the naked eye. In these circumstances, the flame is pale and the reaction zone spreads to the other regions of the chamber. The combustion temperature is uniformly distributed while the NO_x formation is reduced and hot spots are eliminated. In the MILD combustion regime, the peak temperature (and consequently the mean temperature of the furnace) is lower than conventional combustion due to the chamber temperature being uniformly distributed without any constituted flame (Hosseini et al., 2013).

5.1.2 Secondary Air Temperature

The secondary oxidant is heated at consistent heater setting and the heated oxidant temperature is measured. This test was run without a fuel supply (no flame is ignited). The temperature setting for the heater is 673 K. The temperature is measured at two locations: within the heater after the heating element and downstream of the EGR pipe (after the air is mixed with the EGR). The test was conducted without EGR flow to record the temperature at both locations. The temperature was recorded 20 minutes after the heater was started and the temperature readings varied based on the secondary oxidant flow rate (Table 5.1). A further test without a fuel supply was conducted for heated secondary air with and without an exhaust extraction fan to study the effect of the exhaust fan on the chamber temperature. The chamber's temperature was recorded after 20 and 85 minutes of the heating of the air supply. The effect of the chamber temperature with and without exhaust extraction and flame conditions are presented in the following section.

5.1.2.1 Chamber Temperature With Exhaust Extraction

The experiment for the heated secondary air with exhaust extraction was conducted for 85 minutes. This test was run without a fuel supply (no flame is

Table 5.1: Heated secondary oxidant temperature recorded 20 minutes after the heater started.

Air flow rate (L/min)	**11.8**	**23.6**	**35.4**	**47.2**	**59.0**	**70.8**
Internal heater (in K)	660	652	645	639	635	631
Downstream of EGR (in K)	300	303	306	308	310	313

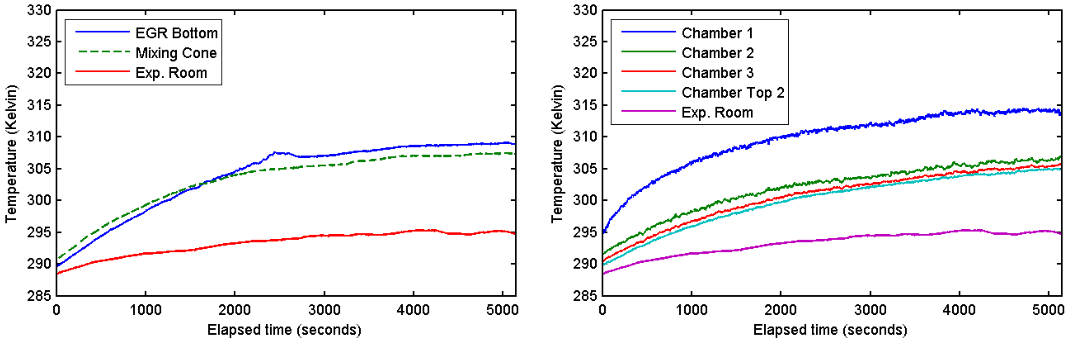

(a) EGR mixed with air and mixing temperature

(b) Chamber temperature

Figure 5.1: Effect of heated secondary air temperature with exhaust extraction fan and without combustion.

ignited). The temperatures were recorded at the heating element, downstream of the EGR pipe, within the mixing cone and within the chamber. The room temperature at the beginning of the test was 288.48 K and it increased to 295.01 K after 85 minutes due to the air in the room being heated by the heated air supply. The recorded heater temperature (inside the heater pipe after the heating element) after 85 minutes was 667.49 K, which was lower than the heater temperature setting of 673.0 K (deviation is less than 1.0 %). This is due to the air at room temperature being induced to the heater, then heated to 673.0 K. When the supply air left the heater, the heated air temperature was reduced due to heat loss to the surroundings and the heater wall.

Figure 5.1 shows the temperature for downstream of the EGR, the mixing cone and the chamber for 85 minutes of the heater running without combustion in the chamber. After the heated secondary air was supplied for 85 minutes, the downstream of EGR temperature increased 6.7 % from 289.55 K to 308.95 K and the mixing temperature increased 5.7 % from 290.64 K to 307.19 K. The temperature at downstream of the mixing between the secondary air and the EGR was 308.95 K which reduced by 0.56 % to 307.19 K at the mixing cone. The maximum chamber temperature was 314.05 K after 75 minutes and this was higher than that of the EGR and the mixing cone. This is due to EGR flowing back to the chamber and playing a role in preheating the chamber air. The location of the combustion chamber temperature reading for both the experimental and numerical work can be seen in Figure 5.2. The annular air nozzle outer diameter (D_a) is 60 mm.

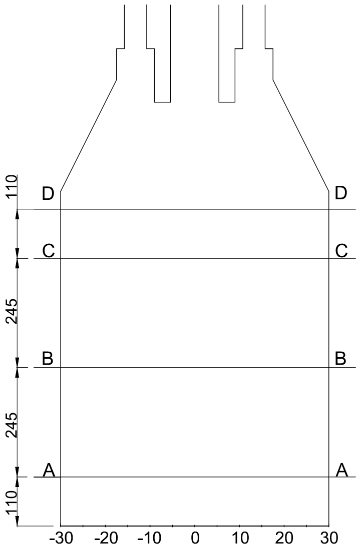

Figure 5.2: Chamber axial location for temperature measurement. Downstream distance (in mm) from injection location, x/D_i: station A-A = 5.2, B-B = 16.9, C-C = 28.5, D-D = 33.8.

Figure 5.3 shows the temperature in the combustion chamber at x/D_i of 5.2 (cross-section of A-A in the Figure 5.2). The supplied secondary air was heated for 20 and 85 minutes and the experiment was conducted without combustion. The centre temperature is increased from 295 K at the beginning of the test to 306.95 K and 314.03 K after heater is continuously powered ON for 20 and 85 minutes respectively. The centre temperature increased by 2.7 % and the wall temperature increased by 2.3 % from 20 to 85 minutes.

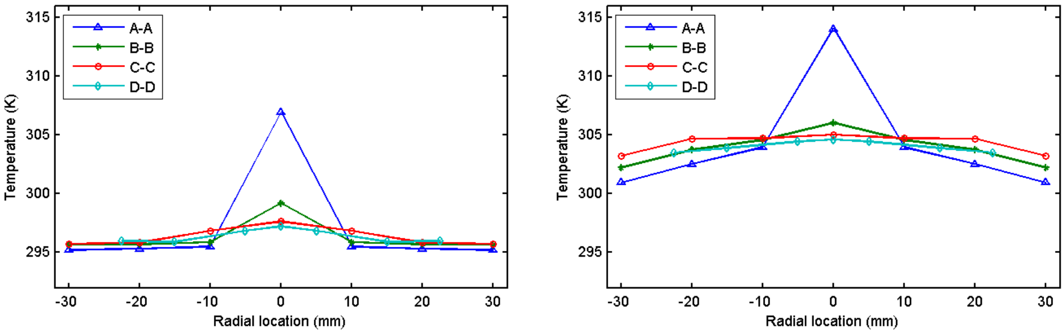

(a) After 20 minutes (b) After 85 minutes

Figure 5.3: Effect of heated secondary air temperature with exhaust extraction fan and without combustion for the chamber.

5.1.2.2 Chamber Temperature Without Exhaust Extraction

The experiment was repeated the following day for the heated secondary air without exhaust extraction and was conducted for 85 minutes. This test was run without a fuel supply, thus no flame was ignited. The room temperature at the start of the test was 288.39 K and after 85 minutes increased to 294.66 K

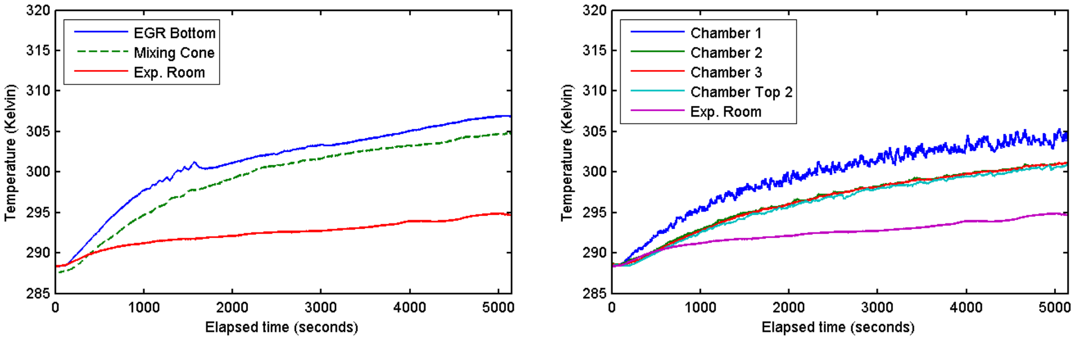

(a) EGR and mixing temperature (b) Chamber temperature

Figure 5.4: Effect of heated secondary air temperature without combustion and exhaust extraction fan.

due to the air in the experimental room being heated by the heated air supply in the experiment. Figure 5.4 shows the temperature for downstream of the EGR, mixing cone and chamber with the heater running for 85 minutes without combustion in the chamber. The heater temperature (inside the heater pipe after the heating element) after 85 minutes was recorded at 666.94 K. This is a reduction of 6.06 K (0.90 %) from the heater temperature setting of 673.0 K. These results are similar to the heated secondary air with exhaust extraction fan and without combustion.

Figure 5.5 shows the heating of secondary air without exhaust extraction fan for 20 and 85 minutes according to the installation of thermocouples location (Figure 5.2). After the heated secondary air was supplied for 85 minutes, the downstream of EGR temperature increased by 6.1 % from 289.39 K to 306.93 K and the mixing temperature increased by 5.9 % from 287.72 K to 304.81 K. The temperature for the secondary air mixed with the EGR at downstream of the EGR was 306.93 K and reduced by 0.69 % to 304.81 K at the mixing cone. The centre temperature increased by 2.87 % and 5.37 % from 288.62 K at the beginning of the test to 296.89 K and 304.11 K after it was continuously heated for 20 and 85 minutes respectively. At the same time, the wall temperature increased by 2.2 % and 4.13 % accordingly. Figures 5.3 and 5.5 show that the chamber temperature (with and without exhaust extraction) increased by 7 K between 20 and 85 minutes (about 1 K for each 10 minutes). Due to no combustion processes occurring, the temperature at the downstream of the EGR and the mixing area was not affected by the exhaust fan extraction. The temperature downstream of the EGR was 307 K and 309 K with and without exhaust extraction respectively. This temperature difference of 2 K can be accounted for by the room temperature difference at the start of the experiment which was also 2 K. From the chamber and downstream of the EGR temperature, for the case of without combustion process, the exhaust extraction fan does not affect the heated secondary air supply.

5.1.3 Flame Conditions

The burner and combustion chamber have been described in detail in Section 4.2. The burner consists of a central fuel jet within an annular nozzle for the hot and diluted secondary oxidant supply. The secondary oxidant supply is heated by an external heater and hot flue gas through an EGR. Fuel and oxidant supply are controlled separately. The auto-ignition temperature for biogas is 923 K (Seadi et al., 2008; Nathan et al., 2010); it is higher than methane which is 873 K (Robinson and Smith, 1984). Compared to methane, biogas has a higher self-ignition temperature, narrower flammability limits and lower flame speed (Willyanto et al., 2013). These properties make biogas harder to burn compared to methane. Figure 5.6 shows the biogas flame propagation for the experimental work observed through the high-temperature glass window for a 12.7 mm (half-inch) burner. Inside a burner the pressure remains almost constant, the flow is a low Mach number and the heat losses to the walls are small (Poinsot and Veynante, 2005). The experimental testing shows primary and secondary combustion zone methane and air flame (Figure 5.7). The flame height for the primary and secondary zones are 95 mm and 230 mm respectively. The temperature at the primary combustion zone is 1,482 K whereas the temperature at the top of the primary combustion zone is 1,702 K. This is due to the fuel and oxidant mixing throughout the primary flame so the combustion process is not complete at the upstream and middle-stream of the primary flame. At the top of the primary zone, the mixing process is completed and the combustion is at the maximum and produces the highest heat released. The temperature starts to decline when the flame enters the secondary zone.

5.2 Flame Ignition

The ignition for the non-premixed, partially-premixed and premixed flames are conducted with 10.82 L/min (10 kPa) and 15.30 L/min (20 kPa) methane fuel sup-

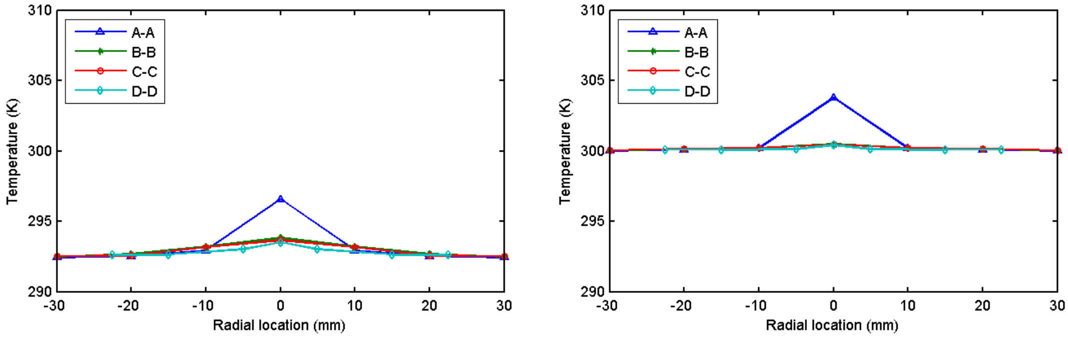

(a) After 20 minutes (b) After 85 minutes

Figure 5.5: Effect of heated secondary air temperature without combustion and exhaust extraction fan for the chamber.

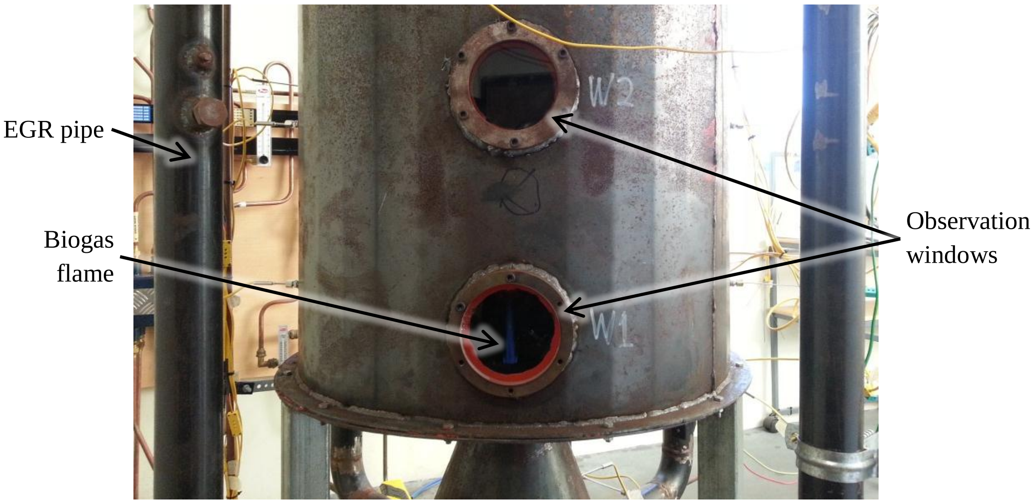

Figure 5.6: Biogas flame observed through high-temperature glass window.

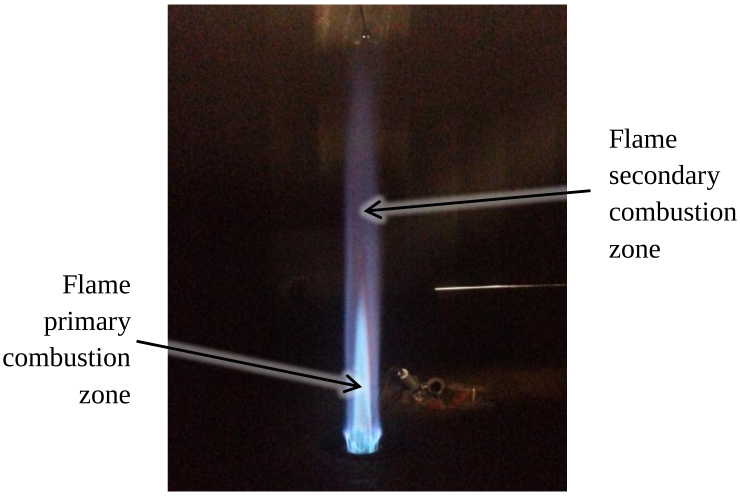

Figure 5.7: Flame primary and secondary combustion zone for methane at $\lambda = 2.0$ (image size is 225 mm × 275 mm).

plies. Figure 5.8 shows the flame temperature recorded five minutes after the flame temperature reached a steady state. The details of the ignition step by step image can be found in Appendix C. The summaries of the ignition for the non-premixed, partially-premixed and premixed flames are shown in Table 5.2.

The heated secondary air also increased the overall mixture temperature to assist the ignition process and ignited quicker than non-heated mixtures. The fastest ignition occurred for partially-premixed with heated secondary air where the mixture ignited 0.43 seconds after the spark started. For the premixed flame the ignition started after 0.70 seconds and the slowest ignition was the non-premixed flame with non-heated secondary air, which ignited 0.83 seconds after the spark started. The partially-premixed flame ignited slightly quicker than the premixed flame because the secondary air supply is preheated. This condition assisted the ignition process when the reactant temperature is slightly higher compared to that of the premixed flame (without secondary air supply). The λ for the partially-premixed fuel stream is 2.90, identical with the λ for the premixed mixture. The partially-premixed mixture needs a higher ignition energy because of the higher volume of reactant (due to higher air content becoming a diluent to the mixture) needing more heat to preheat the reactant before it ignited. The radical pool (example: O and H atoms) is harder to form because of this diluent. For partially-premixed and premixed flames, the λ are 3.66 and 2.90 respectively. More ignition images for various cases of fuel supply, without secondary air for premixed and non-premixed, heated and non-heated secondary air can be found in Appendix C.

Table 5.2: Summary of ignition started for 10.82 L/min (10 kPa) methane with non-premixed (NPF), partially-premixed (PPF) and premixed (PF) flame (HY is preheating, HN is without preheating and SAN is without secondary air).

Case	**NPF HN**	**NPF HY**	**PPF HN**	**PPF HY**	**PF SAN**
Frame number	25	20	18	13	21
Ignited (sec)	0.83	0.67	0.60	0.43	0.70

5.2.1 Ignition of Methane Non-Premixed Flame

The ignition for the non-premixed flame was conducted for the non-heated and heated 23.6 L/min secondary air and is reported in the below subsection. Non-premixed combustion mode occurs when the fuel is injected through the fuel nozzle (the primary air valve is closed). The oxidant supply is only through the secondary air inlet and is later mixed with fuel at the downstream of the flow at the burner just before the reactants are ignited. Figure 5.9 shows the ignition timing of 10.82 L/min (10 kPa) methane non-premixed flame with 23.6 L/min non-heated secondary air. Ignition started at 0.83 seconds after the spark started (frame

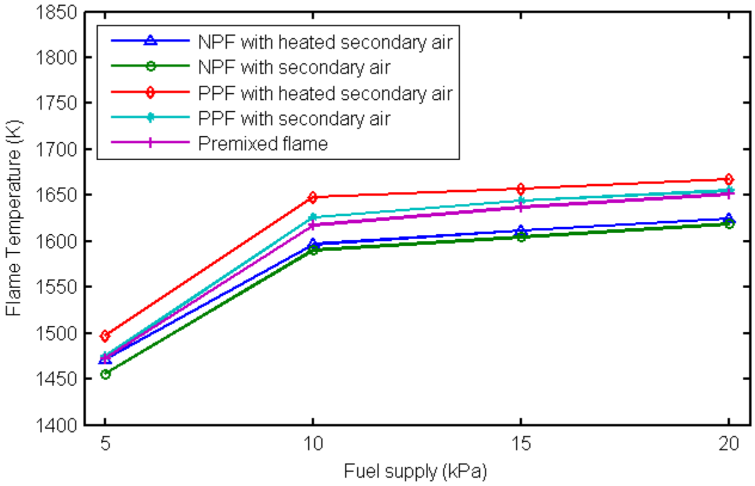

Figure 5.8: Flame temperature for the ignition of the non-premixed, partially-premixed with heated and non-heated secondary air and premixed flame without secondary air.

25). A yellow sooty diffusion flame did not occur at the ignition of 10.82 L/min (10 kPa) with 23.6 L/min of secondary air due to the lower fuel rate not producing a rich fuel condition. However, for the 15.30 L/min (20 kPa) of methane for both NPF with non-heated secondary air (Figure C.2) and NPF with heated secondary air (Figure C.3), the combustion produced a yellow sooty diffusion flame at 3.0 seconds (frame 90) and 5.0 seconds after the spark started (frame 150) when the mixture was at rich during the propagation before the flame reached a steady state.

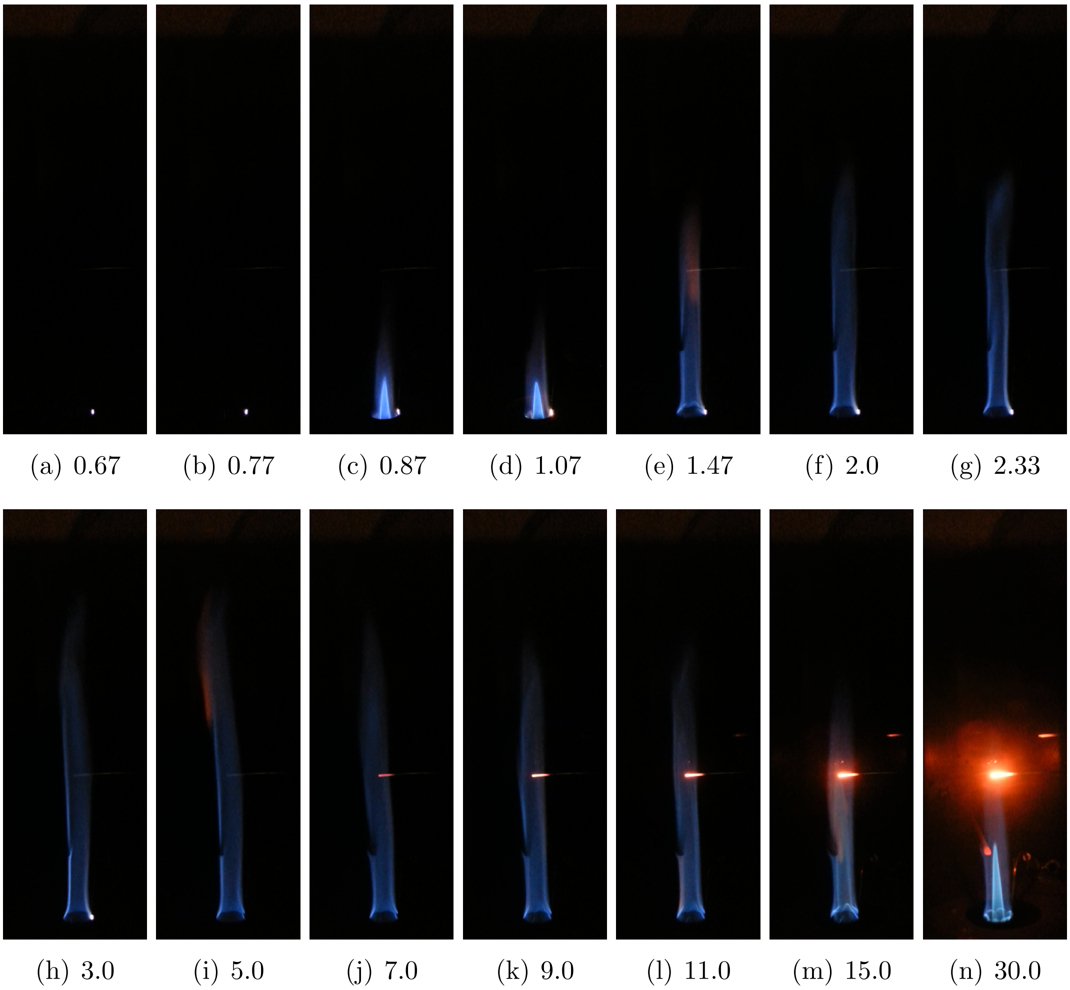
(a) 0.67 (b) 0.77 (c) 0.87 (d) 1.07 (e) 1.47 (f) 2.0 (g) 2.33

(h) 3.0 (i) 5.0 (j) 7.0 (k) 9.0 (l) 11.0 (m) 15.0 (n) 30.0

Figure 5.9: Time (seconds) from beginning of the test for 10.82 L/min (10 kPa) methane non-premixed flame with 23.6 L/min non-heated secondary air with 30 fps recording rate (image size is 100 mm × 300 mm).

Figure 5.10 shows the ignition timing of a 10.82 L/min (10 kPa) methane non-premixed flame with 23.6 L/min heated secondary air. Frame by frame checking for the ignition start point shows that the ignition started at 0.67 seconds after the spark started (frame 20). At 0.63 seconds after the spark started (frame 19), the ignition was not started yet. Heated secondary air assisted the ignition to start earlier compared to the ignition for the secondary air without heating.

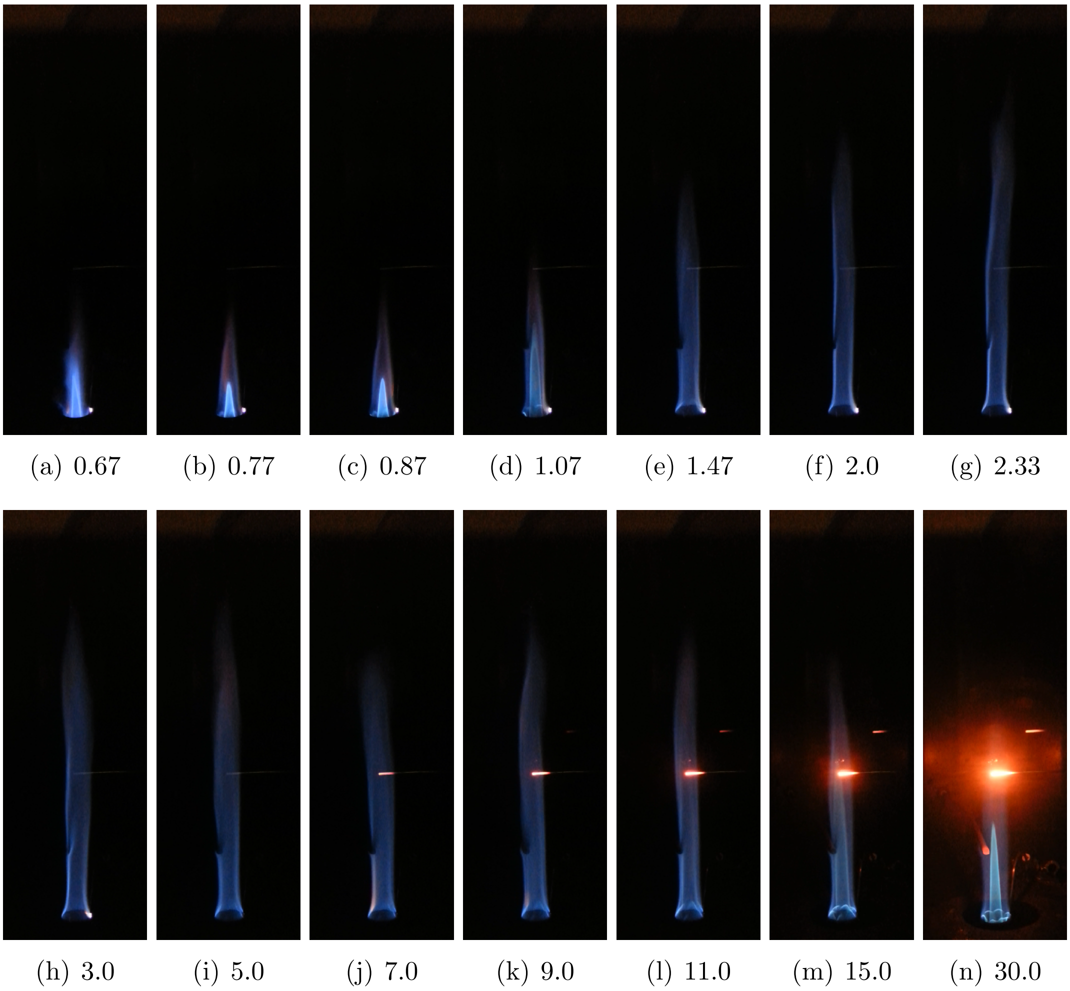
(a) 0.67 (b) 0.77 (c) 0.87 (d) 1.07 (e) 1.47 (f) 2.0 (g) 2.33

(h) 3.0 (i) 5.0 (j) 7.0 (k) 9.0 (l) 11.0 (m) 15.0 (n) 30.0

Figure 5.10: As per Figure 5.9 with heated secondary air.

5.2.2 Ignition of Methane Partially-Premixed Flame

The ignition for a partially-premixed flame was conducted for non-heated and heated 23.6 L/min secondary air and is reported in the below subsection. A partially-premixed setting means that the fuel and primary air are mixed upstream of the fuel nozzle. The reactant mixture was again mixed with the secondary air downstream of the burner nozzle just before the flame ignited. The step by step flame images for the partially-premixed combustion ignition can be seen in Figures 5.11 and 5.12. Methane at 10.82 L/min (10 kPa) was partially-premixed with atmospheric air upstream of the fuel nozzle and then mixed with 23.6 L/min non-heated secondary air. The ignition spark was active until 3 seconds after the spark started (frame 90). The fuel supply was started 0.5 seconds after the spark started. The flame was fully steady 30 seconds of the spark started. From 1.07 seconds (frame 32) until 15.0 seconds after the spark started (frame 450), the flame propagated in a wild mode due to the combustion consuming local oxygen in the chamber. The flame nearly lifted-off at 3.0 seconds after the spark started (frame 90) and part of the flame lifted-off at 5.0 seconds after the spark started (frame 150). 30 seconds the spark ignited was divided into two zones. The flame height for the primary zone was 68 mm and for the secondary flame zone (including the flame brush) was 235 mm. Figure 5.11 shows the ignition timing for the methane at 10.82 L/min (10 kPa) partially-premixed with non-heated secondary air at the upstream of the fuel nozzle and then mixed with non-heated secondary air at 23.6 L/min. Detailed one by one ignition frame images show that the ignition started at 0.60 seconds after the spark started (frame 18). Partially-premixed fuel and oxidant at the fuel nozzle help the ignition to start earlier compared to non-premixed ignition.

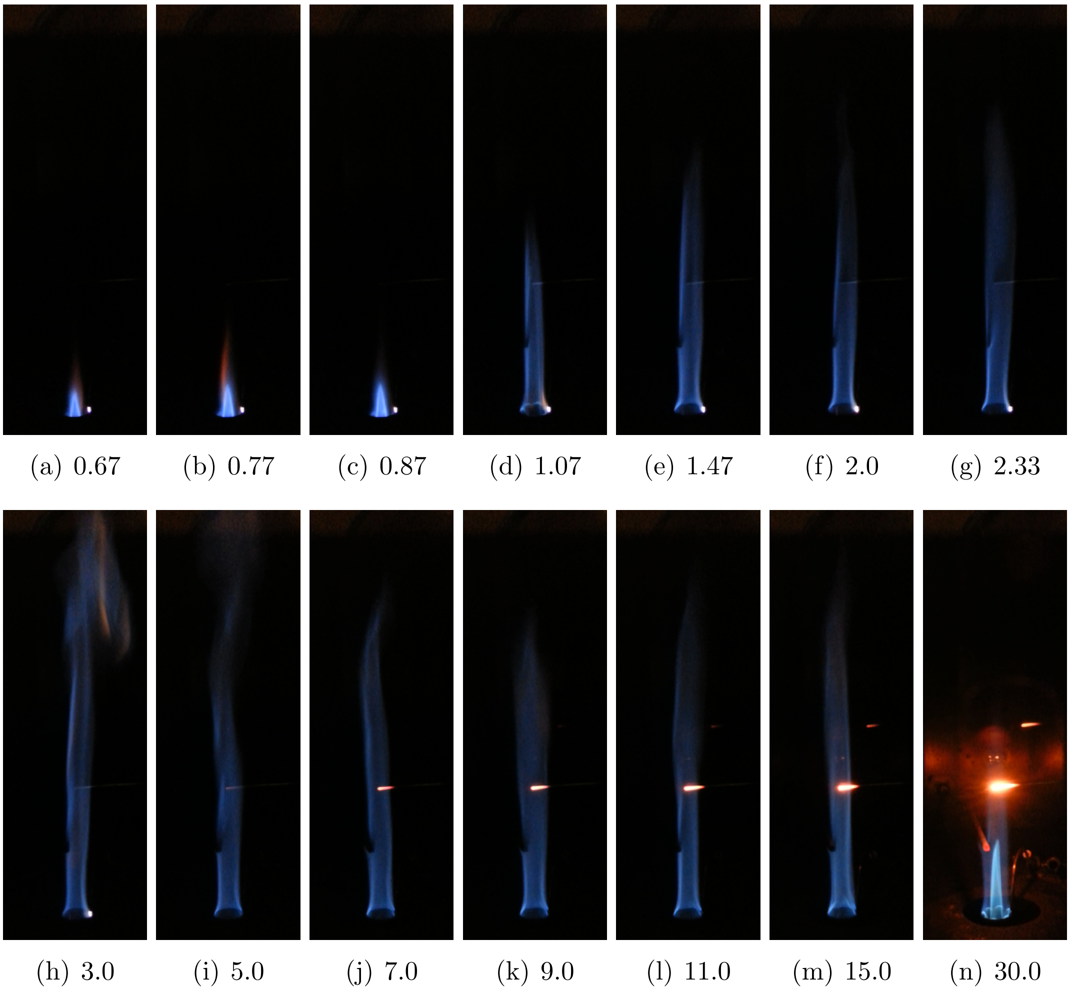
(a) 0.67 (b) 0.77 (c) 0.87 (d) 1.07 (e) 1.47 (f) 2.0 (g) 2.33

(h) 3.0 (i) 5.0 (j) 7.0 (k) 9.0 (l) 11.0 (m) 15.0 (n) 30.0

Figure 5.11: Time (seconds) from beginning of the test for 10.82 L/min (10 kPa) methane partially-premixed flame with 23.6 L/min non-heated secondary air with 30 fps recording rate (image size is 100 mm × 300 mm).

Figure 5.12 shows the ignition timing of a partially-premixed flame with heated secondary air. Methane 10.82 L/min (10 kPa) with 23.6 L/min heated secondary air was injected. The difference between this test and that in the previous section is the heated and non-heated supplied secondary air. Frame by frame checking for ignition shows that it started earlier at 0.43 seconds after the spark started (frame 13). Heated secondary air and partially-premixed fuel and oxidant at the fuel nozzle help the ignition to start earlier compare to non-premixed ignition. For the case of non-heated secondary air, the flame ignition delay is 1.07 seconds after the spark started, while for heated secondary air, the ignition started earlier at 0.67 seconds after the spark started (frame 20). The comparison can be seen clearly from Figures 5.11 and 5.12.

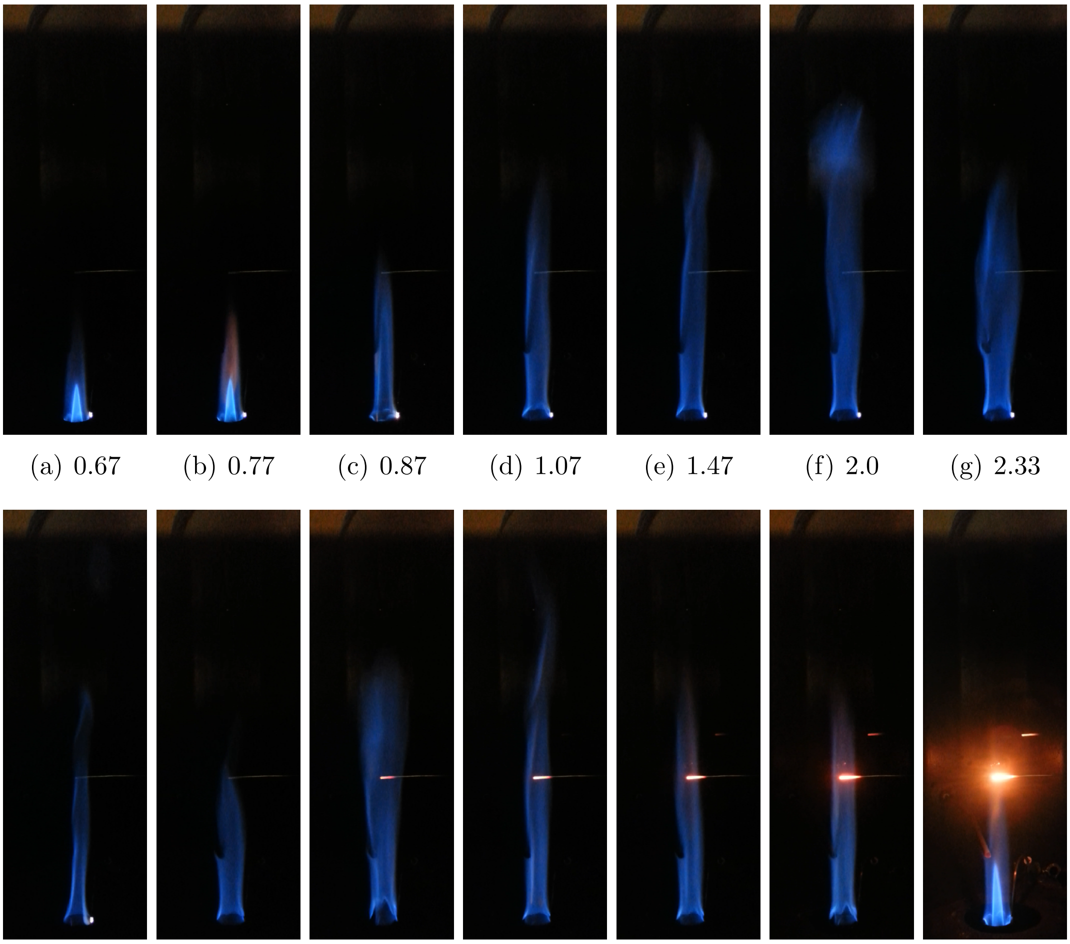

(a) 0.67 (b) 0.77 (c) 0.87 (d) 1.07 (e) 1.47 (f) 2.0 (g) 2.33

(h) 3.0 (i) 5.0 (j) 7.0 (k) 9.0 (l) 11.0 (m) 15.0 (n) 30.0

Figure 5.12: As per Figure 5.11 with heated secondary air.

5.2.3 Ignition of Methane Premixed Flame

Figure 5.13 shows methane at 10.82 L/min (10 kPa) premixed with non-heated atmospheric air at the downstream of the fuel nozzle without secondary air. When the flame is ignited without a secondary air supply, the flame becomes a fully premixed flame. The ignition started at 0.70 seconds after the spark started (frame 21) and achieved a steady flame at 20 seconds after the spark started (frame 600). Premixed fuel and oxidant at the fuel nozzle help the ignition to start earlier compared to non-premixed ignition. The flame achieved full steady propagation at 29 seconds after the spark started (frame 870). The steady flame temperature recorded at thermocouple location 1 (refer to Figure 4.16) was 1,581 K.

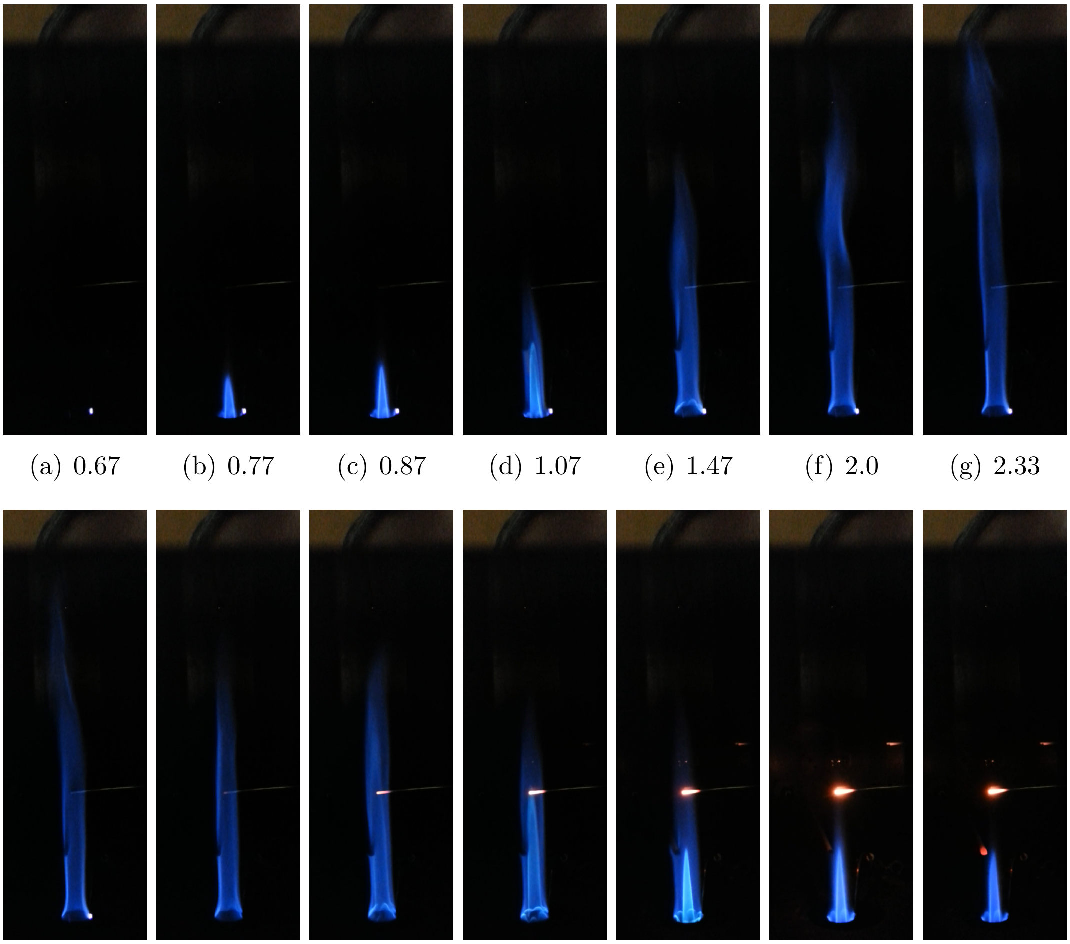

(a) 0.67 (b) 0.77 (c) 0.87 (d) 1.07 (e) 1.47 (f) 2.0 (g) 2.33

(h) 3.0 (i) 5.0 (j) 7.0 (k) 9.0 (l) 11.0 (m) 15.0 (n) 30.0

Figure 5.13: Time (seconds) from beginning of the test for 10.82 L/min (10 kPa) methane premixed flame without secondary air with 30 fps recording rate (image size is 100 mm × 300 mm).

5.2.4 Ignition of Biogas Non-Premixed Flame

Figure 5.14 shows biogas at 15.30 L/min (20 kPa) non-premixed with non-heated secondary air. The ignition started at between 3.0 seconds (frame 90) and 5.0 seconds (frame 150) and started to achieve a steady flame at 30 seconds after the spark started (frame 900). To check the flame ignition timing, a seconds analysis was conducted for the frames between 3.0 seconds and 5.0 seconds. From frame by frame checking, it can be seen that the ignition started at 3.3 seconds after the spark started (frame 100) as shown in Figure 5.15. The biogas is a lower calorific value gas and therefore is harder to ignite compared to methane. Methane ignited between 0.67 seconds (frame 20) and 1.0 seconds (frame 30) which is less than 1.0 seconds after the spark started, but biogas ignited at 3.33 seconds after the spark started. The flame ignited and started very slow and at low flame height. The average flame height at the beginning of the ignition was about 66.9 mm. The highest flame height was at 7.0 seconds after the spark started (frame 210) which was 230.4 mm. The steady flame height at 30 seconds after the spark started (frame 900) was 208.9 mm. The steady flame temperature was 1,586.2 K.

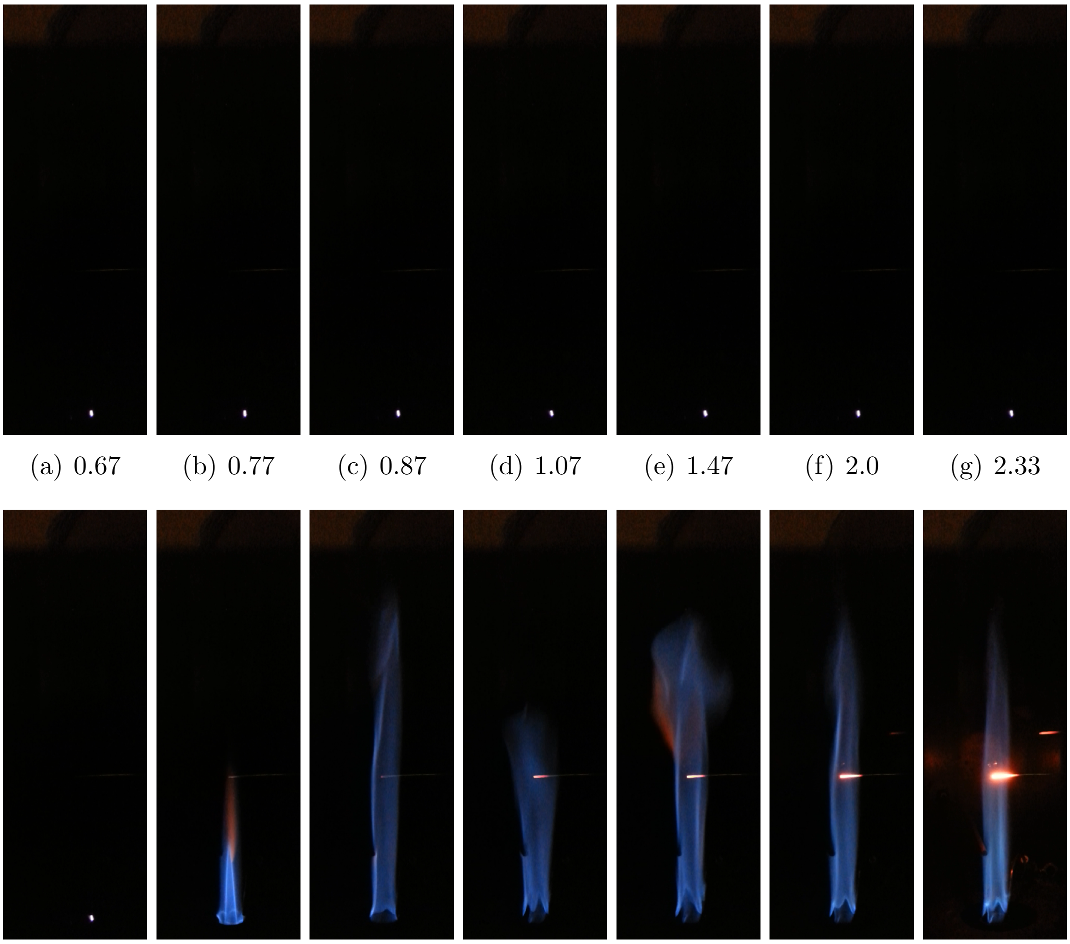

(a) 0.67 (b) 0.77 (c) 0.87 (d) 1.07 (e) 1.47 (f) 2.0 (g) 2.33

(h) 3.0 (i) 5.0 (j) 7.0 (k) 9.0 (l) 11.0 (m) 15.0 (n) 30.0

Figure 5.14: Time (seconds) from beginning of the test for 15.30 L/min (20 kPa) biogas non-premixed flame without secondary air with 30 fps recording rate (image size is 100 mm × 300 mm).

5.3 Excess Air Combustion: Open and Closed Window

The experiment for open and closed observation window number 1 was carried out to compare the combustion products in the exhaust gas. The image of an observation window can be seen in Figure 4.4. The open window will let the atmospheric air freely flow through the combustion chamber and a closed window will not allow excess air flow through the combustion chamber. The flow through chamber experiment where window number 1 is open was undertaken only for this comparison. The rest of the experiments were conducted with all three observation windows closed. This was due to the experimental oxidant supply (mainly atmospheric air) needing to be controlled and always measured as part of the experimental setup and parameters.

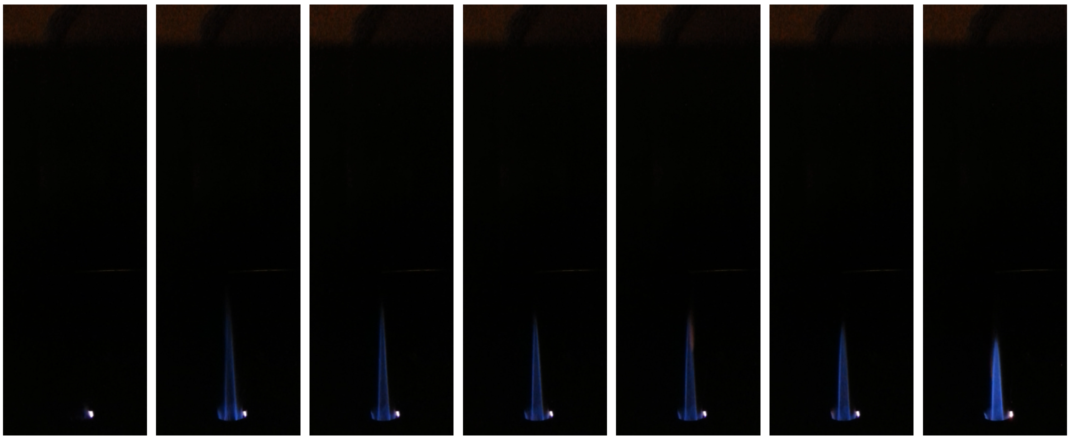

(a) 3.30 (b) 3.33 (c) 3.40 (d) 3.47 (e) 3.53 (f) 3.60 (g) 3.67

Figure 5.15: Time between 3.3 seconds and 3.67 seconds for Figure 5.14 (image size is 100 mm × 300 mm).

5.3.1 Ignition Testing

The ignition timing for the experiment of open and closed window number 1 is summarised in Table 5.3. For the case of closed window number 1, the flame takes 3 seconds to be stable until the oxygen in the chamber is consumed. This is measured by closing all the air supplies (primary and secondary) to the combustion chamber. When the fuel is ignited without external air supply, the flame is blown-off (extinguishes) after 3 seconds, having consumed the local oxygen in the combustion chamber. The above test shows that after the flame is ignited for 3 seconds, all local oxygen in the combustion chamber is consumed and further combustion will start to use the oxygen supplied from primary and secondary sources.

The flame propagation achieved a steady state more quickly for the case of open window number 1 compared to the case of closed window number 1. This is due to the local oxygen in the chamber quickly being replace by the excess air supply flowing into the combustion chamber through the opened window number 1. The starting point for the spark to ignite and start the ignition process varied

Table 5.3: The ignition timing for the experiment of excess air flow through (window number 1 open) and no excess air flow through (closed window number 1).

Item	**Open (seconds)**	**Closed (seconds)**
Ignition button ON	0	0
Spark ignited	60	60
Gas supplied	61	61
Flame ignited	61	61
Flame stable	62	64
Spark end	65	65

from 60 to 70 seconds depending on the readiness of the transformer. For the initial test, the transformer requires longer to initiate ignition, but this time is reduced after five ignition tests. The transformer (model Techrite Codice 1820) made by Techrite Technology (Techrite, 2014) was used to increase the ignition voltage and was installed together with the ignition unit to ensure the spark was sufficient enough to ignite the air/fuel mixture.

The experiment was conducted to compare the ignition of open and closed window number 1 to check the effect of excess air. The partially-premixed flame of methane at 10.82 L/min (10 kPa) with heated secondary air at 11.8 L/min was used. For the experiment of excess air flow through while window number 1 open, Figure 5.16(a) to (f) shows the flame started from ignition and propagated to a steady flame. For the case of no excess air flow through while window number 1 closed, the flame propagations are shown in Figure 5.16(g) to (l)). A steady flame at 45 seconds after the spark started shows a very clear difference between the two cases where for open window number 1, the excess air supply produced conditions similar to a fully non-premixed flame. Both flames (Figure 5.16) ignited at 0.77 seconds after the spark started and flame lift-off occurred at 0.87 seconds after the spark started for window number 1 open and 5.67 seconds after the spark started for window number 1 closed. For the case of window number 1 open, the flame reached a steady state more quickly than with all windows closed. For the closed window, the flame reached a steady state at 45 seconds after the spark started, the flame having blue cone and diffusion flame brush. The blue cone and diffusion flame brush can be observed for both partially-premixed and premixed flame. The height of the diffusion flame brush is about double of the height of the blue cone. Amell (2007) conducted a premixed experiment and observed the blue cone and diffusion flame brush.

5.3.2 Combustion Product

Figure 5.17 shows the λ for observation window number 1 both open and closed. The location of the measurements is at the exhaust pipe and downstream of the EGR pipe. When there was zero secondary air supply, the λ value measured at downstream of the EGR pipe was identical to the λ value measured at the exhaust pipe. When the EGR was mixed with the secondary air supply, the λ was higher since the oxygen mole fraction in the secondary air was higher than the oxygen mole fraction in the downstream of the EGR pipe. This oxygen increased the λ value. The λ for open observation window number 1 is the same even when the fuel supply is slightly increased. This is due to a higher fuel flow rate inducing a higher air flow rate and the burning was lean. The λ for an open window number 1 is 4.25. When window number 1 is closed, the λ reduces when the fuel supply is increased. The oxygen in the chamber is reduced in order to mix with fuel. When the observation window is closed, the λ is 3.2 and 2.3 when the fuel supply is 10.82 L/min (10 kPa) and 21.60 L/min (40 kPa) respectively.

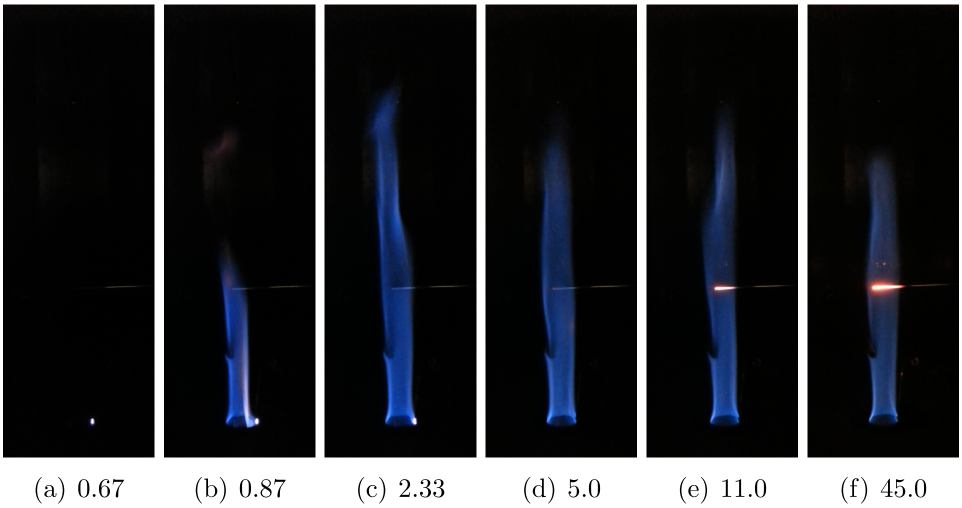
(a) 0.67 (b) 0.87 (c) 2.33 (d) 5.0 (e) 11.0 (f) 45.0

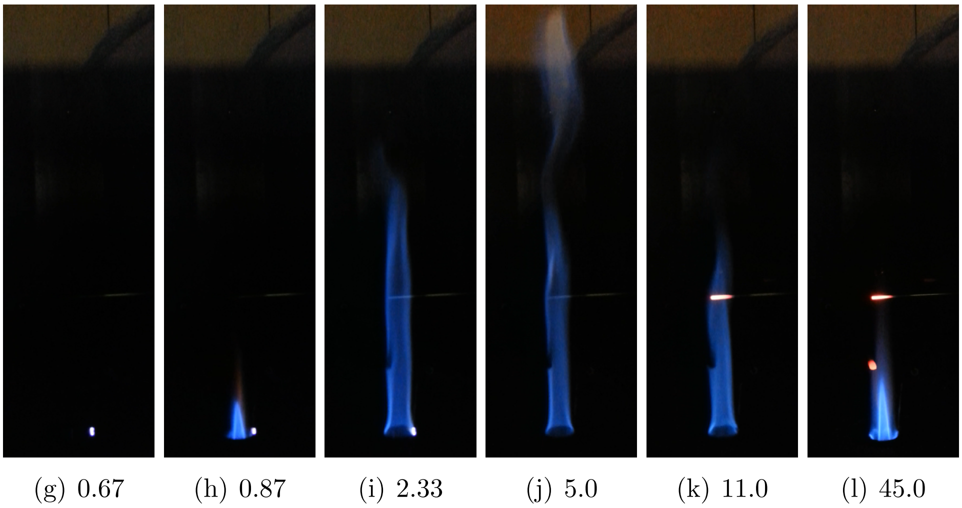
(g) 0.67 (h) 0.87 (i) 2.33 (j) 5.0 (k) 11.0 (l) 45.0

Figure 5.16: Time (seconds) from the beginning of the test for partially-premixed flame methane of 10.82 L/min (10 kPa) with 11.8 L/min of heated secondary air with 30 fps recording rate where (a) to (f) is window number 1 open and (g) to (l) is window number 1 closed (image size is 100 mm × 300 mm).

Figure 5.18 shows the combustion products for the fuel supply of 10.82 L/min (10 kPa), 15.30 L/min (20 kPa), 18.70 L/min (30 kPa) and 21.60 L/min (40 kPa). The comparison for open and closed observation window number 1 is plotted for oxygen, carbon dioxide, oxides of nitrogen and water vapour. Excess oxygen (Figure 5.18(a)) is consistent for open window when fuel is increased but it reduced drastically for the closed window case. This is consistent with the results for λ. Carbon dioxide (Figure 5.18(b)) was low when fuel supply was low and increased when fuel supply increased. When the fuel supply increased, carbon dioxide slightly reduced for open window due to the exhaust gas being diluted by excess air and increased for closed window proportionally with the carbon species increase in the fuel stream. The NO_x (Figure 5.18(c)) shows same trend for both open and closed windows. An open window produced higher NO_x than a closed window due to the combustion having plenty of oxygen supply. The closed window provides limited oxygen and reduced the formation of NO_x in the

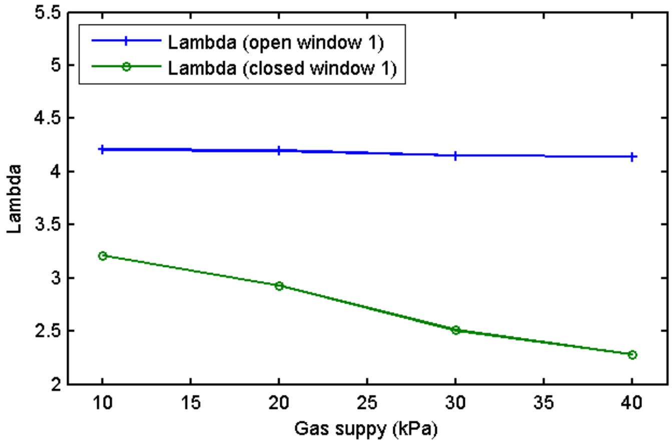

Figure 5.17: Comparison of open and closed observation window number 1 for exhaust gas λ measurement of exhaust pipe.

.

combustion product. Overall, for both open and closed window, NO_x is very low at below 10 ppm showing the combustion is highly efficient and produces very low emissions. Water vapour (Figure 5.18(d)) shows that water vapour increases with the increase of gas supply. This is due to more reactions by methane and air producing more water vapour. During the experiment, the water vapour can be observed on the inside of the high-temperature glass windows.

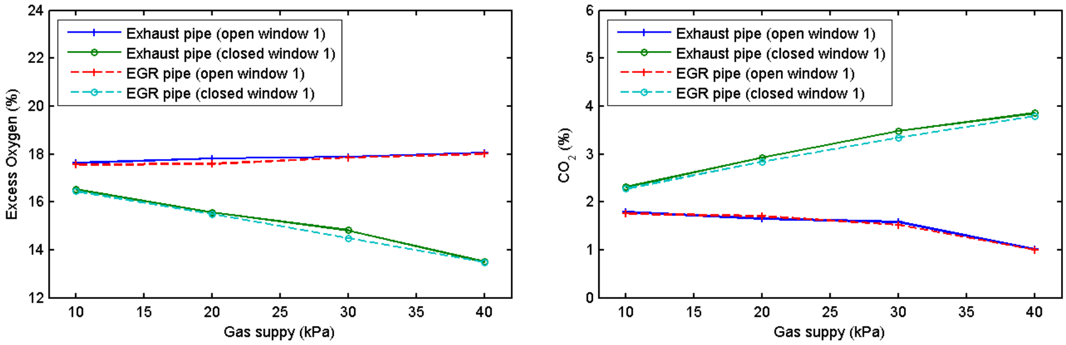

(a) O_2

(b) CO_2

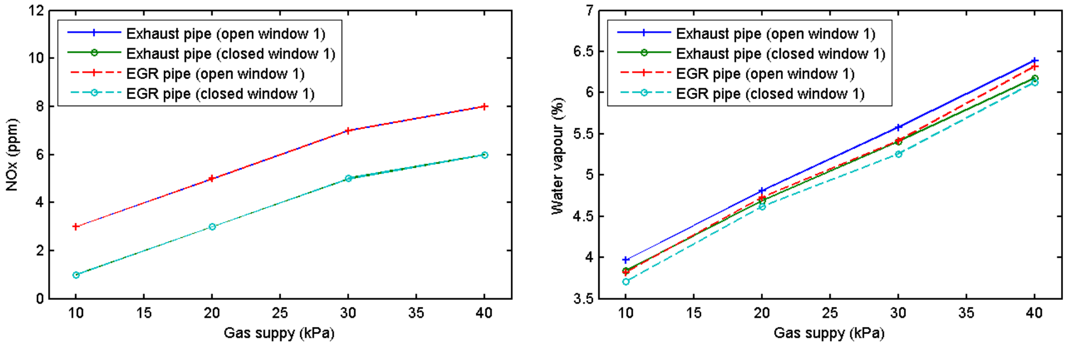

(c) NO_x

(d) H_2O

Figure 5.18: Comparison of open and closed observation window number 1 on exhaust gas measurement at exhaust pipe and EGR pipe.

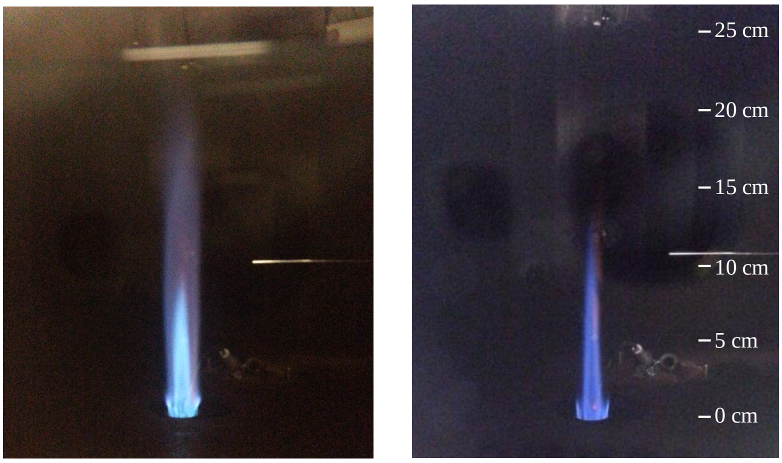

(a) Methane fuel (b) Biogas fuel

Figure 5.19: Photograph of the flame for the same volume flow rate of combustible fuel (image size is 245 mm × 310 mm).

5.4 Comparison of Methane and Biogas Flames

The operating conditions for the premixed methane and biogas flames are summarised in Table 5.4. The Reynolds number for both fuel jet is below 4,000 and it shows the fuel jets is in laminar to transition flow state. Cold flow is normally in transition when the flow Reynolds number is between 2,300 and 4,000. Figure 5.19 shows a photograph of the flames for the combustion of methane and biogas. From Figure 5.19, it can be seen from the observation that the biogas flame has a lower luminosity compared to the methane flame. The methane mass flow rates are identical for both flames requiring the biogas fuel stream flow rate to be higher (Equation 5.1 and Equation 5.2). For the biogas flame, carbon dioxide was added so it was 40 % mole fraction. The flame height for methane fuel and biogas fuel is 260 mm and 140 mm respectively. The Methane flame is bigger and brighter compare to the biogas flame, while the biogas flame has very low luminosity, is weak and easily extinguishes (reaches flame blow-off). The biogas air flame shows only one combustion zone compared to two in methane air combustion. Due to the weakness and low luminosity of the biogas flame, to the naked eye it is quite difficult to distinguish the flame brush and the flame appears faint. The same observation was reported for the natural gas combustion with 3 % oxygen mole fraction on the experimental work for jet hot co-flow by Medwell (2007). The combustion equation for the stoichiometric chemical process for Figure 5.19(a) written in Equation (5.1) and one mole of biogas (60 % methane (1.0 mole) and 40 % carbon dioxide (0.67 mole)) and two mole of air in Equation (5.2) for Figure 5.19(b).

$$\begin{aligned} \mathrm{CH_4} + (2\mathrm{O_2} + 7.52\mathrm{N_2}) &\rightarrow \mathrm{CO_2} + 2\mathrm{H_2O} + 7.52\mathrm{N_2} && (5.1) \\ (\mathrm{CH_4} + 0.67\mathrm{CO_2}) + (2\mathrm{O_2} + 7.5\mathrm{N_2}) &\rightarrow 1.67\mathrm{CO_2} + 2\mathrm{H_2O} + 7.5\mathrm{N_2} && (5.2) \end{aligned}$$

Table 5.4: Operating conditions for methane and biogas premixed flames.

Fuel	**Methane**	**Biogas**
Fuel supply	10.82 L/min	15.12 L/min
Primary oxidant temperature	295 K	295 K
Secondary oxidant flow rate	0	0
λ	2.01	2.05
$\mathrm{Re}_{\mathrm{fuel}}$	1871	3409

5.4.1 Flame Temperature

Figure 5.20 shows the methane and biogas flame temperature measurement with the fuel supply for 80 minutes and following shut-off. For the methane flame (Figure 5.20(a)), the average and maximum temperatures for the combustion are 1,720 and 1,780 K respectively. The peak temperature is reached after 50 seconds and a steady flame maintained. Figure 5.20(b) shows the biogas flame temperature for about 80 minutes. Pure methane is ignited and, when the flame is stable, carbon dioxide is injected to mix with the methane and become synthetic biogas. At the beginning, the temperature is not stable for about 100 seconds and when the flame temperature reduces to the optimum level, the flame is stable (the temperature measurement is steady). At the stable biogas flame (from 15 to 80 minutes) the minimum, average and maximum temperatures for the flame are 1,497 K, 1,558 K and 1,603 K respectively.

The same methane mass flow rate is used for both flames (Figure 5.19), so the same amount of energy in the form of heat release through the exhaust gas is produced. One mole of methane produced one mole of carbon dioxide (Equation 5.1) compared to one mole of methane plus 0.67 mole of carbon dioxide produced 1.67 mole of carbon dioxide (Equation 5.2). This condition will produce a lower flame temperature for biogas than methane because the same heat produced must heat more mass. From the biogas stoichiometric combustion equation (Equation 5.2) the added 0.67 mole fraction of carbon dioxide is a diluent which will not be involved in the combustion and will flow out through the exhaust gas. The biogas flame temperature is lower than that of the methane flame by 125 K due to biogas containing a lower percentage of the combustible gas. The biogas has a lower calorific value giving a lower heat output (Dai et al., 2012; Hosseini et al., 2013).

5.4.2 Lambda

When the volume flow rate is maintained at 10.82 L/min for premixed methane and biogas flames, the combustion equations are Equation 5.1 and Equation 5.3 respectively. The combustion conditions are summarised in Table 5.5. $\mathrm{Re}_{\mathrm{air/fuel\ nozzle}}$ is the Reynolds number for the partially-premixed air/fuel nozzle where the reactant is burned in the chamber, where $\mathrm{Re}_{\mathrm{fuel\ nozzle}}$ is the Reynolds number upstream of the fuel nozzle for the fuel stream before being premixed. The fuel was injected

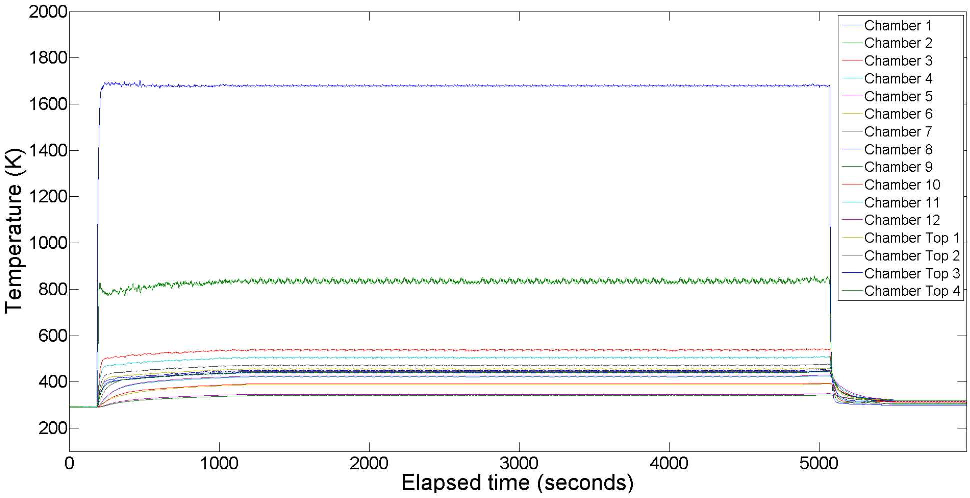

(a) Methane flame

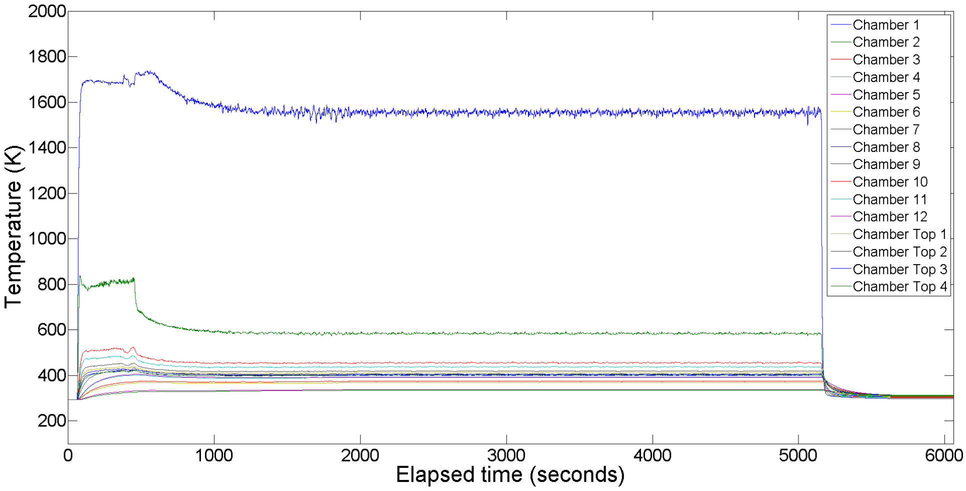

(b) Biogas flame

Figure 5.20: Methane and biogas flame in-furnace temperature.

with a high fuel jet that premixed the air/fuel and later supplied the premixed reactant to the partially-premixed air/fuel nozzle upstream for the combustion process.

$$(0.6\mathrm{CH_4} + 0.4\mathrm{CO_2}) + (1.2\mathrm{O_2} + 4.5\mathrm{N_2}) \quad \rightarrow \quad (\mathrm{CO_2} + 1.2\mathrm{H_2O} + 4.52\mathrm{N_2}) \tag{5.3}$$

The comparison of λ for 80 minutes of methane and biogas combustion is plotted in Figure 5.21. The λ value for the methane combustion is steady at 2.01 and biogas is steady at a higher λ of 2.98. The λ for the combustion of biogas is higher due to the lower methane content in the biogas for the same air flow rate, therefore producing higher excess oxygen in the exhaust gas.

Table 5.5: Operating conditions for methane and biogas premixed flames.

Fuel	**Methane**	**Biogas**
Fuel supply	10.82 L/min	10.82 L/min
Primary oxidant temperature	295 K	295 K
Secondary oxidant supply	0	0
λ	2.01	2.98
$\mathrm{Re}_{\text{air/fuel nozzle}}$	1,971	2,841
$\mathrm{Re}_{\text{fuel nozzle}}$	18,708	28,407

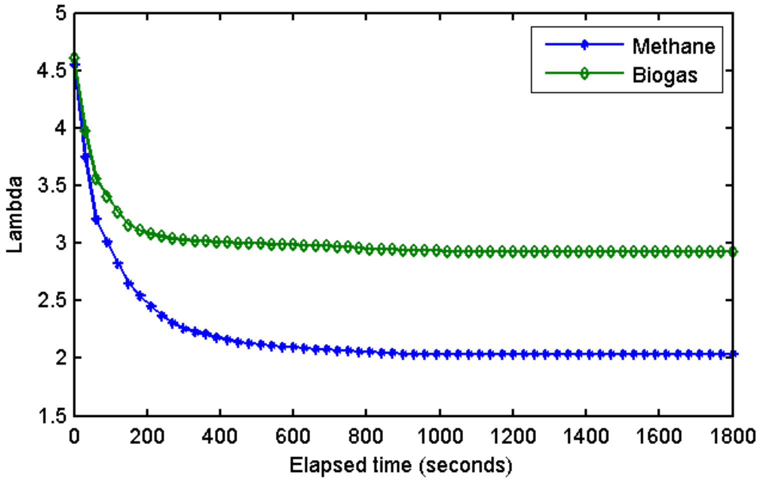

Figure 5.21: Lambda value comparison for methane and biogas combustion.

5.5 Non-Premixed, Partially-Premixed and Premixed Flames

The comparisons for the non-premixed, partially-premixed and premixed flames were conducted for 15.30 L/min (20 kPa) methane to study the flame behaviour and combustion product. For the non-premixed and partially-premixed flames, the secondary air supply was 23.8 L/min and for the premixed flame, there was no secondary air supply: the only air supply was from the primary source at the fuel jet nozzle upstream of the fuel flow (supply). The fuel flow rate was kept constant for all the cases and the secondary air flow rate was also kept constant for all the cases of non-premixed and partially-premixed flames. The test is summarised in Table 5.6 and each test was run and data collected after 20 minutes of the stable flame. Table 5.7 summarises the results. λ is 4.30 for the non-premixed flame, lower at about 3.66 for the partially-premixed flame and reduced to the lowest at 2.90 for premixed flame. Unburned hydrocarbon is below detection limits with the apparatus used for all cases and this condition is in line with excess oxygen in the exhaust gas due to lean combustion. This excess oxygen supply also had an effect on the flame temperature. For the premixed flame, the temperature is lower than for the partially-premixed flame.

Excess oxygen in the exhaust gas is highest for the non-premixed flame and lowest for the premixed flame. These conditions lead to lower temperature for non-premixed compared to partially-premixed. Flame temperature for partially-premixed is the highest due to better air-fuel partially mixed at fuel jet nozzle and again secondary air mixed with air-fuel mixtures at the burner nozzle. This condition produced good air-fuel mixtures for a more complete combustion process. Carbon dioxide and NO_x is slightly higher for partially-premixed and almost the same level for all the cases. NO_x is slightly higher for partially-premixed due to the flame being hotter than in the other cases. Carbon monoxide is below detection limits with the apparatus used for all the cases.

5.6 Chamber Temperature and Combustion Products

The experiment for 100 minutes of 10.82 L/min (10 kPa) methane non-premixed combustion was conducted to study the temperature distribution for the combustion chamber, the EGR, the wall and the exhaust gas. The composition of the combustion products at the exhaust and downstream of the EGR pipe were also recorded.

5.6.1 Chamber Temperature

The combustion chamber's temperature distributions are classified as the main temperature results that need to be examined. The temperature distributions in the combustion chamber will be the key to whether the combustion achieved the MILD condition. Figure 5.22 shows chamber temperature distributions measured at 16 locations. The hottest temperature is the centre area above the flame. The temperatures at locations 1 and 2 are the highest which are 1,600 K and 800 K respectively. The temperatures at other locations are relatively homogeneously distributed and the temperatures are in the range of 350 K to 400 K. The measurement shows that for each location, there are 0.8% to 1.2% increases in temperature for 3,000 seconds time interval. This value is a very small change and was omitted from the analysis.

Table 5.6: Summary of NPF, PPF and PF combustion experimental setup (HY is with preheating, HN is without preheating and SAN is without secondary air).

Flame type	**NPF HN**	**NPF HY**	**PPF HN**	**PPF HY**	**PF SAN**
Fuel	Yes	Yes	Yes	Yes	Yes
Primary air	No	No	Yes	Yes	Yes
Secondary air	Yes	Yes	Yes	Yes	No
Air heater	No	Yes	No	Yes	No

Table 5.7: NPF, PPF and PF combustion with and without secondary air preheating (HY is with preheating, HN is without preheating and SAN is without secondary air).

Item	**NPF HN**	**NPF HY**	**PPF HN**	**PPF HY**	**PF SAN**
Flame Temperature	1567.4	1570.7	1598.2	1601.3	1552.6
λ	4.30	4.25	3.68	3.65	2.90
UHC	0	0	0	0	0
CO	0	0	0	0	0
CO_2	2.1	1.9	2.2	2.1	2.0
NO_x	2.0	2.0	3.0	3.0	2.0
O_2	17.4	17.6	17.1	16.9	15.5

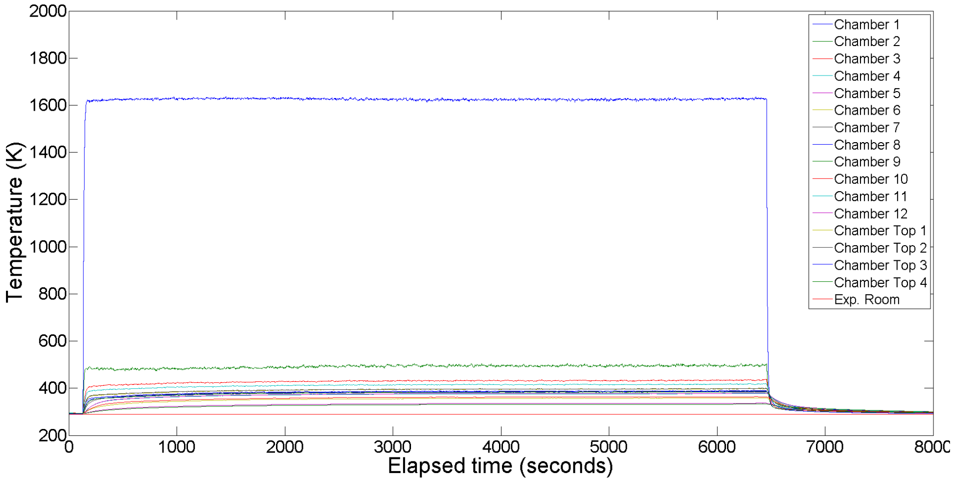

(a) All thermocouples

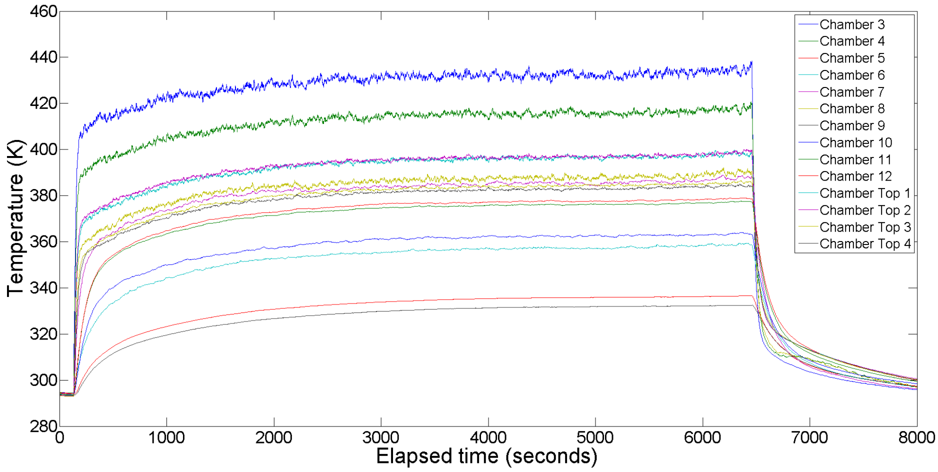

(b) Excluding TC1 and TC2

Figure 5.22: Recorded chamber temperature profile.

5.6.2 EGR Temperature

Some of the hot combustion products are recirculated back to the combustion chamber through the EGR pipe. The EGR temperature is the temperature that

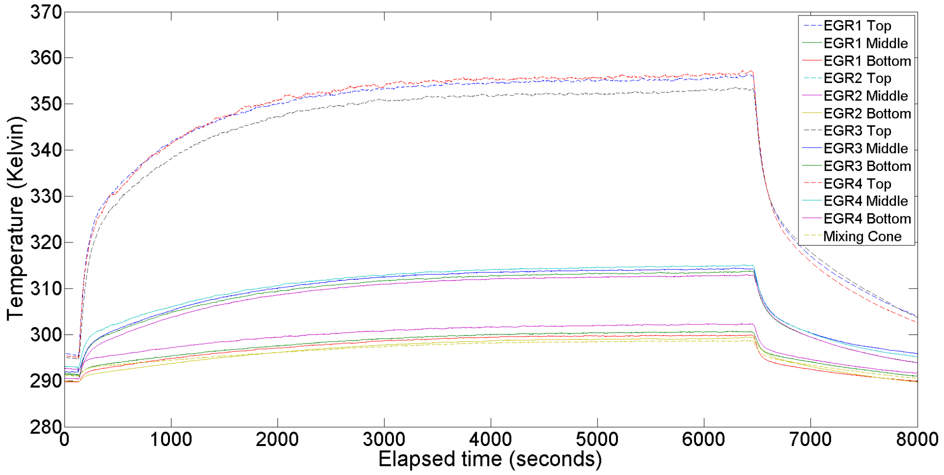

Figure 5.23: EGR temperature profile measured at all four EGR pipe.

.

will preheat the fresh supply oxidant through the secondary air supply. The EGR directly reduced the amount of energy that was required to preheat the reactants, thereby saving on energy costs and increasing the efficiency of the system. The temperature at the upstream of the EGR flow (EGR inlet), centre of the EGR pipe and downstream of the EGR (bottom of the EGR pipe) were measured in order to determine the effect of the EGR pipe on the EGR flow temperature. The most important temperature is at the end of the EGR. This temperature will preheat the fresh oxidant that is injected through the air supply pipe attached to each side of the four EGR pipes before the mixture enters the chamber. Figure 5.23 shows the temperature measurement for the EGR at upstream, middle and downstream of all four EGR pipes. The EGR upstream temperature is the highest, followed by the middle and downstream temperatures. The measurement shows that for each location, there are 0.2% to 0.7% increases in temperature for the 3,000 seconds time interval. This value is a very small change and was omitted from the analysis. The preheating results shows that the preheating temperature is very low and it is lower than fuel autoignition. This level of preheating is far too low to be of any use for MILD combustion. The combustion equation of methane with EGR Ratio (ER) can be seen in Equation 5.4.

$$\mathrm{CH_4 + 2O_2 + 7.5N_2 + ER(CO_2 + 2H_2O + 7.5N_2) \rightarrow (1 + ER)(CO_2 + 2H_2O + 7.5N_2)} \tag{5.4}$$

Since some of the products are recirculated back through the combustion chamber, any unburned hydrocarbons and carbon monoxide will have another chance to re-burn and it will reduce the unburned hydrocarbons and carbon monoxide released to the atmosphere through the exhaust pipe. This will also increase the combustion efficiency since almost all the reactants will be consumed.

5.6.3 Air Dilution Temperature

The temperature of air dilution by the EGR was measured. This temperature is important to ensure that temperature of the oxidant inlet to the combustion

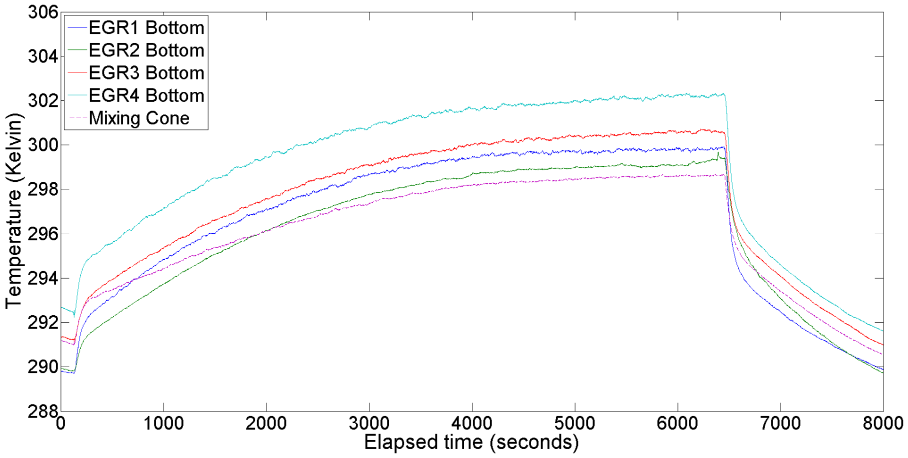

Figure 5.24: Downstream of EGR and secondary oxidant mixing temperature measured at mixing cone.

chamber is higher than room temperature and will help the process of self-ignition of the reactant. The goal is to increase the temperature of this oxidant above the fuel self-ignition temperature, which is difficult to achieve in this case without preheating the supply air using an air heating element. The preheating of the reactant also occurred around the flame base and front continuously during the combustion. Figure 5.24 shows the EGR and secondary oxidant mixing temperatures measured at the mixing cone before this diluted oxidant entered the combustion chamber.

5.6.4 Chamber Wall Temperature

The burner wall temperature is measured with a K-type thermocouple at five locations: four along one side on the combustion chamber wall and one located at the slanting chamber wall (Figure 4.16). The profile of the wall temperature can be seen in Figure 5.25. The wall takes about one hour to reach a steady temperature of 315 K for the combustion of 10.82 L/min (10 kPa) methane non-premixed with secondary air of 23.6 L/min. The highest wall temperature was 315 K, recorded at the top chamber location (slanting chamber wall) and the lowest temperature was about 306 K, recorded at the lowest wall location. More likely convection mixes products with air near the wall better further downstream.

5.6.5 Temperature and Pressure at P1 and P2

The EGR flow rate was measured using two pressure transducers installed at locations P1 and P2. The temperature for locations P1 and P2 as shown in Figure 5.26 are determined using two K-type thermocouples. The temperature for the EGR pipe takes longer to reach a steady state condition. It takes 90 minutes for the P1 and P2 temperatures to achieve 330 K and 310 K respectively. The distance between P1 and P2 is 1.1 m and the temperature drop between these

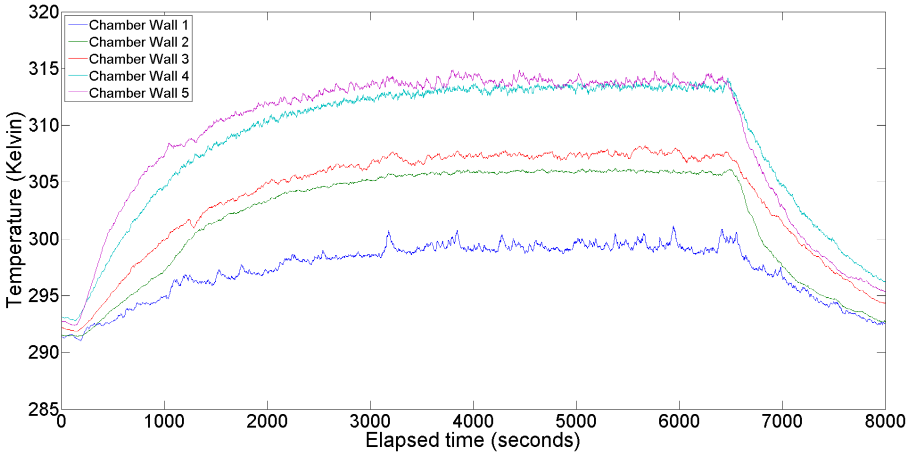

Figure 5.25: Burner wall temperature profile.

.

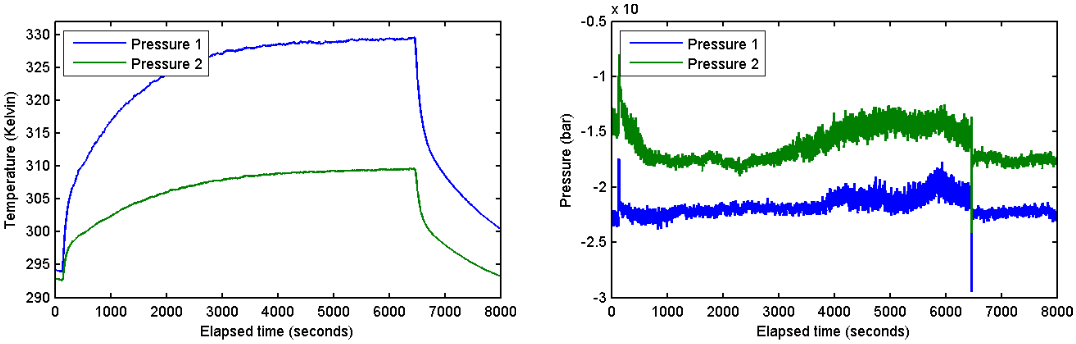

(a) Temperature (1 is top line) (b) Pressure (1 is bottom line)

Figure 5.26: Temperature and pressure for P1 and P2.

two location is 20 K. Pressure was simultaneously recorded at locations P1 and P2 with a sample trace in Figure 5.26(b). There are two transient processes: at 100 seconds, due to the fuel supply starting for the ignition and near the end (at 6,500 seconds), the fuel supply is stopped to end the combustion. After the fuel supply is turned off, the pressure drops slightly due to only the secondary air having a continuous supply.

Figure 5.27 shows the EGR velocity for the experiment, calculated from the pressure difference, for exhaust extraction system ON and OFF. The average EGR velocity of 0.618 m/s is not very sensitive to the secondary air flow rate or the usage of the exhaust extraction system. When the exhaust extraction fan is OFF, the EGR velocity is slightly higher than when it is ON.

5.6.6 Combustion Product

The combustion product such as unburned hydrocarbon, carbon dioxide, water vapour and oxides of nitrogen is measured in the experiment. In the MILD regime, the maximum flame temperature is lower compared to the maximum

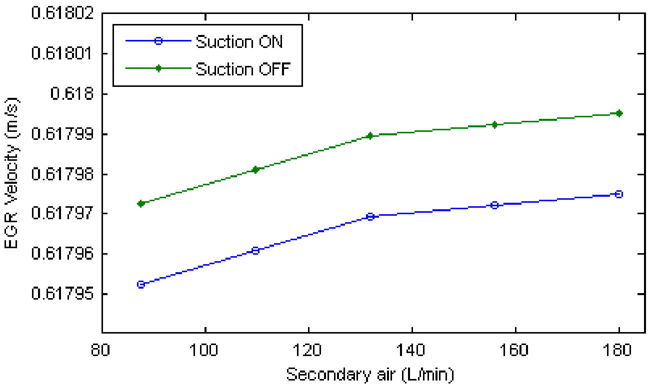

Figure 5.27: EGR velocity for exhaust extraction (suction) ON and OFF.

temperature for conventional combustion, while the average temperature in the furnace can be even higher (thanks to the air pre-heating). With a reduction in the maximum flame temperature, this also reduces the potential damage to the furnace and indirectly will reduce the furnace operation cost. However, it also reduces efficiency (since the ultimate goal of virtually any furnace is heating, which requires a temperature differential). Besides, furnace materials are capable of withstanding typical flame temperatures for long periods of time. A sample case of partially-premixed methane at 10.82 L/min (10 kPa) with 23.8 L/min secondary air supply was selected for the investigation of the combustion products. Figure 5.28 shows the combustion product for NO_x, CO_2 and O_2 recorded at the exhaust pipe and downstream of the EGR pipe with λ recorded only at the exhaust pipe. The measurement is started when the flame is steady after 20 minutes of combustion. Figure 5.28(a) shows the λ value for the 80 minutes of shown combustion. The λ slightly reduced from 3.52 to 3.48, becoming consistent after 50 minutes of combustion, while the species were consistent.

Oxygen is part of the combustion reactant and when lean combustion occurred, part of the combustion product is excess oxygen. Excess oxygen is extra oxygen that is not involved in the combustion process. In that condition, oxygen will be released through the exhaust pipe if there is not enough fuel to consume the oxygen in the oxidant stream. Figure 5.28(b) shows excess oxygen in the combustion of methane. Oxygen is consistent at 16.6 % and 17.3 % for the exhaust pipe and downstream of the EGR respectively. Carbon dioxide is part of normal combustion products. Figure 5.29 shows the carbon dioxide measured at the exhaust pipe and downstream of the EGR from 10.82 L/min (10 kPa) partially-premixed methane with heated 47.2 L/min secondary air supply compared to Figure 5.28(c). Carbon dioxide content in the exhaust gas pipe is consistent after 15 minutes of combustion, as is the oxygen mole fraction. The level of carbon dioxide in the EGR is lower than in the exhaust pipe due to it already being diluted by the secondary air supply, but it increases slowly throughout the combustion.

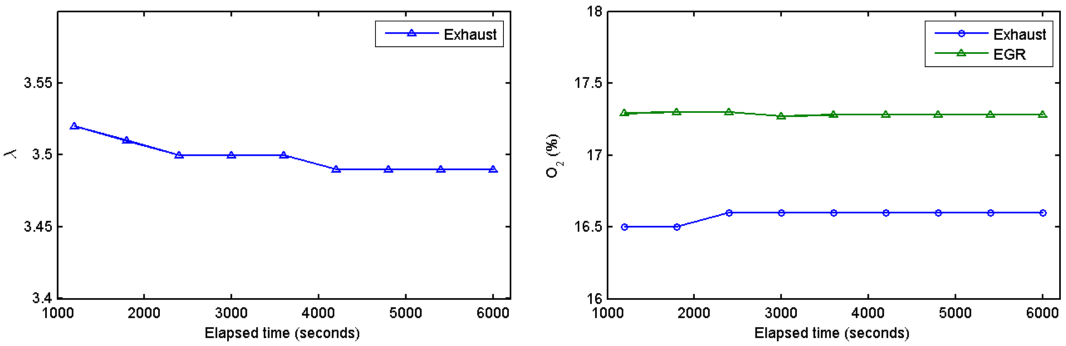

(a) λ (b) O_2

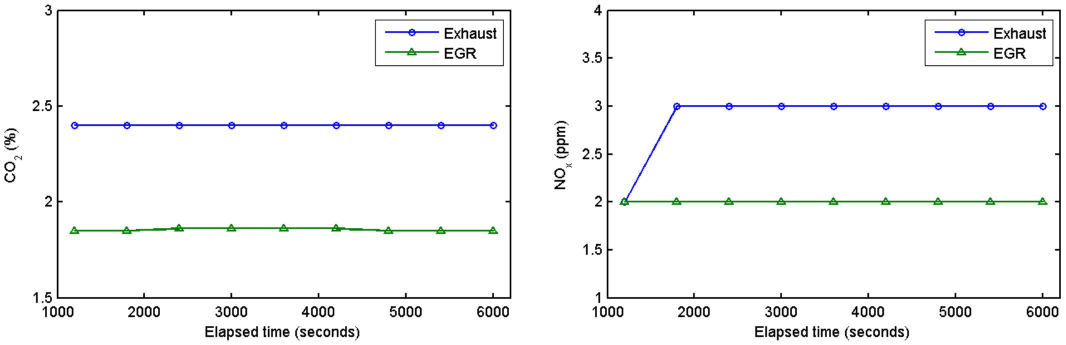

(c) CO_2 (d) NO_x

Figure 5.28: Comparison of exhaust gas compositions at exhaust pipe and downstream of the EGR pipe.

One of the MILD flame characteristics is the reduction in the flame temperature, which also reduces the potential heat loss to the surroundings. The most critical unwanted combustion product for gas fuel is oxides of nitrogen. Since the production of NO_x is strongly linked to the combustion temperature (Heywood, 1988; Kutz, 2006), a reduction of combustion temperature will certainly reduce the production of thermal NO_x. The NO_x is measured at the ex-

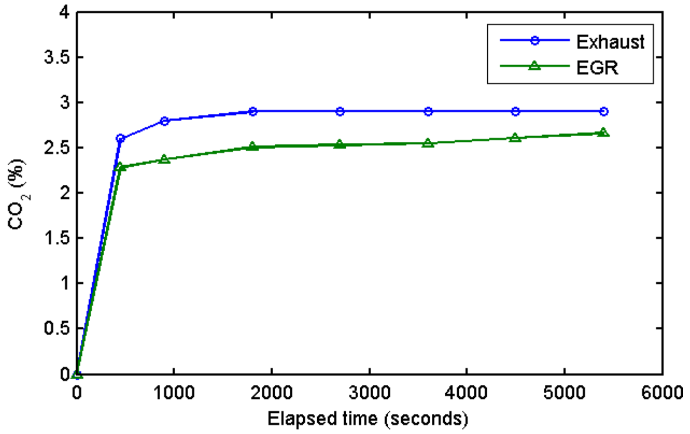

Figure 5.29: Exhaust and EGR gas dilution on methane combustion for carbon dioxide.

haust pipe and after the oxidant is mixed with the EGR at the downstream of the EGR pipe. Overall NO_x pollution is below 3 ppm (Figure 5.28(d)) throughout the combustion, which is acceptable for the combustion process. Unburned hydrocarbon is one of the incomplete combustion processes where some fuel (species containing only C + H atoms) is part of the exhaust gas. Unburned hydrocarbon is the leftover fuel that not is burned during the combustion process. This unburned hydrocarbon will flow out through the exhaust gas and some of it will flow back to the combustion chamber through the EGR pipe. Figure 5.30 shows unburned hydrocarbon from methane combustion. After 10 minutes of combustion, unburned hydrocarbon reduced to below detection limits with the apparatus used. In all the experimental work and experimental repetitions conducted, there were almost zero (below detection limits with the apparatus used) unburned hydrocarbons detected after 20 minutes of combustion in the exhaust gas measured at the exhaust pipe and the EGR pipe.

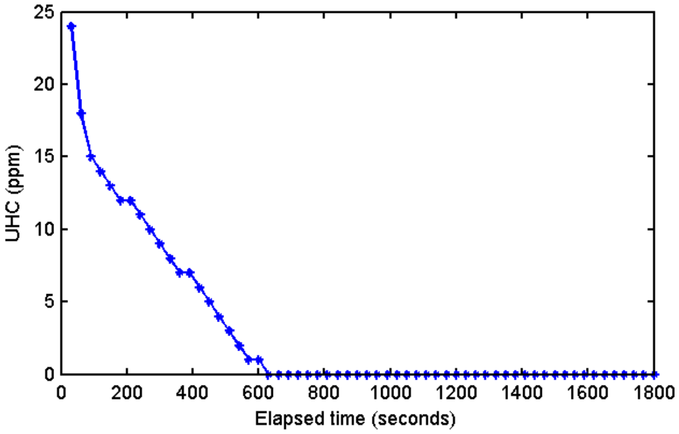

Figure 5.30: Unburned hydrocarbon release with exhaust gas

Incomplete combustion will produce pollutant emissions. The carbon monoxide release through exhaust gases can be an indicator of incomplete combustion being produced when there is insufficient oxygen to form CO_2. In the current experiment, by using methane as a fuel, almost zero (below detection limits with the apparatus used) carbon monoxide is recorded by the gas analyser due to all the carbon content from the methane involved in the chemical reaction in combustion being transformed to carbon dioxide. This shows that the combustion is completed with excess oxygen released together with the exhaust gas. Water vapour is one of the combustion products from methane. Figure 5.31 shows water vapour deposited at the high-temperature window glass during the combustion process. Figure 5.32 shows water vapour from partially-premixed 10.82 L/min (10 kPa) methane with heated 23.6 L/min secondary air supply. The water vapour reached maximum and was steady after 450 seconds of combustion.

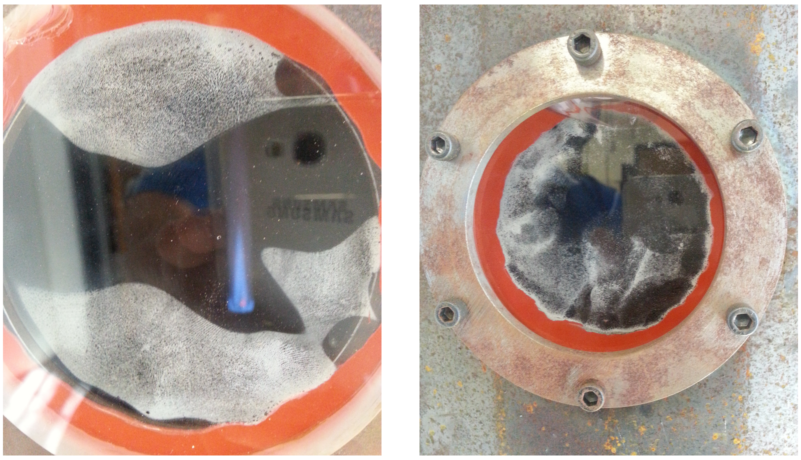

(a) Window 1 (upstream) (b) Window 3 (downstream)

Figure 5.31: Water vapour deposited at the glass window after a period of the combustion. The water vapour later evaporated.

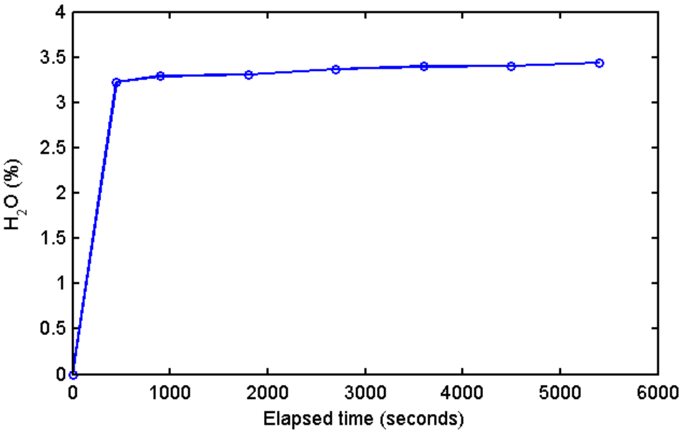

Figure 5.32: Water vapour in exhaust gas for methane combustion.

5.7 Oxygen Dilution

The dilution of the oxygen mole fraction is one of the keys to achieving the MILD condition. The pressure difference for partially-premixed methane at 10.82 L/min (10 kPa) with heated secondary air at 673 K and a flow rate of 47.2 L/min can be seen in Figure 5.33(a). The average pressure at pressure transducer 1 is 195 Pa and pressure transducer 2 is 30 Pa. The mean difference between pressure transducers 1 and 2 is 165 Pa. The mean temperature recorded for pressure transducers 1 and 2 are 344 K and 325 K respectively. The mean temperatures difference between pressure transducers 1 and 2 is 19 K (Figure 5.33(b)). For the case of 13.30 L/min (15 kPa) partially-premixed methane combustion, the pressure difference is 159 Pa and the temperature difference is 25 K. This pressure different shows that the EGR flow dilutes and preheats the secondary air supply.

Figure 5.34 shows the oxygen mole fraction measured at the exhaust pipe and

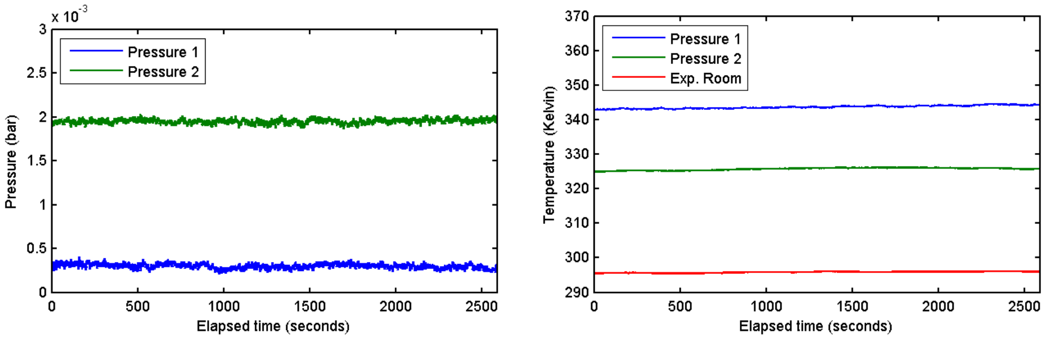

(a) Pressure (1 is bottom line) (b) Temperature (1 is top line)

Figure 5.33: Pressure and temperature for pressure transducers 1 and 2.

downstream of the EGR to analyse the dilution of oxygen by the EGR. The oxygen mole fraction in the exhaust gas is consistent after 15 minutes of combustion. The oxygen mole fraction in the downstream of the EGR pipe which was mixed with secondary air supply reduced steadily and reached the same percentage after 90 minutes of combustion.

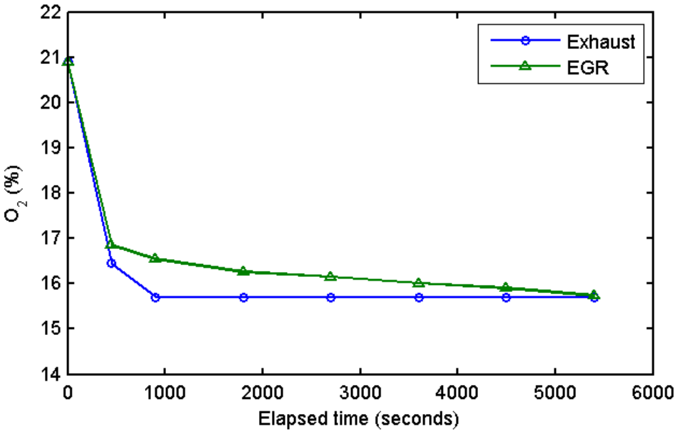

Figure 5.34: Exhaust gas and EGR gas dilution on methane combustion for oxygen.

5.8 Effect of Secondary Air on Flame Geometry

The experiment for the non-premixed flame was conducted for methane and biogas flames, both using 10.82 L/min (10 kPa) of fuel. These were to study the effect of the secondary air flow rate on the flame geometry, temperature and combustion product. The heated secondary air at 11.8 L/min to 70.8 L/min is injected. The heating element is set at 673 K to preheat the secondary air. Figure 5.35 shows the temperature for the non-premixed flame of methane and biogas. All the flame digital images (30 frames per second) discussed in this chapter were obtained from the video recorded using the digital camera. The methane flame has a higher temperature than the biogas flame because methane has a higher calorific value compared to biogas. The flame adiabatic temperature for biogas is 120 K lower than pure methane.

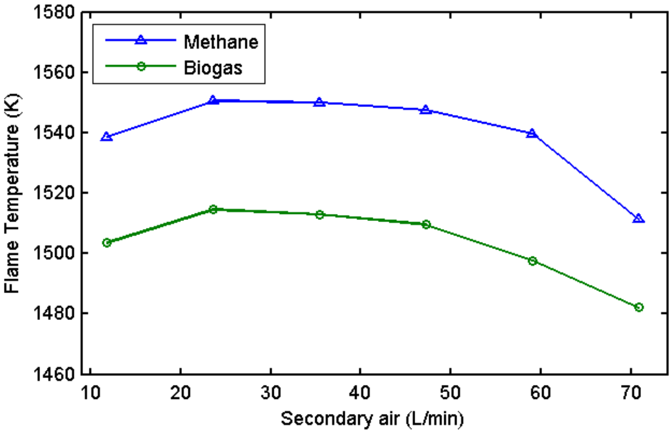

Figure 5.35: Comparison of non-premixed flame temperature for methane and biogas fuel at x/D_i of 5.2 (A-A).

.

Figure 5.36 shows methane and biogas at 10.82 L/min (10 kPa) with various secondary air flow rates from 11.8 L/min to 70.8 L/min. For the methane flame (Figure 5.36(a) to (f)) the lower secondary air flow rate, the flame is clearly divided into two zones but when the secondary air flow rate is at 47.2 L/min, the primary zone starts to disappear. After the secondary air reaches 59.0 L/min, the primary flame zone is completely disappeared. Overall flame height is increased from 167 mm for 11.8 L/min of secondary air flow rate to 186 mm when the secondary air flow rate is 70.8 L/min. As with the methane, an experiment was conducted for biogas and the flame images are shown in Figure 5.36(g) to (l). The primary zone disappeared later than with the methane flame: at 59.0 L/min of secondary air supply flow rate, the primary zone was still very clear and only disappeared at secondary air flow rate of 70.8 L/min. Overall flame height is increased from 137 mm for 11.8 L/min of secondary air flow rate to 182 mm when secondary air flow rate is 70.8 L/min.

5.9 Effect of Secondary Air on Exhaust Gas

The effect of non-preheated and preheated secondary air on the exhaust gas was studied using methane fuel. The exhaust flow rate and combustion products are discussed in the section below.

5.9.1 Preheating Secondary Air for Biogas

The products for partially-premixed combustion are discussed in this section. Methane and biogas at 10.82 L/min (10 kPa) was injected with primary air and mixed with various heated secondary air flow rates in the range of 11.8 L/min to 70.8 L/min. The EGR vent damper is kept to 100% open to let some of the exhaust gas flow. The heating element was set at 673 K to preheat the

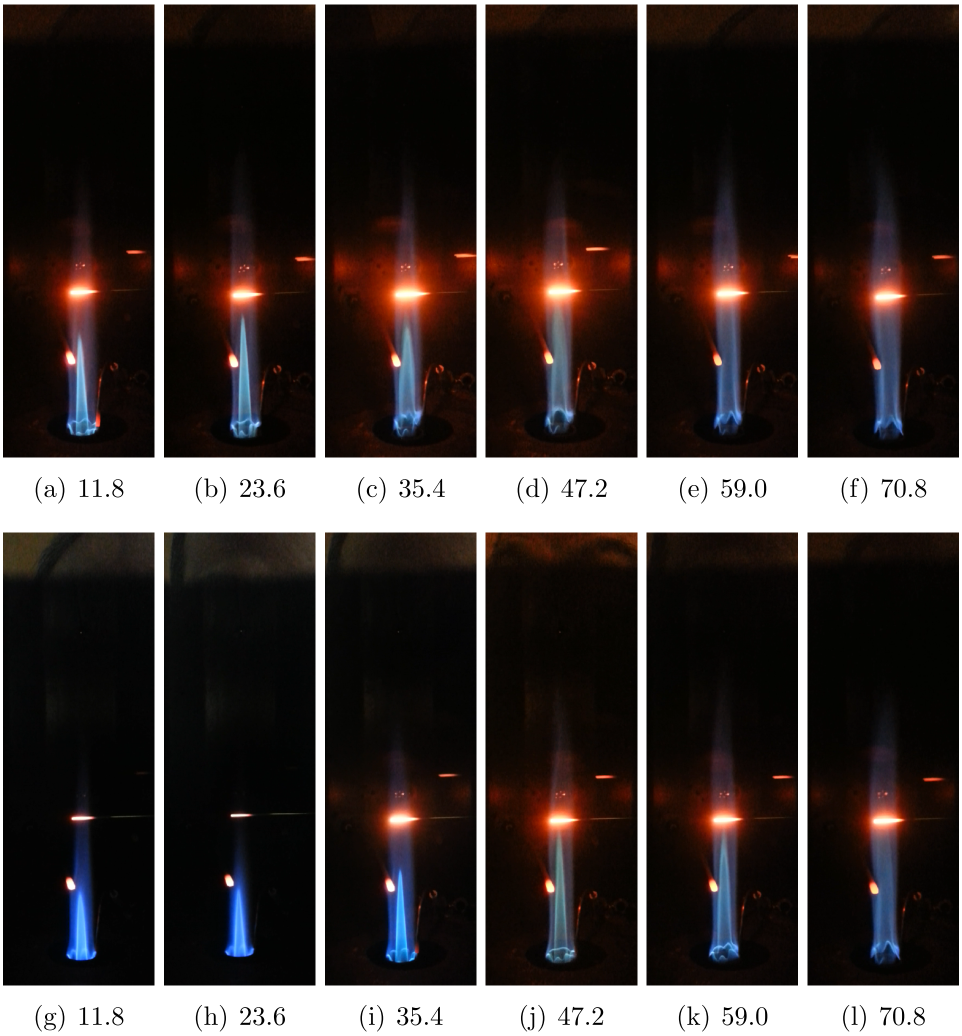
(a) 11.8 (b) 23.6 (c) 35.4 (d) 47.2 (e) 59.0 (f) 70.8

(g) 11.8 (h) 23.6 (i) 35.4 (j) 47.2 (k) 59.0 (l) 70.8

Figure 5.36: Heated secondary air flow rate in L/min for 10.82 L/min (10 kPa) of non-premixed methane flame ((a) to (f)) and non-premixed biogas flame ((g) to (l)) (image size is 100 mm × 300 mm).

secondary air. Figure 5.37 shows the temperature for the partially-premixed flame of methane and biogas. The trend of the temperature result is similar to the non-premixed flame (Figure 5.35). The temperature for the higher secondary air flow rate starts to reduce due to excess secondary air acting as a diluent and making the flame temperature lower. Beside the diluent, the strain rate effect did not occur in this case because the flow was in transition mode. Different strain rate is equal to different turbulence levels (which are most likely to occur with different flow speeds). Flames experiencing high strain rate can lead to extinction.

Figure 5.38 shows the combustion products measured at the exhaust pipe after 20 minutes of steady flame. The combustion λ for biogas is slightly higher than for methane and the trend is similar to excess oxygen. The λ was increased when the secondary air supply was increased while the fuel supply is fixed. For NO_x, both methane and biogas premixed flames are 2 ppm for all flow rates

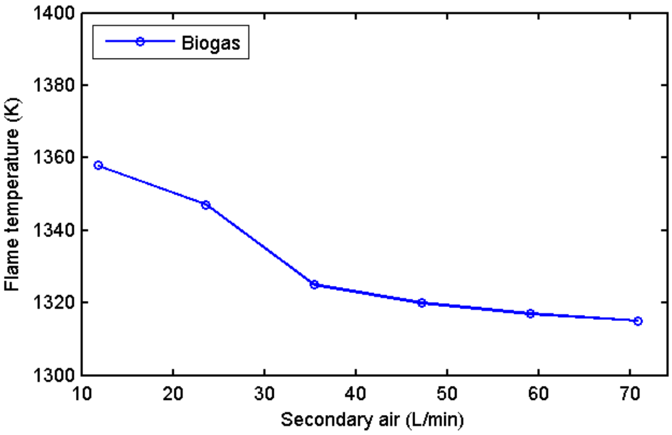

Figure 5.37: Partially-premixed flame temperature for biogas fuel at x/D_i of 5.2 (A-A).

.

whereas for carbon monoxide, biogas produced about 10 ppm at an early stage of the combustion, but it is below detection limits with the apparatus used after 20 minutes of steady flame. For methane, almost zero (below detection limits with the apparatus used) carbon monoxide is recorded and for both methane and biogas unburned hydrocarbon is detected for 3 to 5 minutes of the combustion and then is below detection limits with the apparatus used when the flame is steady.

5.9.2 Non-Preheating Secondary Air for Methane

An experiment was conducted to study the effect of non-preheating secondary air to the exhaust gas. The methane fuel supplied at 10.82 L/min (10 kPa) is injected with various volume flow rates of secondary air supply. The EGR vent damper is kept open to let some of the exhaust gas flow. This is allowed to study the effect of EGR flow on preheating the oxidant. The gases at the exhaust pipe and downstream of the EGR pipe (after the EGR is mixed with the secondary air) are analysed. Figure 5.39 shows that the λ is identical when zero secondary air supply flows through the EGR pipe, i.e. the compositions of the exhaust gas split through the exhaust pipe and the EGR are the same. The supply fuel is 10.82 L/min (10 kPa) and the secondary air is in the range of 0 L/min to 94.4 L/min.

The λ value is increased when the secondary air supply is increased due to excess oxygen content in the atmospheric air used as the secondary air supply. Exhaust gas λ measured at the exhaust pipe is nearly consistent for the secondary air supply of 0 L/min to 47.5 L/min but suddenly increased when the secondary air flow rate increased to 70.5 L/min and 94.4 L/min. The λ at downstream of the EGR pipe is dramatically increased from 1.95 at zero secondary air supply to 5.5 at 94.4 L/min. This is because the downstream of the EGR pipe received the

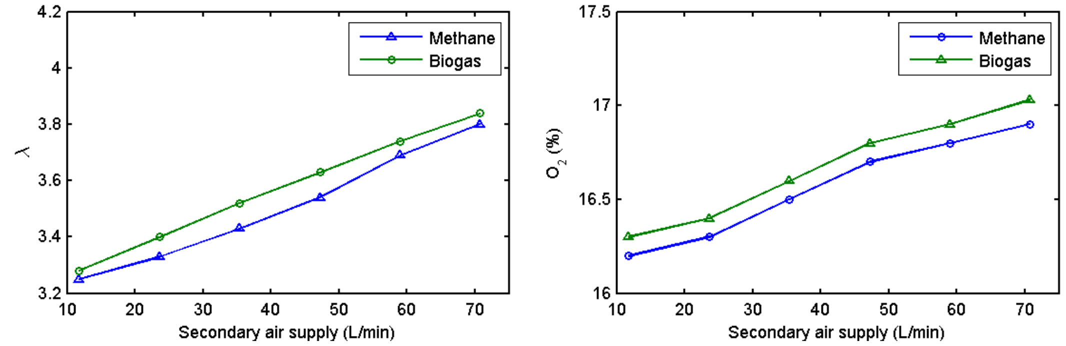

(a) λ (b) O_2

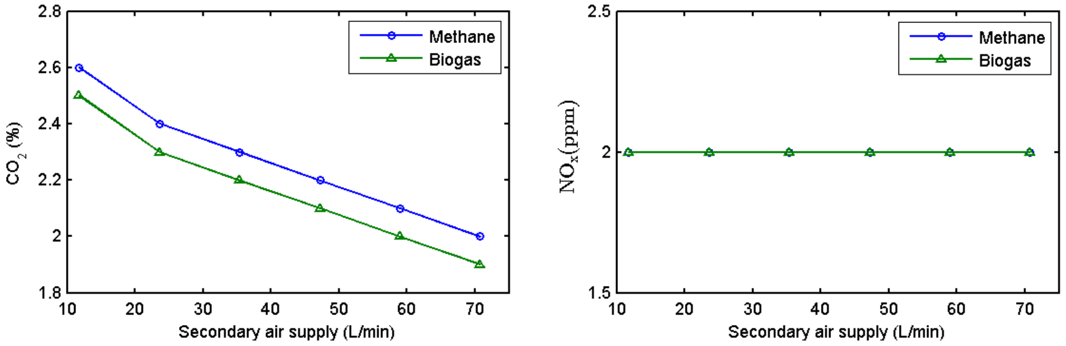

(c) CO_2 (d) NO_x

Figure 5.38: Comparison of partially-premixed methane and biogas flame on combustion product.

fresh air from the secondary air supply, which increased the oxygen. Figure 5.40 shows the exhaust gas data for NO_x emission, carbon dioxide, oxygen and water vapour produced by the combustion and measured at the exhaust pipe. NO_x emission (Figure 5.40(a)) was slightly higher at the lower secondary air supply

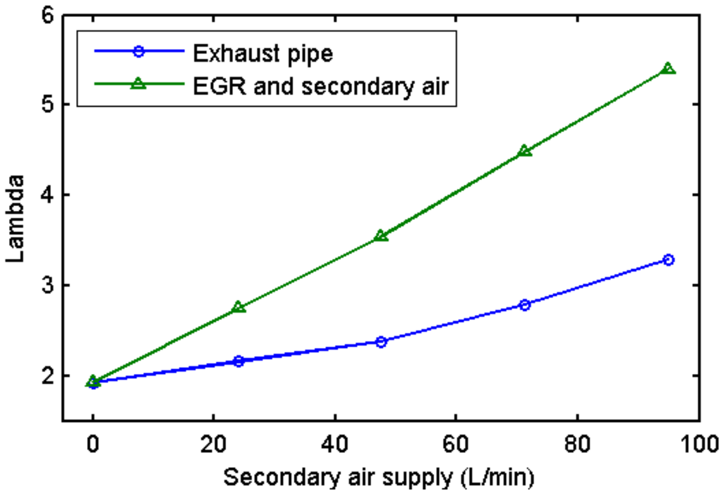

Figure 5.39: Comparison of secondary air supply on λ measurement for exhaust gas in exhaust pipe and EGR pipe.

.

and reduced when the secondary supply air was increased. The secondary air supply caused the reduction in chamber temperature and limited the formation of NO_x. Downstream of the EGR pipe, the secondary air supply slightly diluted the exhaust gas, reducing the amount of NO_x.

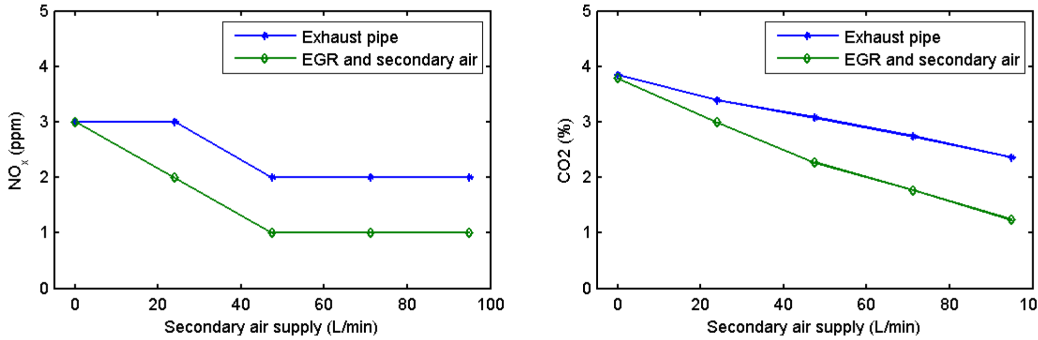

(a) NO_x (b) CO_2

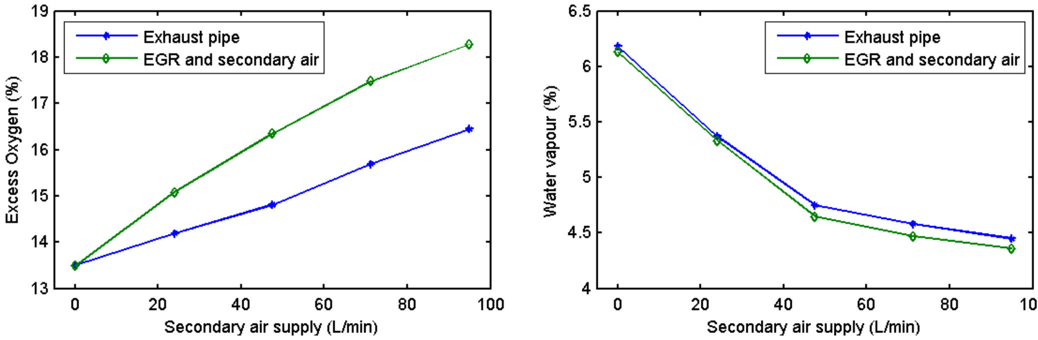

(c) O_2 (d) H_2O

Figure 5.40: Exhaust gas measurement of methane with secondary air supply for exhaust pipe and EGR pipe.

Carbon dioxide is reduced when the secondary air supply is increased (Figure 5.40(b)). Similar to NO_x emission, carbon dioxide detected downstream of the EGR is lower than the exhaust pipe due to the exhaust gas in the downstream of the EGR being diluted by the supplied secondary air. The oxygen mole fraction in the exhaust gas naturally increased when the secondary air supply was increased (Figure 5.40(c)). Water vapour reduced when the secondary air supply flow rate increased (Figure 5.40(d)). In the combustion process, when the same amount of methane fuel is used, the same amount of hydrogen is released from the CH_4 covalent bond and the hydrogen will be involved in the chemical reaction with the oxygen to become H_2O. The formation of water vapour is consistent because hydrogen limits the chemical reaction. When the volume of secondary air is increased, the volume of exhaust gas will simultaneously increase and the volume of water vapour relative to the volume of exhaust gas is reduced.

5.10 Effect of EGR and Heated Secondary Air

Experimental work was conducted to study the effect of heated and non-heated secondary air with and without EGR flow. The secondary air flow rate is injected at 11.8 L/min, 23.6 L/min, 35.4 L/min and 47.2 L/min for all four cases. A total of 16 experiments were conducted for the effect of secondary air and EGR on the chamber temperature and combustion products. The room temperature at the beginning of the experimental work was 290 K. The heating element was set at a maximum temperature of 673 K.

5.10.1 Chamber Temperature

The chamber's temperature for all the 16 experiments are plotted in Figures 5.41 and 5.42 for the case of heated secondary air with and without EGR flow respectively. For the case of non-heated secondary air with and without EGR flow, the results are shown in Figures 5.43 and 5.44 respectively. For each case, the temperature of 16 locations in the combustion chamber were measured and recorded. The thermocouple locations are shown in Figure 5.2. The chamber temperature for the case of heated secondary air with EGR flow (Figure 5.41) gives the highest flame temperature compared to the other three cases. The heated secondary air and EGR help to increase the chamber temperature. The flame temperature for heated secondary air without EGR flow (Figure 5.42) is lower than for heated secondary air with EGR flow. The effect of EGR flow on the flame temperature without the heated secondary air can be seen in Figure 5.43. When a non-heated secondary air supply is used for both with and without EGR flow, the chamber temperature is lower compared to when the heated secondary air supply is used. The lowest flame temperature occurred in the case of non-heated secondary air without EGR flow (Figure 5.44).

Figure 5.45 shows the flame and exhaust temperatures taken from the Figures 5.41, 5.42, 5.43 and 5.44. The flame temperatures are reduced when higher secondary air is supplied to the combustion chamber. In these cases, the secondary air is in excess and acting as a diluent to reduce the flame temperature. The highest temperature is when the secondary air is heated and EGR is used while the lowest flame temperature is when the secondary air used is non-heated and the EGR is OFF. Note that when the heated secondary air is used without the EGR, it gives a higher flame temperature compared to the use of EGR with the non-heated secondary air. The use of the air heating element and the EGR gives a positive effect to the increase of the chamber temperature. The effect of the air heating element is higher compared to the effect of the EGR to the flame and exhaust temperatures. These conditions of flame and exhaust temperatures for all the 16 experiments are summarised in Figure 5.45. Figure 5.45(b) shows the exhaust temperature is increased when the higher temperature secondary air is supplied. This is due to the large volume of the combustion chamber (0.33 m^3)

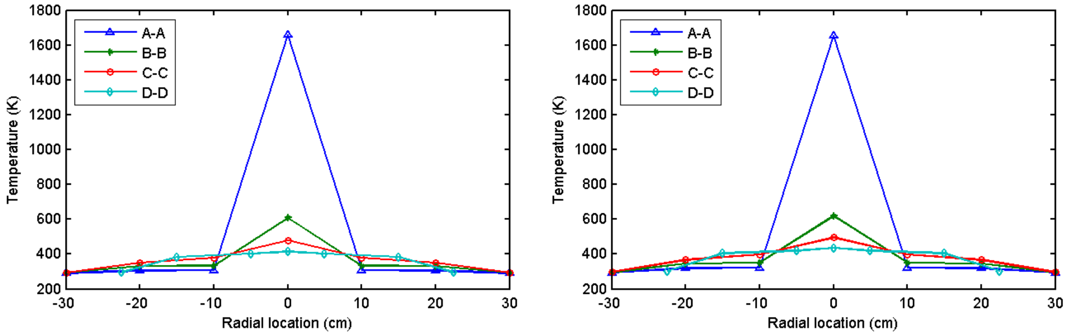

(a) 11.8 L/min (b) 23.6 L/min

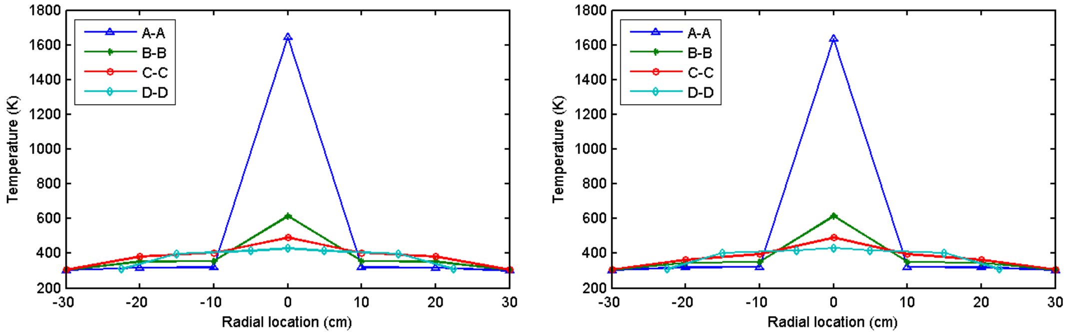

(c) 35.4 L/min (d) 47.2 L/min

Figure 5.41: Effect of heated secondary air and EGR on chamber temperature at different flow rates.

compared to the power output from the combustion, this lower secondary air gives slow exhaust flow out through the exhaust pipe. This slow flow brings a low volume of exhaust gas, resulting in a low temperature for the exhaust gas.

Figure 5.46(a) shows the temperature downstream of the EGR mixing with the supplied secondary air. The EGR temperature is the mean temperature calculated from all four EGR pipes. Figure 5.46(b) shows the mixing cone temperature where all EGR pipes are combined and then mixed. The mixing cone temperature is almost identical to the downstream of EGR temperature. The differences are less than 1.0 K. The temperatures for both downstream of the EGR and the mixing cone are increased with the increase of the secondary air supply. This is the effect of the EGR flow because when the secondary air is increased, the EGR flow is increased (higher volume flow rate of hot exhaust gas).

5.10.2 Combustion Product

An experiment for the partially-premixed methane at 15.30 L/min (20 kPa) with 11.8 L/min to 47.2 L/min non-heated secondary air was conducted to study the combustion products. In this experiment, carbon monoxide and unburned hydrocarbon are reported as below detection limits with the apparatus used after 20 minutes of combustion and the flame has reached steady state. Both com-

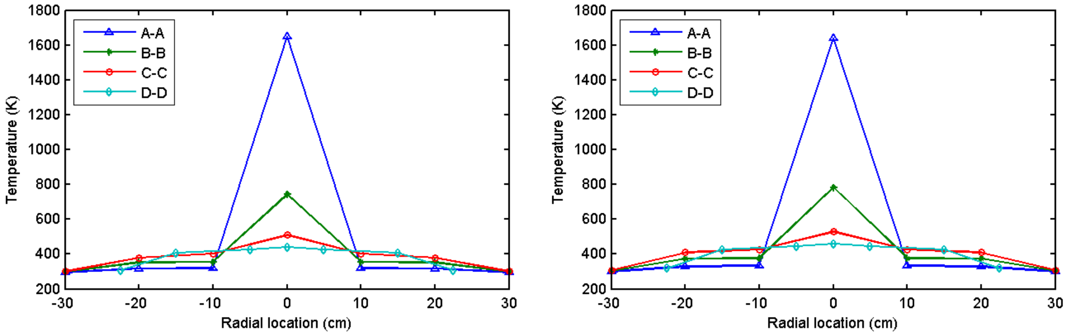

(a) 11.8 L/min (b) 23.6 L/min

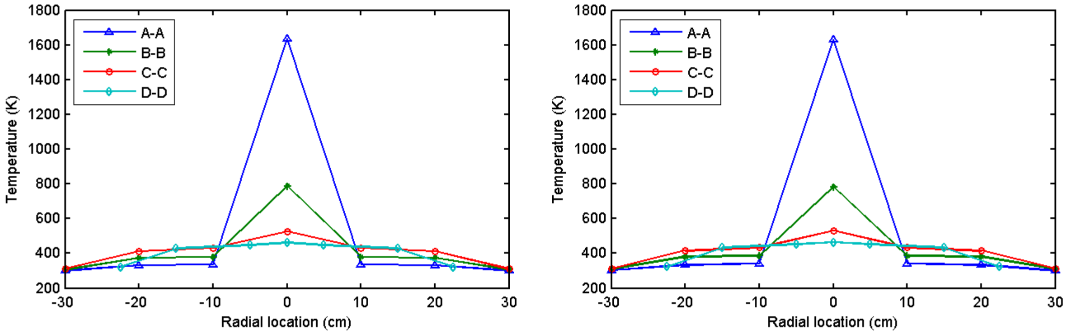

(c) 35.4 L/min (d) 47.2 L/min

Figure 5.42: Effect of heated secondary air to chamber temperature (without EGR) at different flow rates.

bustion products (carbon monoxide and unburned hydrocarbon) are consistently measured as below detection limits with the apparatus used for all the cases. Figure 5.47(a) shows the NO_x emission for the experiments. The NO_x is 3 ppm at the low secondary air supply and reduced to 2 ppm at the higher secondary air supply. This is due to the effect of the flame temperature and the volume of secondary air acted as a diluent to reduce the NO_x concentration.

Heating of the secondary air and use of the EGR affects NO_x. When both are used, the NO_x is 3 ppm for 11.8 L/min and 23.6 L/min secondary air, while when neither is used, the NO_x is 3 ppm and 2 ppm for 11.8 L/min and 23.6 L/min of secondary air respectively. When the EGR is used, the results are identical for both the heated and non-heated secondary air. The similar trend was observed with the unused of EGR. Figure 5.47(b) shows carbon dioxide for heated and non-heated supplied secondary air with and without the EGR. For the case where both the heated secondary air and the EGR being used and where the secondary air is non-heated and the EGR is not used, carbon dioxide is slightly increased with the higher secondary air supply by a factor of 1.3 %. When either the heated secondary air or the EGR is used, carbon dioxide is increased from the low to the high secondary air supply by a factor of 4.02 %. Generally, carbon dioxide is slightly increased with the increase of the secondary air supply and not significantly affected by the heated secondary air and EGR.

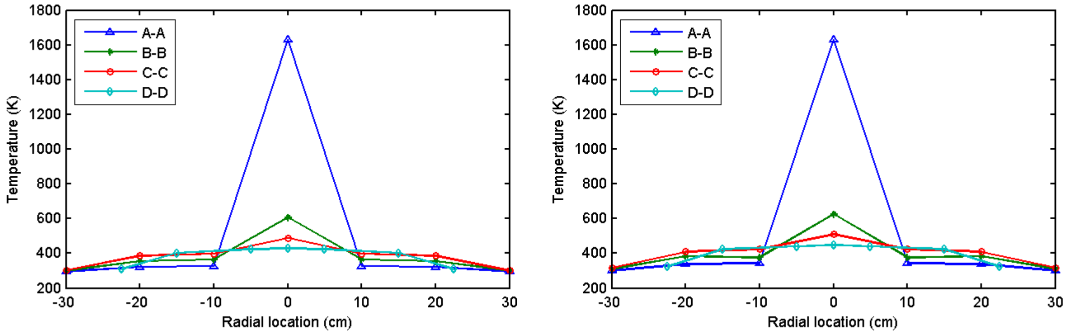

(a) 11.8 L/min

(b) 23.6 L/min

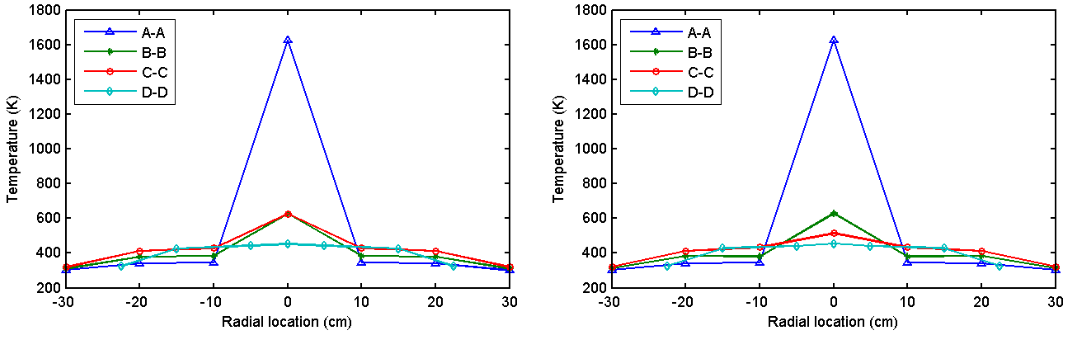

(c) 35.4 L/min

(d) 47.2 L/min

Figure 5.43: Effect of secondary air (without preheating) and EGR to chamber temperature at different flow rates.

Figure 5.48(a) shows the oxygen mole fraction downstream where the EGR is mixed with the secondary air supply, calculated from the mean of the downstream of all four EGR pipes. The oxygen mole fraction is almost constant for all air flows when the EGR vent damper is closed (EGR flow is zero). When the EGR vent damper is open, the oxygen mole fraction is increased from about 14.0% to 16.5 %. For the higher secondary air supply, the excess oxygen in the combustion flowed together with the EGR and increased the oxygen mole fraction downstream of the EGR. The heating and non-heating of the secondary air does not affect the oxygen mole fraction at the downstream of the EGR. Figure 5.48(b) shows the water vapour measured at the same location as Figure 5.48(a). The EGR flow does not give significant effect to the water vapour content in the downstream of the EGR pipes. Similar to the oxygen mole fraction, the heating and non-heating of the secondary air does not affect the water vapour in the EGR pipe. There is only a small effect when the heater is used to preheat the secondary air: the water vapour slightly reduced compared to non-heated secondary air.

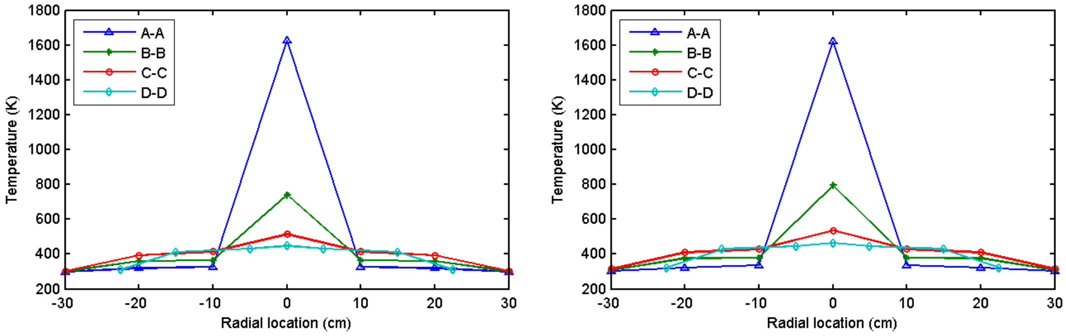

(a) 11.8 L/min (b) 23.6 L/min

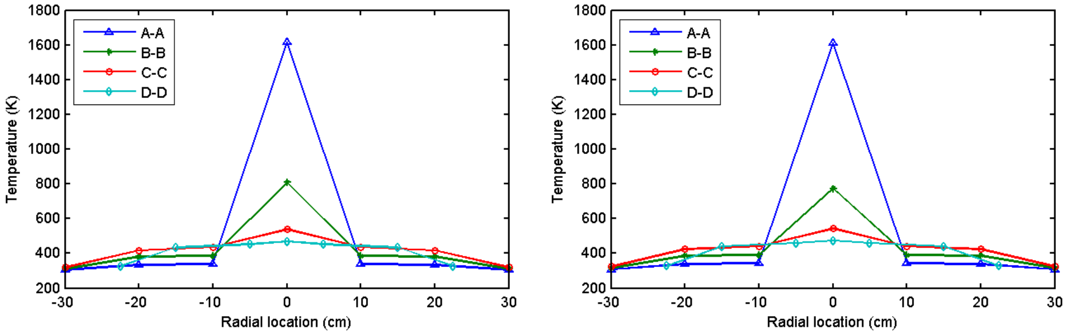

(c) 35.4 L/min (d) 47.2 L/min

Figure 5.44: Effect of secondary air (without preheating) to chamber temperature (without EGR) at different flow rates.

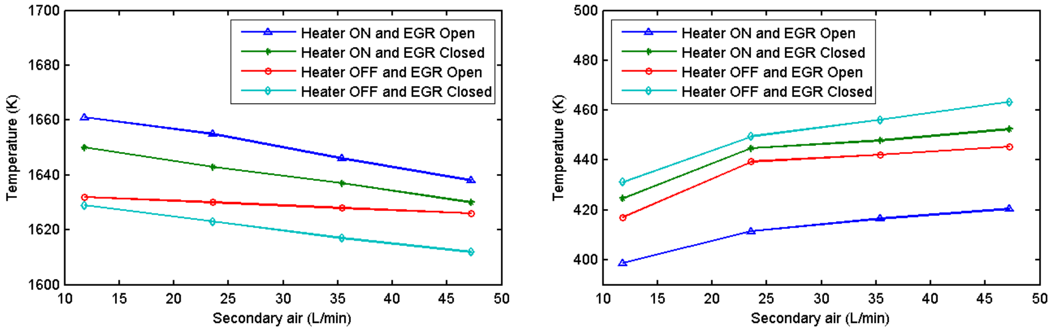

(a) Flame temperature (b) Exhaust temperature

Figure 5.45: Effect of heated and non-heated secondary air with and without EGR.

5.11 Comparison of Experimental and Numerical Results

In this section, the results obtained from the numerical work are compared and validated with the results from the in-furnace measurements from the experimental work. The numerical modelling is an attractive and cost-effective option to predict the behaviour of combustion (Charest et al., 2010). However, part of the numerical modelling must be validated by experimental results to ensure the models are accurate and acceptable. In this work, the same furnace and burner

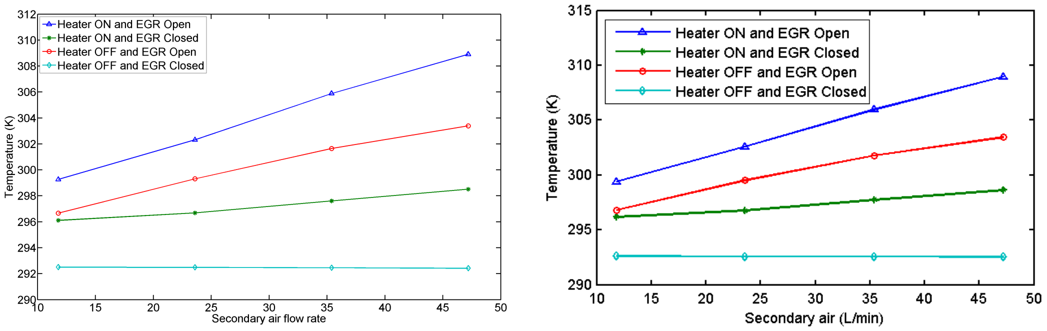

(a) Downstream of the EGR pipe (b) Mixing cone

Figure 5.46: Effect of heated and non-heated secondary air with and without EGR.

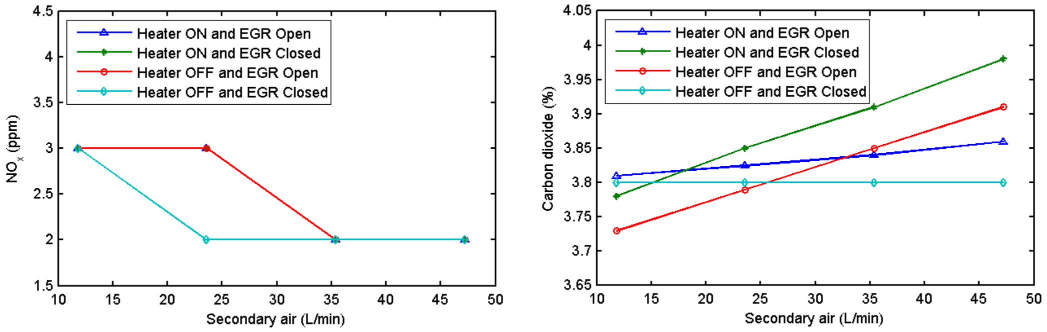

(a) NO_x (b) CO_2

Figure 5.47: Effect of heated and non-heated secondary air with and without EGR on exhaust gas compositions.

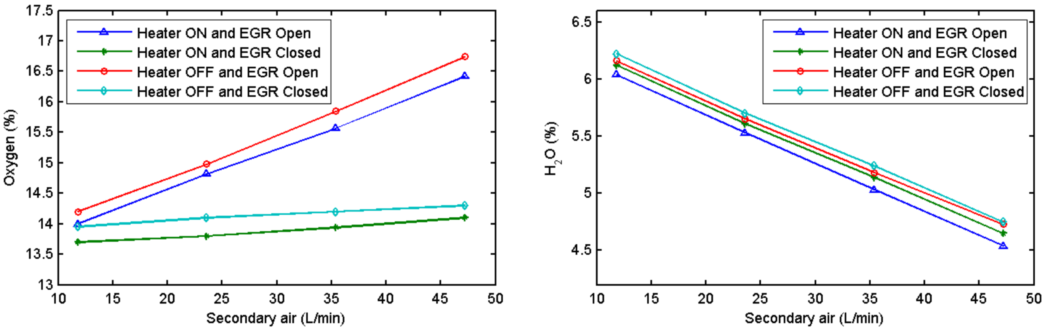

(a) Oxygen mole fraction (b) Water vapour content

Figure 5.48: Effect of heated and non-heated secondary air with and without EGR on exhaust gas compositions.

design for both methane and biogas flames were used and compared for validation between the experimental and the numerical works. A sample case of the experimental and numerical work for the methane and biogas at 10.82 L/min (10 kPa) were used with the λ values of 3.42 and 3.87 respectively.

5.11.1 Methane Flame

Figure 5.49 shows the comparison for the experimental and numerical temperature results for the partially-premixed methane at 10.82 L/min (10 kPa) with λ of 3.42. The figures for each chamber's cross-section at x/D_i of 5.2 (A-A), 16.9 (B-B), 28.5 (C-C) and 33.8 (D-D) are individually separated and can be seen in Figure 5.50. The computed static temperature from the numerical work is in fair agreement with the experimental results, especially on the centreline of the flame front from upstream to downstream of the flame. The numerical modelling for the MILD combustion is mostly based on the Reynolds–Averaged Navier–Stokes (RANS) equations using the standard as well as realisable k–ε models (Orsino et al., 2001; Christo and Dally, 2005; Danon et al., 2010). RANS is a reasonably accurate model to predict the temperature and combustion products. In this case, the results of the simulation slightly over-predict the flame temperatures by about 2 %. Hosseini and Wahid (2014) in the study of flameless combustion confirmed that the numerical solution has about 5 % prediction error compared to the experimental results. These discrepancies could be attributed to errors related to the measurement equipment (Hosseini and Wahid, 2014).

For the numerical modelling for the centreline of the flame, the temperature is 1,432 K and it over-predicted compared to the experimental temperature, recorded at 1,409 K, by 1.6 %. Along the flame centreline, the predicted local flame temperature at x/D_i of 16.9 (B-B), 28.5 (C-C) and further downstream of 33.8 (D-D), the over-prediction is about 1 % to 3 % and this is good agreement between the experimental and numerical work. At the distances of 100 mm and 200 mm from

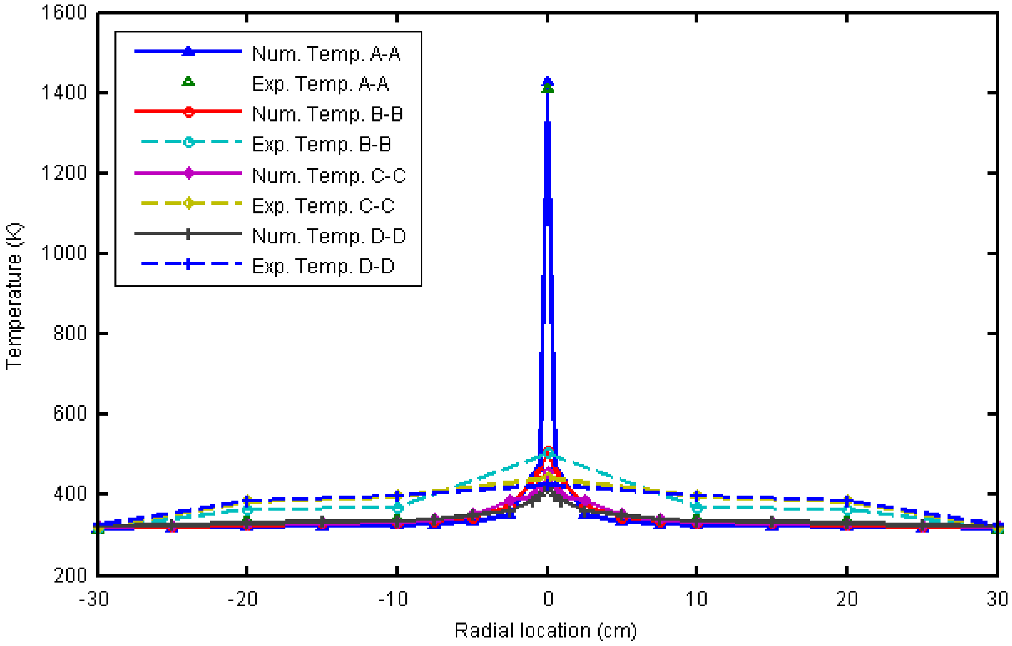

Figure 5.49: Comparison of experimental and numerical results for the partially-premixed methane at 10.82 L/min (10 kPa) with the $\lambda = 3.42$.

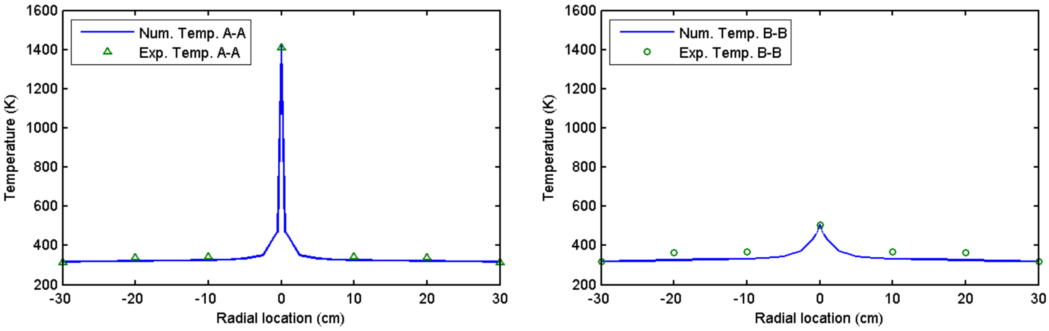

(a) $x/D_i = 5.2$ (A-A) (b) $x/D_i = 16.9$ (B-B)

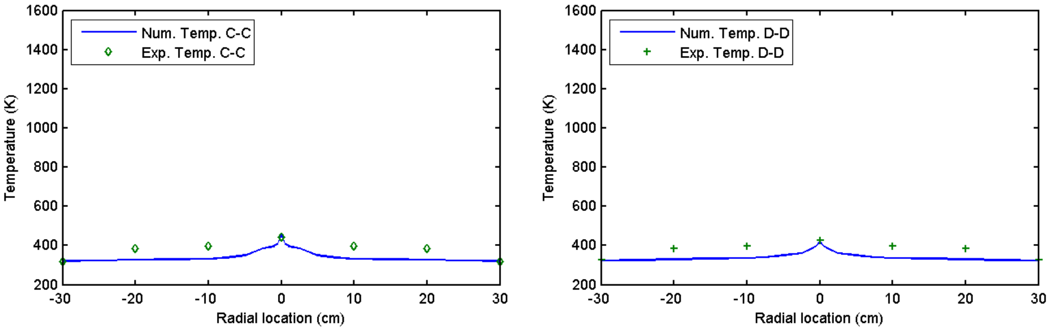

(c) $x/D_i = 28.5$ (C-C) (d) $x/D_i = 33.8$ (D-D)

Figure 5.50: Comparison of experimental and numerical results for Figure 5.49.

the flame centreline, the numerical results under-predict by 5 % to 18 % from upstream to downstream of the flame. This is due to the deficiencies of the radiation model in the numerical modelling, thereby under-predicting the temperature of the flow field. In the experimental work, the lower-temperature regions are warmed due to the radiation process from the heat of the flame. Charest et al. (2010) in the numerical modelling for laminar flame found that the local temperature is under-predicted by about 9.5 % to 19 %. Similar agreement between experimental and numerical results were also reported by Smooke et al. (1999). To improve the prediction, Smooke et al. (1999) increased the inlet temperatures and methane was consumed at a slower rate and reached further downstream in the calculations. This under-predicted behaviour for the methane concentrations may also be a result of uncertainties at the fuel inlet boundary. The accuracy of the wall temperature comparison is $< 1.0\,\%$ where it under-predicted at x/D_i of 5.2 (A-A), 16.9 (B-B), 28.5 (C-C) and over-predicted at x/D_i of 33.8 (D-D) (Figure 5.50).

Figure 5.51 shows the comparison between an experimental and a numerical analysis for the partially-premixed methane. The experimental and the numerical analysis were both run for $3.31 < \lambda < 3.81$. The experiments were run with the primary and secondary air supply and λ was measured at the exhaust outlet. The primary air supply induced at the fuel jet nozzle upstream of the fuel supply and the volume flow rate cannot be controlled. For the secondary air, however, the supply can be controlled and adjusted to the small variants of λ from 3.31 to 3.81. The flame temperature is increased in-line with the increase of the λ due to the location the x/D_i of 5.2 (A-A) and the height of the flame where the thermocouple was installed. The highest gap of over-prediction for the temperature between the numerical and experimental results is 41 K (2.9 %) at $\lambda = 3.31$. The over-prediction reduces when the λ is increased.

The combustion products are presented in Figure 5.52. Figure 5.52(a) and (b) shows oxygen and carbon dioxide at the exhaust and the EGR for the combustion of methane. The oxygen is in good agreement both downstream of the EGR pipes and at the exhaust pipe. For the carbon dioxide that was measured at the downstream of the EGR pipe, the numerical result is under-predicted at lower λ compared to the experiment. At this point, the difference is about 19 % but moves toward good agreement with the experiment when λ increased. To summarise, for the oxygen and carbon dioxide, the oxygen is over-predicted by 0.02 % to 0.17 % and the carbon dioxide by 0.5 % to 19 %. The measurement equipment could have contributed to these discrepancies (Arghode, 2011; Hosseini and Wahid, 2014). From Figure 5.51, when λ is 3.31, the temperature is over-predicted by 2.1 % (numerical prediction is 1,405 K and experiment is 1,375 K).

The water vapour for methane combustion only plotted for the numerical modelling at $\lambda = 3.81$ is about 4.45 % and 1.74 % for the exhaust pipe and EGR pipe respectively (Figure 5.52(c)). The water vapour at the downstream of the EGR pipe is diluted by incoming fresh supply secondary air and it reduced from 4.45 % at the upstream of the EGR pipe to 1.74 % at the downstream of the EGR pipe. At the downstream of the EGR pipe, the combustion produced the same amount of water vapour at the lower λ due to the limit of water vapour from the hydrogen atom in the methane fuel. However for the exhaust pipe, at the lower λ, the water vapour is slightly increased to 5.33 % due to the lower diluent from the lower supply of secondary air.

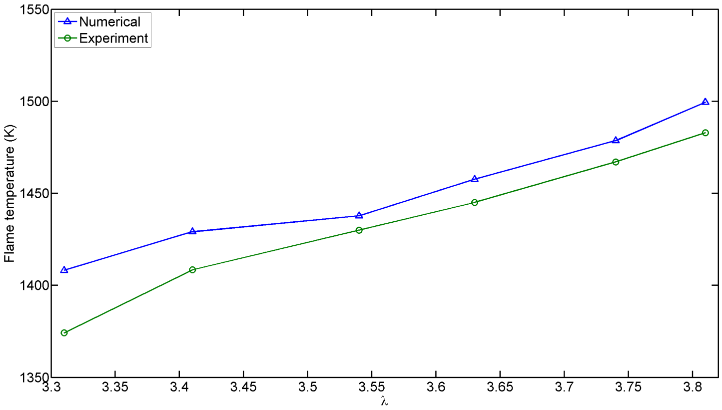

Figure 5.51: Comparison of experimental and numerical results for the partially-premixed methane flame temperature at x/D_i of 5.2 (A-A).

.

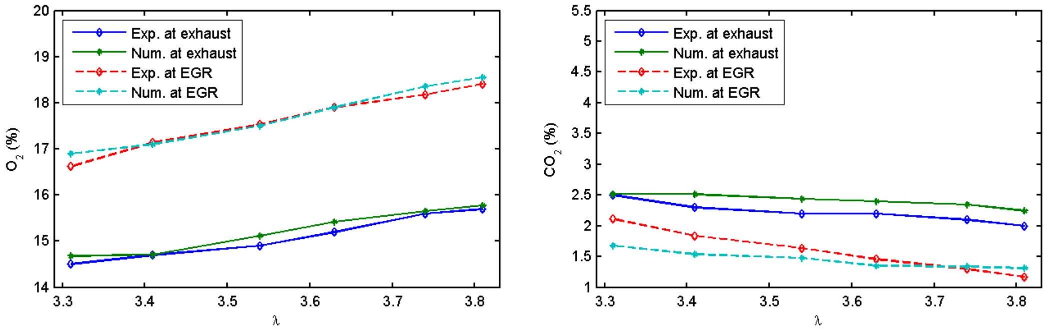

(a) O_2 (b) CO_2

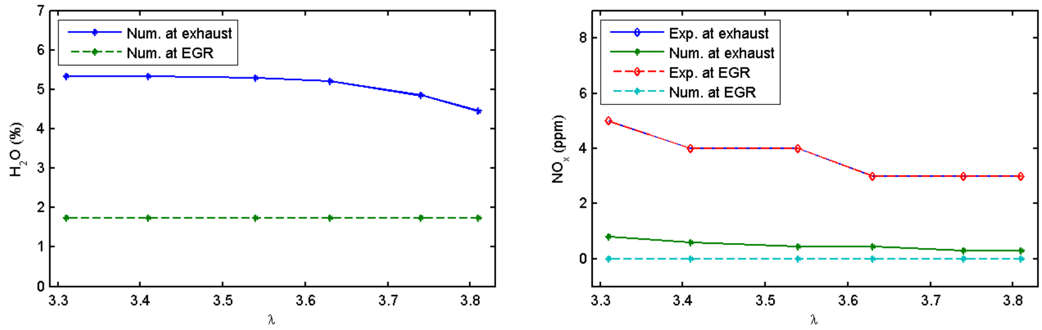

(c) H_2O (d) NO_x

Figure 5.52: Various species at the exhaust and the EGR for the combustion of methane.

Figure 5.52(c) and (d) shows the water vapour and NO_x at the exhaust pipe and the downstream of the EGR pipes for the combustion of the partially-premixed methane. The experimental NO_x for both locations is essentially identical. The experimental NO_x is under-predicted at the exhaust pipe; the numerical study predicted 1 ppm but the experiment detected NO_x at 3 ppm to 5 ppm depending on the λ. The NO_x is 5 ppm at lower λ and reduced to 3 ppm at higher λ. The NO_x results are in line with the earlier experimental work with 20 kW heat input using natural gas; the NO_x is about 3 ppm (Colorado et al., 2010). These measurement errors between the experimental and numerical modelling are within the acceptable limits where for the NO_x measurement the gas analyser has the accuracy of ±3.0 % (Table 4.9) for the detection ranges of 0–4,000 ppm. In the gas fire furnace and consumer cars and light trucks (European regulation), the level of NO_x must be below 5 ppm.

The numerical modelling results for 10.82 L/min (10 kPa) of partially-premixed methane with λ of 3.42 is shown in Figures 5.53 to 5.56. Figure 5.53 shows the temperature for the full range and the restricted range of 300 K to 550 K for the combustion chamber including EGR, secondary air supply and fuel supply pipe. The flame temperature is 1,432 K and the wall temperature is 321 K. Figure 5.54 shows the various species mole fractions, where Figure 5.54(a) shows unburned hydrocarbon that is excess from the combustion. The contour shows that almost

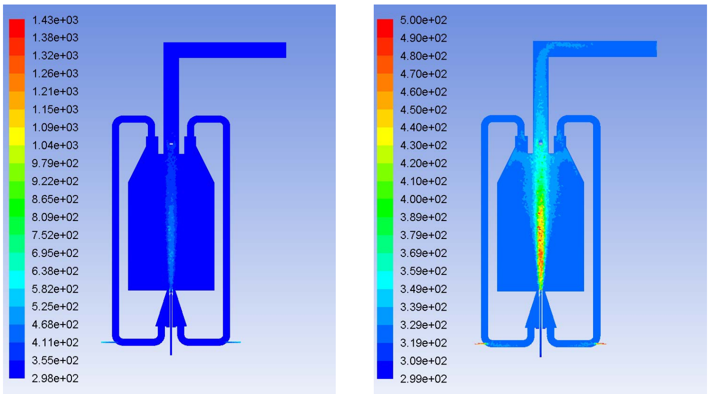

(a) Full range (b) 300 to 550 K

Figure 5.53: Temperature contour for combustion of 10.82 L/min (10 kPa) methane at $\lambda = 3.42$ with oxygen 21 % in oxidant supply.

zero unburned hydrocarbon is released from the combustion. It shows that all the methane is consumed and left no trace of unburned hydrocarbon released through the exhaust or circulated through the EGR stream. Figure 5.54(b) shows the oxygen mole fraction for the whole combustion chamber. The oxygen mole fraction for the secondary air supply is 21 % and the mole fraction is reduced to 15.5 % when it is diluted by the EGR. This is because the oxygen mole fraction in the EGR is 9.5 %, which is lower than the oxygen mole fraction in the secondary air supply. The oxygen mole fraction at the combustion (flame) zone is almost zero due to it being consumed by the combustion process in the chemical reaction with the methane.

Figure 5.54(c) shows the contour of the water vapour for the combustion chamber. The water vapour mole fraction of 16.3 % is very high at the combustion (flame) zone due to the intense chemical reaction that continuously produces the water vapour. It is diluted and reduced to about 8.16 % at the other areas in the combustion chamber including the upstream and middle-stream of the EGR pipes. At the downstream of the EGR pipes and mixing cone, the water vapour is diluted by the fresh secondary air supply and further reduced to 3.63 %. Figure 5.54(d) shows the contour of the NO_x for the combustion chamber. The contour shows that the NO_x is high (27 ppm) at the flame area due to the chemical reaction still being incomplete. When the chemical reaction is completed, the NO_x is detected as 1.0 ppm at the exhaust and the EGR pipes.

Figure 5.54(e) shows the contour of the carbon dioxide, which has the same behaviour as the water vapour. The carbon dioxide shows the same trend with the NO_x where it is high (8.5 %) at the flame area and detected at a lower amount (4.5 %) for other areas including the combustion chamber and EGR pipes. This is because the carbon dioxide is distributed throughout the combustion chamber and reduces the concentration. Figure 5.54(f) shows the contour of the carbon monoxide, which is only detected at the flame area. This carbon monoxide was

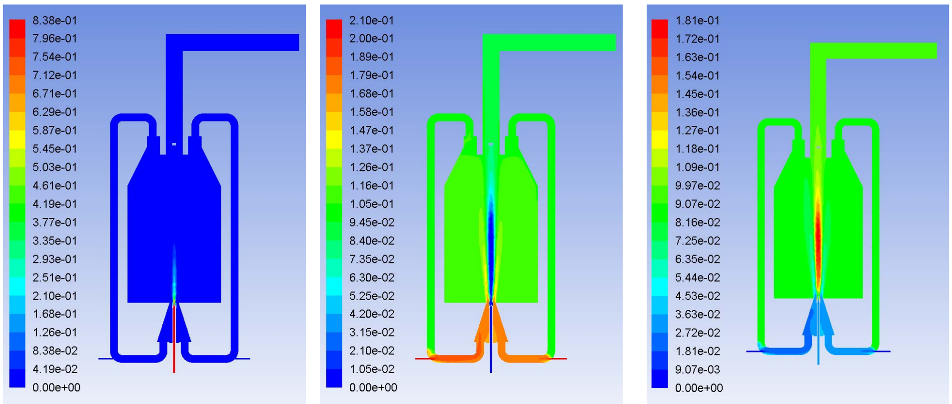

(a) CH_4 (b) O_2 (c) H_2O

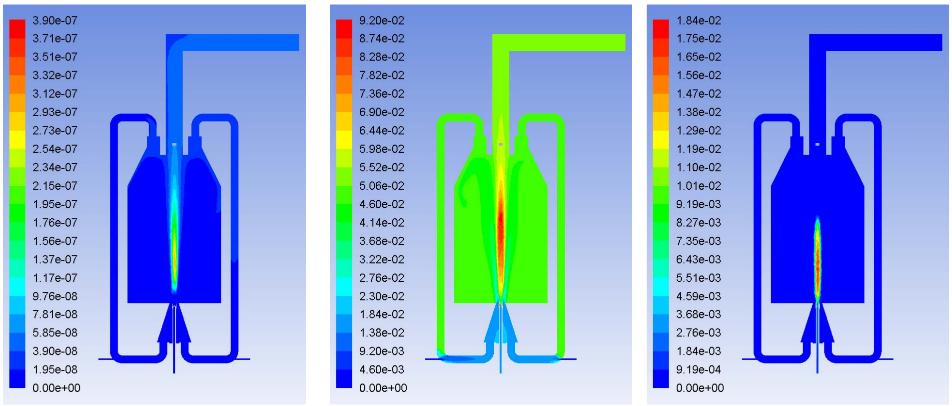

(d) NO_x (e) CO_2 (f) CO

Figure 5.54: Species mole fraction for combustion of 10.82 L/min (10 kPa) methane at $\lambda = 3.42$ with oxygen 21 % in oxidant supply.

detected during the continuous chemical reactions (combustion process), but the reactions were quickly completed to produce carbon dioxide as a combustion by-product.

A sample of combustion products was selected to study the profile along the centreline of the flame zone. Figure 5.55 shows the carbon monoxide profile for the methane flame centreline of the combustion chamber, including the flame front. The highest carbon monoxide is at the downstream distance from injection locations, x/D_b=23.3 and reaches almost zero (below detection limits with the apparatus used) at x/D_b=80.0. In the previous experiment using natural gas (97 % methane), carbon monoxide reached its minimum level at the downstream distance from the injection locations, x/D_b=375.0 (Colorado et al., 2010). Figure 5.56 shows the chamber density, the velocity magnitude and the pressure distributions. Beside the flame and the locations where the chemical reaction occurred, the chamber density is about 1.00–1.16 kg/m^3. The density is low in the vicinity of the chemical reaction and the high velocity zone. The pressure distribution is uniformly distributed with a low level of pressure throughout the combustion chamber. The pressure is slightly high at the air and fuel supply in-

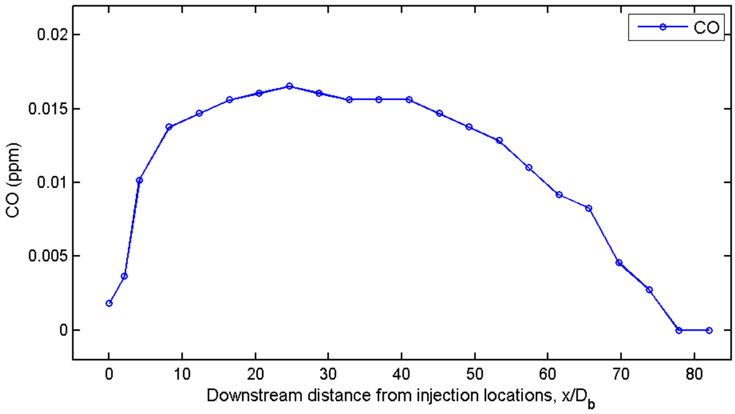

Figure 5.55: CO profile along the centreline of the combustion chamber for 10.82 L/min (10 kPa) methane with $\lambda = 3.42$. The nozzle diameter, D_b=7.5 mm.

lets, as can be seen in Figure 5.56(c). The open end at the top of the combustion chamber means the pressure is always at atmospheric pressure. More results from the numerical modelling for the methane flames can be found in Appendix D.

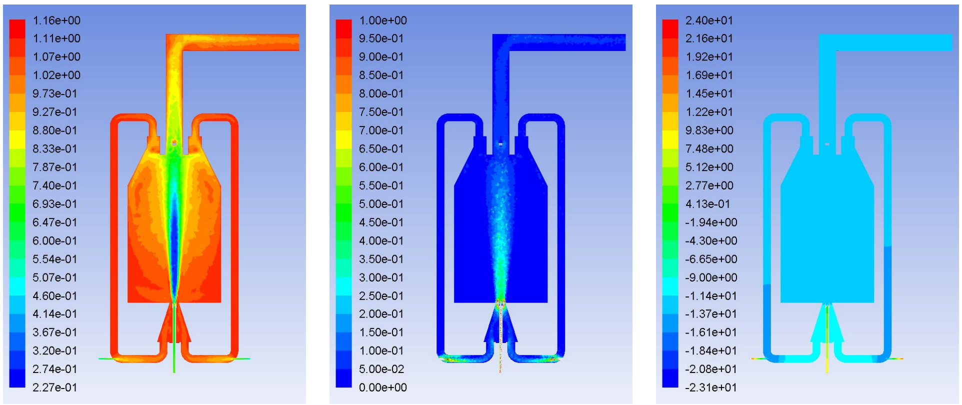

(a) Density (b) Velocity magnitude (c) Pressure

Figure 5.56: Chamber density, velocity magnitude and gauge pressure distribution for combustion of biogas at $\lambda = 3.42$ with oxygen 21 % in oxidant supply.

5.11.2 Numerical Sensitivity Test

Simulations were conducted for the methane fuel to study the sensitivity of the secondary air supply temperature to the flame temperature and combustion products. The secondary air temperature was set at the range of 320 K to 667 K to analyse the behaviour at the exhaust pipe and the downstream of the EGR pipes. One of the MILD strategies is the preheating of the supplied combustion air to assist in achieving MILD combustion by producing a lower temperature field in the chamber compared to conventional combustion (Medwell, 2007). The preheating of the secondary air provides a relatively small power addition compared to the power that is gained from the methane fuel combustion (Appendix A). The total energy input for the furnace is 6.21 kW with 6.03 kW from the combustion

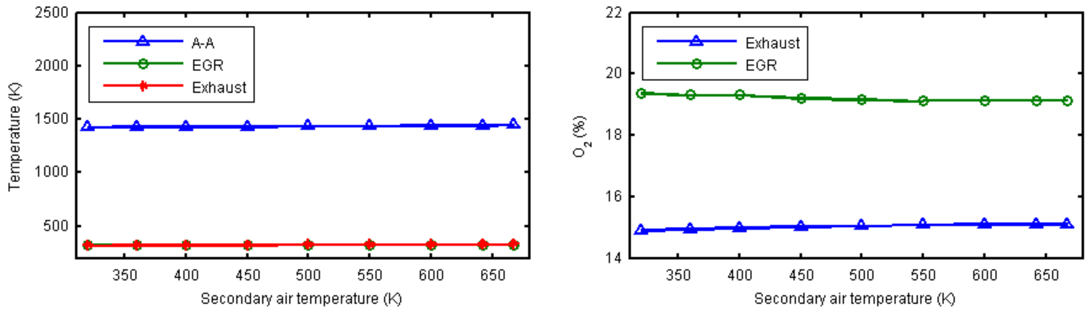

(a) Temperature (b) O_2

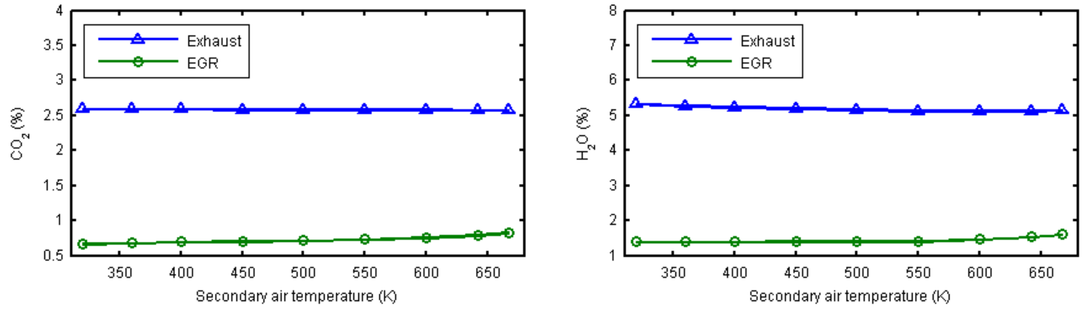

(c) CO_2 (d) H_2O

Figure 5.57: Comparison of temperature and combustion products at exhaust and downstream of EGR of 10.82 L/min (10 kPa) methane at $\lambda = 3.42$ with oxygen 21 % in oxidant supply.

of methane fuel and 0.18 kW from the air heating element. Because the density of the heated air changes, the inlet conditions were carefully chosen to ensure that a constant mass flow rate is applied to ensure that the same stoichiometry is simulated in all cases. At the temperature of 320.15 K and pressure of 101.325 kPa, the air density is 1.1060 kg/m^3 and the calculated mass flow rate is 1.6071×10^{-3} kg/s.

Figure 5.57 shows the comparison of the combustion temperatures and products for the heating of the secondary air at the range of 320 K to 667 K. Figure 5.57(a) shows the flame temperature slightly increased when the preheating temperature was increased. The chamber temperature is 1,429.4 K and 1,448.6 K at preheated secondary air of 320 K and 667 K respectively. The temperature for the exhaust gas was not affected by the preheating temperature, it was consistently recorded at 324.5 K for all the cases. At this location, the chemical reaction is fully completed and the exhaust gas has experienced the cooling process. For the downstream of the EGR pipes, the temperature is 318.8 K and 331.8 K at preheated secondary air of 320 K and 667 K respectively. These conditions show a small effect of preheating secondary air: the temperature is increased by 4.1 % by the 108 % increase in secondary air supply temperature. The result is similar to the test for the effect of the heating element on the secondary air temperature where the heating element temperature provides a small effect on the secondary air temperature, as summarised on Table 5.1.

Table 5.8: Effect of wall temperature boundary conditions and oxygen mole fractions on flame temperature.

Wall temperature (K)	**Oxygen mole fraction**		
	3 %	**9 %**	**21 %**
320	536.1 K	956.7 K	1,424.6 K
500	628.5 K	1,086.0 K	1,561.0 K
750	720.1 K	1,206.6 K	1,720.9 K

Figure 5.57(b) shows the excess oxygen in the exhaust gas is slightly increased from 14.92 % to 15.12 % when the preheated temperature of secondary air increased. The small increases in the chamber temperature show that the combustion consumed slightly less oxygen when the secondary air was supplied with a higher preheated temperature. For the excess oxygen at the downstream of the EGR pipes, the oxygen mole fraction is higher than the exhaust pipe after being mixed with the 21 % oxygen mole fraction from the secondary (atmospheric) air. The secondary air oxygen mole fraction was diluted by the EGR to 19.24 %. The results for the carbon dioxide (Figure 5.57(c)) are similar to the water vapour (Figure 5.57(d)), where both reduced slightly the exhaust pipe and slightly increased at the downstream of the EGR pipes when the chamber temperature was slightly increased.

The effect of the wall temperature boundary conditions was studied using numerical modelling and summarised in Table 5.8. The methane fuel supply was fixed at 10.82 L/min (10 kPa) with $\lambda = 2.0$ used with secondary air. The variable parameters are the wall temperature of 320 K, 500 K and 750 K and supply oxygen mole fraction of 3 %, 9 % and 21 %. The wall temperature affects the flame temperature. For the case of 3 % oxygen mole fraction, when the wall temperature boundary condition increased by 56.3 % (320 K increased to 500 K), the flame temperature was increased by 17.2 %. For the case of 21 % oxygen mole fraction, when the wall temperature boundary condition increased by 56.3 %, the flame temperature is increased by 9.6 %. The effect of the wall temperature boundary condition slightly decreased when higher temperature wall boundary conditions were used. For the case of 3 % oxygen mole fraction, when the wall temperature boundary condition increased 50.0 % (500 K increased to 750 K), the flame temperature was increased 14.6 % (628.5 K increased to 720.1 K). From this numerical sensitivity study, it can be seen that the flame temperature is very sensitive to the boundary conditions (the combustion chamber wall).

5.11.3 Biogas Flame

The biogas flame comparison of the experimental and numerical work is conducted at the same conditions as the methane flame (Figure 5.58). The figures for each chamber's cross-section of x/D_i of 5.2 (A-A), 16.9 (B-B), 28.5 (C-C) and 33.8

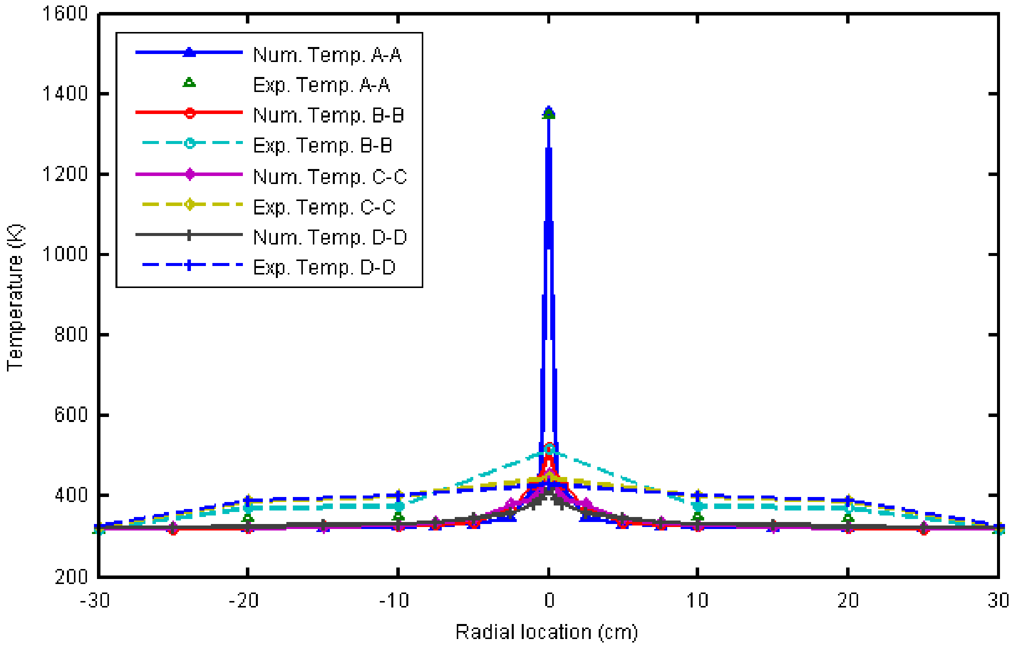

Figure 5.58: Comparison of experimental and numerical results for biogas at 10.82 L/min (10 kPa) with the $\lambda = 3.87$.

(D-D) are individually separated and can be seen in Figure 5.59. The difference in flame temperature between the experiment and simulation results are 13 K, which is 1 %. Further downstream of the flame, the difference between centreline experimental and numerical results at the locations of x/D_i of 5.2 (A-A), 16.9 (B-B), 28.5 (C-C) and 33.8 (D-D) are 1.03 %, 1.95 % and 2.16 % respectively. This error is $< 5\,\%$ as in the comparison of the experiments and simulations by Hosseini and Wahid (2014) and still achieves acceptable accuracy of within 3 % (Burke et al., 2009).

The downstream of the wall temperature prediction using the numerical modelling compared to the experimental is in good agreement: $< \pm 1\,\%$ (Figure 5.59). At 100 mm and 200 mm away from the wall and the centre of the flame, the temperature is under-predicted by about 7 % to 19 %. The treatment of thermal radiation is used to predict the temperature and species concentrations (Vishkanta and Menguc, 1987) using the discrete ordinates model (Carlson and Lathrop, 1968; Fiveland, 1984) to evaluate the radiation flux term. The radiation model used under-predicts the temperature of the flow field. This prediction error is similar to the previous simulation work which under-predicted the flame temperature by 9.5 % to 19.0 % (Charest et al., 2010; Smooke et al., 1999).

The experimental work for the biogas partially-premixed flame is conducted with primary and secondary air supplies. The λ recorded is varied by changing the secondary air supply flow rates. The numerical modelling results are validated with the experimental analysis at the same conditions to ensure the numerical

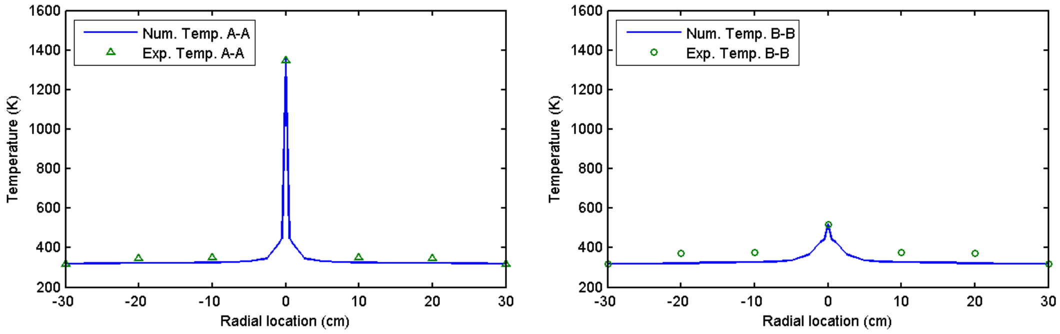

(a) x/D_i of 5.2 (A-A) (b) x/D_i of 16.9 (B-B)

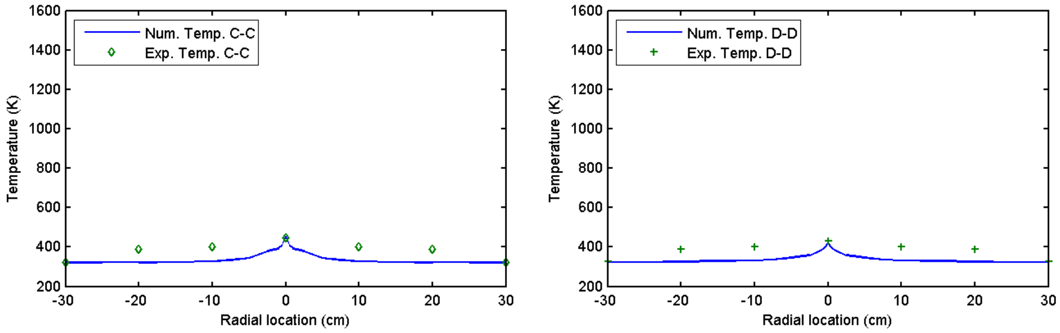

(c) x/D_i of 28.5 (C-C) (d) x/D_i of 33.8 (D-D)

Figure 5.59: Comparison of experimental and numerical results for Figure 5.58.

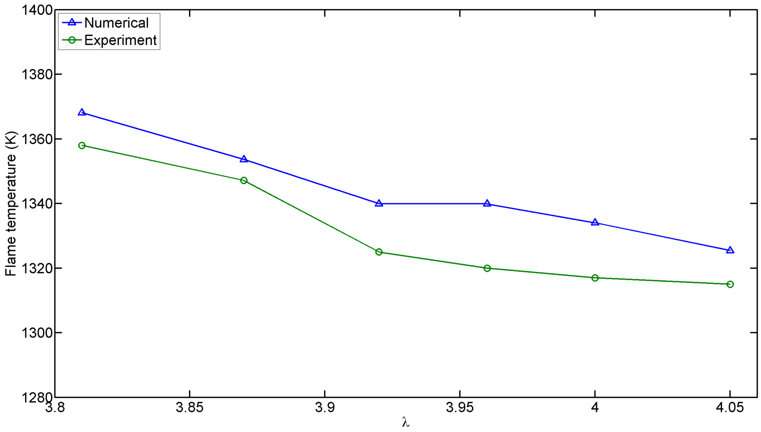

Figure 5.60: Comparison of the numerical and the experimental partially-premixed biogas flame temperature at x/D_i of 5.2 (A-A).

modelling results are reasonably accurate and acceptable. Figure 5.60 shows the comparison of the partially-premixed biogas for the λ of 3.81 to 4.05. The biogas flame temperature is reduced when the λ is reduced because of the excess air supplied being a diluent. The comparison between experimental and numerical results shows the numerical modelling over-predicts by about 1 % to 2 %. This prediction error is below 3.0 % and reasonably accurate.

The comparison of the varies species from the exhaust gas are presented in Figure 5.61. For the unburned hydrocarbon, the result for the biogas flame is identical to the case of the methane flame. For both methane and biogas fuels, this is because when lean combustion is used, all the methane is consumed leaving almost zero (below detection limits with the apparatus used) unburned hydrocarbon behind. For the excess oxygen, both exhaust pipe and downstream of the EGR pipes show similar results for the biogas and methane flames. The excess oxygen for both fuels was compared at the λ of 3.81. For the exhaust pipe, the excess oxygen for methane and biogas is 16.02 % and 15.70 % respectively, while for the downstream of the EGR pipes, it is 18.70 % and 18.41 % respectively. At both locations, the biogas flame leaves higher excess oxygen compared to methane due to higher λ for biogas combustion giving higher supply of oxygen mole fraction and higher oxygen consumed when the combustion of methane will reduce the oxygen mole fraction for methane flame. For the oxygen mole fraction, the error between the experimental and numerical results is about 2.5 % for both the exhaust pipe and the downstream of the EGR pipes. The oxygen mole fraction at the downstream of the EGR pipes is higher than at the exhaust pipe. This behaviour occurred because the fresh oxygen mole fraction supply from the secondary air supply diluted the exhaust gas and, as a result, increased the oxygen mole fraction at the downstream of the EGR pipes. However, for the carbon dioxide, the error between the experimental and numerical results is higher (about 12 %) for the EGR pipe at the λ of 3.81. The difference is reduced to 0.5 % when the λ is increased to 4.05. For the exhaust pipe, the numerical modelling is under-predicted by about 2.0 % to 5.0 %. The biogas measurement error for the oxygen and carbon dioxide shows a similar trend with methane. The measurement equipment could contribute to these discrepancies (Arghode, 2011; Hosseini and Wahid, 2014).

The NO_x and water vapour at the exhaust pipe and the downstream of the EGR pipes for the combustion of partially premixed biogas are shown in Figure 5.61(c) and (d). For the case of water vapour, it is a similar condition to the methane combustion. Only the numerical result is reported here. The trend for the water vapour is identical to the methane combustion where at λ of 3.81, the water vapour is about 3.45 % and 0.86 % for the exhaust pipe and EGR pipe respectively. The water vapour at the downstream of the EGR pipe is diluted by the incoming fresh supply secondary air. The water vapour for the biogas is lower than the methane combustion because of its lower calorific value. Similar to the case of methane fuel, the experimental NO_x for the exhaust pipe and the downstream of the EGR pipes are essentially identical. The NO_x is under-predicted at both locations: the numerical modelling predicted almost zero ppm of NO_x but the experimental results show that the NO_x is 4 ppm at the lower λ and it reduced to 2 ppm at the higher λ. These measurement difference are within acceptable limits where the exhaust gas analyser has the accuracy of ±3.0 % (Table 4.9) for the NO_x detection ranges of 0–4,000 ppm. The biogas produced lower NO_x compared

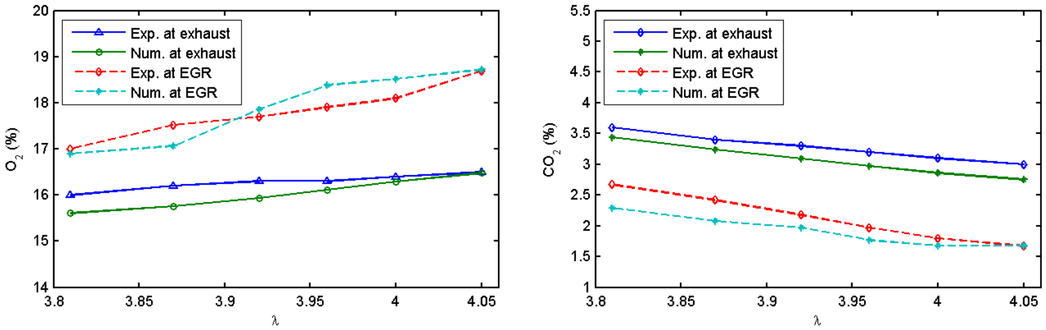

(a) O_2 (b) CO_2

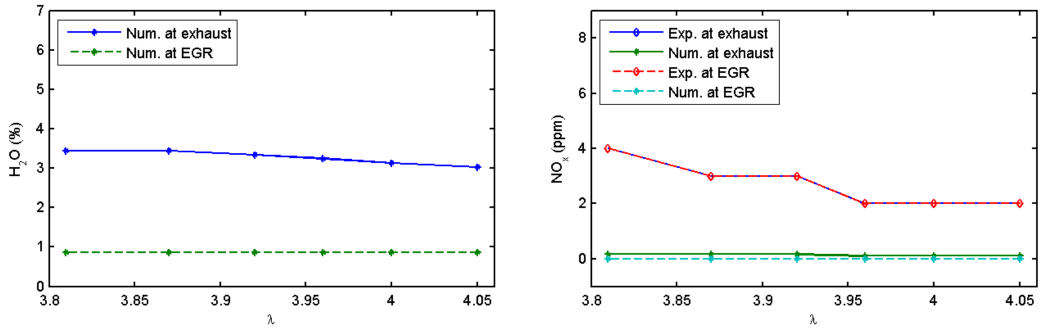

(c) H_2O (d) NO_x

Figure 5.61: Various species at the exhaust and the EGR for the combustion of biogas.

to the methane flames. These results are in line with the experimental results by Colorado et al. (2010) using biogas and natural gas. In their experiments, biogas produced 2 ppm of NO_x whereas for the natural gas, it produced 3 ppm of NO_x. Similar results for the experiment of biogas produced about 2 ppm of NO_x (Hosseini and Wahid, 2013).

The numerical modelling results for 10.82 L/min (10 kPa) of a partially-premixed biogas with the λ of 3.87 is shown in Figures 5.62 to 5.65. Figure 5.62 shows the temperature for a full range and a restricted range of 300 K to 550 K for the combustion chamber including the EGR, secondary air supply and fuel supply pipe. The flame temperature is 1,361 K and the wall temperature is about 319 K. The flame temperature is slightly over-predicted (0.96 %) compared to experimental result (1,348 K). This shows good agreement between the experimental and numerical modelling as the prediction error is $< 1\,\%$. The biogas flame temperature is lower than the methane flame temperature (1,432 K) by 5.0 % and the wall temperature is lower than the methane wall temperature (321 K) by 0.62 %. Figure 5.63 shows various species mole fractions for the combustion chamber where almost zero unburned hydrocarbon is released through the exhaust pipe or recirculated through the EGR stream (Figure 5.63(a)). Figure 5.63(b) shows the excess oxygen mole fraction for the combustion chamber. The secondary air supply consists of 21 % oxygen mole fraction and it diluted to 15.8 % after being

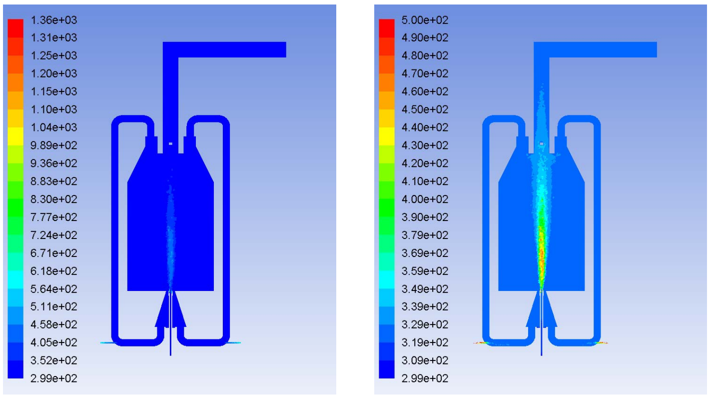

(a) Full range (b) 300 to 550 K

Figure 5.62: Temperature contour for combustion of 10.82 L/min (10 kPa) biogas at $\lambda = 3.87$ with oxygen 3 % in oxidant supply.

mixed with the EGR. The oxygen mole fraction at the combustion zone is almost zero due to it being where the fuel stream enters the combustion chamber, so that region is very rich (and it consumes any oxygen that is there).

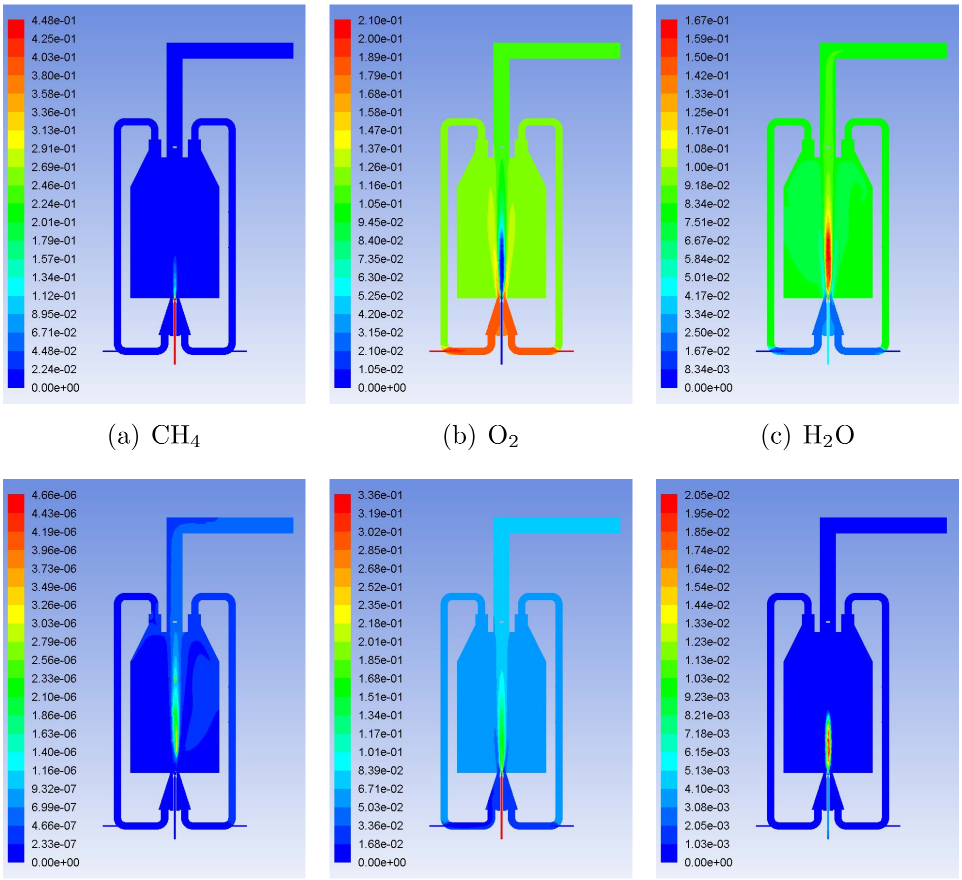

(a) CH_4 (b) O_2 (c) H_2O

(d) NO_x (e) CO_2 (f) CO

Figure 5.63: Combustion products for combustion of 10.82 L/min (10 kPa) biogas at $\lambda = 3.87$ with oxygen 3 % in oxidant supply.

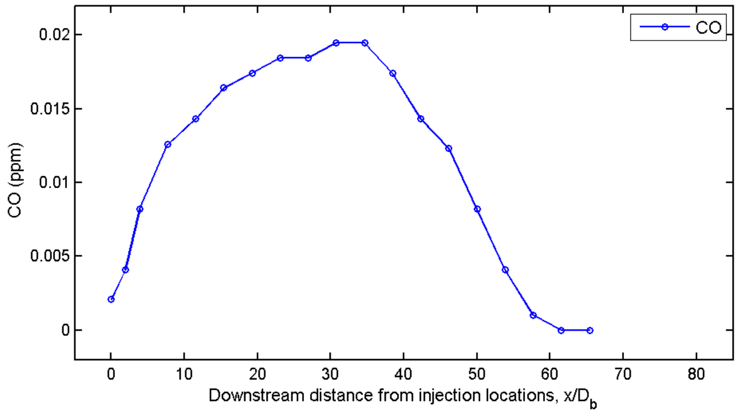

Figure 5.64: CO profile along the centreline of the combustion chamber for 10.82 L/min (10 kPa) biogas with $\lambda = 3.87$. The nozzle diameter, D_b=7.5 mm.

Figure 5.63(c) shows the distribution of the water vapour for the combustion chamber. The water vapour is 7.5 % throughout the whole combustion chamber and EGR pipes except for the combustion (flame) zone, where it is 16.7 %. Similar to the methane flame, the water vapour is high at the flame area due to the intense chemical reaction that produces the water vapour. It is then distributed to other areas in the combustion chamber. Figure 5.63(d) shows the contour of the NO_x for the combustion chamber. The contour shows that the NO_x is high (29 ppm) at the flame area due to the chemical reaction still being incomplete. When the chemical reaction is completed, the NO_x is detected as 2.0 ppm at the exhaust and the EGR pipes. Figure 5.63(e) shows the contour of the carbon dioxide, which has the same behaviour as the water vapour because it is produced in the same mode. The carbon dioxide shows the same trend as the NO_x where it is high (14.2 %) at the flame area and lower (5.8 %) for other areas including the combustion chamber and EGR pipes. This is due to the carbon dioxide being dissociated throughout the combustion chamber and reducing the concentration. Figure 5.63(f) shows the contour of the carbon monoxide which is only detected at the flame area. This carbon monoxide was detected during the continuous chemical reactions (combustion process), but the reactions are quickly completed to produce carbon dioxide as a combustion by-product.

Similar to methane, the biogas combustion product of carbon monoxide was studied at the profile along the centreline of the flame zone. Figure 5.64 shows the carbon monoxide profile for the biogas flame centreline of the combustion chamber at the flame front. The highest carbon monoxide is at the downstream distance from the injection locations, x/D_b= 30.0 and reaches almost zero at x/D_b= 63.3. In the experiment using biogas (50 % methane), carbon monoxide reached its minimum at the downstream distance from the injection locations, x/D_b=375.0 (Colorado et al., 2010).

Figure 5.65 shows the chamber density, the velocity magnitude of the flow field and the pressure distributions. Apart from the flame area where the chemical

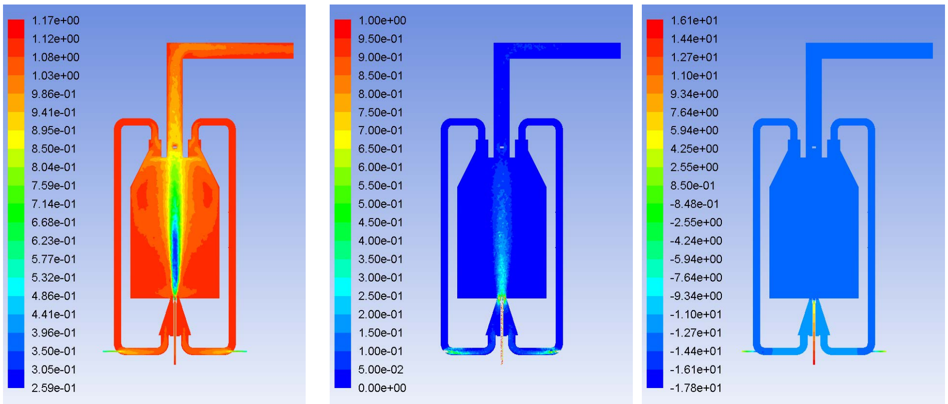

(a) Density (b) Velocity magnitude (c) Pressure

Figure 5.65: Chamber density, velocity magnitude and gauge pressure distribution for the combustion of biogas at $\lambda = 3.87$ with oxygen 21 % in oxidant supply.

reaction occurred, the chamber density is about 1.01–1.16 kg/m^3. The density is low in the vicinity of the chemical reaction and the high velocity zone in the combustion chamber. The trend is equivalent to the case of the methane flame: the maximum velocity of 13.80 m/s occurred at the air/fuel nozzle burner due to the small nozzle size for both air and fuel. The other higher velocity area is after the secondary air inlet at each side of the EGR pipes and within the primary jet stream through the combustion chamber. Other than these zones, the velocity is very low throughout the combustion chamber. The pressure distribution is uniformly distributed with a low level of pressure throughout the combustion chamber. The pressure is slightly high at the air and fuel supply inlets, as can be seen in Figure 5.56(c). The open end at the top of the combustion chamber causes the pressure to always be at atmospheric pressure.

5.12 Numerical Modelling of MILD Combustion

The numerical modelling for the same geometry as an experiment is carried out. These studies used a lower oxygen mole fraction in the oxidant supply to the chamber. The conditions were set to achieve a MILD combustion regime. The wall boundary condition is kept at 500 K to help the chemical reaction in the flow field and the region near the wall.

5.12.1 Methane Flame

The temperature contour for the numerical modelling of the methane is shown in Figure 5.66. The maximum temperature in the combustion chamber is 715 K and the chamber average temperature is about 500 K. The intervals of the contour lines for the temperature profile in Figure 5.66(a) and (b) are 22 K and 13 K respectively. That shows the chamber temperature distribution is uniformly dis-

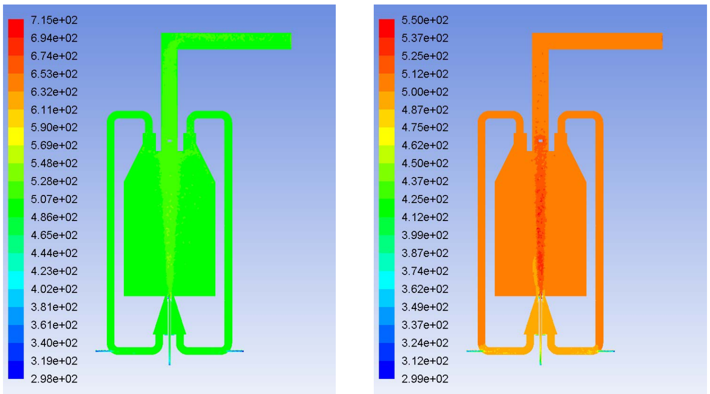

(a) Full range (b) From 300 to 550 K

Figure 5.66: Temperature contour for combustion of 10.82 L/min (10 kPa) methane at $\lambda = 1.0$ with oxygen 3 % in oxidant supply.

tributed with the homogeneous temperature profile. This homogeneous condition meets one of the important requirement of MILD conditions where the temperature uniformity ratio is less than 20 % (Tsuji et al., 2003). The temperature uniformity ratio is the highest to average temperature divided by the average temperature.

Figure 5.67 shows important species for the numerical modelling of methane with the oxygen mole fraction of 3 % and the λ was set at 1.0. Figure 5.67(a) shows almost zero unburned hydrocarbon is released from the combustion because all methane is consumed by the combustion. Figure 5.67(b) shows the oxygen mole fraction for the combustion chambers. The oxygen mole fraction for the secondary air supply was 3.0 % and the mole fraction was reduced to 2.2 % when it was diluted by the EGR at the downstream of the EGR pipes. This is due to the oxygen mole fraction in the EGR pipes at the upstream and middle-stream of the EGR pipes being 0.75 %, which is much lower than the oxygen mole fraction in the secondary air supply. The oxygen mole fraction at the combustion (flame) zone is almost zero due to it being consumed by the combustion process in the chemical reaction with the methane. Figure 5.67(c) shows the contour of water vapour for the combustion chamber. The water vapour at the flame area was 1.92 % and increased to 2.96 % far downstream of the flame due to the chemical reaction being fully completed at the downstream of the flame. The water vapour at the EGR pipes was 2.22 % and diluted to 0.59 % after it mixed with the secondary air supply.

Figure 5.67(d) shows the contour of the NO_x for the combustion chamber. The contour shows that the NO_x is almost zero ppm within numerical precision for the whole combustion chamber and the EGR pipes, including the flame and chemical reaction area. Figure 5.67(e) shows the contour of the carbon dioxide, which has the same behaviour as the water vapour because it is produced in the same mode. The carbon dioxide was detected at its highest (1.78 %) at the flame area and

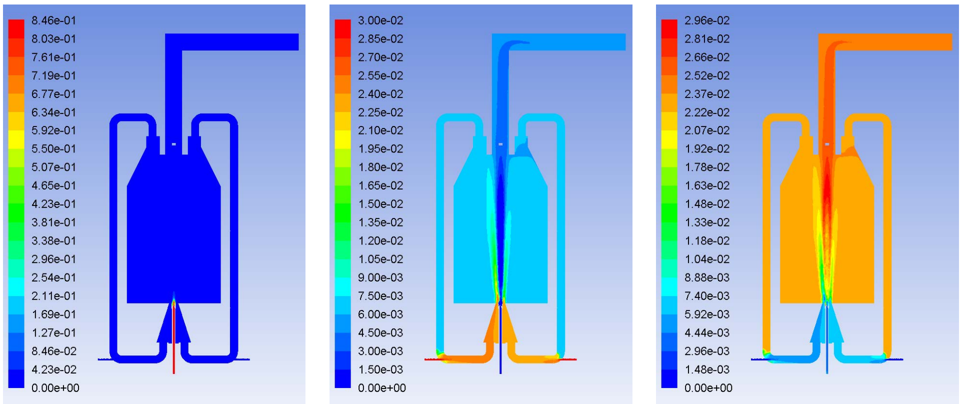

(a) CH_4 (b) O_2 (c) H_2O

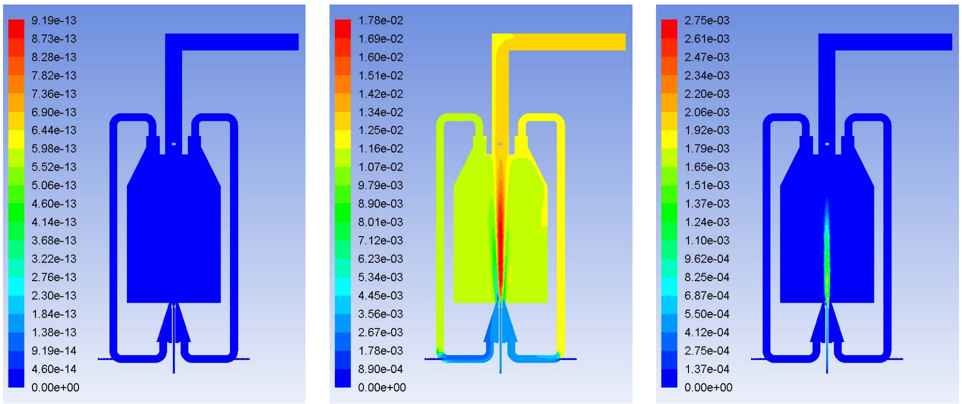

(d) NO_x (e) CO_2 (f) CO

Figure 5.67: Combustion products for combustion of 10.82 L/min (10 kPa) methane at $\lambda = 1.0$ with oxygen 3 % in oxidant supply.

detected at a reduced level (1.07 %) at the other areas, including the combustion chamber and EGR pipes. This is because the carbon dioxide was distributed throughout the combustion chamber and reduced the concentrations. It was later diluted to 0.27 % at the downstream of the EGR pipes. Figure 5.67(f) shows the carbon monoxide mole fraction where only detected at the continuous chemical reactions (flame area). It later re-formed to carbon dioxide after reacting with the oxygen. The numerical modelling was repeated for the same conditions as the previous case except for the higher λ of 3.30. The temperature results (Figure 5.68) shows a similar trend to the case of $\lambda = 1.0$ (Figure 5.66). Compared to the previous case, the maximum temperature in the combustion chamber is slightly higher (731 K) and the average chamber temperature is slightly lower (487 K). This is due to the excess oxygen from the higher λ becoming the diluent and reducing the average chamber temperature. The chamber temperature distribution is uniformly distributed and becomes a homogeneous temperature profile.

Figure 5.69 shows the combustion products for the numerical modelling of methane with the oxygen mole fraction of 3 % and the λ set at 3.30. Similar to the

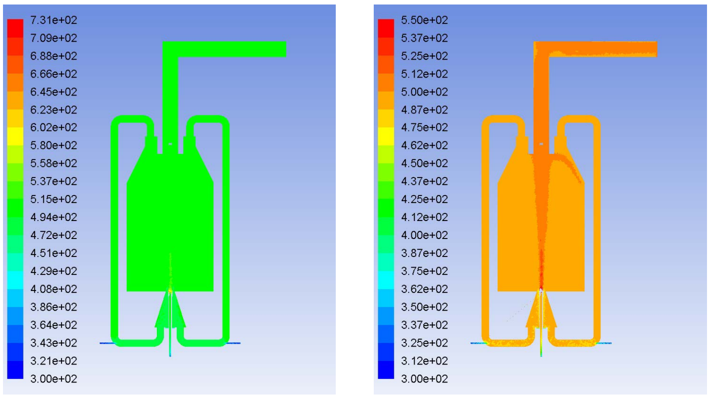

(a) Full range (b) From 300 to 550 K

Figure 5.68: Temperature contour for combustion of 10.82 L/min (10 kPa) methane at $\lambda = 3.30$ with oxygen 3 % in oxidant supply.

methane case of $\lambda = 1.0$, Figure 5.69(a) shows zero unburned hydrocarbon since the methane was consumed by the combustion. Figure 5.69(b) shows the oxygen mole fraction for the combustion chambers. The oxygen mole fraction for the secondary air supply was 3.0 % and the mole fraction was reduced to 2.85 % when it was diluted by the EGR at the downstream of the EGR pipes. This is because the oxygen mole fraction in the EGR pipes at the upstream and middle-stream of the EGR pipes are 2.25 % which is lower than the oxygen mole fraction in the secondary air supply. This is higher than the case of the $\lambda = 1.0$ because the higher λ means higher excess oxygen in the secondary air supply. Figure 5.69(c) shows the water vapour for the combustion chamber at the flame area was 2.79 % and reduced to 0.84 % far downstream of the flame. The water vapour at the EGR pipes was 0.70 % and diluted to 0.14 % after it was mixed by the supplied secondary air.

Figure 5.69(d) shows the contour of the $\mathrm{NO_x}$ for the combustion chamber. A miniscule amount (0.06 ppm) is produced in the flame due to excess oxygen, but it is quickly dissociated. Figure 5.69(e) shows the contour of the carbon dioxide, which has the same behaviour as the water vapour because it is produced in the same manner. The carbon dioxide is highest (1.74 %) at the flame area and lowest (0.35 %) at the other areas, including the combustion chamber and EGR pipes. This is because the carbon dioxide is distributed throughout the combustion chamber and reduced the concentrations. It was later measured at almost zero at the downstream of the EGR pipes. Figure 5.69(f) shows the contour of the carbon monoxide, which is almost zero throughout the combustion chamber and the EGR pipes. This condition is similar to other cases of $\lambda = 1.0$ and 3.0.

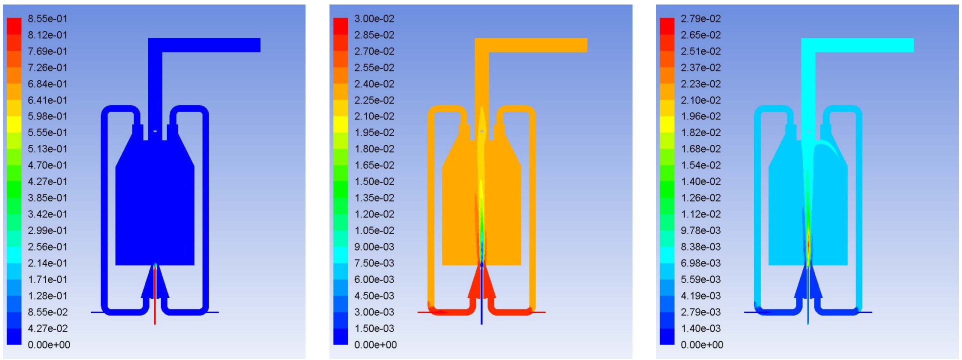

(a) CH_4 (b) O_2 (c) H_2O

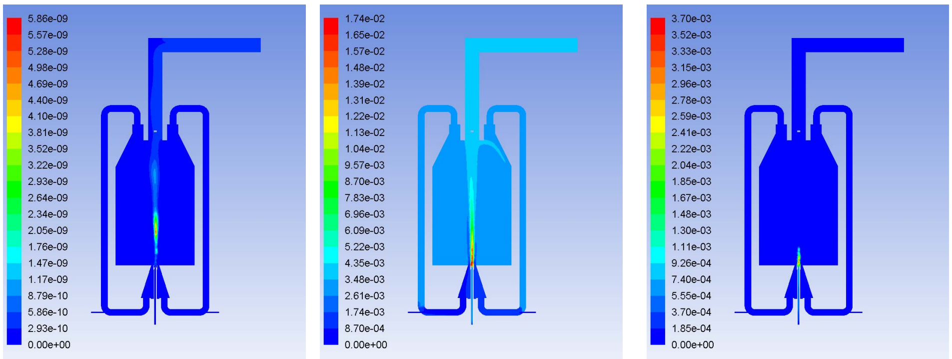

(d) NO_x (e) CO_2 (f) CO

Figure 5.69: Combustion products for combustion of 10.82 L/min (10 kPa) methane at $\lambda = 3.30$ with oxygen 3 % in oxidant supply.

5.12.2 Biogas Flame

The numerical modelling for the biogas case is shown in Figure 5.70. The oxygen mole fraction used is 3 % at the stoichiometric λ. The maximum temperature in the combustion chamber is 691 K and the chamber average temperature is about 500 K. The intervals of the contour lines for the temperature profile in Figure 5.70(a) and (b) are 20 K and 13 K respectively. That shows the chamber temperature distribution is uniformly distributed with the homogeneous temperature profile (Tsuji et al., 2003). Figure 5.71 shows the unburned hydrocarbon and combustion products for the biogas with the oxygen mole fraction of 3 % at the stoichiometric λ. Figure 5.71(a) shows almost zero unburned hydrocarbon that is excess from the combustion. Similarly to the previous cases, the methane is consumed by the combustion. Figure 5.71(b) shows the oxygen mole fraction for the combustion chambers. The oxygen mole fraction behaviour is similar to the methane flame case where the secondary air supply was 3.0 % and the mole fraction was reduced to 2.4 % when it was diluted by the EGR at the downstream of the EGR pipes. The oxygen mole fraction in the combustion chamber is 0.15 % because almost all the oxygen was consumed by the combustion. Figure 5.71(c) shows the contour of water vapour for the combustion chamber: the behaviour is similar to the methane case.

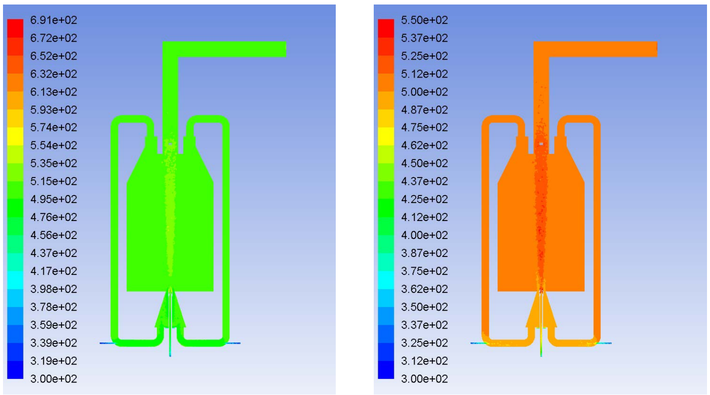

(a) Full range (b) From 300 to 550 K

Figure 5.70: Temperature contour for combustion of 10.82 L/min (10 kPa) biogas at $\lambda = 1.0$ with oxygen 3 % in oxidant supply.

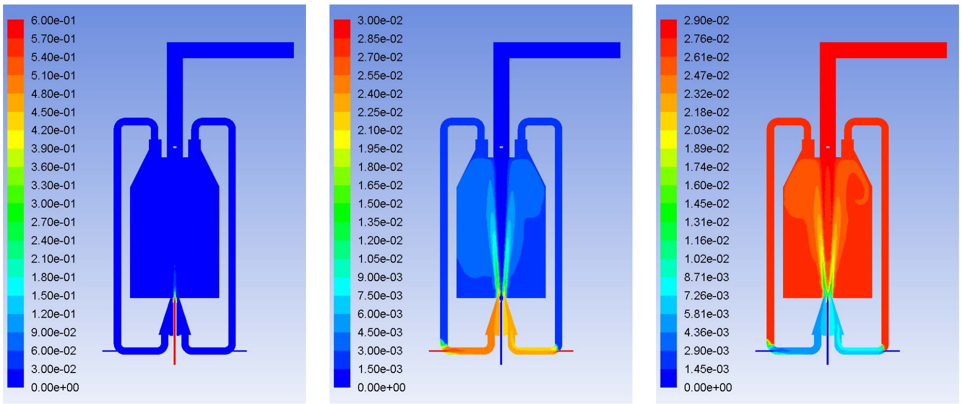

(a) CH_4 (b) O_2 (c) H_2O

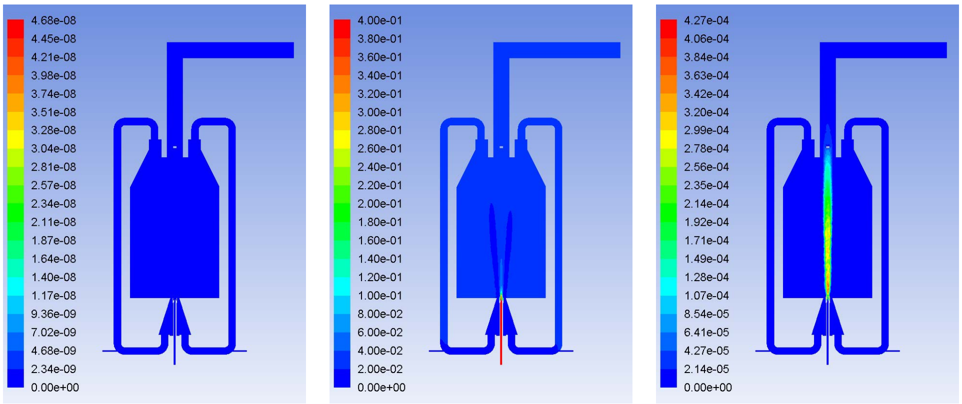

(d) NO_x (e) CO_2 (f) CO

Figure 5.71: Species mole fraction for combustion of 10.82 L/min (10 kPa) biogas at $\lambda = 1.0$ with oxygen 3 % in oxidant supply.

Figure 5.71(d) shows the contour of the NO_x for the combustion chamber. In a similar trend to the other cases, the contour shows that the NO_x is almost zero ppm for the whole combustion chamber and the EGR pipes. Figure 5.71(e) shows the contour of the carbon dioxide, which was detected at about 2.0 %

throughout the combustion chamber and EGR pipes. This is higher than the methane case because the carbon dioxide content in the biogas fuel was not involved in the combustion reaction and exhaust out through the exhaust pipe and EGR pipes. It was later diluted to 0.27 % at the downstream of the EGR pipes. Figure 5.71(f) shows the contour of the carbon monoxide, which is almost zero and similar to other cases except for the flame area. The carbon monoxide is detected at a very low measurement of 0.03 %. Figure 5.72 shows the numerical study with MILD regime conditions is repeated for a higher λ of 3.30. The maximum temperature in the combustion chamber is 721 K and the average chamber temperature is about 500 K. The intervals of the contour lines for the temperature profile in both Figure 5.72(a) and (b) are 21 and 13 K respectively. Similar to the other cases, it shows that the chamber temperature distribution is uniformly distributed and is a homogeneous temperature profile.

Figure 5.73 shows the combustion products for the numerical modelling of biogas with the oxygen mole fraction used being 3 % and the λ being 3.30. Similar to the case of methane with the $\lambda = 3.30$, Figure 5.73(a) shows almost zero unburned hydrocarbon, since the methane was consumed by the combustion. For the oxygen mole fraction, there was a similar trend to the methane case of $\lambda = 3.30$. Figure 5.73(b) shows the oxygen mole fraction for the secondary air supply was 3.0 % and the mole fraction was reduced to 2.85 % when it is diluted by the EGR at the downstream of the EGR pipes. This is because the oxygen mole fraction in the EGR pipes at the upstream and middle-stream of the EGR pipes is 2.10 %. For the water vapour (Figure 5.73(c)), the results are similar to the methane for the case of $\lambda = 3.3$ (Figure 5.69(c)). The water vapour at the flame area was 2.73 % and reduced to 0.84 % far downstream of the flame. The water vapour at the EGR pipes was 0.70 % and diluted to 0.13 % after mixed with the supplied secondary air. In the other areas of the chamber, the water vapour was 0.68 %.

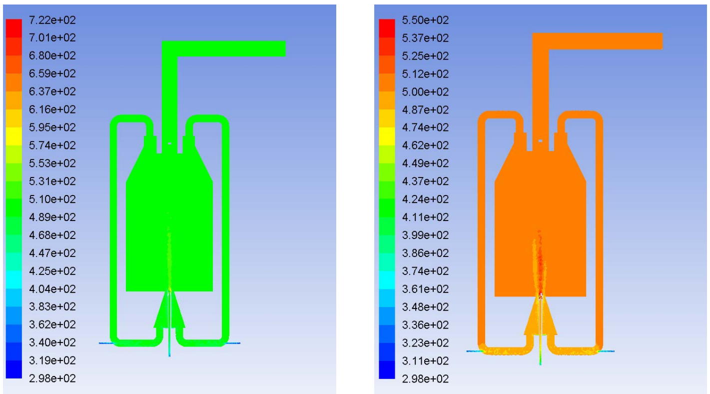

(a) Full range (b) From 300 to 550 K

Figure 5.72: Temperature contour for combustion of 10.82 L/min (10 kPa) biogas at $\lambda = 3.30$ with oxygen 3 % in oxidant supply.

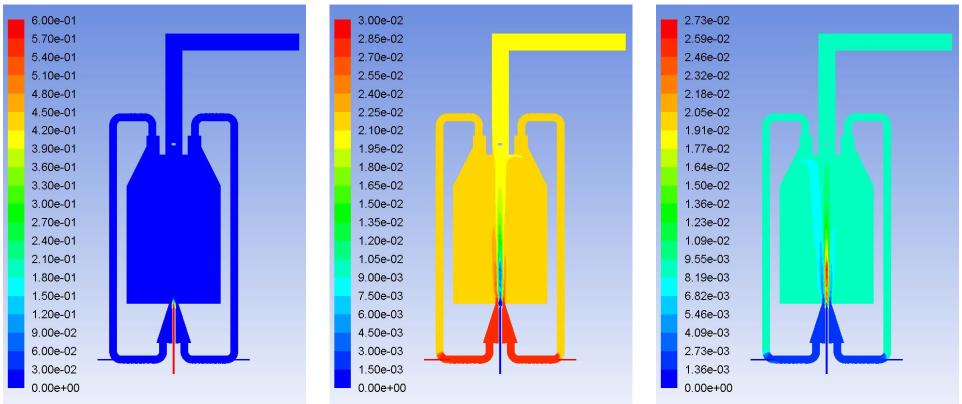

(a) CH_4 (b) O_2 (c) H_2O

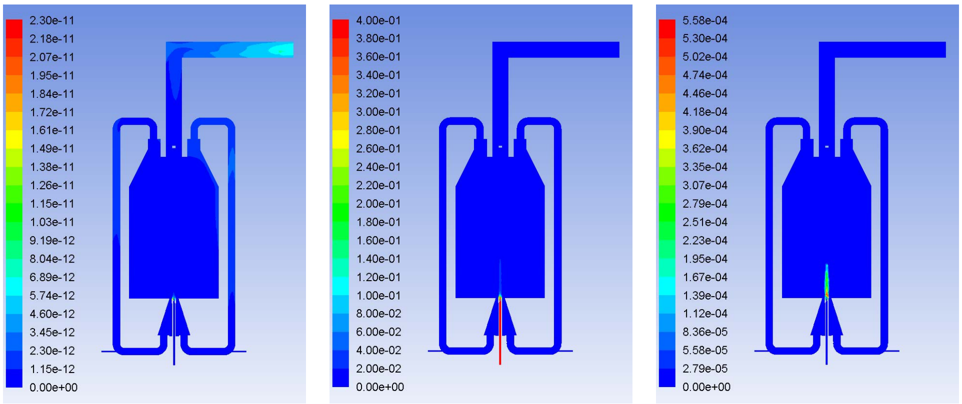

(d) NO_x (e) CO_2 (f) CO

Figure 5.73: Combustion products for combustion of 10.82 L/min (10 kPa) biogas at $\lambda = 3.30$ with oxygen 3 % in oxidant supply.

Figure 5.73(d) shows the contour of the NO_x for the combustion chamber. In a similar trend to the other methane and biogas case, the contour shows that the NO_x is almost zero ppm for the whole combustion chamber and the EGR pipes. Figure 5.73(e) shows the contour of the carbon dioxide which is 2.0 % throughout the combustion chamber and the EGR pipes. This is similar to the case of biogas with $\lambda = 1.0$. Figure 5.73(f) shows the contour of the carbon monoxide, which is almost zero throughout the combustion chamber and the EGR pipes. This condition is similar to the case of biogas with $\lambda = 1.0$ and 3.3. Figure 5.71(f) shows the contour of the carbon monoxide, which is almost zero throughout the combustion chamber and the EGR pipes and it is similar to other cases except for the flame area, where the carbon monoxide is detected at the very low level of 0.02 %. This is because at the flame area, the continuous chemical reactions produce carbon monoxide, and later it reacts with the oxygen to form the carbon dioxide.

5.13 Experimental Limitation for MILD Combustion

The overall combustion chamber, fuel supply and air supply systems were newly developed for this study. The furnace structure and fuel supply system create the boundary of the limitation to the experimental parameters, especially fuel supply flow rates. The standard nozzle used limited the operational gas supply to a maximum of 50 kPa, which limited methane fuel flow rates up to 24.2 L/min. The limitations of the experimental setup that reduce the potential to achieve MILD combustion are listed below:

(i) The furnace commissioning and ignition testing by a certified gas fitter found that the 1 mm nozzle bluff-body was not successfully igniting the reactants. It was suggested to replace it with a 12.7 mm standard industrial premixed nozzle. The level of premixed reached an optimal level when the flame was most stable (Baudoin, 2010). The test for the ignition was successful and the maximum gas supply pressure for the new standard 12.7 mm nozzle is 100 kPa. For safety reasons, during the testing and commissioning it was advised that the maximum gas supply pressure be limited to 50 kPa (Aylward, 2014).

(ii) The furnace has a very low fuel supply only giving 6.21 kW furnace power, including the 0.18 kW thermal input from the electric air heating element. With the furnace total volume of 0.33 m^3, the thermal intensity is 18.8 kW/m^3 atm. This value of thermal energy is below the minimum required to achieve and maintain a MILD combustion threshold condition in the combustion chamber. The minimum thermal input for the furnace is about 0.1 MW/m^3 atm.

(iii) A low fuel jet velocity resulted in a low Reynolds number. With a 24.2 L/min fuel flow rate, the air-fuel mixture jet Reynolds number at the burner is 303 and 551 for methane and biogas respectively. A Reynolds number of above 4,000 is required for the fuel jet to be turbulent and promote the turbulent reactant mixing thereby sustaining the flame propagation.

(iv) The MILD regime temperature is about 1,100 K to 1,600 K. The current in-furnace measurement system and instrument cabling surrounding the combustion chamber can only withstand a maximum temperature of 378 K and the majority of the K-type thermocouples used for in-furnace measurement are limited to 1,373 K.

MILD combustion can be achieved by a combustor with higher thermal intensity. Examples of high thermal intensity MILD combustors are: a FLOX combustor with a thermal intensity of 68.0 MW/m^3 at the Institute of Combustion Technology, Stuttgart, Germany (Lammel et al., 2010); a 36.7 kW small combustor with a thermal intensity of 12.2 MW/m^3 at the Chinese Academy of Sciences, Beijing, China (Huang et al., 2014); a small laboratory scale 6.25 kW combustor with a very high thermal intensity in the range of 5.0 MW/m^3 atm to 453.0 MW/m^3 atm (Arghode and Gupta, 2011*b*). In their paper, Arghode and Gupta (2013) summarised 14 other combustors (laboratory and industrial) worlwide that have successfully demonstrated and realised the MILD technology for furnace applications. These 14 all had a thermal intensity of about 0.1 MW/m^3 atm to 1.0 MW/m^3 atm. All the laboratory and industrial furnaces, thermal inputs show that a minimum of 0.1 MW/m^3 atm is required to achieve and sustain MILD combustion.

5.14 Summary

In this chapter, the experimental results were discussed and compared with the numerical modelling results. The computed static temperature is in fair agreement with the experimental results, with the numerical sensitivity test to study the chamber wall temperature boundary condition affecting the flame temperature. The development of a combustion burner to achieve the MILD condition can be performed using CFD rather than using costly experimental trial and error. Biogas is better than methane due to its lower peak temperature making the combustion chamber and burner last longer and be more operationally economical. The temperature of the biogas is reduced due to it being a lower calorific value fuel. The ignition process was discussed, with the fuel self-ignition temperature for methane being 873 K and for the biogas being 923 K. The ignition tests were conducted for the methane non-premixed flame, methane partially-premixed flame, methane premixed flame and biogas non-premixed flame. The quickest ignition occurred for the case of the methane partially-premixed flame with the preheated secondary air supply. The comparison of methane and biogas flames showed clear differences. The biogas flame height is about half that of the methane flame. The cases of no flame with the exhaust extraction and without the exhaust extraction were conducted to study the effect of the exhaust fan on the chamber temperature. The exhaust extraction fan does not significantly affect the chamber or EGR temperatures.

The effect of the preheated and non-preheated secondary air on the exhaust gas was studied. Both methane and biogas premixed flames produced NO_x of 2 ppm for all flow rates, whereas for carbon monoxide, biogas produced about 10 ppm at an early stage of the combustion, but it reduced to almost zero (below detection limits with the apparatus used) after 20 minutes of steady flame. The effect of the EGR and heated secondary air on the chamber temperature and combustion product was studied. The mixing cone temperature is almost identical to the downstream of the EGR temperature. The temperatures for both downstream of the EGR and the mixing cone are increased with the increase of the secondary air supply at each side of the EGR pipes. The non-premixed, partially-premixed and premixed flames were studied with methane fuel. Unburned hydrocarbon is almost zero (below detection limits with the apparatus used) for all cases and this condition is in line with excess oxygen in the exhaust gas due to lean combustion. This excess oxygen supply also had an effect on the flame temperature. For the premixed flame, the temperature is lower than for the partially-premixed flame. Further numerical modelling for the experimental furnace shows that when the oxygen dilution and the oxidant preheating were applied, the model can achieve MILD combustion. The limitation of the developed furnace was discussed with the minimum thermal input of $0.1\,\mathrm{MW/m^3}$ atm being required to achieve and sustain the MILD combustion regime.

Chapter 6

Numerical Results and Discussion

The chamber temperature distributions and exhaust gas species were numerically analysed for the newly developed air/fuel nozzle. The bluff-body burner was studied to achieve homogeneous temperature distribution toward the MILD combustion regime. This chapter presents the further numerical modelling results for the various parameters on the oxygen mole fraction and volume flow rate for the secondary air supply, fuel flow rate and exhaust gas opening for the flue gas outlet.

6.1 Introduction

Further numerical modelling was conducted to study the performance of a newly developed air/fuel bluff-body burner with a 1.0 mm fuel nozzle. All numerical modelling in this chapter used this bluff-body burner. The other furnace geometries are similar to the developed combustion chamber and the CFD detailed setup and configurations as described in Chapter 3. The furnace configuration used in this chapter provides well defined inlets for the oxidant and fuel supply, boundary conditions and outlet of the exhaust gas. The CFD models were developed to evaluate the the air-fuel equivalence ratio and the exhaust damper opening to achieve the MILD combustion regime. The temperatures were measured at various locations of the combustion chamber, the exhaust pipe, the EGR pipes and the mixing cone. The exhaust gas concentrations (UHC, NO_x, CO, H_2O and CO_2) were measured at the exhaust pipe and the downstream of the EGR pipes. The configurations of the bluff-body air/fuel nozzle and supply inlets are summarised in Table 6.1.

Table 6.1: Typical data for bluff-body burner and reactant supply inlets in Figure 6.1.

Item	**Symbol**	**Dimensions**
Fuel supply	$\mathrm{F_s}$	10 mm diameter × 1 inlet
Fuel nozzle	$\mathrm{F_n}$	1 mm diameter centre of burner
Air supply	$\mathrm{A_s}$	10 mm diameter × 4 inlets
Bluff-body diameter	$\mathrm{D_b}$	40 mm annulus
Air nozzle outer diameter	$\mathrm{A_n}$	60 mm

6.2 Air/Fuel Bluff-body Burner

The simulations were conducted for the non-premixed combustion with a smaller fuel nozzle compared to the previous simulations and experimental nozzle. Figure 6.1 shows the schematic diagram for the air/fuel bluff-body burner. One of the functions of the bluff-body burner is to stabilise the flame propagation in order to avoid flame extinction. The bluff-body nozzle is an obstacle in a flow field causing the turbulence field with a resulting recirculation zone used for the flame stabilisation (Lackner et al., 2010). Balachandran (2005) used the ramjet combustor design guideline by Zelinski et al. (1960) to design his bluff-body burner. It has been found that the nozzle geometry and the blockage ratio affects the flame stabilisation process. The flame structures were influenced by the characteristics of the recirculation zone affected by the blockage ratio. Increasing the blockage ratio would increase the recirculation zone length.

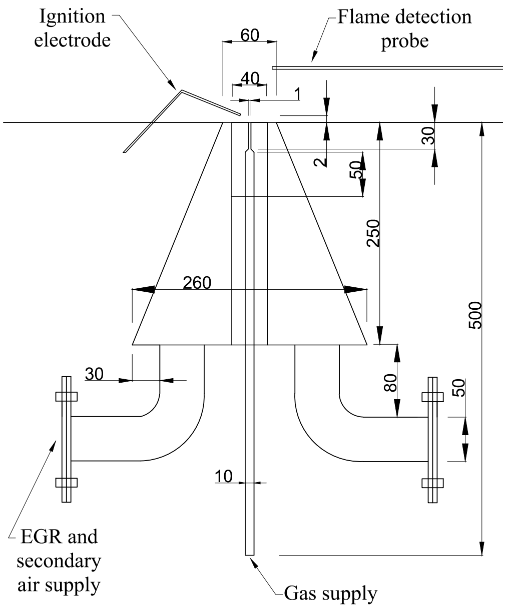

Figure 6.1: Schematic diagram for air/fuel bluff-body burner (all dimensions in mm).

Similarly, the increase in the bluff-body cone angle would lead to an increase in the intensity of the recirculation in the bluff-body wake (Esquiva et al., 2001). The air/fuel nozzle was designed to ensure the proper mixing process of the fuel and oxidant through the recirculation process in the mixing zone. In addition to being an efficient mixing process, the motivation of this design was to ensure a stable flame propagation. In this numerical modelling, the fuel nozzle is at the centre of the burner and the annular air nozzle surrounded the fuel nozzle.

6.3 Combustion Characteristics

The flame temperatures are one of the main results and the most important criteria to prove that the MILD combustion regime was achieved. The simulation results for the temperature distributions are shown in Figures 6.2 and 6.3. The temperature contour for synthetic air with 7 % oxygen mole fraction and atmospheric air with exhaust opening of 95 % are compared in Figure 6.2(a) and (b). The chamber average temperature for the combustion of biogas and synthetic air with a reduced oxygen mole fraction is lower (842 K) compared to the normal atmospheric oxygen level (1,175 K). A similar comparison for the exhaust opening of 5 % is shown in Figure 6.2(c) and (d). The chamber average temperature for the combustion of biogas with synthetic air with a reduced oxygen mole fraction is lower (848 K) compared to the normal atmospheric oxygen level (1,185 K).

The maximum chamber temperature was achieved near stoichiometric conditions and was reduced approximately by half when synthetic air with a 7 % oxygen mole fraction was used instead of atmospheric air. This is a consequence of the extra thermal load caused by the inert nitrogen. Figure 6.3(a) and (b) shows the combustion chamber contour of average temperatures for exhaust openings of 95 % and 5 % for small temperature ranges of 820 K to 870 K and 1,150 K to 1,230 K respectively. The majority of both domains is close to the average temperature of the combustion chamber: for synthetic air with a 7 % oxygen, the displayed temperature range is between 820 K and 870 K and for the atmospheric air, the temperature range is between 1,160 K and 1,220 K. Figure 6.3(c) and (d) show the equivalent results to Figure 6.3(a) and (b) for exhaust openings of 5 %. The majority of both domains is close to the average temperature of the combustion chamber: for synthetic air with a 7 % oxygen, the displayed temperature range is between 825 K and 870 K and for the atmospheric air, the temperature range is between 1,150 K and 1,230 K. This result signifies that the chamber average temperature is identical for both 5 % and 95 % exhaust opening, so the EGR is effective even for small amounts.

6.3.1 Chamber Temperature Profile

The temperature profiles for the combustion chamber at the axial locations as per Figure 6.4 are presented. Figures 6.5, 6.6 and 6.7 show the temperature

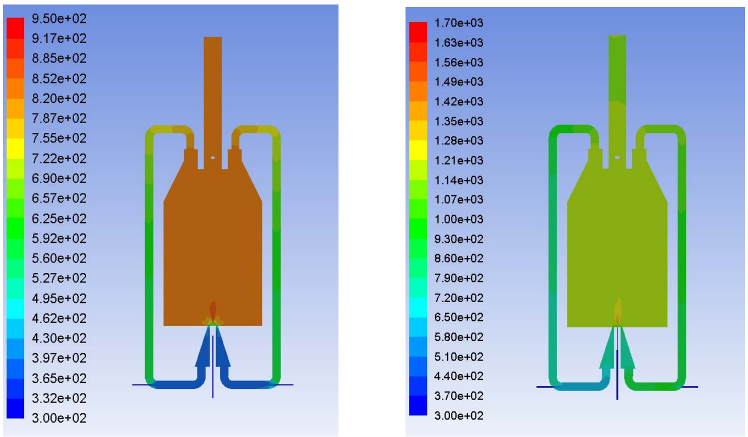

(a) synthetic air, 7 % O_2 (b) atmospheric air, 21 % O_2

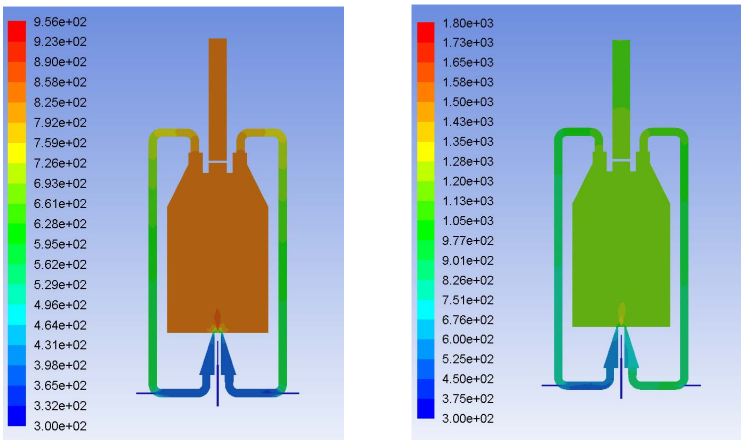

(c) synthetic air, 7 % O_2 (d) atmospheric air, 21 % O_2

Figure 6.2: Combustion temperature (K) for the exhaust opening of 95 % for (a) and (b) and 5 % for (c) and (d).

distributions for the inlet velocities of 8 m/s, 10 m/s and 15 m/s respectively with the λ range of 0.20 to 2.50 (all three figures use the same scale). Figure 6.4 shows the axial location for the various stations where temperatures were measured. There are six axial locations selected downstream from the injection location. The value of x/D_b at each location is: station A-A = 2.8, B-B = 8.9, C-C = 15.0, D-D = 17.8, E-E = 20.3, F-F = 22.8. The oxygen mole fractions for the secondary oxidant supply were set at 3 %, 7 %, 9 %, 12 %, 15 % and 21 %. The mixing ratio for the oxygen-nitrogen was varied to produce the desired level of oxygen mole fractions. In the previous experimental and numerical studies for MILD combustion, 3 % and 9 % oxygen mole fractions were used to study the flame speed, temperature, extinction (Medwell et al., 2007; Medwell et al., 2008) and flame temperature and behaviour (Colorado et al., 2009). In the experiment for lifted methane-air jet flames in a vitiated co-flow by Cabra et al. (2005), a 12 % oxygen mole fraction was used.

The difference between the maximum and average temperatures with various supply oxygen mole fractions is due to the lack of uniformity near the bluff-body

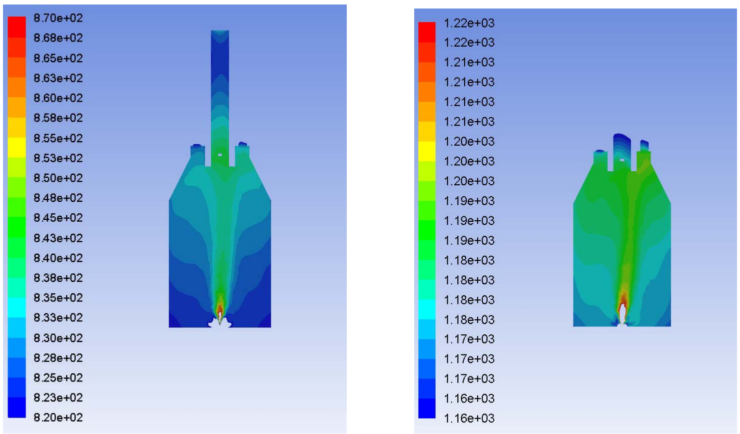

(a) synthetic air, 7 % O_2 (b) atmospheric air, 21 % O_2

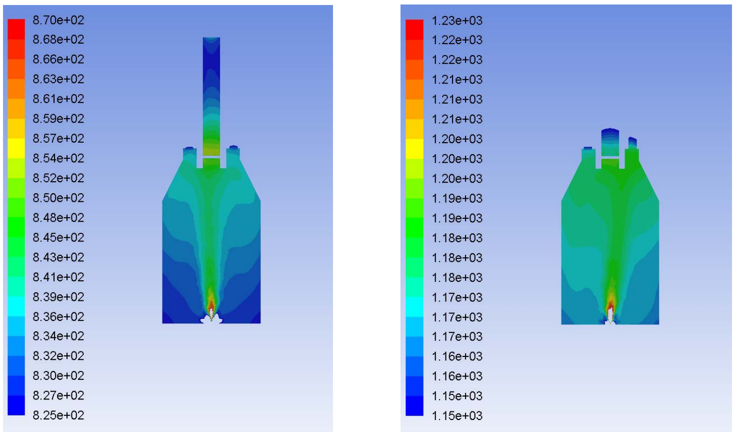

(c) synthetic air, 7 % O_2 (d) atmospheric air, 21 % O_2

Figure 6.3: As per Figure 6.2 showing limited temperature ranges.

burner. For the 3 % oxygen mole fraction, while there is a significant difference, the extra load of nitrogen keeps the temperature rise along the fuel jet to a minimum. Note that this is still MILD conditions. Table 6.2 summarises the uniformity ratio (the difference between the maximum and the minimum divided by the maximum temperature) for the case of the 15 m/s air flow rate. A similar trend is seen for the case of the combustion with air flow rates of 8 m/s and 10 m/s. The small temperature distribution range proves that MILD combustion was achieved for the simulation for synthetic air with oxygen mole fractions of 3 % to 21 %. For 21 % oxygen, the uniformity ratio was the highest, which is caused by the temperature rise almost exclusively being contained within $r/D_b \leq 2$.

In this study, the wall temperature was set at room temperature, so the temperature profiles are not as uniform as for a higher wall temperature of 1,300 K (Graca et al., 2013), with the largest variations occurring near the bluff-body (station A-A). The lower the oxygen mole fraction in the supply air, the lower the flame temperature. This is because the more oxygen supplied, the more fuel can be involved in the reaction and produces more heat that increases the flame

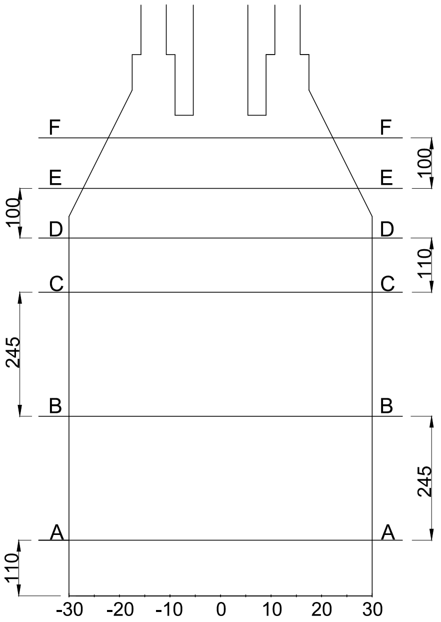

Figure 6.4: Temperature profile axial location for bluff-body diameter, D_b=40 mm. Downstream distance from injection locations, x/D_b: Station A-A = 2.8, B-B = 8.9, C-C = 15.0, D-D = 17.8, E-E = 20.3, F-F = 22.8.

Table 6.2: The oxygen mole fraction in air supply and MILD condition for Figure 6.7 at the λ of 0.35 to 2.47. The uniformity ratio is the difference between the maximum and the minimum divided by the maximum temperature.

Oxygen mole fraction	**3 %**	**7 %**	**9 %**	**12 %**	**15 %**	**21 %**
Uniformity ratio	< 2.3 %	< 3.8 %	< 4.1 %	< 4.2 %	< 4.3 %	< 4.4 %
MILD condition	Yes	Yes	Yes	Yes	Yes	Yes

temperature. The air stream velocity was kept constant. At the reactant mixing area slightly above the air/fuel nozzle, the equivalence ratio is very small and it is near the rich flammability limits. The effect of air supply velocity on the flame temperature was very clear. For the 12 % oxygen mole fraction of the secondary air supply, the flame station A-A temperature is 1,043 K, 1,094 K and 1,168 K for the case of λ of 0.75, 0.94 and 1.41 respectively. A similar trend was observed for the other oxygen mole fractions in Figures 6.5, 6.6 and 6.7. The higher the supplied air volume to the combustion chamber, the higher the flame temperature.

6.3.2 Chamber Average and Maximum Temperature

The temperature distributions in Figure 6.2 show that the hottest zone is slightly above the fuel nozzle where the streams first reacted. Figure 6.8 shows the maximum and average temperatures for the combustion chamber and the air mixing temperature (the downstream of the EGR) with the exhaust openings of 5 % and 95 %. The average chamber temperature for both exhaust openings of 5 % and

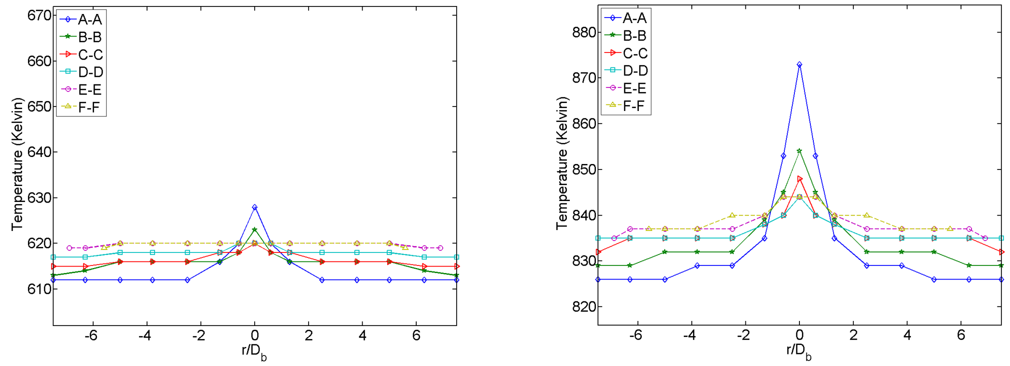

(a) 3 % oxygen, $\lambda = 0.20$ (b) 7 % oxygen, $\lambda = 0.44$

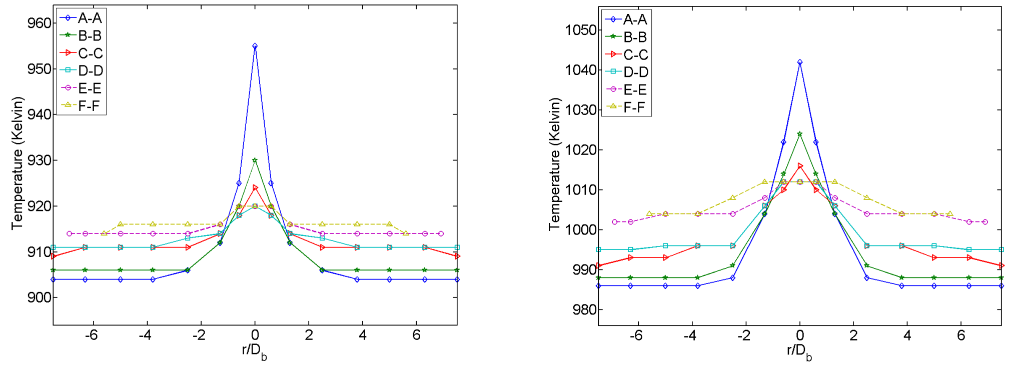

(c) 9 % oxygen, $\lambda = 0.56$ (d) 12 % oxygen, $\lambda = 0.75$

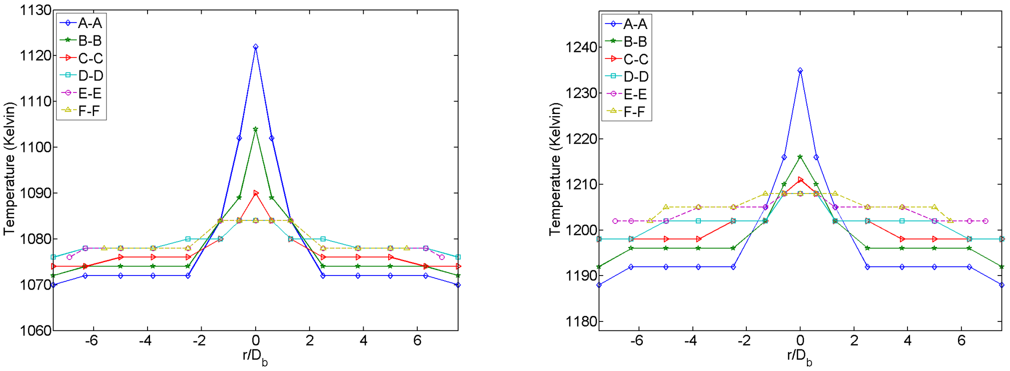

(e) 15 % oxygen, $\lambda = 0.94$ (f) 21 % oxygen, $\lambda = 1.32$

Figure 6.5: Temperature profile of the axial location for 8 m/s air inlet velocity with different oxygen mole fractions (y-axis shows a change of 170 K from bottom to top).

95 % are below 1,300 K. The average and maximum chamber temperatures were almost identical at 3 % inlet oxygen mole fraction and the differences were slightly increase with the increased of the inlet oxygen mole fraction. The simulations were conducted for the case of 21 % oxygen mole fraction (atmospheric air) with the λ of 1.0. Figure 6.9 shows the maximum and average chamber temperatures and air mixing temperature for different air inlet velocities. The result shows

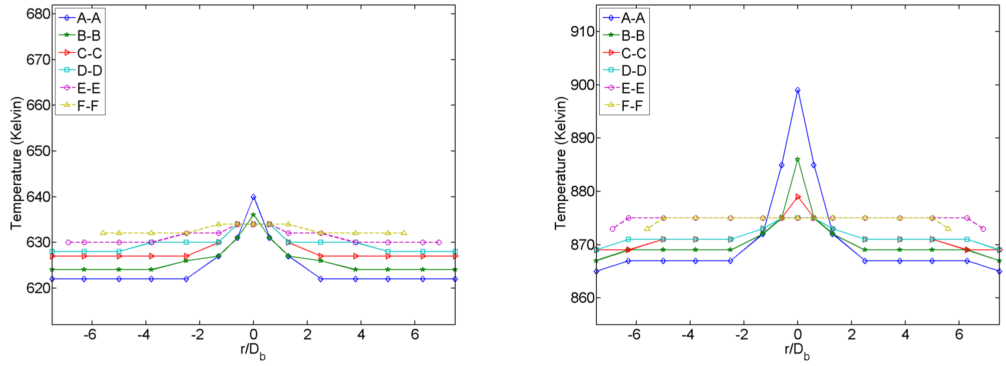

(a) 3 % oxygen, $\lambda = 0.25$ (b) 7 % oxygen, $\lambda = 0.55$

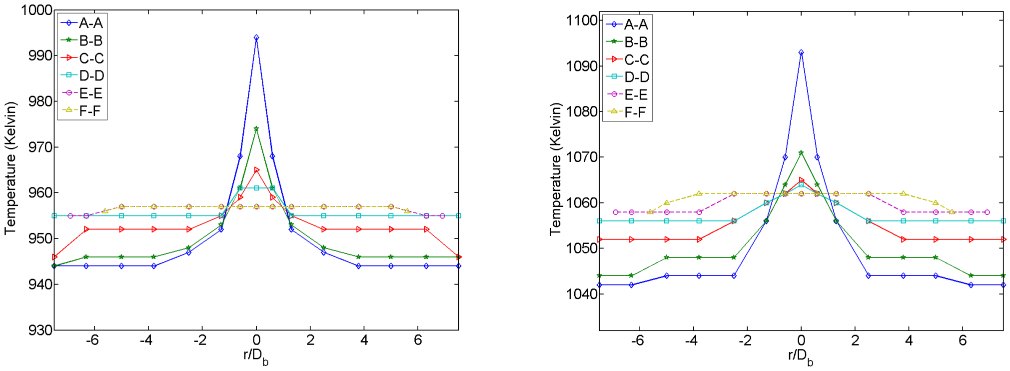

(c) 9 % oxygen, $\lambda = 0.70$ (d) 12 % oxygen, $\lambda = 0.94$

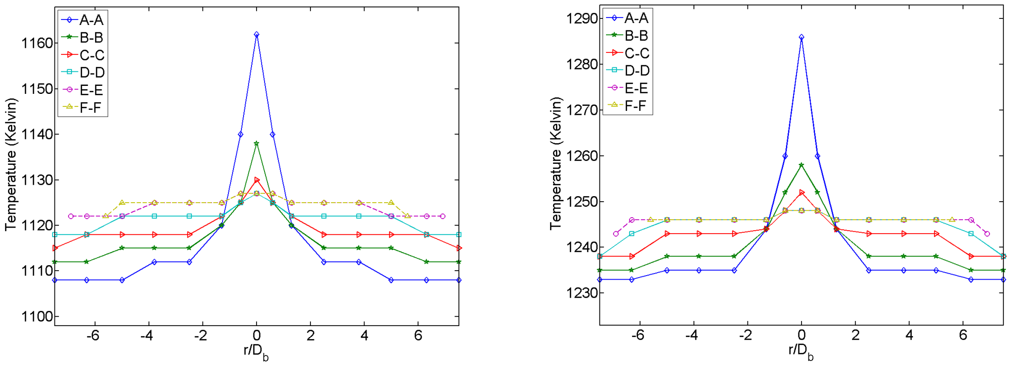

(e) 15 % oxygen, $\lambda = 1.17$ (f) 21 % oxygen, $\lambda = 1.64$

Figure 6.6: As per Figure 6.5 for air inlet velocity of 10 m/s.

that the effect of air inlet velocity is negligible on the chamber temperature but it is significantly affected by the exhaust opening. All the maximum and average chamber temperatures and air mixing temperatures are nearly identical for the air inlet velocity of 7 m/s to 15 m/s. A very small increase of the temperature can be seen for the case of 7 m/s to 15 m/s. The average maximum temperature for the exhaust openings of 95 % and 5 % are about 1,800 K and 950 K for the inlet velocity of 7 m/s to 15 m/s. A similar trend is observed for the case of average chamber temperature and air mixing temperature.

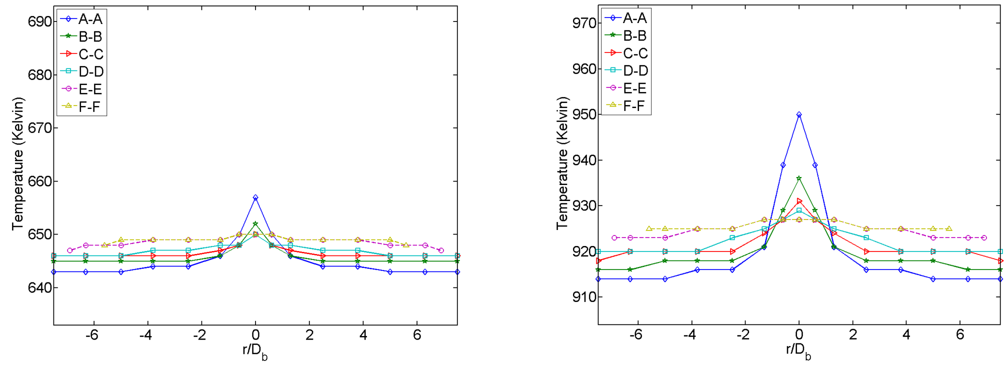

(a) 3 % oxygen, $\lambda = 0.35$ (b) 7 % oxygen, $\lambda = 0.82$

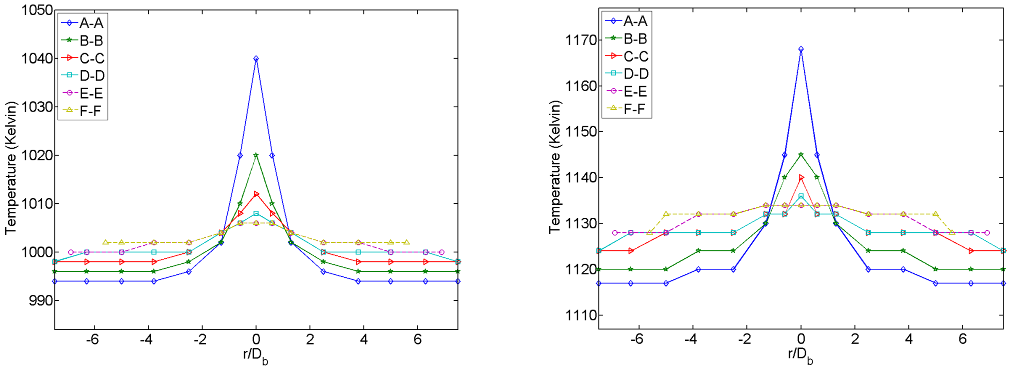

(c) 9 % oxygen, $\lambda = 1.06$ (d) 12 % oxygen, $\lambda = 1.41$

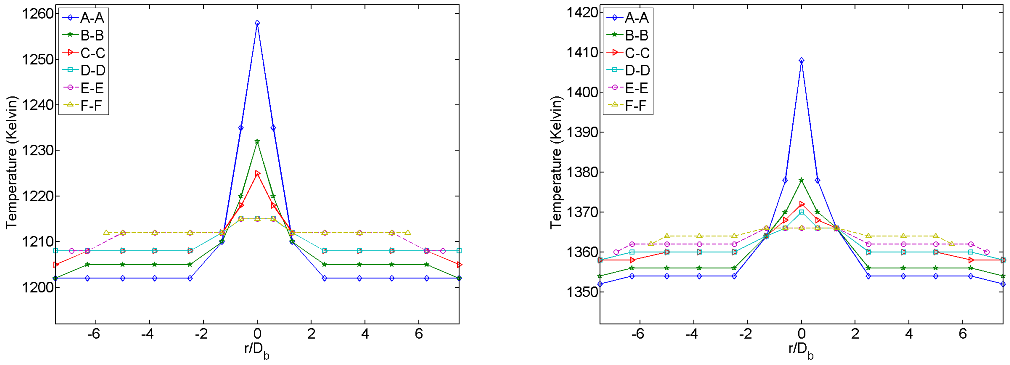

(e) 15 % oxygen, $\lambda = 1.76$ (f) 21 % oxygen, $\lambda = 2.47$

Figure 6.7: As per Figure 6.5 for air inlet velocity of 15 m/s.

6.4 Oxygen Dilution

Oxygen dilution is very important to achieve the MILD combustion regime: the oxygen mole fraction must be in the range of 3–13 % (Li et al., 2011). Oxygen dilution can be determined by measuring the EGR mass flow rate, fuel mass flow rate, and fresh air mass flow rate. The dilution ratio (K_v) can be calculated using Equation 2.2 (Wünning and Wünning, 1997). Figure 6.10 shows biogas combustion with λ of 1.0 and air inlet velocity of 10 m/s. The supply oxygen

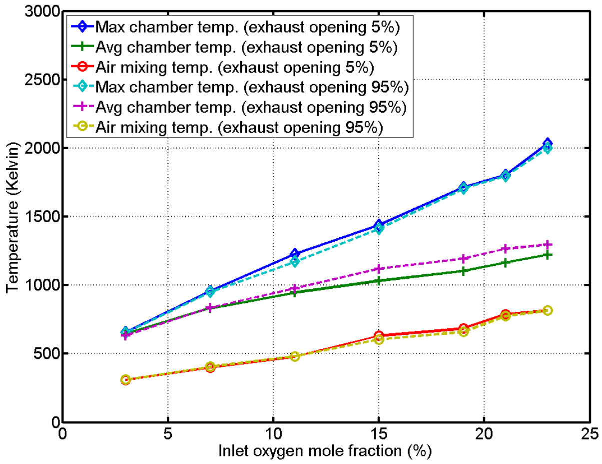

Figure 6.8: Maximum and average chamber and mixing temperatures for biogas (λ = 1.0 and air inlet velocity of 10 m/s.) Exhaust opening 5 %, –; Exhaust opening 95 %, - -.

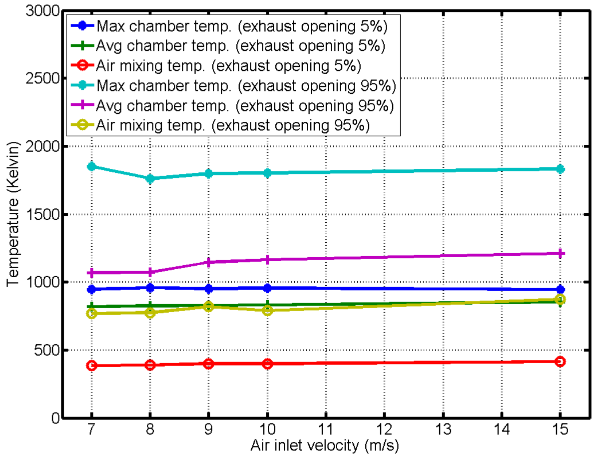

Figure 6.9: Effect of air inlet velocity on chamber and mixing temperatures for biogas (with $\lambda = 1.0$ and 21 % oxygen mole fraction).

mole fraction is the oxygen mole fraction in the secondary air supply. The fuel flow rate is varied based on the oxygen mole fraction in the secondary air so λ is 1.0. For the 21 % oxygen mole fraction, the oxygen is diluted to 12.6 %. There is a similar trend with the other oxygen mole fractions from 3 % to 21 %. There are very small differences between the exhaust openings of 5 % and 95 %. In this case, the exhaust opening does not significantly affect the oxygen mole fraction dilutions.

Figure 6.11 shows the corresponding reduction for the data in Figure 6.10. The diluted oxygen mole fractions were measured after the supplied air had mixed with the EGR at the downstream of the EGR pipes. For the 21 % inlet oxygen mole fraction, the ratio of diluted oxygen mole fraction is 40 %, where the oxidant is reduced from 21.0 % to 12.6 %. The ratio was increased monotonically with the increase in the oxygen mole fraction. The result for both exhaust openings of 5 % and 95 % is nearly identical. This result shows that the exhaust opening does not have a significant effect on the EGR flow rate. This is because of the design at the top part of the chamber to ensure the exhaust gas was trapped and utilised as EGR. The exhaust pipe at the centre of the furnace was purposely lowered to create an annulus exhaust gas trap. Figure 6.12 shows the contour of the oxygen mole fraction for the combustion chamber and EGR pipes. The secondary air velocity is 10 m/s and the λ is 1.0. Oxygen dilution occurred downstream of the EGR. The stoichiometric combustion consumes almost all the oxygen. When the exhaust gas with zero oxygen mole fraction is mixed with the fresh air with 3 % and 12 % oxygen, it is diluted to 2.4 % and 9.6 % respectively.

6.5 Combustion Product

The exhaust gas composition of the MILD combustion fuelled with gas is the same as for the traditional combustion. The exhaust gas includes carbon dioxide, water vapour, carbon monoxide, oxides of nitrogen and unburned hydrocarbon. Each of the exhaust gases is discussed in the subsections below. Figure 6.13 shows the biogas combustion temperatures for the 7 % oxygen mole fraction with the same air inlet (8 m/s) for three different fuel inlet velocities: low at 2.2 m/s ($\lambda = 1.06$), medium at 3.0 m/s ($\lambda = 0.78$) and high at 6.7 m/s ($\lambda = 0.35$). The maximum chamber temperatures for the λ of 1.06, 0.78 and 0.35 are 1,000 K, 955 K and 927 K respectively. The chamber's maximum temperature increased as stoichiometry was approached.

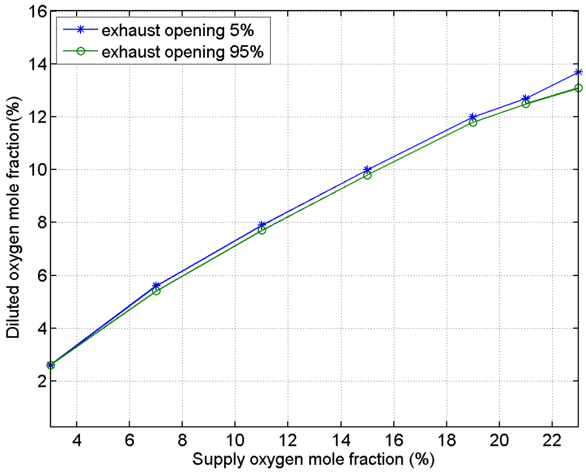

Figure 6.10: Diluted oxygen mole fraction entering chamber compared to inlet mole fraction for biogas combustion ($\lambda = 1.0$).

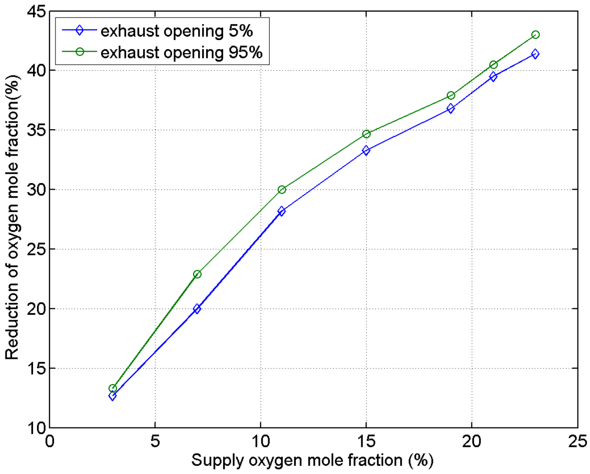

Figure 6.11: The reduction of oxygen mole fraction due to dilution of the inlet oxidant.

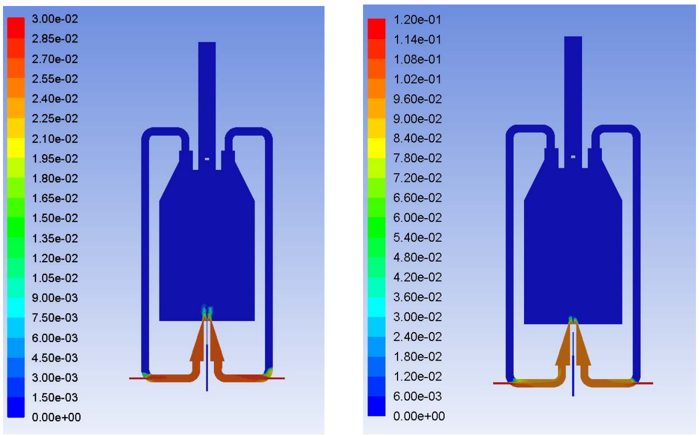

(a) 3 % oxygen (b) 12 % oxygen

Figure 6.12: The oxygen dilution for the air inlet of 3 % and 12 % oxygen mole fraction ($\lambda = 1.0.$).

The highest temperature is observed slightly above the wake of the bluff-body since this is the primary mixing zone for the fuel and oxidiser. The mixture at this region is close to stoichiometric conditions, so it is inevitable that it is relatively hot. Also, this is adjacent to the recirculation region of the fuel with some of the oxidiser stream, so the increased residence time with reduced dilution causes the higher temperature. Once this mixture is further diluted with the rest of the oxidiser stream, the MILD condition is able to dominate and reduce the temperature to the almost constant levels detected further downstream. When there are sufficiently high inlet velocities and diluted oxygen, MILD conditions are developed in the chamber and the primary mixing zone is small, thereby releasing only a fraction of the total heat. Figure 6.14 shows the results from Figure 6.13 with the range of temperature being 45 K in each. The uniformity ratios for these cases are 5.4 %, 5.5 % and 5.6 % respectively. This uniformity ratio is similar to that defined earlier except it is the difference between the maximum and the average temperature divided by the average temperature (Yang and Blasiak, 2006; Colorado et al., 2010).

The remainder of this section presents the results of further simulations conducted for the synthetic air of 7 % and 21 % oxygen mole fractions with air supply rates of 8 m/s, 10 m/s and 15 m/s. The fuel supplies were varied to meet the λ values of 0.35, 0.78, 1.06, 2.0, 3.5 and 5.0. The purpose of the simulations is to discuss the performances of the biogas combustion. Section 6.5.1, Figure 6.15 shows the chamber temperature for the cases when the air inlet has 7 % and 21 % oxygen mole fractions. The atmospheric air produces higher combustion temperatures compared to the synthetic air with 7 % oxygen mole fraction. The same trend appeared where the maximum temperature was achieved near stoichiometric conditions and the temperature reduced as the mixture became more lean or rich. The reduction in the temperature as the mixture becomes more lean is because the higher the λ, the higher the oxidant supply, and it cools down the combustion temperature (Quaak et al., 1999; Saanum et al., 2007). This is because the higher nitrogen in the 7 % synthetic oxidant and excess oxygen from the high oxidant supply acted as diluents to the flame temperature. The homogeneous temperatures were achieved for the cases of both 7 % and 21 % oxygen mole fractions. The majority of the chamber temperatures ($\lambda = 1.06$) for the cases of 7 % and 21 % oxygen mole fractions are 835 K to 880 K and 1,160 K to 1,220 K respectively. The uniformity ratio for the 7 % and 21 % oxygen mole fractions are 5.4 % and 5.2 %.

6.5.1 Unburned Hydrocarbon

Unburned hydrocarbon occurred when the combustion conditions were too rich (too much fuel or insufficient oxygen to complete the reactions). Figure 6.16 demonstrates the effects of unburned hydrocarbon levels in the current system.

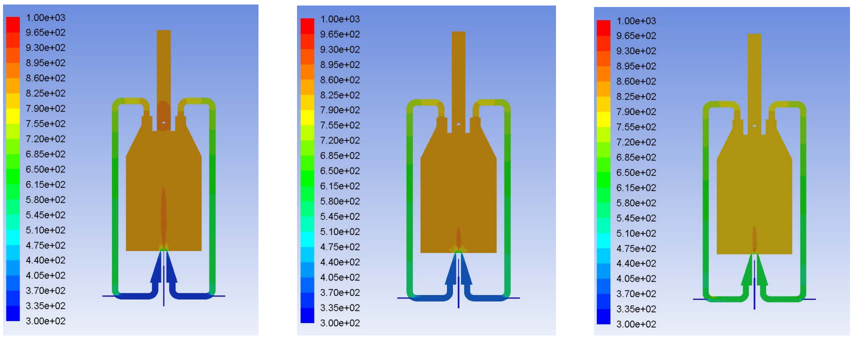

(a) λ of 1.06 (b) λ of 0.78 (c) λ of 0.35

Figure 6.13: Chamber temperature for 7 % oxygen mole fraction and 8 m/s air supply.

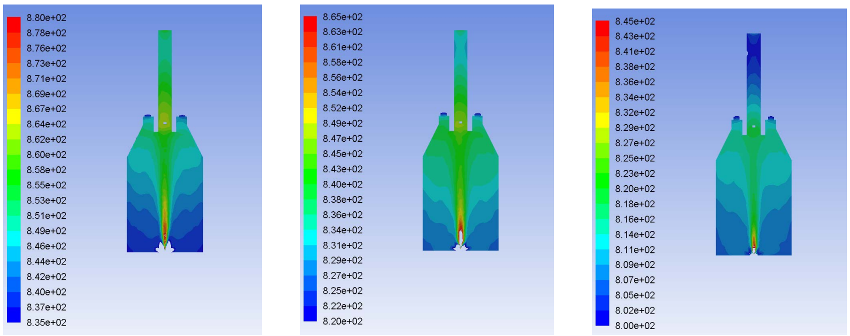

(a) λ of 1.06 (b) λ of 0.78 (c) λ of 0.35

Figure 6.14: As per Figure 6.13 showing limited temperature ranges.

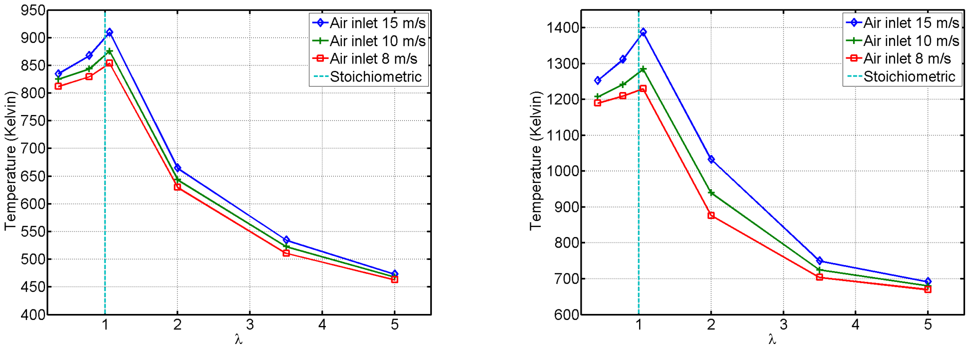

(a) 7 % oxygen (b) 21 % oxygen

Figure 6.15: Chamber temperature for the air inlet of 7 % and 21 % oxygen mole fractions.

In Figure 6.16(a), the mixing of the air supply with the EGR produces unwanted chemical reactions in the EGR pipes prior to the combustion chamber. Figure 6.16(b) shows a desirable operating condition with homogeneous temperature causing the mixing of EGR and air to merely preheat the air. The combustion process achieves the MILD combustion state: the majority of the domain's temperature distribution is from 822 K to 844 K, which is a variation of 2.7 % and there is only the small region near the bluff-body that is hotter. The ranges are considered to be uniformly small. This is in agreement with the condition that the MILD combustion regime is achieved when the temperature uniformity ratio is less than 23 % (Tsuji et al., 2003). Figures 6.17 and 6.18 show that the combustion consumes all the oxygen at lower λ, leaving unburned hydrocarbons, while a significant amount of oxygen remains at lean conditions, consuming all the fuels. This greater consumption of methane produces the higher flame temperatures. At the rich fuel combustion, the chemical reaction leaves unburned hydrocarbon for both 7 % and 21 % oxygen mole fractions (Figure 6.17).

The secondary air supply of 8 m/s gives a slightly higher unburned hydrocarbon compared to the secondary air of 10 m/s and 15 m/s. This is due to being the

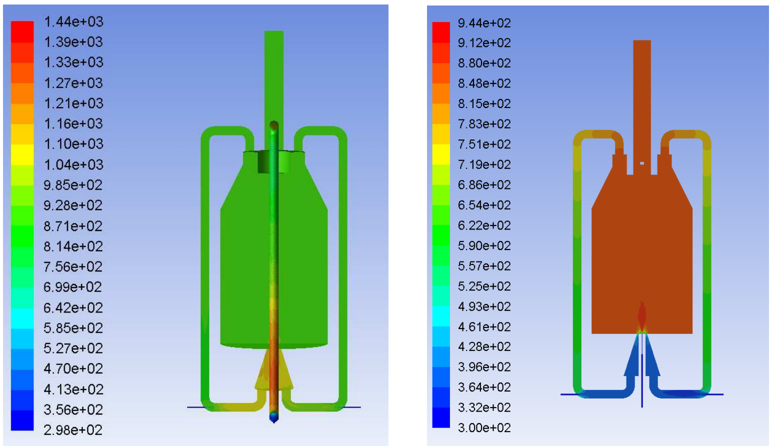

(a) unwanted burning (b) proper burning

Figure 6.16: Temperature contours for (a) unwanted burning at downstream of EGR pipes for 21 % oxygen mole fraction with 10.0 m/s air inlet and λ of 0.78. (b) proper burning for 7 % oxygen mole fraction with 10.0 m/s air inlet and λ of 1.06.

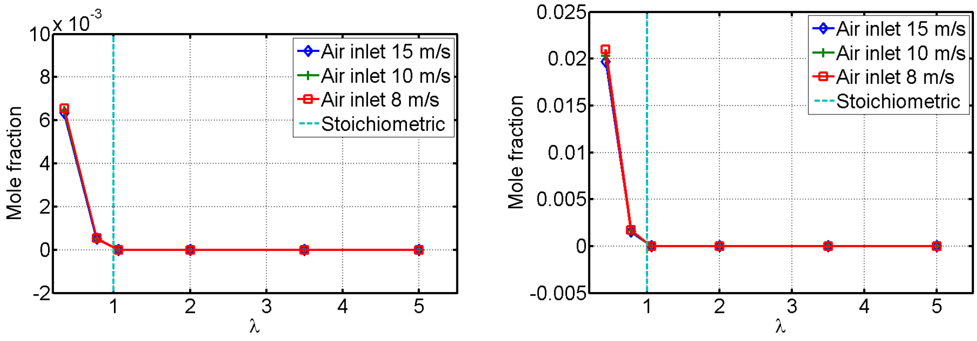

(a) 7 % oxygen (b) 21 % oxygen

Figure 6.17: Unburned hydrocarbon in exhaust for the air inlet of 7 % and 21 % oxygen mole fractions.

most fuel rich case, which is the same fuel flow rate with the lowest secondary air supply flow rate giving the richest mixture. A similar trend is shown in the case of the secondary air supply with 21 % oxygen mole fraction with the λ of 0.78. For the case of the 21 % oxygen mole fraction, the unburned hydrocarbon mole fraction reduces almost to zero and the λ increases from 0.35 to 0.78. Later, when the λ is higher than 1.0 (lean combustion), the unburned hydrocarbon mole fraction is zero. Similar results occurred for the secondary air supply with 7 % oxygen mole fraction.

6.5.2 Oxygen

Figure 6.18 shows the excess oxygen for the case of secondary air supply with 7 % and 21 % oxygen mole fractions. The excess oxygen was zero at the lowest λ because the rich fuel mixtures consumed all the oxygen in the oxidant sup-

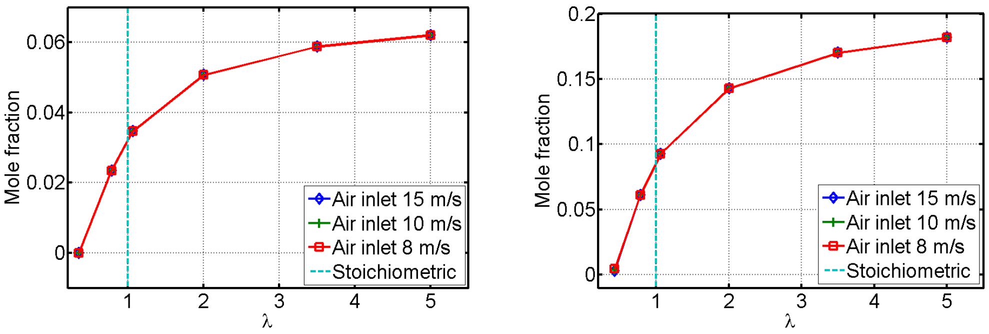

(a) 7 % oxygen (b) 21 % oxygen

Figure 6.18: Excess oxygen in exhaust for the air inlet of 7 % and 21 % oxygen mole fractions.

ply, resulting in the unburned hydrocarbon. The excess oxygen logarithmically increased as λ increased. The rapid rise in the rich region from zero is caused as more of the hydrocarbons are consumed (Figure 6.17), then all the carbon monoxide is converted to carbon dioxide as stoichiometric conditions are reached (Figure 6.26). The rate of increase decreases with λ as this is just the oxygen that is remaining in lean conditions.

6.5.3 Oxides of Nitrogen

Oxides of nitrogen (NO_x) was the pollutant that produced from the combustion and it is harmful to the environment. Figure 6.19(a), (b) and (c) shows the mole fraction of NO_x and Figure 6.19(d), (e) and (f) shows the rate of production of NO_x. It is almost identical for all the cases at the λ of 1.06, 0.78 and 0.43 with all values zero, considering numerical precision. Figure 6.20 shows the oxides of nitrogen, where significant amounts were only formed for the richest case with 21 % oxygen. Despite the higher concentration of nitrogen in the 7 % oxygen case, the temperature was below 1,000 K and therefore far from the temperature that is favourable for NO_x formation (Scheele et al., 2008).

The reacting mixture was diluted by the products that enter the chamber and this dilution reduced the flame temperature and simultaneously reduced creation of thermal NO_x formation. For the fuel rich combustion, the dilution process is low because of the low oxidant supply. Under lean conditions, the atmospheric air produced approximately 0.1 ppm NO_x, while the 7 % oxygen mole fraction produced zero oxides of nitrogen within numerical precision. This shows that the configuration can produce negligible pollutants without the expense of separating out N_2 before the combustion chamber. The rate of thermal NO_x production for the for 7 % oxygen mole fraction and 8 m/s air supply with the low, medium and high fuel supply were compared in Figure 6.21. These values are essentially zero to numerical precision, which corresponds to the very low concentrations that are produced.

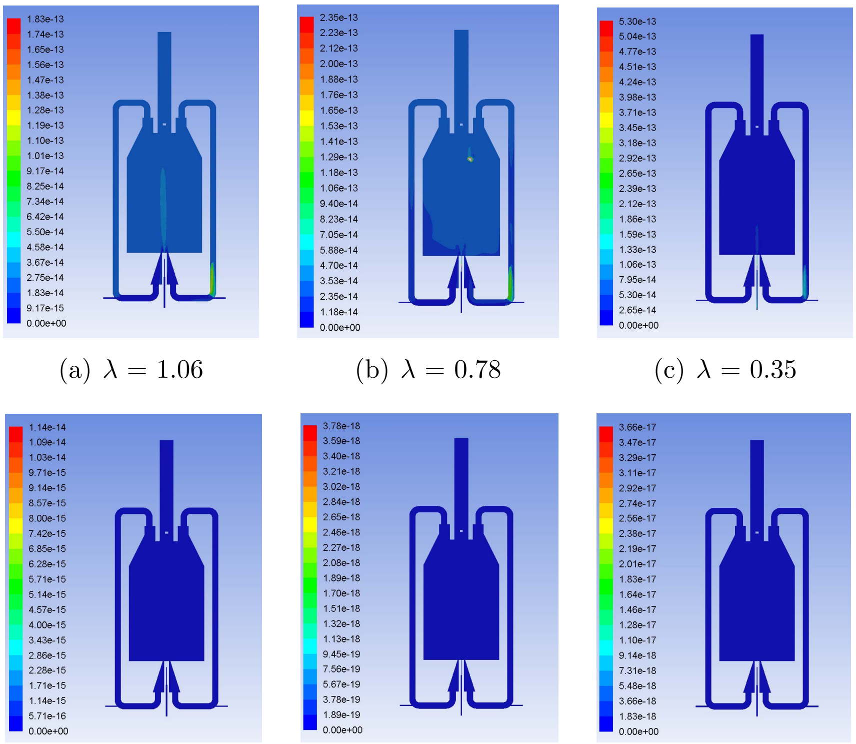

(a) $\lambda = 1.06$ (b) $\lambda = 0.78$ (c) $\lambda = 0.35$

(d) $\lambda = 1.06$ (e) $\lambda = 0.78$ (f) $\lambda = 0.35$

Figure 6.19: (a) to (c) for mole fraction of NO_x with 8 m/s air supply with 7 % oxygen mole fraction and (d) to (f) for the rate of NO_x.

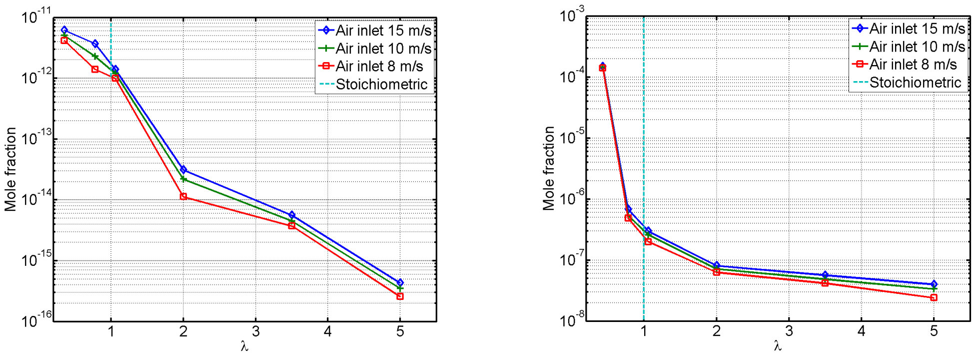

(a) 7 % oxygen (b) 21 % oxygen

Figure 6.20: Pollutant NO_x in exhaust for the air inlet of 7 % and 21 % oxygen mole fractions.

6.5.4 Carbon Dioxide

Figure 6.22 shows the carbon dioxide mole fraction for the combustion of 7 % and 21 % oxygen mole fractions in the oxidant stream. The higher air-fuel equivalence ratio gave lower carbon dioxide in the combustion chamber because it was diluted by the excess air. The trend continues for all values of λ (Figure 6.23). The trend is identical for the case of 21 % oxygen mole fraction (Figure 6.22(d) to (f)). The higher fuel supply cause the higher level of carbon dioxide to be released through

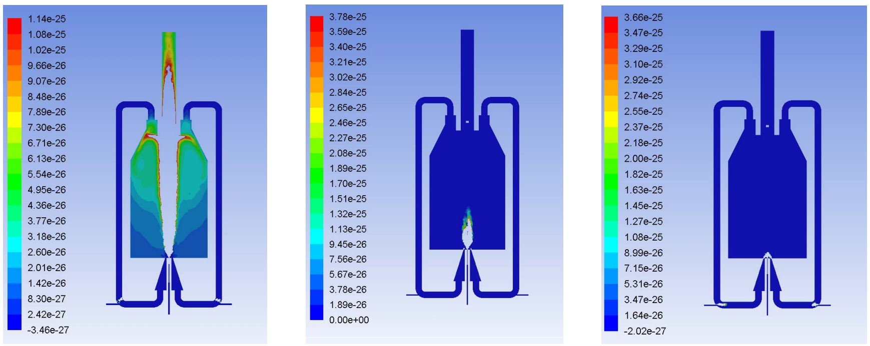

(a) $\lambda = 1.06$ (b) $\lambda = 0.78$ (c) $\lambda = 0.35$

Figure 6.21: Rate of thermal nitrogen oxide production for 8 m/s air supply with 7 % oxygen mole fraction.

the exhaust pipe. This is because the fuel composition is 60 % methane and 40 % carbon dioxide. The higher the fuel supply, the more carbon dioxide injected to the combustion process. The carbon dioxide released for the case of 21 % oxygen mole fraction is higher than the case of 7 % oxygen mole fraction because of the lower dilution by nitrogen. Figure 6.24 shows the carbon dioxide mole fraction normalised by the oxygen mole fraction in the oxidant stream. These show how much carbon dioxide is produced for each mole of oxygen (filtering out the effects of the extra nitrogen). For this normalised condition, the case of 7 % oxygen mole fraction produces more carbon dioxide than 21 %: more complete combustion occurs, so the combustion efficiency is higher and pollutants are reduced.

6.5.5 Carbon Monoxide

Carbon monoxide is a product of incomplete combustion due to insufficient oxygen to enable complete oxidation to form of carbon dioxide. Carbon monoxide is only produced when there is no excess oxygen (Figure 6.18). Because of its hazardous nature, its production should be minimised. Figure 6.25 shows the carbon monoxide with 7 % and 21 % of oxygen mole fractions in the oxidant stream. For both synthetic air and atmospheric air, the carbon monoxide is essentially zero for stoichiometric conditions, but is produced for rich conditions. The higher the fuel supply injected to the combustion chamber, the higher the carbon monoxide released as a combustion product to the atmosphere. At rich fuel condition, the carbon monoxide mole fraction decreases with the increase of λ. The high temperature combustion for the 21 % oxygen mole fraction produces more carbon monoxide (Dally et al., 2010; Wünning, 1991) than the 7 % oxygen mole fraction (Figure 6.26). Under lean conditions, the pollutants carbon monoxide and unburned hydrocarbon are effectively almost zero; this proves that the proposed configuration is viable for clean combustion. Figure 6.27 shows the carbon monoxide mole fraction normalised by the oxygen mole fraction in the oxidant stream. These show how much carbon monoxide is produced for each mole of oxygen (filtering out the effects of the extra nitrogen). The result is similar to

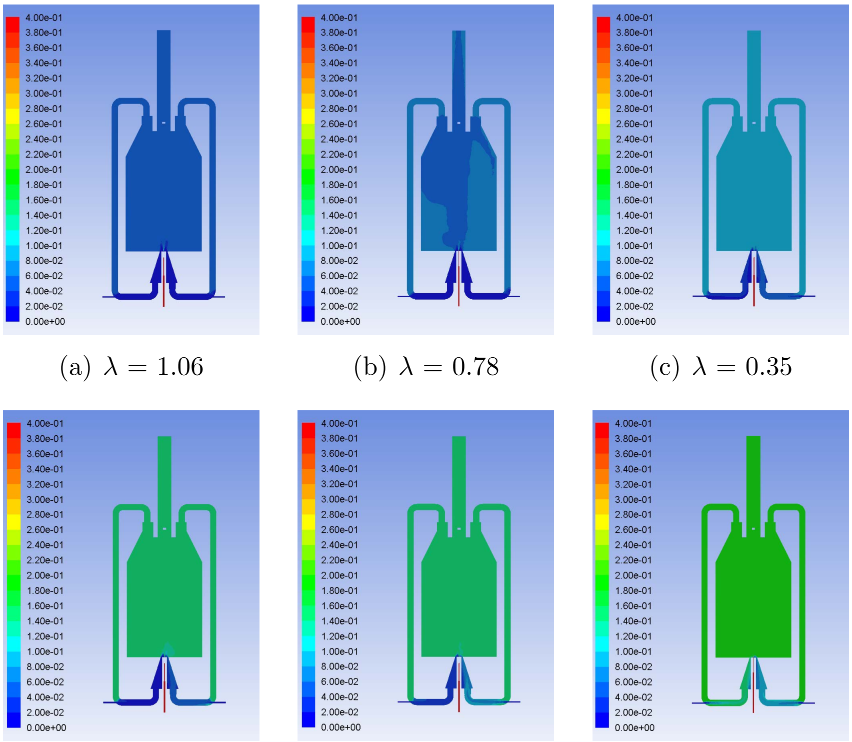

(a) $\lambda = 1.06$ (b) $\lambda = 0.78$ (c) $\lambda = 0.35$

(d) $\lambda = 1.06$ (e) $\lambda = 0.78$ (f) $\lambda = 0.43$

Figure 6.22: Carbon dioxide mole fraction for 10 m/s air supply with 7 % ((a) to (c)) and 21 % ((d) to (f)) oxygen mole fractions.

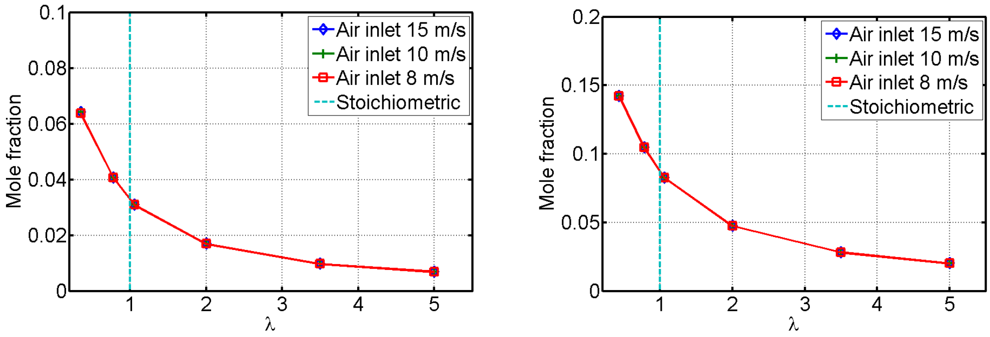

(a) 7 % oxygen (b) 21 % oxygen

Figure 6.23: Carbon dioxide mole fraction in exhaust for the air inlet of 7 % and 21 % oxygen mole fractions.

carbon dioxide where for this normalised condition, the case of 7 % oxygen mole fraction produces less carbon monoxide than 21 %: more complete combustion occurs, so the combustion efficiency is higher and pollutants are reduced.

6.5.6 Water Vapour

Figure 6.28 shows the water vapour for the combustion of 7 % and 21 % oxygen mole fractions. The amount of water vapour produced decreases with λ. This is because the higher supply of the nitrogen in the oxidiser stream acts as a diluent

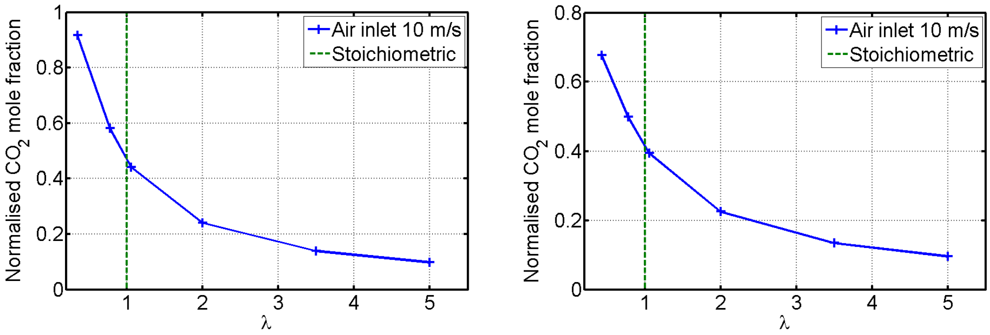

(a) 7 % oxygen (b) 21 % oxygen

Figure 6.24: Carbon dioxide mole fraction in the exhaust normalised by the oxygen mole fraction in the secondary air stream.

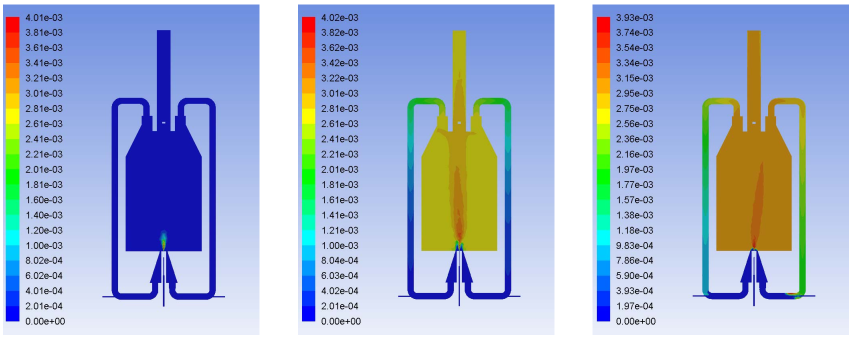

(a) $\lambda = 1.06$ (b) $\lambda = 0.78$ (c) $\lambda = 0.35$

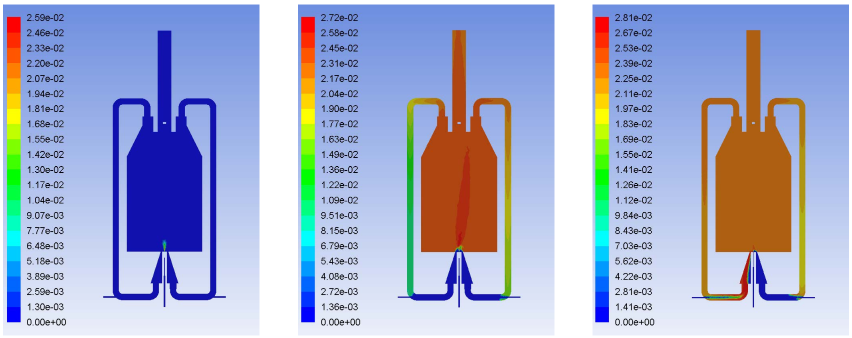

(d) $\lambda = 1.06$ (e) $\lambda = 0.78$ (f) $\lambda = 0.43$

Figure 6.25: Carbon monoxide mole fraction for 10 m/s air supply with 7 % ((a) to (c)) and 21 % ((d) to (f)) oxygen mole fractions.

to reduce the water vapour mole fraction. The water vapour in the exhaust gas for the 21 % oxygen mole fraction is higher than for the 7 % oxygen mole fraction. This is because there is less nitrogen to act as a diluent.

6.6 Summary

The biogas combustion temperature distributions and the combustion products including the exhaust gas emissions of a MILD combustion burner system were

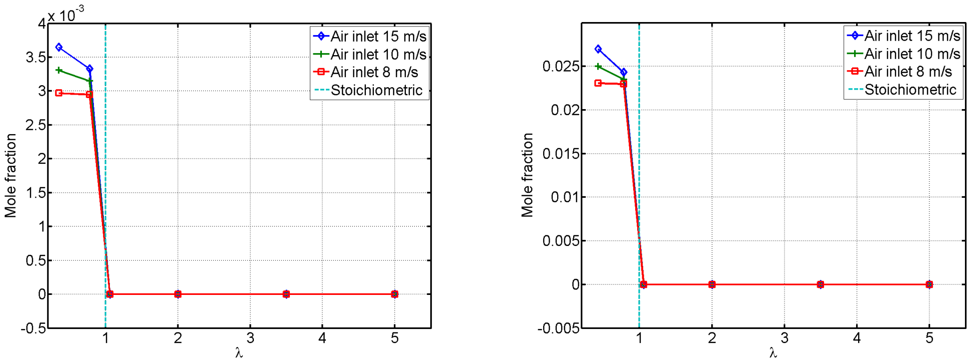

(a) 7 % oxygen (b) 21 % oxygen

Figure 6.26: Pollutant carbon monoxide in exhaust for the air inlet of 7 % and 21 % oxygen mole fractions.

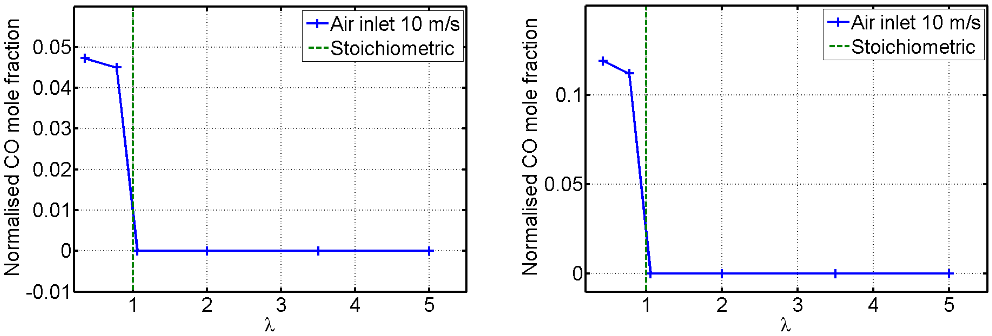

(a) 7 % oxygen (b) 21 % oxygen

Figure 6.27: Carbon monoxide mole fraction in the exhaust normalised by the oxygen mole fraction in the secondary air stream.

numerically investigated. In the present chapter, the air/fuel nozzle was modified from the standard industrial nozzle used in the previous chapter for experimental and numerical modelling. The bluff-body air/fuel nozzle was used to promote the turbulent flow at the area of the air and fuel mixing. The mole fractions of the unburned hydrocarbon, oxygen, oxides of nitrogen, carbon dioxide, carbon monoxide and water vapour were reported for various λ. The higher the air supply volume to the combustion chamber, the higher the flame temperature until it reaches stoichiometric combustion. The chamber temperature distributions were found to be in a small range: between 820 K and 870 K for the synthetic air with 7 % oxygen mole fraction and between 1,150 K and 1,230 K for atmospheric air. The air inlet velocity has no effect on the chamber and air mixing temperatures. The numerical analysis has met the purpose of the study and the final result for the chamber's temperature distribution shows that the objective of MILD combustion was numerically achieved. The rich fuel combustion ($\lambda < 1.0$) resulted in the chemical reaction leaving some amount of unburned hydrocarbon and consumed almost all the oxygen mole fractions. For both 7 % and 21 % oxygen mole fractions, when the λ increased from 1.0 to 5.0 (lean combustion), the unburned

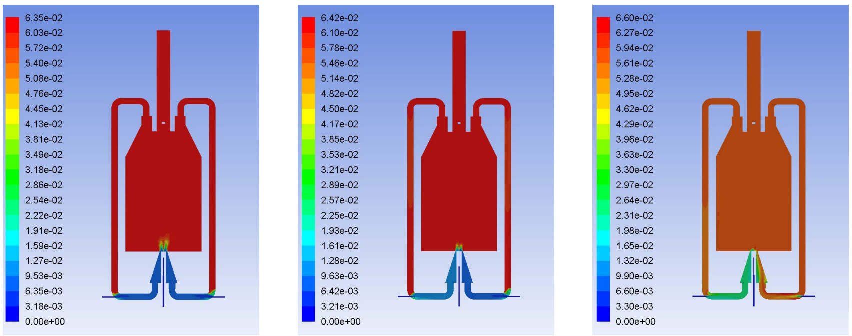

(a) $\lambda = 1.06$ (b) $\lambda = 0.78$ (c) $\lambda = 0.35$

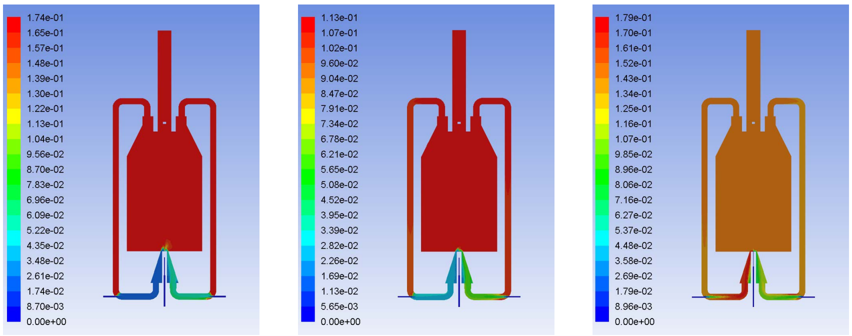

(d) $\lambda = 1.06$ (e) $\lambda = 0.78$ (f) $\lambda = 0.43$

Figure 6.28: Water vapour mole fraction for 10 m/s air supply with 7 % ((a) to (c)) and 21 % ((d) to (f)) oxygen mole fractions.

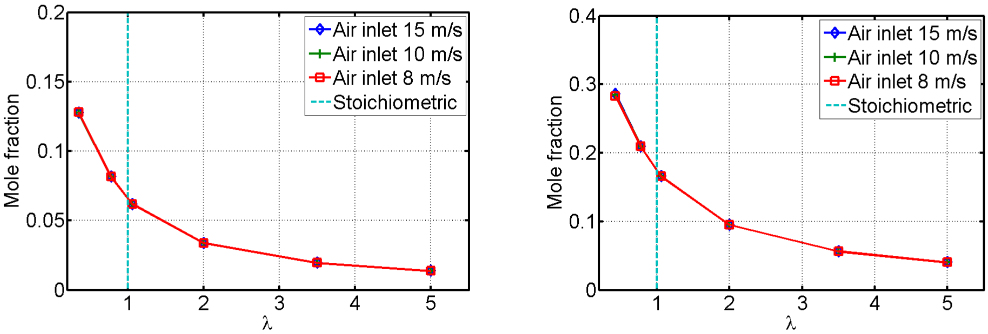

(a) 7 % oxygen (b) 21 % oxygen

Figure 6.29: Water vapour in exhaust for the air inlet of 7 % and 21 % oxygen mole fractions.

hydrocarbon, NO_x, carbon dioxide, water vapour and carbon monoxide were all reduced. Only the excess oxygen is increased due to there being insufficient fuel to consume the supplied oxygen. For both the 7 % and 21 % oxygen mole fractions, when the carbon dioxide mole fraction is normalised by the oxygen mole fraction in the oxidant stream, it shows how much carbon dioxide is produced for each mole of oxygen (filtering out the effects of the extra nitrogen). The case of the 7 % oxygen mole fraction produces more carbon dioxide than the 21 %: more complete combustion occurs, so the combustion efficiency is higher and pollutants are reduced. The use of the synthetic air with a lower oxygen mole fraction gives the additional advantage that it is easier to achieve the MILD combustion regime. This is because oxygen dilution by mixing with the products stream is not necessary if it is already below 13 % oxygen mole fraction in the oxidant stream. The synthetic air also reduced the flame temperature and this lower operational temperature will possibly make the burner last longer.

Chapter 7

Conclusions

Experiments and numerical modelling have been used in this thesis to investigate MILD combustion flame characteristics and the performance of the combustion in an open-end furnace using methane and biogas. The open-end furnace is open at one end with enclosed walls to capture and utilise the heat from the flame and the volume of exhaust gas to be utilised as EGR. The CFD technique was utilised to carry out the parametric studies to design and optimise the combustion chamber. The summary of findings is presented in the following sections along with the recommendations for future work.

7.1 Introduction

MILD combustion for furnaces has been in the combustion research mainstream for many years with significant contributions continuing to be made using both experiments and numerical modelling. Most of the previous MILD combustion research had focused on the closed furnace with internal or external oxygen dilutions and oxidant preheating. The fundamentals of MILD combustion are not fully understood because only limited number of experimental and simulation studies have been conducted in this field. In this study, the development of the experimental test rig was begun using CFD to design and optimise the furnace geometry and air–fuel equivalence ratio. The numerical modelling was conducted using the commercial software ANSYS Fluent. The combustion chamber development started with a basic enclosed wall and open top combustion chamber. Then four external EGR pipes were added. The final model was to improve the top part of the chamber design to ensure it collected the exhaust gas to be utilised as EGR. This model was then fabricated for the experimental testing and also for further numerical modelling with a bluff-body air-fuel nozzle.

7.2 Summary of Findings

The MILD combustion for an open furnace was studied experimentally as well as numerically. The parameters were the fuel composition (methane and biogas), the air–fuel equivalence ratio and the air-fuel nozzle geometry. In this thesis, numerical modelling and an experimental apparatus were developed to study the MILD combustion in an open-end furnace with an enclosed chamber and external EGR to preheat and dilute the secondary supply air. For the case of 15 kPa partially-premixed methane combustion, the preheating temperature is 25 K. After the numerical model was validated by the experimental results, further numerical modelling was conducted for the standard industrial burner and the new bluff-body burner. Both burners were numerically operated in MILD combustion.

7.2.1 Experimental Work

A laboratory scale open-end furnace combustion chamber with external EGR and in-furnace measurement apparatus was designed and fabricated to conduct the experiments and to validate the numerical models. The experimental investigation of the ignition characteristics and the flame behaviour of non-premixed, partially-premixed and premixed combustion were conducted. Each ignition test was repeated at least three times. The ignition studies for non-premixed, partially-premixed and premixed combustion were important to ensure the flames were successfully ignited before the further study of the flame behaviour. The flame and exhaust gas temperatures, exhaust gas species concentrations and chamber wall temperatures were measured. There was no modification required for the furnace to be flexible enough to use either methane or biogas (lower calorific value gas) as its fuel. The methane flow rate was kept constant for both methane and biogas; for biogas, carbon dioxide was added to produce 60% methane and 40% carbon dioxide based on volume. Tests for the ignition were conducted for the methane non-premixed flame, methane partially-premixed flame, methane premixed flame and biogas non-premixed flame. The methane partially-premixed flame with the preheated secondary air supply showed the quickest flame ignition. The biogas is harder to ignite compared to methane which ignited 0.67 seconds after the spark started. Biogas ignited at 3.33 seconds after the spark started.

The chamber temperatures for the case of no combustion process with the exhaust extraction and without the exhaust extraction were measured to study the effect of the exhaust fan on the chamber temperature. The exhaust extraction fan does not significantly affect the chamber and EGR temperatures. The experiment for open and closed observation window number 1 was conducted and found that for the case of window number 1 open, the flame reached a steady state more quickly than with all observation windows closed. The experiments to compare the methane and biogas partially premixed flames were conducted at lean conditions. The flame height for methane and biogas fuel is 34.7 and 18.7 jet diameters downstream of the jet exit respectively. The methane flame is bigger and brighter compared to the biogas flame, while the biogas flame has very low luminosity, is weak and easily reaches flame blow-off. The biogas flame shows only one combustion zone compared to two in methane combustion. The combustion is completed with zero unburned hydrocarbons detected and excess oxygen was recorded for both the exhaust pipe and the downstream of the EGR pipes. The exhaust gas composition at the exhaust pipe consists of a lower oxygen mole fraction compared to the downstream of the EGR pipes. The NO_x emissions for methane and biogas are very low ($< 3\,\text{ppm}$) for both locations. The partially-premixed methane flame temperature is 1,483 K which is 8.6 % higher than the biogas flame temperature.

The methane non-premixed, partially-premixed and premixed combustion were conducted and the flame temperature for partially-premixed is the highest. In all cases, the EGR temperature decreased with distance along the EGR pipe, while the highest recorded wall temperature was at the top of the chamber. The temperatures for both downstream of the EGR and the mixing cone are increased with the increase of the secondary air supply. The effect of the EGR and the heated secondary air on the chamber temperature and exhaust gas was studied. The mixing cone temperature is almost identical compared to the downstream of the EGR. The temperatures for the mixing cone and the downstream of the EGR are increased with the increase of the secondary air supply at each side of the EGR pipes. Unburned hydrocarbon is zero for all cases and it is in line with excess oxygen in the exhaust gas due to lean combustion. The carbon dioxide and NO_x is slightly higher for partially-premixed and almost the same level for the other cases. NO_x is slightly higher for partially-premixed due to the flame being hotter than in the other cases. Carbon monoxide is zero for all the cases.

7.2.2 Numerical Modelling Work

In addition to the experimental work, the three-dimensional CFD for the MILD combustion has been extensively conducted by many researchers for various burners and combustion chambers. In this study, the commercial software ANSYS Fluent (version 14.5) was utilised to develop and optimise the furnace geometry and air-fuel supply ratio. The numerical sensitivity test was conducted and the result shows that the flame temperatures are very sensitive to the combustion chamber wall boundary conditions. In this research, the results of the numerical modelling are slightly over-predicted (2 %) with regards to the flame temperatures compared to the experimental results. Overall, the experimental temperatures and exhaust gas species are in good agreement with the numerical modelling results.

The numerical modelling for the same furnace geometry with the experimental setup shows both methane and biogas fuel achieved the MILD regime when the appropriate parameters were used. Similar results were obtained when further numerical modelling for the experimental furnace with a bluff-body air-fuel nozzle was conducted. The recirculation of the reactant mixing can be achieved by the bluff-body nozzle design. When appropriate oxygen dilution and the oxidant preheating temperature are applied, the open-end furnace can achieve the MILD combustion regime. For the oxygen mole fraction of 21 %, the bluff-body burner can achieve homogeneous temperature in the chamber but the standard industrial burner cannot. The main difference is the bluff-body burner gives the turbulent mixing of the reactants due to the recirculation process. The results obtained from the numerical work are compared and validated with the in-furnace measurements results from the experimental work. Both methane and biogas fuel achieved the desired results. The flame temperature for the numerical modelling for the methane and biogas were over-predicted by 1.13 % and 0.73 % respectively, which is good agreement.

7.3 Contribution of the Study

This research has established new hardware and enhancement of a body of knowledge which advances the understanding of MILD combustion. The open furnace with the effect of external EGR to preheat and dilute the oxidant was studied. The open-end furnace with the enclosed chamber was numerically operated in the MILD combustion regime for both the standard industrial burner and the new bluff-body burner. The chamber temperature distributions were numerically homogeneous. The results of the study are summarised below:

(i) Successfully used the commercial CFD package (ANSYS Fluent version 14.5) to design and optimise the open-end furnace.

(ii) Developed, constructed and commissioned the experimental test rig that has relatively low operating costs. The total volume for the combustion chamber being 0.33 m^3. The gas supplies are methane, carbon dioxide, oxygen and nitrogen and can be mixed to re-produce the low calorific value gas (biogas) and low oxygen mole fraction oxidant (synthetic air).

(iii) Conducted the experimental work for the methane and biogas using various air-fuel equivalence ratios.

(iv) Compared and validated the numerical model with the experimental results. Both chamber temperatures and exhaust gas compositions were in good agreement.

(v) Carried out further numerical modelling using the same furnace geometry except using a bluff-body burner, which successfully achieved the MILD combustion.

Application of the MILD combustion mode to furnace and industrial burners is still in the early stages, thus it is imperative to further study it for industrial applications. The disadvantage of the EGR system is the external recirculation of exhaust gas will required additional external infrastructure to make the EGR system work as required. This external infrastructure will incur a small additional cost but it is believed the overall cost is lower compared to the closed furnace. This is because the thick furnace wall insulation result in higher overall structural cost. The outcomes for this project are:

(i) The combustion of methane and biogas with high thermal efficiency and low environmental pollutants in open furnace MILD combustion has higher advantages compared to it disadvantages. One of the advantages is the EGR that is used to preheat the reactant. Thus the amount of energy that is required to externally preheat the reactants is dramatically reduced, thereby saving on energy costs and increasing the efficiency of the system.

(ii) The fuel can be changed (methane or biogas) without needing any modification of the combustion chamber, burner or gas supply system. This results in a cheaper operational cost and allows flexible operational with respect to the fuel.

(iii) More understanding is required of the requirements for an open-end MILD combustion furnace, the flame behaviours and exhaust gas emissions produced from the methane and biogas combustion.

(iv) The industrial applications for the MILD combustion technique in an open furnace has high potential to reduce industrial heating costs and directly affects the cost of the consumer's end products.

(v) Biogas has an advantage over methane because its lower peak temperature will make the combustion chamber and the burner last longer and be more economical to operate. This is balanced against the weakness of the biogas where it has a lower calorific value.

7.4 Recommendations For Future Work

The MILD regime is a relatively new combustion technology and needs further research before it can be fully utilised in industrial heating. There is still scope for further study to make the open-end furnace MILD combustion more dependable and usable and to present a better understanding of the process considering all the independent parameters that affect the combustion performance characteristics. This section describes some of the proposed issues identified for further research:

(i) The experimental and numerical modelling could be exploited for different air and fuel flow configurations, burner and nozzle geometries and fuel compositions.

(ii) The experimental apparatus can also be used to investigate the flame behaviour of different fuels with EGR without any furnace modification.

(iii) Adding the insulation layer to the chamber wall using refractory bricks to reduce heat losses to the atmosphere and a heating system of the exhaust gases recirculated to increase the temperature of the inlet gases. These two modifications will lead to a large increase of the furnace temperature towards the MILD combustion region.

(iv) The experimental work for a one-inch burner or a bigger size burner would produce higher thermal intensity that could be experimentally tested.

(v) The new range of 2 mm to 10 mm fuel nozzles could be modelled and tested numerically. In addition to the total heat released, the main effect of the nozzle size is the turbulent mixing of air/fuel injected to the combustion chamber.

(vi) The preheating of the secondary oxidant to a higher temperature and analysis of the effect on the combustion performance.

(vii) The experimental and numerical modelling could be carried out for various EGR flow rate to study the effect to the combustion performance.

(viii) To investigate also MILD combustion at least two modifications must be designed and implemented: a substantial internal insulation of the furnace (for example using refractory bricks) and a heating system of the exhaust gases recirculated. While the first will reduce both the furnace volume and the heat loss, the second will increase the temperature of the inlet gases; these two modifications will lead to a large increase in the furnace temperature towards the MILD combustion region.

(ix) The ignition optimisation could be undertaken by the various parameters including the voltage supply, the ignition rod size, the air-fuel equivalence ratio and the air flow through operation.

(x) The instantaneous measurements for the gas velocity and flow field in the combustion chamber using advanced and precise non-intrusive measurement methods. The laser technique is proposed including Laser Doppler Anemometry.

(xi) The feasibility study of systems with a high level of fuel preheating and the possibility to adjust "more independently" the external and internal recirculation.

References

Abd-Alla, G. H., Soliman, H. A., Badr, O. A. and Abd-Rabbo, M. F. 2001, 'Effects of Diluents and Intake Air Temperature in Exhaust Gas Recirculation of an Indirect Injection Dual Fuel Engine', *Energy Conversion and Management* **42**, 1033–1045.

Abtahizadeh, S. E. 2014, 'Numerical Study of MILD Combustion from Laminar Flames to Large Eddy Simulation of Turbulent Flames with Flamelet Generated Manifolds', PhD thesis, Eindhoven University of Technology, The Netherlands.

Abtahizadeh, S. E., van Oijen, J. A. and de Goey, L. P. H. 2012, 'Numerical Study of MILD Combustion with Entrainment of Burned Gas Into Oxidizer and/or Fuel Streams', *Combustion and Flame* **159(6)**, 2155–2165.

Abuelnuor, A. A., Mazlan, A., Wahid, A., Saat, A., Adalla, M. O. and Hosseini, S. E. 2013, 'Pollutant Reduction and Energy Saving in Industrial Sectors by Applying High Temperature Air Combustion Method', *International Journal on Heat and Mass Transfer* **1 (1)**, 121–130.

Abuelnuor, A. A., Wahid, A. M., Saat, A. and Osman, M. 2014, 'Characterization of a Low NOx Flameless Combustion Burner Using Natural Gas', *Jurnal Teknologi* **66(2)**, 121–125.

AET 2012, 'The Formation of NOx', `http://www.alentecinc.com/papers`. Allied Environmental Technologies, Inc, (accessed on 14 Jun 2012).

Afarin, Y. and Tabejamaat, S. 2013, 'Effect of Hydrogen on H2/CH4 Fame Structure of MILD Combustion using the LES Method', *International Journal of Hydrogen Energy* **38**, 3447–3458.

Ahmed, S. F. and Mastorakos, E. 2010, 'Correlation of Spark Ignition with the Local Instantaneous Mixture Fraction in a Turbulent Nonpremixed Methane Jet ', *Combustion Science and Technology* **182**, 1360–1368.

Airliquide 2012, 'Pure Gas Material Safety Data Sheets', `http://airliquide.com.au`. (accessed on 07 Sept 2012).

Allwayzy, S. A., Yusaf, T. and Raed, A. A. 2014, 'Biofuels from Fresh Water Microalgae Chlorella Vulgaris (FWM-CV) for Diesel Engine', *Energies* **7**, 1–25.

Amell, A. 2007, 'Influence of Altitude on the Height of Blue Cone in a Premixed Flame', *Applied Thermal Engineering* **27(2-3)**, 408–412.

Aminian, J., Galletti, C., Shahhosseini, S. and Tognotti, L. 2011, 'Key Modelling Issues in Prediction of Minor Species in Diluted-preheated Combustion Conditions', *Applied Thermal Engineering* **31**, 3287–3300.

Aminian, J., Shahhosseini, S. and Bayat, M. 2012, 'Numerical Investigation of the Application of High Temperature Air Combustion in An Industrial Furnace', *Journal of Power and Energy* **226(5)**, 694–705.

Anunputtikul, W. and Rodtong, S. 2004, 'Laboratory Scale Experiments for Biogas Production from Cassava Tubers', *Asian Journal on Energy and Environment* **8(1)**, 444–453.

Arghode, V. K. 2011, 'Development of Colorless Distributed Combustion for Gas Turbine Aapplication', PhD thesis, University of Maryland, US.

Arghode, V. K. and Gupta, A. K. 2011*a*, 'Development of High Intensity CDC Combustor for Gas Turbine Engine', *Applied Energy* **88**, 963–973.

Arghode, V. K. and Gupta, A. K. 2011*b*, 'Investigation of Forward Flow Distributed Combustion for Gas Turbine Application', *Applied Energy* **88**, 29–40.

Arghode, V. K. and Gupta, A. K. 2013, 'Role of Thermal Intensity on Operational Characteristics of Ultra-low Emission Colorless Distributed Combustion', *Applied Energy* **111**, 930–956.

Arrieta, C. E. and Amell, A. A. 2014, 'Highly Flexible Burner Concept for Research on Combustion Technologies with Recirculation of Hot Combustion Products', *Applied Thermal Engineering* **63**, 559–564.

ASC 2013, 'Australian Combustion Services Furnace Burner', `http://www.combust.com.au`. (accessed on 22 Jun 2013).

Ashrafi, M., Proll, T., Pfeifer, C. and Hofbauer, H. 2008, 'Experimental Study of Model Biogas Catalytic Steam Reforming: Thermodynamic Optimization', *Energy and Fuel* **22**, 4182–4189.

Awosope, I. O., Kandamby, N. H. and Lockwood, F. C. 2006, 'Flameless Oxidation Modelling on Application to Gas Turbine Combustors', *Journal Energy Institute* **79(2)**, 75–83.

Aylward, P. 2014, 'Combustion Experiment Gas Supply Limit', Personal Communication. 22 Mar, USQ Combustion Laboratory.

Balachandran, R. 2005, 'Experimental Investigation of the Response of Turbulent Premixed Flames to Acoustic Oscillations', PhD thesis, University of Cambridge, UK.

Balat, M. and Balat, H. 2009, 'Biogas as a Renewable Energy Source A Review', *Energy Sources, Part A* **31(14)**, 1280–1293.

Baltasar, J., Carvalho, M. G., Coelho, P. and Costa, M. 1997, ‘Flue Gas Recirculation in a Gas-fired Laboratory Furnace’, *Fuel* **76(10)**, 918–929.

Bardina, J. E., Huang, P. G. and Coakley, T. J. 1997, ‘Turbulence Modeling Validation, Testing, and Development’, Technical report, NASA, US.

Baudoin, E. 2010, Large Eddy Simulation of Turbulent Premixed and Partially Premixed Combustion , PhD thesis, Department of Energy Sciences, Lund Institute of Technology.

Baukal, C., Bauk, C. and Schwartz, R. 2001, *The John Zink Combustion Handbook*, CRC Press, Florida, US.

Bilger, R. W. 1980, ‘Turbulent Flows with Non-premixed Reactants’, *in* P. A. Libby and F. A. Williams, eds, ‘Turbulent Reacting Flows’, Vol. 44 of *Topics in Applied Physics*, Springer-Verlag, Berlin, pp. 65–113.

Biogas 2012, ‘Biogas Composition’, `http://www.biogas-renewable-energy.info/biogas_composition.html`. (accessed on 07 Sept 2012).

Bohac, S. V. and Assanis, D. N. 2001, ‘Quantification of Local Ozone Production Attributable to Automobile HC Emissions’, *SAE Technical Paper* **-**, 2001–01–3760.

Borjesson, P. and Mattiasson, P. 2008, ‘Biogas as a Resource Efficient Vehicle Fuel’, *Trends Biotechnol* **26(1)**, 7–13.

Bowman, C. T. 1992, ‘Control of Combustion-generated Nitrogen oxide Emissions: Technology Driven by Regulation’, *Proceedings of the Combustion Institute* **24(1)**, 859–878.

Bozbas, K. 2008, ‘Biodiesel as an Alternative Motor Fuel: Production and Policies in the European Union’, *Renewable and Sustainable Energy Reviews* **12**, 542–552.

BP 1998, ‘BP Gas Oil Safety Data Sheet. Sheet No: SUK2102’, Technical report, BP Oil UK Ltd, Cedigaz, Paris, France.

Burke, M. P., Chen, Z., Ju, Y. and Dryer, F. L. 2009, ‘Effect of Cylindrical Confinement on the Determination of Laminar Flame Speeds using Outwardly Propagating Flames’, *Combustion and Flame* **156**, 771–779.

Burley, N. A., Powell, R. L., Burns, G. W. and Scroger, M. G. 1978, *The Nicrosil vs Nisil Thermocouple: Properties and Thermoelectric Reference Data*, Washington DC, US. NIST Monograph 161.

Burn, G. W., Scroger, M. G., Strouse, G. E., Croarkin, M. C. and Guthrie, W. E. 1993, *Temperature-electromotive Force Reference Functions and Tables for the Letter-designated Thermocouple Type based on the ITS-90*, Washington DC, US. NIST Monograph 175.

Cabra, R., Chen, J. Y., Dibble, R. W., Karpetis, A. N. and Barlow, R. S. 2005, 'Lifted Methane-air Jet Flames in a Vitiated Coflow', *Combustion and Flame* **143(4)**, 491–506.

Cabra, R., Myhrvold, T., Chen, J. Y., Dibble, R. W., Karpetis, A. N. and Barlow, R. S. 2003, 'Simultaneous Laser Raman-Rayleigh-Lif Measurements and Numerical Modeling Results of a Lifted Turbulent H-2/N-2 Jet Flame in a Vitiated Coflow', *Proceedings of the Combustion Institute* **29**, 1881–1888.

Calchetti, G., Nardo, A. D., Mongibello, G. and Mongiello, C. 2007, MILD Combustion Simulation of Coal Water Slurry, *in* '30th Meeting of Italian Section of the Combustion Institute', Ischia, Italy, pp. 1–6.

Cameretti, M. C., Tuccillo, R. and Piazzesi, R. 2013, 'Study of an Exhaust Gas Recirculation Equipped Micro Gas Turbine Supplied with Bio-Fuels', *Applied Thermal Engineering* **59**, 162–173.

Carlson, B. G. and Lathrop, K. D. 1968, *Computing Methods in Reactor Physics*, Gordon and Breach, London, chapter 'Transport Theory The Method of Discrete Ordinates', pp. 171–266.

Cavaliere, A. and de Joannon, M. 2004, 'MILD Combustion', *Progress in Energy and Combustion Science* **30**, 329–366.

Cavaliere, A., de Joannon, M. and Ragucci, R. 2008, *Lean Combustion Technology and Control*, Elsevier, Oxford, UK, chapter 'Highly Preheated Lean Combustion', pp. 55–94.

Cavigiolo, A., Galbiati, M. A., Effugi, A., Gelosa, D. and Rota, R. 2003, 'MILD Combustion in a Laboratory Scale Apparatus', *Combustion Science and Technology* **175**, 1347–1367.

Charest, M. R. J., Groth, C. P. T. and Omer, L. G. 2010, 'A Computational Framework for Predicting Laminar Reactive Flows with Soot Formation', *Combustion Theory and Modelling* **14(6)**, 793–825.

Cheng, H. B. and Wang, L. 2013, *Biomass Now Sustainable Growth and Use*, In-Tech Open, chapter 'Lignocelluloses Feedstock Biorefinery as Petrorefinery Substitutes', pp. 347–388.

Choi, C. E. and Baek, S. W. 1996, 'Numerical Analysis of Spray Combustion with Nongray Radiation using Weight Sum of Gray Gas Models', *Combustion Science and Technology* **115**, 297–315.

Choi, G. M. and Katsuki, M. 2001, 'Advanced Low NOx Combustion Using Highly Preheated Air', *Energy Conversion and Management* **42(5)**, 639–652.

Christo, F. C. and Dally, B. B. 2005, 'Modelling Turbulent Reacting Jets Issuing Into a Hot and Diluted Coflow', *Combustion and Flame* **142(1-2)**, 117–129.

Chui, E. H. and Raithby, G. D. 1993, 'Computation of Radiant Heat Transfer on a Non-Orthogonal Mesh Using the Finite-Volume Method', *Numerical Heat Transfer B* **23**, 269–288.

Clementson, M. 2007, 'Biogas Basic Data - Sweden', Swedish Gas Center.

CODA 2012, 'Gas Analyser', `http://www.coda.com.au`. (accessed on 22 May 2012).

Colebrook, C. F. 1939, 'Turbulent Flow in Pipes, with Particular Reference to The Transition Region Between Smooth and Rough Pipe Laws', *Journal of the Institution of Civil Engineers* **11(4)**, 133–156.

Colorado, A. F., Herrera, B. A. and Amell, A. A. 2010, 'Performance of a Flameless Combustion Furnace using Biogas and Natural Gas', *Bioresource Technology* **101(7)**, 2443–2449.

Colorado, A. F., Medwell, P. R. and Dally, B. B. 2009, LCV Fuels Emissions of Turbulent Nonpremixed Jet Flames Under MILD Combustion Conditions, *in* 'Australian Combustion Symposium', UQ, Australia, pp. 43–46.

Dai, W., Qin, C., Chen, Z., Tong, C. and Liu, P. 2012, 'Experimental Studies of Flame Stability Limits of Biogas Flame', *Energy Conversion and Management* **63**, 157–161.

Dally, B. B., Craig, R. A. and Mi, J. C. 2008, Dependence of Flameless Combustion on Fuel-air Injection Pattern and Their Momentum Ratio in a Recuperative Furnace, *in* 'Ninth Asia-Pacific International Symposium on Combustion and Energy Utilization', Wuhan, China, pp. 35–40.

Dally, B. B., Fletcher, D. F. and Masri, A. R. 1998, 'Flow and Mixing Fields of Turbulent Bluff-Body Jets and Flames', *Combustion Theory and Modeling* **2**, 193–219.

Dally, B. B., Karpetis, A. N. and Barlow, R. S. 2002, 'Structure of Turbulent Non-premixed Jet Flames in a Diluted Hot Coflow', *Proceedings of the Combustion Institute* **29(1)**, 1147–1154.

Dally, B. B. and Peters, N. 2002, Effect of Fuel Mixture on MILD Combustion, *in* 'Work done during sabbatical at ITM'.

Dally, B. B. and Peters, N. 2007, Heat Loss-induced Oscillation of Methane and Ethylene in a Perfectly Stirred Reactor, *in* 'Sixth Asia-Pacific Conference on Combustion', Nagoya, Japan, pp. 227–230.

Dally, B. B., Riesmeier, E. and Peters, N. 2004, 'Effect of Fuel Mixture on Moderate and Intense Low Oxygen Dilution Combustion', *Combustion and Flame* **137(4)**, 418–431.

Dally, B. B., Shim, S. H., Craig, R. A., Ashman, P. J. and Szegö, G. G. 2010, 'On the Burning of Sawdust in a MILD Combustion Furnace', *Energy and Fuel* **24**, 3462–3470.

Danon, B. 2011, 'Furnaces with Multiple Flameless Combustion Burners', PhD thesis, Delft University of Technology, Netherlands.

Danon, B., Jong, W. D. and Roekaerts, D. J. E. M. 2010, 'Experimental and Numerical Investigation of a FLOX Combustor Firing Low Calorific Value Gases', *Combustion Science and Technology* **182(9)**, 1261–1278.

Davidson, D. L. 2002, 'The Role of Computational Fluid Dynamics in Process Industries', *The Bridge* **32(4)**, 9–14.

de Joannon, M., Sabia, P. and Cavaliere, A. 2010, *Vol 5: New Technologies*, Wiley-VCH, chapter 'MILD Combustion in Handbook of Combustion', pp. 237–256.

de Joannon, M., Sorrentino, G. and Cavaliere, A. 2012, 'MILD Combustion in Diffusion-Controlled Regimes of Hot Diluted Fuel', *Combustion and Flame* **159**, 1832–1839.

Demirel, Y. 2012, *Energy, Green Energy and Technology*, Springer-Verlag London, UK.

Derudi, M. and Rota, R. 2011, 'Experimental Study of the MILD Combustion of Liquid Hydrocarbons', *Proceedings of the Combustion Institute* **33**, 3325–3332.

Derudi, M., Villani, A. and Rota, R. 2007*a*, 'MILD Combustion of Industrial Hydrogen-containing by Product', *Industrial & Engineering Chemical Research* **46(21)**, 6806–6811.

Derudi, M., Villani, A. and Rota, R. 2007*b*, 'Sustainability of MILD Combustion of Hydrogen Containing Hybrid Fuels', *Proceedings of the Combustion Institute* **31(2)**, 3393–3400.

Derudi, M., Villani, A. and Rota, R. 2007*c*, The Influence of Operating Parameters on MILD Combustion Sustainability, *in* 'Proceedings of the 30th Meeting of the Italian Section of the Combustion Institute'.

Devi, R., Saxena, P., Walter, B., Record, B. and Rajendran, V. 2004, 'Pressure Reduction in Intake System of a Turbocharged-Intercooled di DI Diesel Eengine using CFD Merthodology', *SAE Technical Paper* **-**, 2004–01–1874.

Duwig, C., Stankovie, D., Fuchs, L., Li, G. and Gutmark, E. 2008, 'Experimental and Numerical Study of Flameless Combustion in a Model Gas Turbine Combuster', *Combustion Science and Technology* **180(2)**, 279–295.

Dwyer, I. 2013, 'Gas Conversion', `www.dwyer-inst.com`. (accessed on 22 Feb 2013).

Echekki, T. and Chen, J. H. 2003, 'Direct Numerical Simulation of Autoignition in Nonhomogeneous Hydrogen-Air Mixtures', *Combustion and Flame* **134**, 169–191.

Edmund 2012, ‘High Temperature Glass’, `www.edmundoptics.com`. (accessed on 22 April 2012).

Effugi, A., Gelosa, D., Derudi, M. and Rota, R. 2008, ‘MILD Combustion of Methane-derived Fuel Mixtures Natural Gas and Biogas’, *Combustion Science and Technology* **180(3)**, 481–493.

Ersahin, M. E., Gomec, C. Y., Dereli, R. K., Arikan, O. and Ozturk, I. 2011, ‘Biomethane Production as an Alternative Bioenergy Source from Codigesters Treating Municipal Sludge and Organic Fraction of Municipal Solid Wastes’, *Journal of Biomedicine and Biotechnology* **2011(953065)**, 1–8.

Ertesvag, I. S. and Magnussen, B. F. 2000, ‘The Eddy Dissipation Turbulence Energy Cascade Model’, *Combustion Science and Technology* **159**, 213–235.

Esquiva, D. I., Nguyen, H. T. and Escudie, D. 2001, ‘Influence of Bluff-body Shape on the Stabilization Regime of Non-premixed Flame’, *Combustion and Flame* **127**, 2167–2180.

Evans, M. J., Tian, Z. F. and Medwell, P. R. 2013, Modelling Ethylene-Hydrogen Jet Flames in the MILD Combustion Regime, *in* ‘20th International Congress on Modelling and Simulation’, Adelaide, Australia, pp. 1554–1560.

Farnam 2012, ‘Flow Torch FT200’, `http://www.farnam-custom.com`. (accessed on 22 Sept 2012).

Fawaz, A. D. A., Dearden, L. M., Hedley, J. T., Missaghi, M., Pourkashanian, M., Williams, A. and Yap, L. T. 1994, ‘NOx Formation in Geometrically Scaled Gas-fired Industrial Burners’, *Proceedings of the Combustion Institute* **25**, 1027–1034.

Fei, L. P. and Mi, J. C. 2011, ‘Influence of Inlet Dilution of Reactants on Premixed Combustion in a Recurative Furnace’, *Flow, Turbulence and Combustion* **87**, 617–638.

Ferziger, J. and Peric, M. 1999, *Computational Methods for Fluids Dynamics*, Springer Verlag, Berlin.

Fiveland, W. A. 1984, ‘Discrete-Ordinates Solutions of the Radiative Transport Equation for Rectangular Enclosures’, *Journal of Heat Transfer* **106**, 699–706.

Fleck, B., Sobiesiak, A. and Becker, H. 2000, ‘Experimental and Numerical Investigation of the Novel Low NOx CGRI Burner’, *Combustion Science and Technology* **161(1-6)**, 89–112.

Fluent 2006, *FLUENT 6.3 User’s Guide*, FLUENT Inc., New Hampshire, US.

Fluent 2010, *ANSYS FLUENT 13.0 User’s Guide*, ANSYS Inc., Pennsylvania, US.

Fluent 2012, *ANSYS FLUENT 14.5 User's Guide*, ANSYS Inc., Pennsylvania, US.

Frisch, U. 1995, *Turbulence: The Legacy of A.N. Kolmogorov*, Cambridge University Press, UK.

Fuse, R., Kobayashi, H., Ju, Y., Maruta, K. and Niioka, T. 2002, 'NOx Emission from High-Temperature Air/Methane Counter Flow Diffusion Flame', *International Journal of Thermal Sciences* **41**, 693–698.

Galletti, C., Parente, A., Darudi, M., Rota, R. and Tognotti, L. 2009, 'Numerical and Experimental Analysis of NO Emissions from a Lab-Scale Burner Fed with Hydrogen-Enriched Fuels and Operating in MILD Combustion', *International Journal of Hydrogen Energy* **34(19)**, 8339–8351.

Galletti, C., Parente, A. and Tognotti, L. 2007, 'Numerical and Experimental Investigation of a MILD Combution Burner', *Combustion and Flame* **151(4)**, 649–664.

Ganesan, V., Kumar, J. S. and Balasubramanian, V. 2004, 'Flow Field Analysis of a Multi Cylinder SI Engine Air Intake System Using CFD', *SAE Technical Paper* **-**, 2004–28–0010.

GeoTech 2012, 'Gas Analysers ', `http://www.geotechuk.com`. (accessed on 07 April 2012).

Glassman, I. and Yelter, R. A. 2008, *Combustion*, 4th edn, Academic Press, Massachusetts, US.

GM 2011, 'Chemical Safety Data Sheet', Technical report, Gas Malaysia.

Goldstein, R. J., Chen, P. H. and Chiang, H. D. 1998, *Handbook of Heat Transfer*, McGraw-Hill, chapter Measurement of Temperature and Heat Transfer.

Gonzalez, C. D., Arrieta, A. A. and Suarez, J. L. 2009, 'Comparison of Combustion Properties of Simulated Biogas and Methane', *Ciencia, Tecnologia y Futuro* **3(5)**, 225–236.

Graca, M., Duarte, A., Coelho, P. J. and Costa, M. 2013, 'Numerical Simulation of a Reversed Flow Small-scale Combustor', *Fuel Processing Technology* **107**, 126–137.

Griffiths, J. F. and Barnard, J. A. 1985, *Flame and Combustion*, 3rd edn, Chapman and Hall, Glasgow.

Gupta, A. 2004, 'Thermal Characteristics of Gaseous Fuel Flames Using High Temperature air', *Journal of Engineering for Gas Turbines and Power* **126(1)**, 9–19.

Gupta, A. K., Bolz, S. and Hasegawa, T. 1999, 'Effect of Air Preheat Temperature and Oxygen Concentration on Flame Structure and Emission', *Journal of Energy Resources Technology* **121**, 209–216.

Haaland, S. E. 1983, ‘Simple and Explicit Formulas for the Friction Factor in Turbulent Flow’, *Journal of Fluids Engineering (ASME)* **105(1)**, 89–90.

Hairuddin, A. A., Yusaf, T. and Wandel, A. P. 2014, ‘A Review of Hydrogen and Natural Gas Addition in Diesel HCCI Engines’, *Renewable and Sustainable Energy Review* **32**, 739–761.

Hamdi, M. and Hmaeid, B. 2012, ‘Influence of Turbulent Mixing Intensity on the MILD Combustion and The Pollutant Formation’, *International Journal of Energy and Environmental Engineering* **3(22)**, 1–6.

Hasan, A. K. 2013, ‘Investigation of Colorless Distributed Combustion (CDC) with Swirl for Gas Turbine Application’, PhD thesis, University of Maryland, US.

Hasegawa, T., Mochida, S. and Gupta, A. K. 2002, ‘Development of Advanced Industrial Furnace Using Highly Preheated Air Combustion’, *Journal fo Propulsion Power* **18 (2)**, 233–239.

Haworth, D. C. 2010, ‘Progress in Probability Density Function Methods for Turbulent Reacting Flows’, *Progress in Energy and Combustion Science* **36(2)**, 168–269.

He, Y. 2008, ‘Flameless Combustion of Natural Gas in the SJ/WJ Furnace’, PhD thesis, Queens University, Ontario, Canada.

He, Y., Matovic, M. D. and Grandmaison, E. W. 2006, The Investigation of Mixing Patterns in a Model Flameless Combustion System, *in* ‘Spring Technical Meeting of the Canadian Section of the Combustion Institute’, University of Waterloo, Ontario, Canada, pp. 1–10.

Heitor, M. V. and Moreira, A. L. N. 1993, ‘Thermocouples and Sample Probes for Combustion Studies’, *Progress Energy Combustion Science* **19**, 259–278.

Heskestad, G. 1983, ‘Luminous Flame Heights of Turbulent Diffusion Flames’, *Fire SafetyJournal* **5**, 103–108.

Heywood, J. B. 1988, *Internal Combustion Engine Fundamentals*, McGraw-Hill Series in Mechanical Engineering, McGraw Hill, New York.

Hini, Y., Zhang, C. and Ishii, T. 1998, Comparison of Measurements and Predictions of Flame Structure and NOx Emissions in a Gas-Fired Furnace, *in* ‘AIAA/ASME Joint Thermophysics and Heat Transfer Conference, Albuquerque, New Mexico, USA’, Albuquerque, New Mexico, US.

HMC 2012, ‘Hoskins Manufacturing Co. - Thermocouple Type K - Cromel - Alumel’, `http://graphicsdept.com`. (accessed on 10 Aug 2012).

Hosseini, S. E. and Wahid, M. A. 2013, ‘Biogas Utilization: Experimental Investigation on Biogas Flameless Combustion in Lab-scale Furnace’, *Energy Conversion and Management* **74**, 426–432.

Hosseini, S. E. and Wahid, M. A. 2014, ‘Enhancement of Exergy Efficiency in Combustion Systems Using Flameless Mode’, *Energy, Combustion and Management* **86**, 1154–1163.

Hosseini, S. E., Wahid, M. A. and Abuelnuor, A. A. 2013, ‘Biogas Flameless Combustion: A Review’, *Applied Mechanics and Materials* **388**, 273–279.

Hottel, H. C. and Sarofim, A. F. 1967, *Radiative Transfer*, McGraw-Hill, New York.

Hountalas, D. T., Mavropoulos, G. C. and Binder, K. B. 2008, ‘Effect of Exhaust Gas Recirculation (EGR) Temperature for Various EGR Rates on Heavy Duty DI Diesel Performance and Emissions’, *Energy* **33**, 272–283.

Huang, M., Zhang, Z., Shao, W., Xiong, Y., Liu, Y., Lei, F. and Xiao, Y. 2014, ‘Effect of Air Preheat Temperature on the MILD Combustion of Syngas’, *Energy Conversion and Management* **86**, 356–364.

Hussen, A. S. 2014, ‘Microalgae Biofuels for Diesel Engines in Agricultural Applications’, PhD thesis, USQ, Australia.

IEA 2002, *IEA/OECD 2002 Carbon Dioxide Emissions from Fuel Combustion: 1971-2000, Organisation for Economic Cooperation and Development, World Energy Outlook (WEO)*, International Energy Agency, Paris, Paris, France.

IEA 2006, *World Energy Outlook (WEO), Organisation for Economic Cooperation and Development*, International Energy Agency, Paris, France.

Iorio, S. D. 2014, ‘Experimental Investigation on the Combustion Process in a Spark Ignition Optically Accessible Engine Fueled with Methane/Hydrogen Blends’, *International Journal of Hydrogen Energy* **39(18)**, 1–15.

ISA 1982, ‘American National Standard for Temperature Measurement Thermocouples’. ANSI-MC96-1-1982, Instrument Society of America.

Ishii, T., Zhang, C. and Sugijama, S. 1997, Numerical Analysis of NOx Formation Rate in a Regenerative Furnace, *in* ‘Joint Power Generation Conference’, Colorado, US.

Joachim, V. S. 2012, *Energy Efficiency*, In-Tech, chapter ‘Oxyfuel Combustion in the Steel Industry: Energy Efficiency and Decrease of CO_2 Emissions’.

Jonathan, P. 2006, Responses to Questions on the Design Elements of a Mandatory Market-Based Greenhouse Gas Regulatory System, Technical report, World Resources Institute, Washington, US.

Katsuki, M. and Hasegawa, T. 1998, ‘The Science and Technology of Combustion in Highly Preheated Air’, *Proceedings of the Combustion Institute* **27(2)**, 3135–3146.

Keramiotis, C. and Founti, M. A. 2013, ‘An Experimental Investigation of Stability and Operation of a Biogas Fueled Porous Burner’, *Fuel* **103**, 278–284.

Kevin, A. B., Timothy, H. and Jonathan, P. 2005, *Navigating the Numbers Greenhouse Gas Data and International Climate Policy*, World Resources Institute, Washington, US.

Khalil, A. E. E., Arghode, V. K. and Gupta, A. K. 2013, ‘Novel Mixing for Ultra-high Thermal Intensity Distributed Combustion’, *Applied Energy* **105**, 327–334.

Klimenko, A. Y. and Bilger, R. W. 1999, ‘Conditional Moment Closure for Turbulent Combustion’, *Progress of Energy and Combustion Sciences* **25**, 595–687.

Klimenko, A. Y. and Pope, S. B. 2003, ‘A Model for Turbulent Reactive Flows Based on Multiple Mapping Conditioning’, *Physics of Fluids* **15**(7), 1907–1925.

Kobayashi, H., Oono, K., Cho, E.-S., Hagiwara, H., Ogami, Y. and Niioka, T. 2005, ‘Effects of Turbulence on Flame Structure and NOx Emission of Turbulent Jet Non-premixed Flames in High-temperature Air Combustion’, *JSME International Journal* **48(2)**, 286–292.

Kong, S. C. and Reitz, R. D. 2002, ‘Application of Detailed Chemistry and CFD for Predicting Direct Injection HCCI Engine Combustion and Emissions’, *Proceedings of the Combustion Institute* **29**, 663–669.

Kraus, B. J. and Barraclough, S. 2012, ‘New Configuration May Make it Harder to Say No to Thermal Regeneration’, *Industrial Heating* **90(1)**, 24–27.

Kumar, S., Paul, P. J. and Mukunda, H. S. 2007, ‘Prediction of Flame Liftoff Height of Diffusion/partially Premixed Jet Flames and Modeling of Mild Combustion Burners’, *Combustion Science and Technology* **179(10)**, 2219–2253.

Kumar, S., Paul, P. and Mukunda, H. S. 2005, ‘Investigations of the Scaling Criteria for a MILD Combustion Burner’, *Proceedings of the Combustion Institute* **30(2)**, 2613–2621.

Kutz, M. 2006, *Mechanical Engineers Handbook - Energy and Power*, John Wiley & Sons, New Jersey, US.

Labeckas, G. and Slavinskas, S. 2006, ‘The Effect of Rapeseed Oil Methyl Ester on Direct Injection Diesel Engine Performance and Exhaust Emissions’, *Energy Conversion and Management* **47**, 1954–1967.

Lackner, M., Winter, F. and Agarwal, A. K., eds 2010, *Handbook of Combustion: Vol. 5: New Technology*, Wiley-VCH Verlag GmBH & Co.

Lammel, O., Schutz, H., Schmitz, G., Luckerath, R., Stohr, M., Noll, B., Aigner, M., Hase, M. and Krebs, W. 2010, ‘FLOX Combustion at High Power Density and High Flame Temperatures’, *Journal of Engineering Gas Turbine and Power* **132**, 121503–1 – 121503–10.

Lamont, P. A. 1981, 'Common Pipe Flow Formulas Compared with the Theory of Roughness', *Journal of the American Water Works Association* **73(5)**, 274–280.

Launder, B. E. and Spalding, D. B. 1974, 'The Numerical Computation of Turbulent Flows', *Computaional Methed Applied Mechanical Engineering* **3**, 269–289.

Lee, K. W. and Choi, D. H. 2009, 'Analysis of NOx Formation in High Temperature Diluted Air Combustion in a Coaxial Jet Flame using an Unsteady Flamelet Model', *International Journal of Heat and Mass Transfer* **52**, 1412–1420.

Lefebvre, A. H. and Balla, D. R. 2010, *Gas Turbine Combustion, Alternative Fuels and Emissions*, 3rd edn, CRC Press, Taylor and Francis Group, New York.

Li, M., Rao, A., Brouwer, J. and Scout, S. G. 2010, 'Design of Highly Efficient Coal Based IGFC Power Plant', *Journal of Power Source* **195(17)**, 5707–5718.

Li, P. F., Mi, J. C., Dally, B. B., Wang, F. F., Wang, L., Liu, Z. H., Chen, S. and Zheng, C. G. 2011, 'Progress and Recent Trend in MILD Combution', *Science China Technology Sciences* **54**, 255–269.

Li, P., Wang, F., Tu, Y., Mei, Z., Zhang, J., Zheng, Y., Liu, H., Liu, Z., Mi, J. and Zheng, C. 2014, 'MILD Oxy-Combustion Characteristics of Light-Oil and Pulverized-Coal in a Pilot-Scale Furnace', *Energy and Fuel* **-**, 1–28.

Libby, P. A. 1996, *Introduction to Turbulence*, Taylor and Francis, Bristol PA.

Ling, J. and Tun, L. T. Y. 2006, 'CFD Analysis of Non-Symmetrical Intake Manifold for Formula SAE Car', *SAE Technical Paper* **-**, 2006–01–1976.

Liu, F., Becker, H. A. and Bindar, Y. 1998, 'A Comprehensive Study of Radiactive Heat Transfer Modelling in Gas Fire Furnace using the Simple Gray Gas and the Weight Sum of Gray Gas Models', *International Journal of Heat and Mass Transfer* **41**, 3357–3371.

Liu, X. and Zheng, H. 2013, 'Numerical Simulation of Air Inlet Conditions Influence on the Establishment of MILD Combustion in Stagnation Point Reverse Flow Combustor', *Mathematical Problems in Engineering* **2013-593601**, 1–9.

Lloyd, S. A. and Weinberg, F. J. 1974, 'A Burner for Mixtures of Very Low Heat Content', *Nature* **251**, 47–49.

Lloyd, S. A. and Weinberg, F. J. 1975, 'Limits to Energy Release and Utilisation from Chemical Fuels', *Nature* **257**, 367–370.

Luostarinen, S., Luste, S. and Sillanpaa, M. 2009, 'Increased Biogas Production at Wastewater Treatment Plants Through Co-Digestion of Sewage Sludge with Grease Trap Sludge from a Meat Processing Plant', *Bioresource Technology* **100**, 79–85.

Lupant, D., Pesenti, B., Evrard, P. and Lybaert, P. 2007, 'Numerical and Experimental Characterization of a Self-regenerative Flameless Oxidation Burner Operation in a Pilot-scale Furnace', *Combustion Science and Technology* **179(1)**, 437–453.

Maczulak, A. 2010, *Renewable Energy, Sources and Methods*, FF Inc., New York, US.

Mamat, R. 2009, 'Performance and Emission Characteristics of an Automotive Diesel Engine Using Biodiesel Fuel with the Influence of Air Intake Variables', PhD thesis, University of Birmingham, UK.

Mancini, M., Weber, R. and Bollettini, U. 2003, 'Predicting NOx Emissions of a Burner Operated in a Flameless Oxidation Mode', *Proceedings of the Combustion Institute* **29**, 1155–1163.

Maraseni, T. N. and Maroulis, J. 2008, 'Piggery: From Environmental Pollution to a Climate Change Solution', *J Environ Sci Health, Part B Pesticides, Food Contaminants, and Agricultural Waste* **43**, 358–363.

Mardani, A., Tabejamaat, S. and Ghamari, M. 2010, 'Numerical Study of Influence of Molecular Diffusion in the MILD Combution Regime', *Combustion Theory and Modelling* **14**, 747–774.

Mardani, A., Tabejamaat, S. and Mohammadi, M. B. 2011, 'Numerical Study of the Effect of Turbulence on Rate of Reactions in the MILD Combustion Regime', *Combustion Theory and Modelling* **15(6)**, 753–772.

Maruta, K., Muso, K., Takeda, K. and Niioka, T. 2000, 'Reaction Zone Structure in Flameless Combustion', *Proceedings of the Combustion Institute* **28**, 2117–2123.

Mastorakos, E. 2009, 'Ignition of Turbulent Non-premixed Flames', *Progress in Energy and Combustion Science* **35**, 57–97.

Mastorakos, E., Cruz, A. P. D., Baritaud, T. A. and Poinsot, T. J. 1997, 'A Model for the Effects of Mixing on the Autoignition of Turbulent Flows', *Combustion Science and Technology 1997;125:24382.* **125**, 243–282.

Mastrangelo, G., Fadda, E. and Marzia, V. 1996, 'Polycyclic Aromatic Hydrocarbons and Cancer in Man', *Environment Health Perspectives* **104**, 1166–1170.

MATLAB 2014, 'Image and and Video Processing Solutions', `http://www.mathworks.com.au/image-video-processing`. (accessed on 22 Jan 2014).

McAllister, S., Chen, J. Y. and Fernandez-Pello, A. C. 2011, *Fundamentals of Combustion Processes*, Springer Science and Business Media, New York, US.

McCabe, B. 2012, Monitoring the Performance of Anaerobic Ponds in the Treatment of Abattoir Wastewater, *in* 'MINTRAC QLD Environment Network', Churchill, Queensland, Australia, pp. 1–6.

McCabe, B. and Baillie, C. 2012, Assessing the Performance of Covered Anaerobic Ponds at Churchill Abattoir, *in* 'MINTRAC National Environment Conference', Melbourne, Australia, pp. 1–11.

McCabe, B. K., Hamawand, I., Harris, P., Baillie, C. and Yusaf, T. 2014, 'A Case Study for Biogas Generation from covered Anaerobic Ponds Treating Abattoir Wastewater: Investigation of Pond Performance and Potential Biogas Production', *Applied Energy* **114**, 798–808.

Medwell, P. R. 2007, 'A Laser Diagnostic on MILD Combustion', PhD thesis, University of Adelaide, Australia.

Medwell, P. R., Kalt, P. A. M. and Dally, B. B. 2007, 'Simultaneous Imaging of OH Formalehyde and Temperature of Turbulent Non-premixed Jet Flames in a Heated and Diluted Co-flow', *Combustion and Flame* **148(1-2)**, 48–61.

Medwell, P. R., Kalt, P. A. M. and Dally, B. B. 2008, 'Imaging of Diluted Turbulent Ethylene Flames Stabilised on a Jet in Hot Coflow (JHC) Burner', *Combustion and Flame* **152(1-2)**, 100–113.

Merci, B., Naud, B. and Roekaerts, D. 2007, 'Impact of Turbulent Flow and Mean Mixture Fraction Results on Mixing Model Behavior in Transported Scalar PDF Simulations of Turbulent Non-Premixed Bluff Body Flames', *Flow, Turbulence and Combustion* **79**, 41–53.

Mi, J. C., Li, P. F. and Zheng, G. G. 2010, 'Numerical Simulations of Flameless Premixed Combustion in a Recuperative Furnace', *China Journal Chem Engineering* **18(1)**, 10–17.

Michael, L., Munk, B. and Effenberger, M. 2014, 'Agricultural Biogas Production in Germany - From Practice to Microbiology Basics', *Energy, Sustainability and Society* **4**(1), 1–21.

Milani, A. and Wünning, J. G. 2007, 'Flameless Oxidation Technology', *Advanced Combustion and Aerothermal Technologies* **6**, 343–352.

Minamoto, Y., Dunstan, T. D., Swaminathan, N. and Cant, R. S. 2013, 'DNS of EGR-type Turbulent Fame in MILD Condition', *Proceedings of the Combustion Institute* **34**, 3231–3238.

Mingming, H., Zhang, Z., Xiong, Y., Lei, F. and Xiao, Y. 2014, 'MILD Combustion for Hydrogen and Syngas at Elevated Pressures', *Journal of Thermal Science* **23(1)**, 96–102.

Mollica, E., Giacomazzi, E. and Marco, A. D. 2010, RANS based Numerical Study of Hydrogen MILD Combustion, *in* '5th European Conference on Computational Fluid Dynamics', Lisbon, Portugal, pp. 1–20.

Mörtberg, M., Blasiak, W. and Gupta, A. K. 2006, 'Combustion of Normal and Low Calorific Fuels in High Temperature and Oxygen Deficient Environment', *Combustion Science and Technology* **178(7)**, 1345–1372.

MoTeC 2013, 'Lambda Meter', `http://www.capa.com.au`. (accessed on 22 Sept 2013).

Mullinger, P. and Jenkins, B. 2008, *Industrial and Process Furnaces: Principles, Design and Operation*, Elsevier, Oxford, UK.

Muradov, N., Smith, F. and Raissi, A. T. 2008, 'Hydrogen Production by Catalytic Processing of Renewable Methane-rich Gases', *International Journal of Hydrogen Energy* **33**, 2023–2035.

Najafi, G., Ghobadian, B. and Yusaf, T. F. 2011, Biofuel from Microalgae: Alternative, Sustainable and Renewable Fuel, *in* '10th International Conference on Sustainable Energy Technologies', Istanbul, Turki, pp. 1–5.

Nakamura, K., Takayanagi, T. and Sato, S. 1989, 'A Modified Arrhenius Equation', *Chemical Physics Letters* **160**(3), 295 – 298.

Nakamura, T., Smart, J. P. and de Kamp, W. L. V. 1993, 'The Effect of Fuel Air Mixing on NOx Reduction and Heat Transfer in High Temperature Gas Fired Glass Melting Furnaces', *Combustion and Emissions Control* **-**, 213–230.

Nakhla, G., AlSabawi, M., Bassi, A. and Liu, V. 2003, 'Anaerobic Treatability of High Oil and Grease Rendering Wastewater', *Journal of Hazard Material* **102**, 243–255.

NAMC 1952, *North American Combustion Handbook*, NA Combustion Association.

Nathan, G. J., Luxton, R. E. and Smart, J. P. 1992, 'Reduced NOx Emissions and Enhanced Large Scale Turbulence from a Precessing Jet Burner', *Proceedings of the Combustion Institute* **24**, 1399–1405. Comb Institute, Sydney, Australia.

Nathan, S. S., Mallikarjuna, J. M. and Ramesh, A. 2010, 'An Experimental Study of the Biogas-Diesel HCCI Mode of Engine Operation', *Energy Conversion and Management* **51**, 1347–1353.

Neophytou, A., Richardson, E. S. and Mastorakos, E. 2012, 'Spark Ignition of Turbulent Recirculating Non-Premixed Gas and Spray Flames: A Model for Predicting Ignition Probability', *Combustion and Flame* **159**, 1503–1522.

NI 2012*a*, 'National Instrument', `http://www.australia.ni.com`. (accessed on 22 Mar 2012).

NI 2012*b*, *Operating Instructions and Specifications: NI 9213*, National Instruments.

Nielsen, A. B., ed. 2009, *Biogas - Green Energy*, PlanEnergi.

Nikon 2013, 'Nikon DSLR D7100 and AF-S DX NIKKOR 18-200 mm f3.5-5.6G ED VRII Lenses', `http://www.nikon.com.au`. (accessed on 22 Mar 2013).

NIST 2009, 'NIST Chemistry WebBook: Thermophysical Properties of Fluid Systems', `http://webbook.nist.gov/chemistry/`.

Noor, M. M., Wandel, A. P. and Yusaf, T. 2012*a*, 'A Review of MILD Combustion and Open Furnace Design Consideration', *International Journal of Automotive and Mechanical Engineering* **6**, 730–754.

Noor, M. M., Wandel, A. P. and Yusaf, T. 2012*b*, 'A Review of MILD Combustion and Open Furnace Design Consideration', *International Journal of Automotive and Mechanical Engineering* **6**, 730–754.

Noor, M. M., Wandel, A. P. and Yusaf, T. 2013, The Effect of Fuel and Air Injection Velocity on Biogas Ignition of Bluff-body MILD Burner, *in* 'International Conference of Mechanical Engineering Research'. P245, 1-3 Jul, Malaysia.

NRC 2010, '7 Sea Level Rise and the Coastal Environment Advancing the Science of Climate Change', Technical report, National Research Council, US.

Oldenhof, E., Tummers, M. J. and van Veen, E. H. 2010, 'Ignition Kernel Formation and Lift-off Behaviour of Jet-in-hot-coflow Flames', *Combustion and Flame* **157(6)**, 1167–1178.

Oldenhof, E., Tummers, M. J., van Veen, E. H. and Roekaerts, D. J. E. M. 2011, 'Role of Entrainment in the Stabilisation of Jet-in-hot-coflow Flames', *Combustion and Flame* **158**, 1553–1563.

Olsson, J. O., Tunesta, P., Johansson, B., Fiveland, S. B., Agama, R., Willi, M. and Assanis, D. N. 2002, 'Compression Ratio Influence on Max Load of a Natural Gas Fuelled HCCI Engine', *SAE Paper* **02P**, 2002–02P–147.

Orr, F. 2005, *Energy and Climate*, GCEP, Stanford University.

Orsino, S., Weber, R. and Bollettini, U. 2001, 'Numerical Simulation of Combustion of Natural Gas with High Temperature Air', *Combustion Science and Technology* **170(1)**, 1–34.

Papagiannakis, R. G. and Hountalas, D. T. 2004, 'Combution and Exhaust Emision Characteristics of a Dual Fuel Compression Ignitioon Engine Operated with Pilot Diesel Fuel and Natural Gas', *Energy Conversion and Management* **45(18-19)**, 2971–2987.

Parente, A., Galletti, C. and Tognotti, L. 2008, 'Effect of the Combustion Model and Kinetic Mechanism on the MILD Combustion in an Industrial Burner Fed with Hydrogen Enriched Fuels', *International Journal of Hydrogen Energy* **33(24)**, 7553–7564.

Parente, A., Sutherland, J. C., Dally, B. B., Tognotti, L. and Smith, P. J. 2011, 'Investigation of the MILD Combustion Regime via Principal Component Analysis', *Proceedings of the Combustion Institute* **33**, 3333–3341.

Parham, J. J., Nathan, G. J., Smart, J. P., Hill, S. J. and Jenkins, B. G. 2000, 'The Relationship between Heat Flux and NOx Emision in Gas Fired Rotary Kilns', *Energy* **73**, 25–34.

Peng, F. L., Mi, J. C., Dally, B. B., Craig, R. A. and Wang, P. F. 2011, 'Premixed Moderate or Intense Low-Oxygen Dilution (MILD) Combution from a Single Jet Burner in a Lab-Scale Furnace', *Energy and Fuel* **25**, 2782–2793.

Peters, N. 1984, 'Laminar Diffusion Flamelet Models in Non-premixed Turbulent Combustion', *Progress in Energy and Combustion Science* **10(3)**, 319–339.

Peters, N. 2004, *Turbulent Combustion*, 2nd edn, Cambridge University Press, US.

Pierpont, D. A., Montgomery, D. T. and Reitz, R. D. 1995, 'Reducing Particulate and NOx Using Multiple Injections and EGR in a D.I. Diesel', *SAE Technical Paper* **-**, 950217.

Plessing, T., Peters, N. and Wünning, J. G. 1998, 'Laser Optical Investigation of Highly Preheated Combustion with Strong Exhaust Gas Recirculation', *Proceedings of the Combustion Institute* **27(2)**, 3197–3204.

Poinsot, T. and Veynante, D. 2005, *Theoretical and Numerical Combustion*, 2nd edn, Westview Press, Philadelphia, US.

Pomeroy, C. A. 2008, 'Science Watch - Biogas Breakthrough', *The Japan Journal* **Nov**, 1–3.

Pope, S. B. 1985, 'PDF Methods for Turbulent Reactive Flows', *Progress in Energy and Combustion Science* **11(2)**, 119–192.

Pope, S. B. 1991, 'Mapping Closures for Turbulent Mixing and Reaction', *Theoretical and Computational Fluid Dynamics* **2**, 255–270.

Pope, S. B. 2000, *Turbulent Flows*, Cambridge University Press.

Purwanto, H. and Akiyama, T. 2006, 'Hydrogen Production from Biogas using Hot Slag', *International Journal of Hydrogen Energy* **31(4)**, 491–495.

Quaak, P., Knoef, H. and Stassen, H. 1999, *Energy from Biomass: A Review of Combustion and Gasification Technologies*, World Bank. Technical Paper No. 422.

Rafiq, M. H. and Hustad, J. E. 2011, 'Biosyngas Production by Autothermal Reforming of Waste Cooking Oil with Propane using a Plasma Assisted Gliding Arc Reactor', *International Journal of Hydrogen Energy* **36**, 8221–8233.

Rahimi, M., Khoshhal, A. and Shariati, S. M. 2006, ‘CFD Modeling of a Boiler’s Tubes Rupture’, *Applied Thermal Engineering* **26**, 2192–2200.

Rajendran, K., Aslanzadeh, S. and Taherzadeh, M. J. 2012, ‘Household Biogas Digesters: A Review’, *Energies* **5**, 2911–2942.

Ramli, M. Z. 2009, *Adsoprtion of Natural Gas and Hydrogen on Cu3*, University Malaysia Pahang, Malaysia.

Rao 2010, ‘Session on Lifted Flames in Hot Co-flow Coordinator’, *TNF 10 Workshop* **10**, 44–48. 29-31 July, Tsinghua University Beijing, China.

Rashmi, W., Ismail, A. F., Khalid, M. and Faridah, Y. 2011, ‘CFD Studies on Natural Convection Heat Transfer of Al_2 O_3 - Water Nanofluids’, *Heat and Mass Transfer* **47**, 1301–1310.

Raub, J. 1999, *Carbon Monoxide*, 2nd edn, International Programme on Chemical Safety, Geneva, Switzerland.

Riahi, Z., Mergheni, M. A., Sautet, J. C. and Nasrallah, S. B. 2012, ‘Numerical Study of Turbulent Normal Diffusion Flame CH4-Air Stabilized by Coaxial Burner’, *Thermal Science* **1**, 1–20.

Robinson, C. and Smith, D. B. 1984, ‘The Auto-Ignition Temperature of Methane’, *Journal of Hazardous Materials* **8(3)**, 199203.

Roiha, I., Kaikko, J., Jaanu, K. and Vakkilainen, E. 2014, ‘Analysis of High Flue Gas Recirculation for Small Energy Conversion Systems’, *Applied Thermal Engineering* **63**, 218–226.

Saanum, I., Bysveen, M., Tunestal, P. and Johansson, B. 2007, ‘Lean Burn Versus Stoichiometric Operation with EGR and 3-Way Catalyst of an Engine Fuelled with Natural Gas and Hydrogen Enriched Natural Gas’, *SAE International* **2007-01-0015**, 1–11.

Saha, M., Cleary, E. M., Medwell, P. R. and Dally, B. B. 2013, MILD Combustion of Pulverised Coal in a Recuperative Furnace, *in* ‘European Combustion Meeting’, number Paper P4-78, Lund, Sweden, pp. 1–6.

Saha, M., Dally, B. B., Medwell, P. R. and Cleary, E. M. 2014, ‘MILD Combustion Characteristics of Pulverised Coal in a Self-Recuperative Furnace’, *Energy & Fuels* **28**, 6046–6057.

Saleh, K. H. 2014, ‘Initial Development of Ice Crystal Ice Accretion at Conditions Related to Turbofan Operation at High Altitude’, PhD thesis, USQ, Australia.

Salter, B., Park, G. and Schroeder, B. 2013, ‘Does Harvesting Sugarcane Crops More Frequently Increase Biomass Production?’, *Proceedings of the Australian Society of Sugar Cane Technologists* **35**, 1–8.

Salunkhe, D. B., Rai, R. K. and Borkar, R. P. 2012, ‘Biogas Technology’, *International Journal of Engineering Science and Technology* **4(12)**, 4934–4940.

Santilena, T. 2012, 'Opportunities in Biogas: A Comparison Between Germany and the United States', Technical report, University of California, US.

Sato, A., Hashiba, K., Hasatani, M., Sugaiyama, S. and Kimura, J. 1975, 'A Correctional Calculation Method for Thermocouple Measurements of Temperatures in Flames', *Combustion and Flame* **24**, 35–41.

Savariraj, S., Ganapathy, T. and Saravanan, C. G. 2011, 'Experimental Investigation of Performance and Emission Characteristics of Mahua Biodiesel in Diesel Engine', *ISRN Renewable Energy* **6**, –.

Scharler, R. and Obernberger, I. 2000, Numerical Modelling of Biomass Grate Furnace, *in* '5th European Conference on Industrial Furnaces and Boilers', Porto, Portugal, pp. 1–17.

Scheele, J. V., Gart, M., Paul, R., Lantz, M. T., Riegert, J. P. and Soderlund, S. 2008, 'Flameless Oxyfuel Combustion for Increased Production and Reduced CO_2 and NOx Emissions', *Stahl und Eisen* **128(7)**, 35–40.

Scragg, A. H. 2009, *Biofuels Production, App. and Development*, Oxfordshire, UK.

Seadi, T. A., Rutz, D., Prassl, H., Kottner, M., Finsterwalder, T., Volk, S. and Janssen, R. 2008, *Biogas Handbook*, USD, Denmark.

Sepman, A. V., Abtahizadeh, S. E., Mokhov, A. V., Oijen, J. A. V., Levinsky, H. B. and Goey, L. P. H. D. 2013, 'Numerical and Experimental Studies of the NO Formation in Laminar Coflow Diffusion Flames on Their Transition to MILD Combustion Regime', *Combustion and Flame* **160(8)**, 1364–1372.

Sepman, A. V., Mokhov, A. V. and Levinsky, H. B. 2011, 'The Effects of the Hydrogen Addition on the HCN Profiles in Fuel-Rich-Premixed, Burner-Stabilized C1-C3 Alkane Flames', *International Journal of Hydrogen Energy* **36(21)**, 13831–13837.

Shabanian, S. R., Derudi, M., Rahimi, M., Frassoldati, A., Cuoci, A. and Faravelli, T. 2011, Experimental and Numerical Analysis of Syngas MILD Combustion, *in* '34th Meeting of the Combustion Institute (Italian)', Rome, Italy, pp. 1–7.

Shafiee, S. and Topal, E. 2009, 'When Will Fossil Fuel Reserves be Diminished?', *Energy Policy* **37(1)**, 181–189.

Shih, T. H., Liou, W., Shabbir, A., Yang, Z. and Zhu, J. 1995, 'A New k-ε Eddy Viscosity Model for High Reynolds Number Turbulent Flows', *Computers Fluids* **24**, 227–238.

Shim, S. S., Jeong, S. H. and Lee, S. S. 2014, 'Reduction in Nitrogen Oxides Emissions by MILD Combustion of Dried Sludge', *Renewable Energy* **65**, 29–35.

Siemens 2014, ‘Siemens Landis LGB21 350A27 240V Control Box’, `http://www.siemens-landis-supplier.co.uk`. (accessed on 22 Feb 2014).

Simpson, J., Staunton, S. and OShea, M. 2012, ‘A Review of NIR Applications for Process Control Purposes’, *International Sugar Journal* **114(1358)**, 91–95.

Smith, J. A. and Bartley, G. J. J. 2000, ‘Stoichiometric Operation of a Gas Engine Utilizing Synthesis Gas and EGR for NOx Control’, *Journal of Engineering for Gas Turbines and Power* **122**, 617.

Smith, S. T. and Fox, R. O. 2007, ‘A Term-by-Term Direct Numerical Simulation Validation Study of the Multi Environment Conditional PDF Model for Turbulent Reacting Flows’, *Physics of Fluids* **19**, 085102.

Smith, T. F., Shen, Z. F. and Friedman, J. N. 1982, ‘Evaluation of Coefficients for the Weighted Sum of Gray Gases Model’, *Journal of Heat Transfer* **104(4)**, 602–608.

Smooke, M. D. and Giovangigli, V. 1991, Formulation of the Premixed and Nonpremixed Test Problems, *in* M. D. Smooke, ed., ‘Reduced Kinetic Mechanisms and Asymptotic Approximations for Methane-Air Flames’, Vol. 384 of *Lecture Notes in Physics*, Springer–Verlag, pp. 1–28.

Smooke, M. D., McEnally, C. S., Pfefferle, L. D., Hall, R. J. and Colket, M. B. 1999, ‘Computational and experimental study of soot formation in a coflow, laminar diffusion flame’, *Combustion and Flame* **117**, 117–139.

Sobiesiak, A., Rahbar, S. and Becker, H. A. 1998, ‘Performance Characteristics of the Novel Low-NOx CGRI Burner for Use with High Air Preheat’, *Combustion and Flame* **115**, 93–125.

Speight, J. G. 2008, *Synthetic Fuels Handbook: Properties, Process and Performance*, McGraw-Hill, New York, US.

Stefan, S., Klaus, D. W. and Axel, S. 2012, ‘Flame Heights of Di-tert-butyl Peroxide Pool Fires - Experimental Study and Modeling’, *Chemical Engineering Transaction* **26**, 363–368.

Stewart, R. W. 1969, ‘Turbulence and Waves in a Stratified Atmosphere’, *Radio Science* **4(12)**, 1269–1278.

Suzukawa, Y., Sugiyama, S., Hino, Y., Ishioka, M. and Mori, I. 1997, ‘Heat Transfer Improvement and NOx Reduction by Highly Preheated Air Combustion’, *Energy Conversion and Management* **38**, 1061–1071.

Szegö, G. G. 2010, ‘Experiment and Numerical Investigation on a Parallel Jet MILD Combustion Burner System in a Lab Scale Furnace’, PhD thesis, University of Adelaide, Australia.

Szegö, G. G., Dally, B. B. and Nathan, G. J. 2008, ‘Scaling of NOx Emission from a Lab-Scale MILD Combution Furnace’, *Combustion and Flame* **154**, 281–295.

Szegö, G. G., Dally, B. B. and Nathan, G. J. 2009, 'Operational Characteristics of a Parallel Jet MILD Combustion Burner System', *Combustion and Flame* **156(2)**, 429–438.

Szegö, G. G., Dally, B. B., Nathan, G. J. and Christo, F. C. 2003, Design Optimisation of a MILD Combustion Furnace based on CFD Modelling, *in* 'Australian Combustion Symposium and the 8th Australian Flame Days', Monash University, Australia. Paper ID: P047.

Szegö, G. G., Dally, B. B., Nathan, G. J. and Christo, F. C. 2007, Performance Characteristics of a 20 kW Mild Combustion Furnace, *in* '27th Asia-Pacific Conference on Combustion', Nagoya, Japan, pp. 1157–1165.

Tang, T., Wu, J., Ma, A., Gou, X., Liu, L. and Wang, E. 2011, Effect of Recirculated Flue Gas Position on Combustion and NOx Emission for High Temperature Air Combustion, *in* 'International Conference on CDCIEM', Changsha, Hunan, China, pp. 1177–1180.

Tang, Z. G., Ma, P. Y., Li, Y. L., Tang, C. J., Xing, X. J. and Lin, Q. Z. 2010, 'Design the Experiment Research of a Novel Pulverized Coal Gasifier Based on Flameless Oxidation Technology', *CSEE* **30(8)**, 50–55.

TCDirect 2012, 'Thermocouples for Temperatures Measurement', `http://www.tcdirect.net.au`. (accessed on 22 April 2012).

Techrite 2014, 'Techrite: Gas Safety Control and Combustion Specialist', `http://www.techrite.com.au`. (accessed on 06 Feb 2014).

Tennekes, H. and Lumley, J. L. 1972, *A First Course in Turbulence*, MIT Press, Cambridge, MA, US.

Testo 2012, 'Anemometer', `http://www.testo.com.au`. (accessed on 07 Nov 2012).

Thomas, C. E. 2011, *Process Technology Equipment & Systems*, D Cengage, NY, US.

Tobacco, D., Innarella, C. and Bruno, C. 2002, 'Theoretical and Numerical Investigation on Flameless Combustion', *Combustion Science and Technology* **174**, 1–35.

Triantafyllidis, A., Mastorakos, E. and Eggels, R. L. G. M. 2009, 'Large Eddy Simulations of Forced Ignition of a Non-Premixed Bluff-Body Methane Flame with Conditional Moment Closure', *Combustion and Flame* **156**, 2328–2345.

Tsolakis, A., Lau, C. S. and Wyszynski, M. L. 2011, 'Biogas Upgrade to Syn-gas (H2-CO) via Dry and Oxidative Reforming international journal of hydrogen energy', *International Journal of Hydrogen Energy* **36**, 397–404.

Tsuji, H., Gupta, A., Hasegawa, T., Katsuki, M., Kishimoto, K. and Morita, M. 2003, *High Temperature Air Combustion, from Energy Conservation to Pollution Reduction*, CRC Press. Boca Raton, Florida.

Turns, S. R. 2000, *An Introduction to Combustion*, McGraw-Hill, Boston, US.

Turns, S. R. 2006, *An Introduction to Combustion*, McGraw-Hill, Boston, US.

USEIA 1999, 'Natural Gas Issues and Trends', Technical report, Energy Information Administration, Washington DC, US. Report No.: DOE-EIA-0560(1999).

USEIA 2011, 'International Energy Outlook 2011', Technical report, Energy Information Administration, Washington DC, US. Report No.: DOE-EIA-0484(2011).

USEIA 2013, 'International Energy Outlook 2013', Technical report, Energy Information Administration, Washington DC, US. Report No.: DOE-EIA-0484(2013).

USEPA 1999, Nitrogen Oxides, Why and How They Are Controlled, Technical report, US Environmental Protection Agency, US. EPA-456/F-99-006R.

USQ 2012, 'High Performance Computing (HPC) Facilities', `http://hpc.usq.edu.au/facilities`. (accessed on 12 April 2012).

USQ 2013, 'USQ Weather', `http://www.usq.edu.au`. (accessed on 10 Jan 2014).

Vascellari, M., Schulze, S., Nikrityuk, P., Safronov, D. and Hasse, C. 2014, 'Numerical Simulation of Pulverized Coal MILD Combustion Using a New Heterogeneous Combustion Submodel', *Flow, Turbulence and Combustion* **92**, 319–345.

Verssimo, A., Oliveira, R., Coelho, P. J. and Costa, M. 2012, 'Numerical Simulation of a Small-Scale MILD Combustion', *Journal of Physics* **395**, 012003.

Vishkanta, R. and Menguc, M. P. 1987, 'Radiation Heat Transfer in Combustion Systems', *Progress in Energy and Combustion Science* **13**, 97–160.

Volks, T. 2008, *CO_2 Rising: The Worlds Greatest Environmental Challenge*, MIT Press, US.

Wandel, A. P. 2013, 'Conditional Dissipation of Scalars in Homogeneous Turbulence: Closure for MMC Modelling', *Combustion Theory and Modelling* **17(4)**, 707–748.

Wandel, A. P. and Klimenko, A. Y. 2005, 'Testing Multiple Mapping Conditioning Mixing Probability Density Function Simulation', *Physics of Fluids* **17(12)**, 128105–1.

Warnatz, J., Maas, U. and Dibble, R. W. 2006, *Combustion: Physical and Chemical Fundamentals, Modeling and Simulation, Experiments, Pollutant Formation*, 4th edn, Springer-Verlag, Berlin.

Weber, R. 2001, Combustion of Natural Gas, Oil and Coal with Air Preheated to Temperatures in Excess of 1000°C, *in* '13th IFRF Members Conference', Noordwijkerhout, Netherlands.

Weber, R., Orsino, S., Verlaan, A. and Lallemant, N. 2001, ‘Combustion of Light and Heavy Fuel Oils in High Temperature Air’, *Journal of the Institute of Energy* **74**, 38–47.

Weidmann, M., Verbaere, V., Boutin, G., Honor, D., Grathwohl, S., Goddard, G., Gobin, C., Dieter, H., Kneer, R. and Scheffknecht, G. 2014, ‘Detailed Investigation of Flameless Oxidation of Pulverized Coal at Pilot-Scale (230 kW)’, *Applied Thermal Engineering* **70**, 1–6.

Weinberg, F. J. 1971, ‘Combustion Temperatures: The Future’, *Nature* **233**, 239–241.

Westbrook, C. K. and Dryer, F. L. 1984, ‘Chemical Kinetic Modeling of Hydrocarbon Combustion’, *Progress in Energy and Combustion Science* **10(1)**, 1–57.

Wika 2012, ‘Pressure Transducer’, `http://www.wika.com.au`. (accessed on 17 Sept 2012).

Wilcox, D. C. 1994, *Turbulence Modeling for CFD*, DCW Industries Inc., California.

Williams, F. A. 1985, *Combustion Theory: The Fundamental Theory of Chemically Reacting Flow Systems*, second edn, Addison-Wesley Company Inc., London.

Willyanto, A., Wardana, I., Lawes, M. and Hughes, K. J. 2013, ‘Effect of Inhibitors on Biogas Laminar Burning Velocity and Flammability Limits in Spark Ignited Premix Combustion’, *International Journal of Engineering and Technology* **5**(6), 4980–4987.

Wünning, J. 2005, Flameless Oxidation, *in* ‘6th HiTACG Symposium’, Essen, Germany, pp. 1–12.

Wünning, J. A. and Wünning, J. G. 1997, ‘Flameless Oxidation to Reduce Thermal No-Formation’, *Progress in Energy and Combustion Science* **23(1)**(s), 81–94.

Wünning, J. G. 1991, ‘Flammlose Oxidation Von Brennstoff Mit Hochvorgewarmter Luft’, *Chem-Ing-Tech* **63(12)**, 1243–1245.

Wyszynski, W. L., Mamat, R., Xu, H. M., Qiao, J., and Pierson, S. 2008, ‘CFD Analysis of Air Intake System with Negative Pressure on Intake Grill’, *SAE Technical Paper* **SAE Technical Paper 2008-01-1643**, –.

Yang, W. and Blasiak, W. 2006, ‘CFD as Applied to High Temperature Air Combustion in Industrial Furnaces’, *IFRF Industrial Combustion Journal* **200603**, –.

Yuan, J. W. and Naruse, I. 1999, ‘Effects of Air Dilution on Highly Preheated Air Combustion in a Regenerative Furnace’, *Energy and Fuel* **13(1)**, 99–104.

Yusaf, T., Noor, M. M. and Wandel, A. P. 2013, MILD Combustion: The Future for Lean and Clean Combustion, *in* 'International Conference of Mechanical Engineering Research', Kuantan, Malaysia, pp. 1–13. Keynote.

Zelinski, J. J., III, L. J. M., Falk, F. and Bagnall, E. C. 1960, 'The Design of Combustors for Ramjet Engine', *Combustion and Flame* **4**, 343–353.

Zhang, C., Ishii, T. and Sugijama, S. 1997, 'Numerical Modelling of the Thermal Performance of Regenerative Slab Reheating Furnaces', *Numerical Heat Transfer* **32**, 613–631.

Zhenjun, C., Tong, Z. and Chaohua, J. 2010, Thermal and Emission Characteristics of High Temperature Air Combustion, *in* 'Int. Conf. on Mechanic Automation and Control Engineering', Wuhan, China.

Zicari, S. 2003, 'Removal of Hydrogen Sulfide from Biogas Using Cow Manure Compost', Master's thesis, Cornell University, Ney York.

Zou, C., Cao, S., Song, Y., He, Y., Guo, F. and Zheng, C. 2014, 'Characteristics and Mechanistic Analysis of CO Formation in MILD Regime with Simultaneously Diluted and Preheated Oxidant and Fuel', *Fuel* **130**, 10–18.

Appendix A

Chemical Reaction and Gas Properties

This appendix consists of a discussion of chemical reactions, gas properties, gas heating values, fuel and oxidant supply rates and the calculations for furnace power.

A.1 Chemical Reactions

Chemical reactions are fundamental to the combustion process (Heywood, 1988; Turns, 2006). Understanding the combustion chemistry is essential to differentiate the process between global and elementary reactions. The global scale is the reaction of fuel and oxidant with the release of combustion products such as CO_2, H_2O and heat. The combustion process can be written in general hydrocarbon stoichiometric combustion equation as shown in Equation A.1. The global reaction for the methane and air combustion can be seen in Equation A.2:

$$\mathrm{C_nH_m + (n + \frac{m}{4})(O_2 + 3.76N_2)} \rightarrow \mathrm{nCO_2 + \frac{m}{2}H_20 + 3.76(n + \frac{m}{4})N_2} \quad (A.1)$$

$$\mathrm{CH_4 + 2O_2 + 7.52N_2} \rightarrow \mathrm{CO_2 + 2H_2O + 7.52N_2} \quad (A.2)$$

A description of methane and air combustion that involved 279 steps of elementary reactions and 49 species has been identified (Turns, 2006). A reduced chemical reaction for methane combustion developed in 1986 consists of 16 different species and 46 reactions (Smooke and Giovangigli, 1991). The new Arrhenius equation (Equation A.3) modified from the original Arrhenius equation (Equation A.4) is normally used for the chemical reaction.

$$k = AT^n \left(exp \left(-\frac{E}{RT} \right) \right) \quad (A.3)$$

where A is a constant ($\mathrm{k/mols\,m^3\,K}$), T is temperature (K), n is constant, E is activation energy (J/kmol) and R is universal gas constant with the value of $8.3145\,\mathrm{J/mol\,K}$. The chemical reaction rate coefficient depends on the reaction temperature and activation energy. The original Arrhenius equation is as Equation A.4.

$$k = B\left(\exp\left(-\frac{\mathrm{E}}{\mathrm{RT}}\right)\right) \tag{A.4}$$

where B is the pre-exponential frequency factor. The Arrhenius equation has been modified to include the temperature dependence of the pre-exponential factor (Nakamura et al., 1989).

A.2 Gas Properties

The properties of carbon dioxide, nitrogen, oxygen, water vapour and methane at 273 K and 1 atm are displayed in Table A.1.

Table A.1: Properties of carbon dioxide, nitrogen, oxygen, water vapour and methane at 273 K and 1 atm (Turns, 2006; NIST, 2009).

Properties	**CO_2**	**N_2**	**O_2**	**H_2O**	**CH_4**
Density (kg/m^3)	1.98	1.25	1.43	0.83	0.67
Volumetric heat capacity (kJ/(m^3 K)	1.62	1.30	1.32	1.49	1.55
Kinematic viscosity $\times 10^6$ (m^2/s)	7.09	13.3	13.6	10.1	14.5
Thermal conductivity (W/mK)	137	249	250	162	302
Mass diffusivity in air $\times 10^5$ (m^2/s)	1.38	–	1.78	2.2	1.96

The fuel heating values are normally used to quantify the maximum amount of heat generated by combustion with air at 298 K and 101.3 kPa. The amount of thermal heat released from fuel combustion will depend on the phase of water in the products (McAllister et al., 2011). A lower heating value is measured when additional energy is extracted when water vapour is condensed to liquid and when the water is in its gas phase. No additional energy can be extracted and the total energy is called higher heating value.

Methane thermal properties include internal energy, enthalpy, specific heat and heating value. The fuels' heating value in J/mole or J/kg used to measure the maximum amount of heat can be generated by combustion with air at 25°C and 101.325 kPa. Table A.2 shows the heating value for methane and compares it with other fuel and gases. The highest heating value is hydrogen, and methane is the highest among the hydrocarbon fuels.

A.3 Fuel and Oxidant Supply Rate

For methane with the density of 0.6688 kg/m^3 the higher heating value is 55.50 MJ/kg and lower heating value is 50.02 MJ/kg. For propane with the density of 1.882 kg/m^3 the higher heating value is 50.30 MJ/kg and lower heating value is 46.36 MJ/kg. The burner standard capacity per hour was rated for propane.

Table A.2: Heat values of various fuels (McAllister et al., 2011; Demirel, 2012).

Fuel		**g/mol**	**MJ/kg**	**MJ/L**	**BTU/Ib**	**kg/m^3**
Hydrogen	H_2	2.01	141.8	0.0127	61,100	0.0899
Methane	CH_4	16.04	50.0	0.0371	23,900	0.6680
Propane	C_3H_8	44.09	46.4	0.0947	21,700	1.8820
Natural gas	–	18.14	50.0	0.0400	21,600	0.8000
Biogas	–	27.23	33.3	0.0400	14,352	1.2000
Gasoline	$C_nH_{1.87n}$	100–110	47.3	34.042	20,400	719.70
Diesel	$C_nH_{1.75n}$	170–200	44.4	36.941	19,300	832.00
Coal	–	–	21	17.404	11,000	828.75
Wood	–	–	15	9.7637	6,500	650.91

A.3.1 Gas Supply Flow Rate

The gas flow rate is calculated based on the maximum allowable gas operating pressure. For the experimental setup, the standard commercial premixed air inspirator type gas burner was installed having a maximum gas supply of 100 kPa for open air burner without enclosed wall (ASC, 2013). After the testing and commissioning by expert gas fitters, a limiter was applied and the gas supply had to be reduced to a maximum of 50 kPa (Aylward, 2014). This was due to the combination of a few factors including burner with enclosed chamber, exhaust gas extraction system, primary and secondary oxidant supply, gas supply safety interlock and solenoid valve installed in the gas supply line. The fuel flow rate for the experiment and CFD work is summarised in Table A.3.

Table A.3: The conversion table of fuel supply flow rate for the 12.7 mm fuel supply inlet.

Gas pressure (kPa)	**Gas flow (m/s)**
20	2.84
10	1.42

A.3.2 Primary Air Supply Flow Rate

Air was induced together with fuel through the fuel nozzle. To calculate the air supply flow rate, the λ value was used. For the experimental test run using 10.82 L/min air flow rate, the λ reading is 2.65.

$$\begin{aligned}\lambda &= \frac{AFR_{act}}{AFR_{stoi}} \\ &= \frac{M_{air}/M_{fuel}}{AFR_{stoi}} \qquad \text{(A.5)}\end{aligned}$$

Table A.4: The conversion table of air supply flow rate for the 10.0 mm oxidant supply inlet. The compressed air pressure was set at 500 kPa and the flow rate was controlled by the flow meter.

Experimental work	**CFD**
Air flow meter (SCFH)	**Air flow rate (m/s)**
400	10.00
200	5.00
50	1.25

The mass flow rate for air when 10.82 L/min (10 kPa) of fuel was injected to the burner can be calculated as below:

$$\begin{aligned} M_{air} &= \lambda \times M_{fuel} \times AFR_{stoi} \\ &= \lambda \times V_{fuel} \times \rho \times AFR_{stoi} \\ &= 2.65 \times 10.82\, L/min \times 0.6688\, kg/m^3 \times \frac{1\, m^3}{1000\, L} \times \frac{60\, min}{1 hr} \times 9.52 \\ &= 10.95\, kg/hr \end{aligned} \tag{A.6}$$

From the mass flow rate, the volume flow rate for air is:

$$\begin{aligned} V_{air} &= 10.95\, kg/hr \times \frac{1}{1.2041\, kg/m^3} \times \frac{1000\, L}{1\, m^3} \times \frac{1 hr}{60\, min} \\ &= 151.62\, L/min \end{aligned} \tag{A.7}$$

A.3.3 Secondary Air Supply Flow Rate

The maximum air supply through the four sides of the EGR pipe is 400 SCFH (47.20 L/min). Each air supply pipe is 10 mm in diameter and will take 100 SCFH. This maximum experimental air supply can be calculated for CFD air supply as below:

$$\begin{aligned} \text{Air supply} &= 100\, SCFH \times \frac{1\, hr}{3600\, s} \times \frac{1\, m^3}{35.315\, ft^3} \times \frac{1}{7.85 \times 10^{-5}\, m^2} \\ &= 10.0\, m/s \end{aligned} \tag{A.8}$$

The air flow rate was summarised in Table A.4.

A.4 Furnace Power Calculation

The furnace power or total heating value has been calculated by using the methane heating value which is 50.02 MJ/kg. Assume pure methane gas was injected at 10.82 L/min (1.52 m/s) through a 12.7 mm diameter fuel supply pipe. The area (A) of the fuel supply pipe is $1.27 \times 10^{-4}\, m^2$. Total volume flow rate is:

$$\begin{aligned} \dot{V} &= 10.82\, L/min \times \frac{m^3}{1\, L} \times \frac{1\, min}{60\, s} \\ &= 1.803 \times 10^{-4}\, m^3/s \end{aligned} \tag{A.9}$$

The mass flow rate depends on the density of the fluid. The density of methane gas is 0.6688 kg/m^3 (at 293 K and 101.325 kPa), thus mass flow rate ($\dot{m}$) is

$$\begin{aligned} \dot{m} &= \rho\dot{V} \\ &= 0.6688\, kg/m^3 \times (1.803 \times 10^{-4}\, m^3/s) \\ &= 1.206 \times 10^{-4}\, kg/s \end{aligned} \tag{A.10}$$

Heat release by the combustion (ΔH) of methane can be calculated as below.

$$\begin{aligned} q &= \dot{m}\Delta H \\ &= (1.206 \times 10^{-4}\, kg/s) \times 50.02\, MJ/kg \\ &= 6.03\, kW \end{aligned} \tag{A.11}$$

The power of the furnace is 6.0 kW based on 10.82 L/min of methane volume flow rate. The energy input through the air heating element must be counted as the furnace input power. Thermal power provided by the air heating element can be calculated as below:

$$\begin{aligned} Q &= \dot{m}C_p\Delta T \\ &= (1.205 \times 3.93 \times 10^{-4}) \times 1.005 \times (673 - 293) \\ &= 0.18\, kW \end{aligned} \tag{A.12}$$

where $\dot{m}$ is the air mass flow rate (kg/s) calculated at the volume flow rate of 23.6 L/min, C_p is the air specific heat (kJ/(kg K)) at 293 K and ΔT is the air temperature difference (K) between the inlet and outlet of the heating element. Equation A.12 shows the calculation for the energy input from the air heating element. The total energy input for the furnace is 6.21 kW with 6.03 kW from the combustion of methane fuel and 0.18 kW from the air heating element. The energy intensity for the combustion chamber is 18.81 kW/m^3.

Appendix B

Thermocouples and Other Instrumentations

This appendix consists of the detail about thermocouples, data acquisition system, gas analysers specification, high temperature glass window, half inch burner, secondary oxidant heating element, gas supply flow meter, pressure transducers calibration, calculation of EGR flow rate, ignition system with gas safety interlock and sample weather report.

B.1 Data Acquisition System

Figure B.1 shows the LabVIEW data acquisition system diagram.

B.2 Gas Analysers Specification

Two gas analysers were used to measure the exhaust gas composition and residual oxygen in the exhaust gas. A CODA gas analyser was used to measure the exhaust gas emissions (CODA, 2012) and a MOTEC lambda sensor was used to measure the excess oxygen level in the exhaust gas (MoTeC, 2013).

B.2.1 CODA Gas Analyser

The CODA gas analyser specification can be found in Figure B.2. The accuracy of the measurement is between ±3 % and ±5 % (CODA, 2012).

B.2.2 MOTEC Lambda Sensor

The MoTEC PLM (Profesional Lambda Meter) measures λ or Air Fuel Ratio (AFR) with a very fast response time and in a wide range of mixtures. The sensor specifications can be found in Figure B.3. With the accuracy of ±1.5 %,

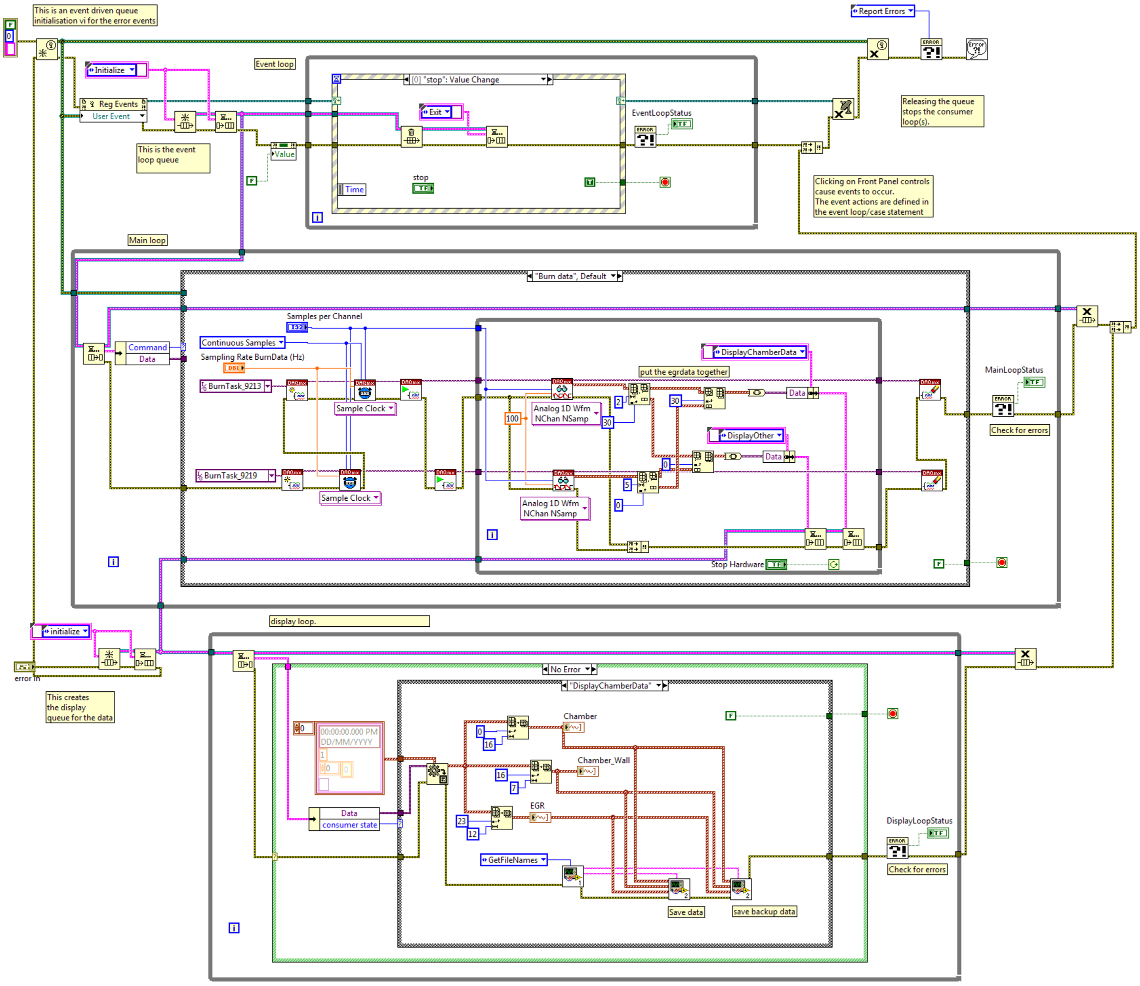

Figure B.1: LabVIEW data acquisition system diagram.

this factory calibrated lambda sensor can detect oxygen and λ in the range of 0–22 % (by volume) and 0.7–32 respectively.

B.3 Thermocouples

The main data measurement in this research is temperature distribution. The thermocouples were used to measure the temperature at various locations.

B.3.1 Thermocouples Installation

A total of 42 thermocouples were installed to measure the temperature at various locations. The TC Direct thermocouples with Standardised Letter Designation (SLD) of K and R were used in this research (TCDirect, 2012). The thermocouple summary and installation location can be found in Table B.1.

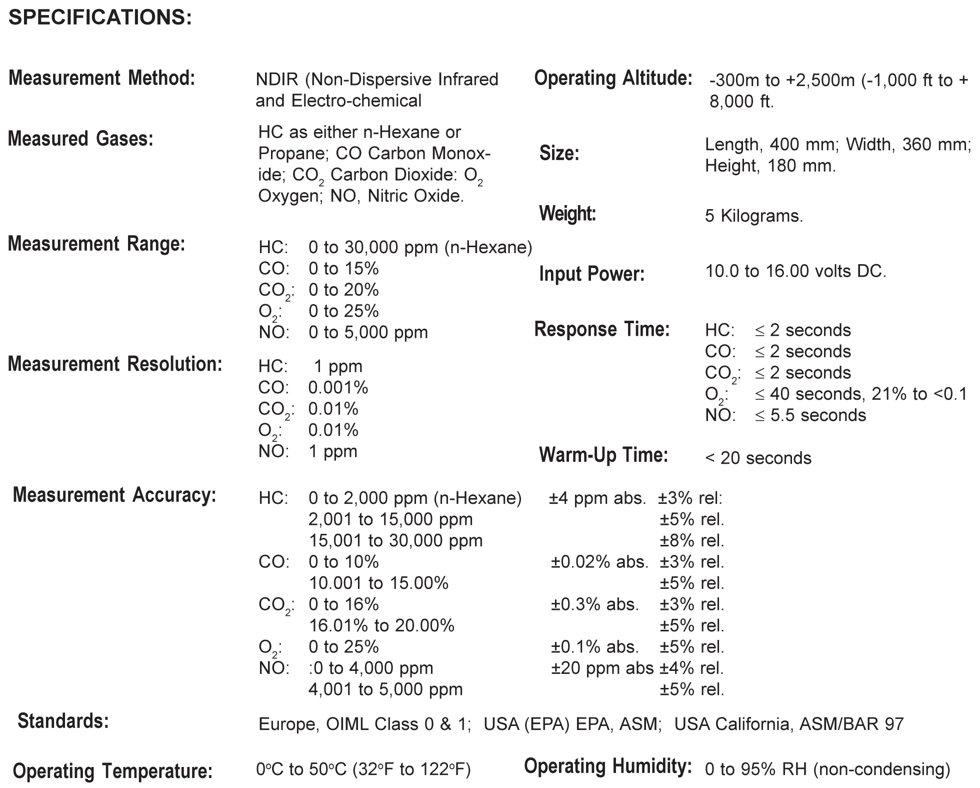

SPECIFICATIONS:

Measurement Method:	NDIR (Non-Dispersive Infrared and Electro-chemical
Measured Gases:	HC as either n-Hexane or Propane; CO Carbon Monoxide; CO_2 Carbon Dioxide: O_2 Oxygen; NO, Nitric Oxide.
Measurement Range:	HC: 0 to 30,000 ppm (n-Hexane) CO: 0 to 15% CO_2: 0 to 20% O_2: 0 to 25% NO: 0 to 5,000 ppm
Measurement Resolution:	HC: 1 ppm CO: 0.001% CO_2: 0.01% O_2: 0.01% NO: 1 ppm
Operating Altitude:	-300m to +2,500m (-1,000 ft to + 8,000 ft.
Size:	Length, 400 mm; Width, 360 mm; Height, 180 mm.
Weight:	5 Kilograms.
Input Power:	10.0 to 16.00 volts DC.
Response Time:	HC: ≤ 2 seconds CO: ≤ 2 seconds CO_2: ≤ 2 seconds O_2: ≤ 40 seconds, 21% to <0.1 NO: ≤ 5.5 seconds
Warm-Up Time:	< 20 seconds

Measurement Accuracy:

HC:	0 to 2,000 ppm (n-Hexane)	±4 ppm abs.	±3% rel:
	2,001 to 15,000 ppm		±5% rel.
	15,001 to 30,000 ppm		±8% rel.
CO:	0 to 10%	±0.02% abs.	±3% rel.
	10.001 to 15.00%		±5% rel.
CO_2:	0 to 16%	±0.3% abs.	±3% rel.
	16.01% to 20.00%		±5% rel.
O_2:	0 to 25%	±0.1% abs.	±5% rel.
NO:	:0 to 4,000 ppm	±20 ppm abs	±4% rel.
	4,001 to 5,000 ppm		±5% rel.

Standards: Europe, OIML Class 0 & 1; USA (EPA) EPA, ASM; USA California, ASM/BAR 97

Operating Temperature: 0°C to 50°C (32°F to 122°F)

Operating Humidity: 0 to 95% RH (non-condensing)

Figure B.2: CODA gas analyser specification (CODA, 2012).

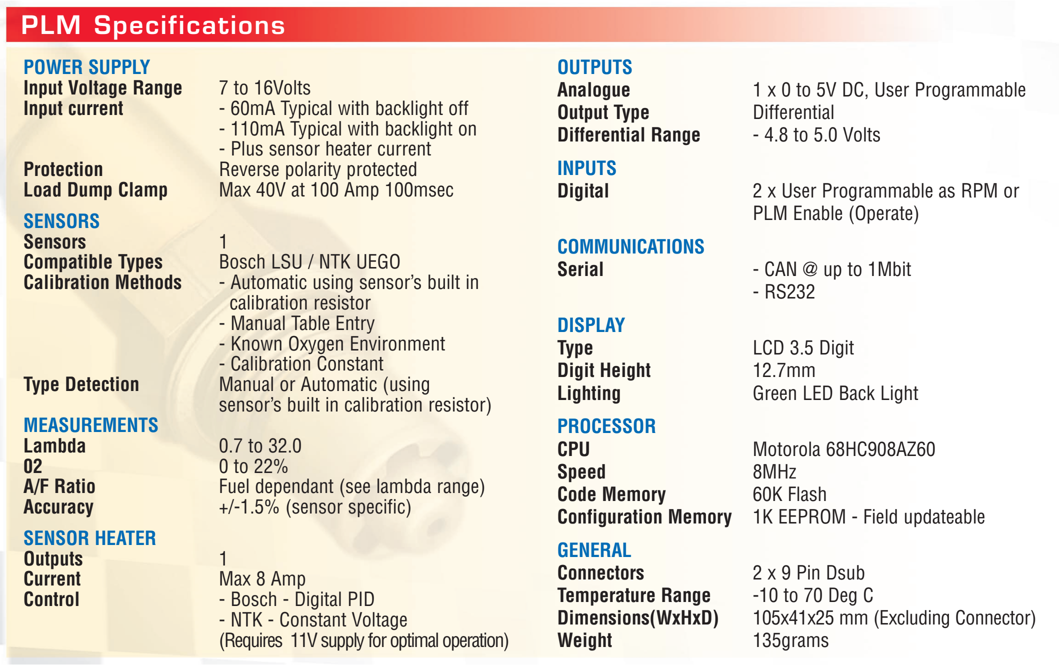

PLM Specifications

POWER SUPPLY	
Input Voltage Range	7 to 16Volts
Input current	- 60mA Typical with backlight off - 110mA Typical with backlight on - Plus sensor heater current
Protection	Reverse polarity protected
Load Dump Clamp	Max 40V at 100 Amp 100msec
SENSORS	
Sensors	1
Compatible Types	Bosch LSU / NTK UEGO
Calibration Methods	- Automatic using sensor's built in calibration resistor - Manual Table Entry - Known Oxygen Environment - Calibration Constant
Type Detection	Manual or Automatic (using sensor's built in calibration resistor)
MEASUREMENTS	
Lambda	0.7 to 32.0
02	0 to 22%
A/F Ratio	Fuel dependant (see lambda range)
Accuracy	+/-1.5% (sensor specific)
SENSOR HEATER	
Outputs	1
Current	Max 8 Amp
Control	- Bosch - Digital PID - NTK - Constant Voltage (Requires 11V supply for optimal operation)

OUTPUTS	
Analogue	1 x 0 to 5V DC, User Programmable
Output Type	Differential
Differential Range	- 4.8 to 5.0 Volts
INPUTS	
Digital	2 x User Programmable as RPM or PLM Enable (Operate)
COMMUNICATIONS	
Serial	- CAN @ up to 1Mbit - RS232
DISPLAY	
Type	LCD 3.5 Digit
Digit Height	12.7mm
Lighting	Green LED Back Light
PROCESSOR	
CPU	Motorola 68HC908AZ60
Speed	8MHz
Code Memory	60K Flash
Configuration Memory	1K EEPROM - Field updateable
GENERAL	
Connectors	2 x 9 Pin Dsub
Temperature Range	-10 to 70 Deg C
Dimensions(WxHxD)	105x41x25 mm (Excluding Connector)
Weight	135grams

Figure B.3: MoTec Profesional Lambda Meter (PLM) technical data and specification (MoTeC, 2013).

Table B.1: The summary of 42 thermocouples installation with Standardised Letter Designation (SLD).

Area	Location	SLD (Type)	Quantity	Size (mm)	
				Diameter	Length
Chamber	Main chamber	K	11	3.0	300
		R	1	1.5	500
	Top chamber	K	4	3.0	300
	Outer wall	K	5	3.0	100
EGR	Upstream	K	4	3.0	100
	Middle	K	4	3.0	100
	Downstream	K	4	3.0	100
	EGR4 (P1–P2)	K	2	3.0	100
Exhaust		K	3	3.0	100
Mixing cone		K	1	3.0	100
Air heating element		K	2	3.0	100
Room temperature		K	1	3.0	100

B.3.2 Standard Thermocouple

A standard thermocouples table was constructed with Standardised Letter Designation (SLD), popular names, materials with colour code, typical temperature ranges and thermopowers at 373 K. In this thesis, an R-type thermocouple has been used to measure the flame temperatures and a K-type thermocouple to measure the temperatures for the combustion chamber, chamber wall, exhaust gas, EGR and oxidant mixing. Details about the standard thermocouples can be found in Table B.2.

B.4 High Temperature Glass Window

The furnace needed a window for the observation of flame propagation and image capturing. The specification for the fused silica is summarised in Table B.3. These high temperature glass is optically flat, clear and features excellent resistance to abrasion and high durability, with a low coefficient of thermal expansion and suitable for harsh environments (Edmund, 2012).

B.5 Secondary Oxidant Heating Element

A Tutco-Farnam air flow heater was used to pre-heat the air supply. The FT200 technical data can be found in Figure B.4. The maximum heated air flow rate is 115 SCFM (3,256 L/min) and maximum heated air temperature is 900 °F (755 K). The model code for the heater is FT200-2000-240-1-1 1/4F-1 1/4F-TF2. The code denotes the heater specification: the heater model-wattage-voltage-phase-inlet fitting-exhaust fitting-thermocouple (Farnam, 2012).

Table B.2: Thermocouple types (Burley et al., 1978; ISA, 1982; Burn et al., 1993; Goldstein et al., 1998; HMC, 2012; Noor et al., 2013)

SLD[a]	**Popular names**	**Materials (color code)**[b] **(positive material appears first)**	**Typical temperature range**[c]	**Thermopower at 373 K, (μV/K)**
T	Copper-constantan	Copper (blue) and a Copper-Nickel alloy[d] (red)	0–673 K	46.8
J	Iron-constantan	Iron (white) - a slightly different Copper-Nickel alloy[e] (red)	63–1033 K[f]	54.4
E	Chromel-constantan	Nickel-Chromium alloy[g] (yellow) and Nickel-Aluminum alloy[h] (purple) vs. a Copper-Nickel alloy[d] (red)	0–1273 K	67.5
N	Nicrosil-Nisil	Nickel-Chromium-Silicon alloy[i] (orange) vs. Nickel-Chromium-Magnesium alloy[i] (red)	0–1570 K	29.6
K	Chromel-Alumel	Nickel-Chromium alloy[g] (red) and Nickel-Aluminium alloy[h]	0–1645 K	41.4
M	-	Nickel-Molybdenum (18 %) and Nickel Cobalt (0.8 %)	273–1673 K	
S	-	Platinum (10 %) Rhodium and Platinum[j]	223–2040 K	7.3
R	-	Platinum (13 %) Rhodium and Platinum[j]	223–2040 K	7.5
B	-	Platinum (30 %) Rhodium and Platinum (6 %) Rhodium[j]	273–2093 K	0.9
C	-	Tungsten (5 %) Rhenium and Tungsten (26 %) Rhenium	273–2593 K	

[a] SLD stands for Standardised Letter Designation. The letter designation is for the combined thermocouple with each individual thermoelement designated by P or N for positive or negative legs, respectively–for example, SN stands for platinum, TP stands for copper, and so on.

[b] The colour codes given in parentheses are the colour of the duplex-insulated wires (ISA, 1982). Colour codes are not available for the noble metal types (S, R, and B). For the base metal types (T, J, E, and K), the overall insulation color is brown.

[c] These temperature ranges are taken from Burn et al. (1993).

[d] This copper-nickel alloy is the same for both EN and TN, often referred to as “Adams constantan” or “constantan”.

[e] This copper-nickel alloy is used in JN. It is similar to, but not always interchangeable with, EN and N. By SAMA specifications, this substance is often referred to as “SAMA constantan”, or “constantan”.

[f] Even though EMF-temperature values are available up to 1473 K (Burn et al., 1993), thermophysical properties of type J thermocouples are not stable above 1030 K.

[g] EP and KP is a nickel-chromium alloy that is usually referred to by its trade name, Chromel (HMC2012).

[h] KN is a nickel-aluminum alloy usually referred to by its trade name, Alumel (HMC2012).

[i] See Burley et al. (1978) for details.

[j] See Goldstein et al. (1998) for details.

Table B.3: High temperature glass window made of fused silica (Edmund, 2012).

Item	**Specifications**
Diameter (inches)	4.00 ±0.04
Thickness (inches)	0.75 ±0.06
Surface Accuracy (λ)	1/4 @ 632.8 nm
Index of Refraction	1.458
Coefficient of Thermal Expansion	$0.55\times10^{-6}/^{\circ}$C
Young's Modulus (GPa)	72.7

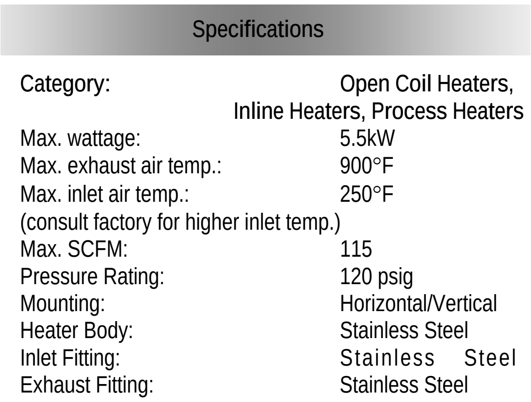

Specifications

Category:	Open Coil Heaters, Inline Heaters, Process Heaters
Max. wattage:	5.5kW
Max. exhaust air temp.:	900°F
Max. inlet air temp.: (consult factory for higher inlet temp.)	250°F
Max. SCFM:	115
Pressure Rating:	120 psig
Mounting:	Horizontal/Vertical
Heater Body:	Stainless Steel
Inlet Fitting:	Stainless Steel
Exhaust Fitting:	Stainless Steel

Figure B.4: Air heater specifications (Farnam, 2012).

The air heating element needed to be connected to the control panel, also called the control cube. The wiring diagram can be found in Figure B.5.

B.6 Gas Supply Flow Meter

Gas and oxidant volume flow rate was controlled and monitored by flowmeters (rotameters) made by Dwyers Industries (Dwyer, 2013). The models used are RMA-21-SSV for CH_4, CO_2 and O_2 and RMB-55-SSV for air and nitrogen. The specification for the flow meters can be found in Figure B.6.

The other flow meter is a hand-held type that was used to measure the exhaust fume suction flow rate. The specifications for the Testo 417 large vane anemometer (Testo, 2012) can be found in Figure B.7.

B.7 EGR Flow Rate Calculation

The EGR flow rate was determined using two point pressure and temperature differences. The temperature difference between the two points is very small (about 1 %), hence to simplify the calculation of the experimental gas flow rate, the exhaust gas flow is assumed to be an incompressible flow. The EGR volume flow rate can be determined using the pressure drop between the two points in the EGR pipe. The diameter of the pipe is constant throughout the flow and the

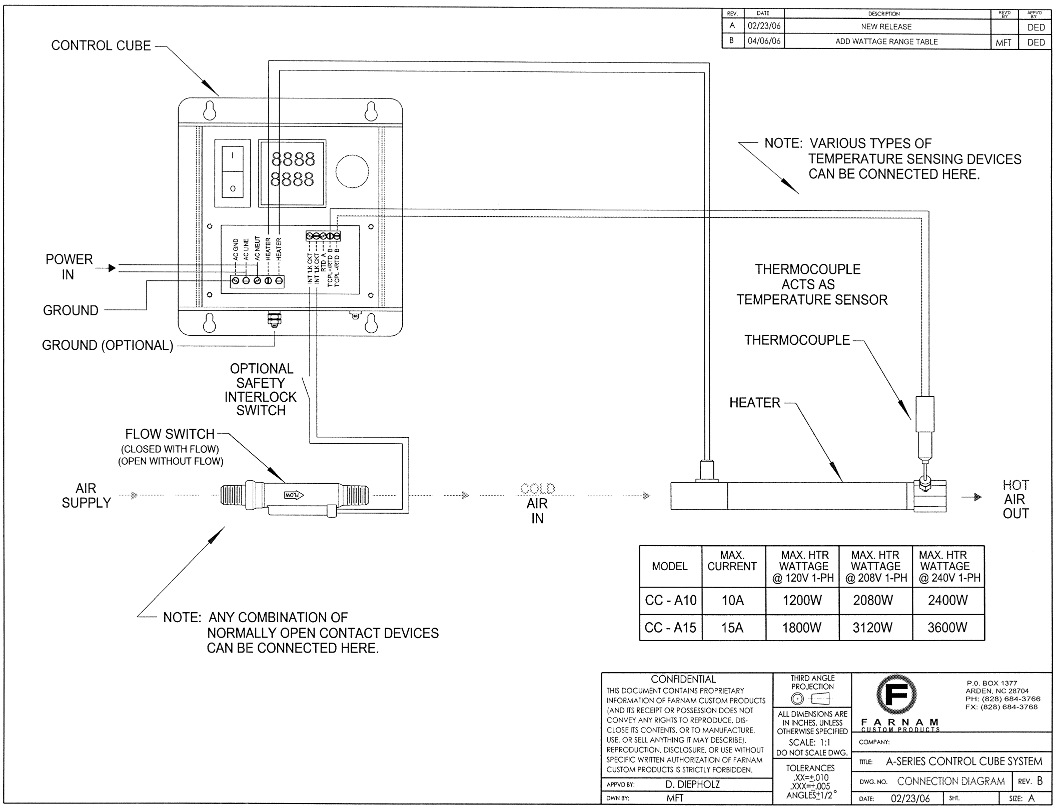

REV.	DATE	DESCRIPTION	REV'D BY	APPV'D BY
A	02/23/06	NEW RELEASE		DED
B	04/06/06	ADD WATTAGE RANGE TABLE	MFT	DED

NOTE: VARIOUS TYPES OF TEMPERATURE SENSING DEVICES CAN BE CONNECTED HERE.

NOTE: ANY COMBINATION OF NORMALLY OPEN CONTACT DEVICES CAN BE CONNECTED HERE.

MODEL	MAX. CURRENT	MAX. HTR WATTAGE @ 120V 1-PH	MAX. HTR WATTAGE @ 208V 1-PH	MAX. HTR WATTAGE @ 240V 1-PH
CC - A10	10A	1200W	2080W	2400W
CC - A15	15A	1800W	3120W	3600W

CONFIDENTIAL
THIS DOCUMENT CONTAINS PROPRIETARY INFORMATION OF FARNAM CUSTOM PRODUCTS (AND ITS RECEIPT OR POSSESSION DOES NOT CONVEY ANY RIGHTS TO REPRODUCE, DISCLOSE ITS CONTENTS, OR TO MANUFACTURE, USE, OR SELL ANYTHING IT MAY DESCRIBE). REPRODUCTION, DISCLOSURE, OR USE WITHOUT SPECIFIC WRITTEN AUTHORIZATION OF FARNAM CUSTOM PRODUCTS IS STRICTLY FORBIDDEN.
APPVD BY: D. DIEPHOLZ
DWN BY: MFT
THIRD ANGLE PROJECTION
ALL DIMENSIONS ARE IN INCHES, UNLESS OTHERWISE SPECIFIED
SCALE: 1:1
DO NOT SCALE DWG.
TOLERANCES
.XX=±.010
.XXX=±.005
ANGLES±1/2°
P.O. BOX 1377
ARDEN, NC 28704
PH: (828) 684-3766
FX: (828) 684-3768
COMPANY:
TITLE: A-SERIES CONTROL CUBE SYSTEM
DWG. NO. CONNECTION DIAGRAM
REV. B
DATE: 02/23/06
SHT.
SIZE: A

Figure B.5: Wiring diagram for air heating element and control cube (Farnam, 2012).

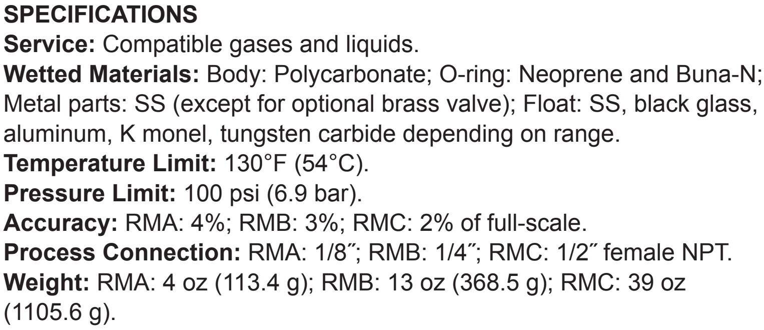

SPECIFICATIONS

Service: Compatible gases and liquids.

Wetted Materials: Body: Polycarbonate; O-ring: Neoprene and Buna-N; Metal parts: SS (except for optional brass valve); Float: SS, black glass, aluminum, K monel, tungsten carbide depending on range.

Temperature Limit: 130°F (54°C).

Pressure Limit: 100 psi (6.9 bar).

Accuracy: RMA: 4%; RMB: 3%; RMC: 2% of full-scale.

Process Connection: RMA: 1/8″; RMB: 1/4″; RMC: 1/2″ female NPT.

Weight: RMA: 4 oz (113.4 g); RMB: 13 oz (368.5 g); RMC: 39 oz (1105.6 g).

Figure B.6: Dwyer flow meter technical data (Dwyer, 2013).

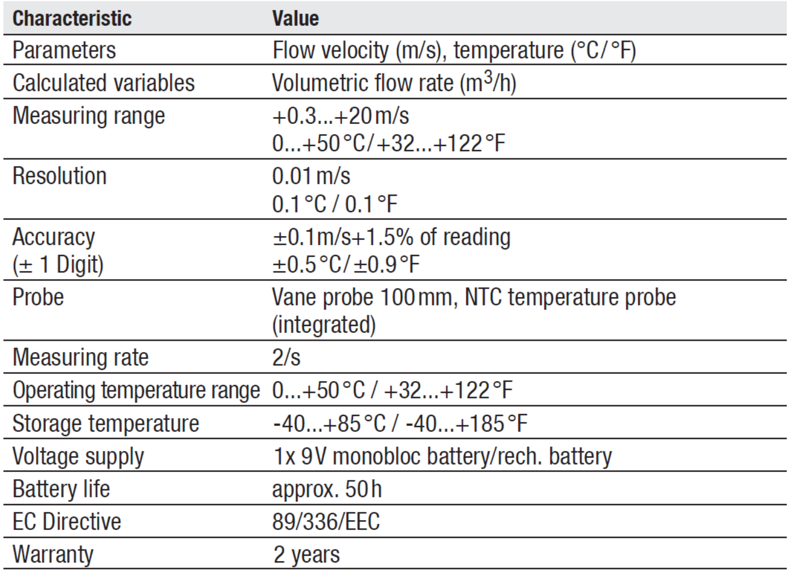

Characteristic	Value
Parameters	Flow velocity (m/s), temperature (°C/°F)
Calculated variables	Volumetric flow rate (m^3/h)
Measuring range	+0.3...+20 m/s 0...+50 °C/+32...+122 °F
Resolution	0.01 m/s 0.1 °C / 0.1 °F
Accuracy (± 1 Digit)	±0.1m/s+1.5% of reading ±0.5 °C/±0.9 °F
Probe	Vane probe 100 mm, NTC temperature probe (integrated)
Measuring rate	2/s
Operating temperature range	0...+50 °C / +32...+122 °F
Storage temperature	-40...+85 °C / -40...+185 °F
Voltage supply	1x 9V monobloc battery/rech. battery
Battery life	approx. 50 h
EC Directive	89/336/EEC
Warranty	2 years

Figure B.7: Testo 417 technical data (Testo, 2012).

flow rate can be calculated using Bernoulli's equation as below:

$$\frac{P_1}{\rho} + 0.5V_1^2 + gH_1 + h_A - h_E - h_L = \frac{P_2}{\rho} + 0.5V_2^2 + gH_2 \qquad \text{(B.1)}$$

where P is the pressure, ρ is the fluid density, V is the fluid flow velocity, g is the gravitational acceleration (9.81 m/s), H is the elevation above a reference point, h_A is the energy added to the system, h_E is the energy removed from the system and h_L is the energy losses from the system. In this case h_A and h_E are assumed to be zero since there is no energy added or removed from the system. For h_L, the friction losses were considered. The pressures P_1 and P_2 were measured at the EGR pipe with the distance $(H_1 - H_2)$ of 1.1 m.

$$\begin{aligned} V_2^2 - V_1^2 &= \frac{2}{\rho}(P_1 - P_2) + 2g(H_1 - H_2) - 2h_L \\ &= 2.22(P_1 - P_2) + 21.58 - 2h_L \qquad \text{(B.2)} \end{aligned}$$

The speeds V_1 and V_2 are assumed to be the same due to the continuity equation for incompressible fluids in constant-area flow. From Equation B.2, h_L can be determined from:

$$h_L = 1.11(P_1 - P_2) + 10.79 \qquad \text{(B.3)}$$

For the incompressible turbulent flow, from the Darcy-Weisbach equation the relation between friction loss and velocity can be written as below:

$$h_L = f\frac{L}{D}\frac{V^2}{2} \qquad \text{(B.4)}$$

where L is pipe length $(H_1 - H_2)$, D is is the hydraulic diameter of the pipe (50 mm) and V is the average velocity of the fluid flow. Equations B.3 and B.4

can be used to solve for V:

$$\begin{aligned}
V^2 &= \frac{2Dh_L}{f(H_1 - H_2)} \\
&= \frac{2(0.05)(1.06(P_1 - P_2) + 10.79)}{f(H_1 - H_2)} \\
&= \frac{0.111(P_1 - P_2) + 1.079}{1.1f} \\
V &= \frac{\sqrt{0.111(P_1 - P_2) + 1.079}}{1.05\sqrt{f}} \qquad \text{(B.5)}
\end{aligned}$$

Because f is a function of V, Equation B.5 must be solved through iteration. The friction factor was solved iteratively using the Colebrook equation (Colebrook, 1939) as below:

$$\frac{1}{\sqrt{f}} = -2\log\left(\frac{e}{3.7D} + \frac{2.51}{Re\sqrt{f}}\right) \qquad \text{(B.6)}$$

where e is the pipe absolute surface roughness. For the coated cast iron, the value for e is 1.28×10^{-4} m (Lamont, 1981). For the initial estimate of the friction factor, an approximation of the implicit Colebrook-White equation (Haaland, 1983) was used as below:

$$\frac{1}{\sqrt{f}} = -1.8\log\left(\left(\frac{e}{3.7D}\right)^{1.11} + \frac{6.9}{Re}\right) \qquad \text{(B.7)}$$

The Reynolds number (Re) is:

$$Re = \frac{\rho VD}{\mu} \qquad \text{(B.8)}$$

where μ is the dynamic viscosity of the exhaust gas. Both the density and dynamic viscosity for the exhaust gas of methane combustion (see Equation A.2) can be calculated using the exhaust gas composition. The exhaust gas consist of a mole of carbon dioxide for every two moles of water vapour and 7.52 moles of nitrogen. Using a mass-weighted average, the dynamic viscosity of the exhaust gas can be calculated as below:

$$\begin{aligned}
\mu &= \frac{44(1.841 \times 10^{-5})}{290.6} + \frac{36(1.265 \times 10^{-5})}{290.6} + \frac{210.6(2.094 \times 10^{-5})}{290.6} \\
&= 1.953 \times 10^{-5} Pa.s \qquad \text{(B.9)}
\end{aligned}$$

The density of the exhaust gas can be calculated as below:

$$P_{mix} = \frac{\rho_{mix}RT}{MW_{mix}} \qquad \text{(B.10)}$$

$$P_i = \frac{\rho_i RT}{MW_i} \qquad \text{(B.11)}$$

$$P_{mix} = \sum_i X_i P_i \qquad \text{(B.12)}$$

where $i \equiv$ species, R is the universal gas constant, $MW \equiv$ mean molecular weight and $X \equiv$ mole fraction. Substituting Equations B.10 and B.11 into Equation B.12 yields:

$$\rho_{mix} \quad = \quad MW_{mix} \sum_i \frac{X_i}{MW_i} \rho_i \tag{B.13}$$

MATLAB code was written to solve Equations B.5, B.8, B.6 and B.7 simultaneously. The code was used to calculate the exhaust gas flow rate in the EGR pipe.

B.8 Ignition System with Gas Safety Interlock

For ignition timing and repetition control, a Techrite AGA6953 model (Techrite, 2014) was used as shown in Figure B.8. The ignition system (Techrite AGA6953) used in this furnace ignition system was equipped with a flame detection system. When a methane flame was burned, the flame detection was intermittent and gave under-voltage intermittent detection to the flame detection probe. This condition triggered the need for an under-voltage detection system. The Siemens Landis Gyr model LGB21 350(A27) (Siemens, 2014) is capable of detecting under-voltage from the flame to assist the flame detection system. The flame detection system also acted as safety gas interlock system. If the flame detection system did not detect the flame, the gas supply was shut off. The specification for the Techrite AGA6953 and Siemens Landis Gyr model LGB21 350(A27) can be found in Figures B.9 and B.10 respectively.

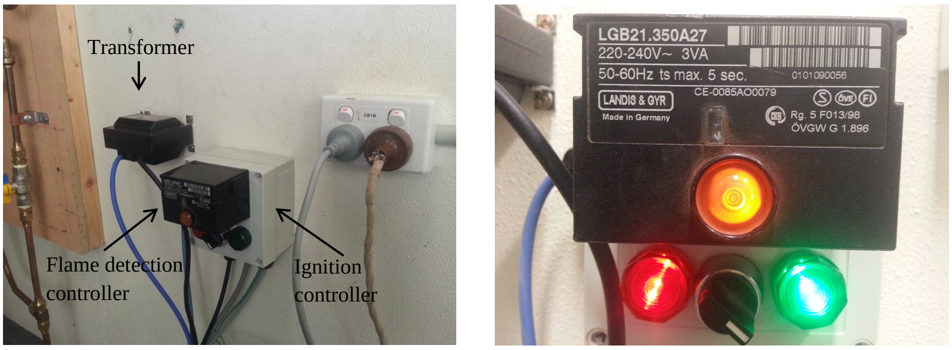

(a) overall control system (b) flame detection controller

Figure B.8: Detail of ignition control system.

B.9 Sample Weather Report

A sample weather report from the USQ internal weather station recorded by The Department of Biological and Physical Sciences, USQ Toowoomba Campus is shown in Figure B.11. The pressure, the relative humidity and the ambient temperature were recorded from sensors on the CODA gas analyser.

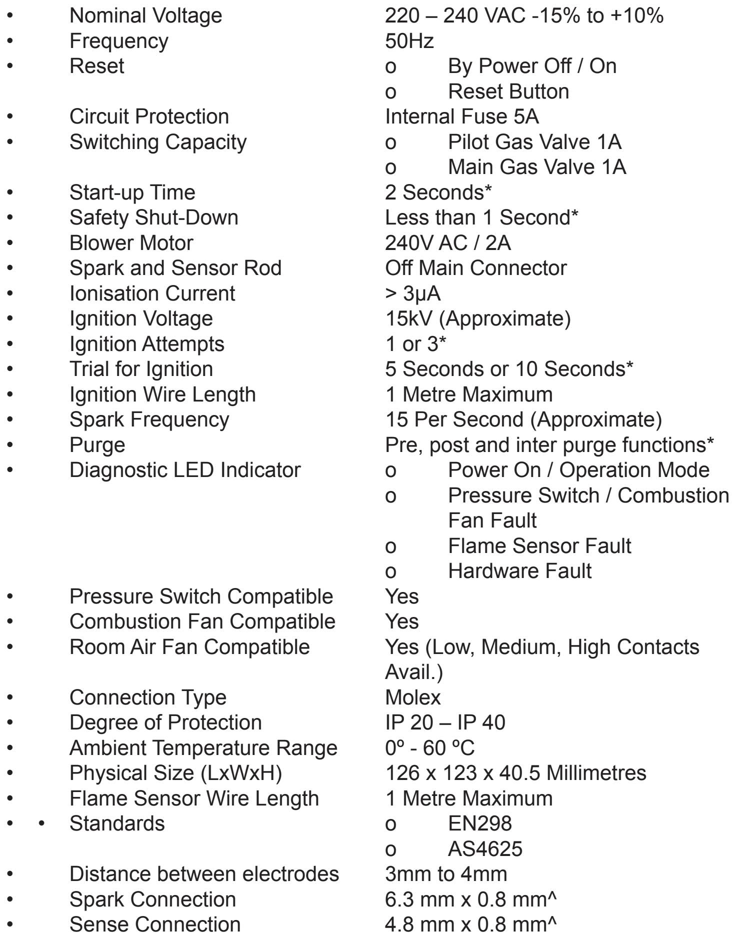

Nominal Voltage	220 – 240 VAC -15% to +10%
Frequency	50Hz
Reset	o By Power Off / On o Reset Button
Circuit Protection	Internal Fuse 5A
Switching Capacity	o Pilot Gas Valve 1A o Main Gas Valve 1A
Start-up Time	2 Seconds*
Safety Shut-Down	Less than 1 Second*
Blower Motor	240V AC / 2A
Spark and Sensor Rod	Off Main Connector
Ionisation Current	> 3µA
Ignition Voltage	15kV (Approximate)
Ignition Attempts	1 or 3*
Trial for Ignition	5 Seconds or 10 Seconds*
Ignition Wire Length	1 Metre Maximum
Spark Frequency	15 Per Second (Approximate)
Purge	Pre, post and inter purge functions*
Diagnostic LED Indicator	o Power On / Operation Mode o Pressure Switch / Combustion Fan Fault o Flame Sensor Fault o Hardware Fault
Pressure Switch Compatible	Yes
Combustion Fan Compatible	Yes
Room Air Fan Compatible	Yes (Low, Medium, High Contacts Avail.)
Connection Type	Molex
Degree of Protection	IP 20 – IP 40
Ambient Temperature Range	0º - 60 ºC
Physical Size (LxWxH)	126 x 123 x 40.5 Millimetres
Flame Sensor Wire Length	1 Metre Maximum
Standards	o EN298 o AS4625
Distance between electrodes	3mm to 4mm
Spark Connection	6.3 mm x 0.8 mm^
Sense Connection	4.8 mm x 0.8 mm^

Figure B.9: Techrite AGA6953 ignition system technical specifications (Techrite, 2014).

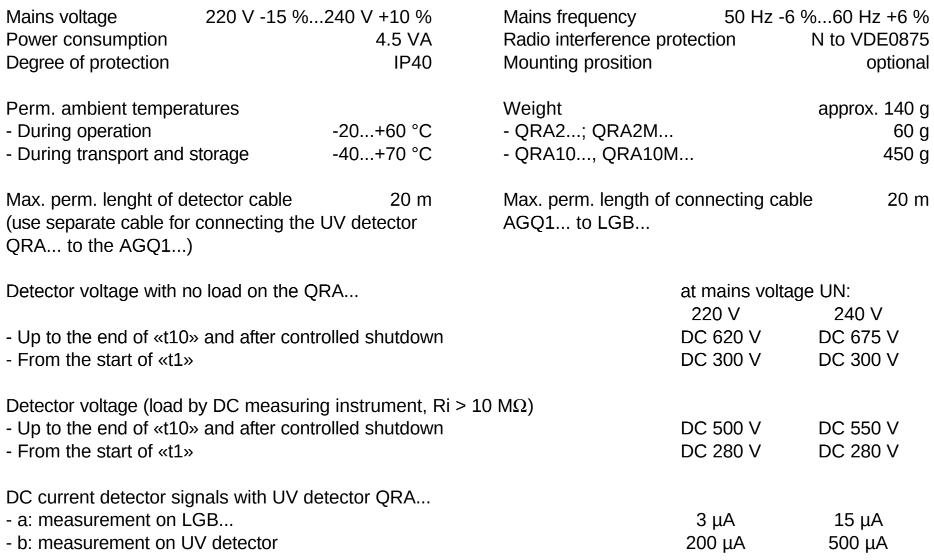

Mains voltage	220 V -15 %...240 V +10 %	Mains frequency	50 Hz -6 %...60 Hz +6 %
Power consumption	4.5 VA	Radio interference protection	N to VDE0875
Degree of protection	IP40	Mounting prosition	optional
Perm. ambient temperatures		Weight	approx. 140 g
- During operation	-20...+60 °C	- QRA2...; QRA2M...	60 g
- During transport and storage	-40...+70 °C	- QRA10..., QRA10M...	450 g
Max. perm. lenght of detector cable (use separate cable for connecting the UV detector QRA... to the AGQ1...)	20 m	Max. perm. length of connecting cable AGQ1... to LGB...	20 m

Detector voltage with no load on the QRA...	at mains voltage UN: 220 V	240 V
- Up to the end of «t10» and after controlled shutdown	DC 620 V	DC 675 V
- From the start of «t1»	DC 300 V	DC 300 V
Detector voltage (load by DC measuring instrument, Ri > 10 MΩ)		
- Up to the end of «t10» and after controlled shutdown	DC 500 V	DC 550 V
- From the start of «t1»	DC 280 V	DC 280 V
DC current detector signals with UV detector QRA...		
- a: measurement on LGB...	3 µA	15 µA
- b: measurement on UV detector	200 µA	500 µA

Figure B.10: flame detection controller Siemens Landis Gyr model LGB21 350(A27) technical specifications (Siemens, 2014).

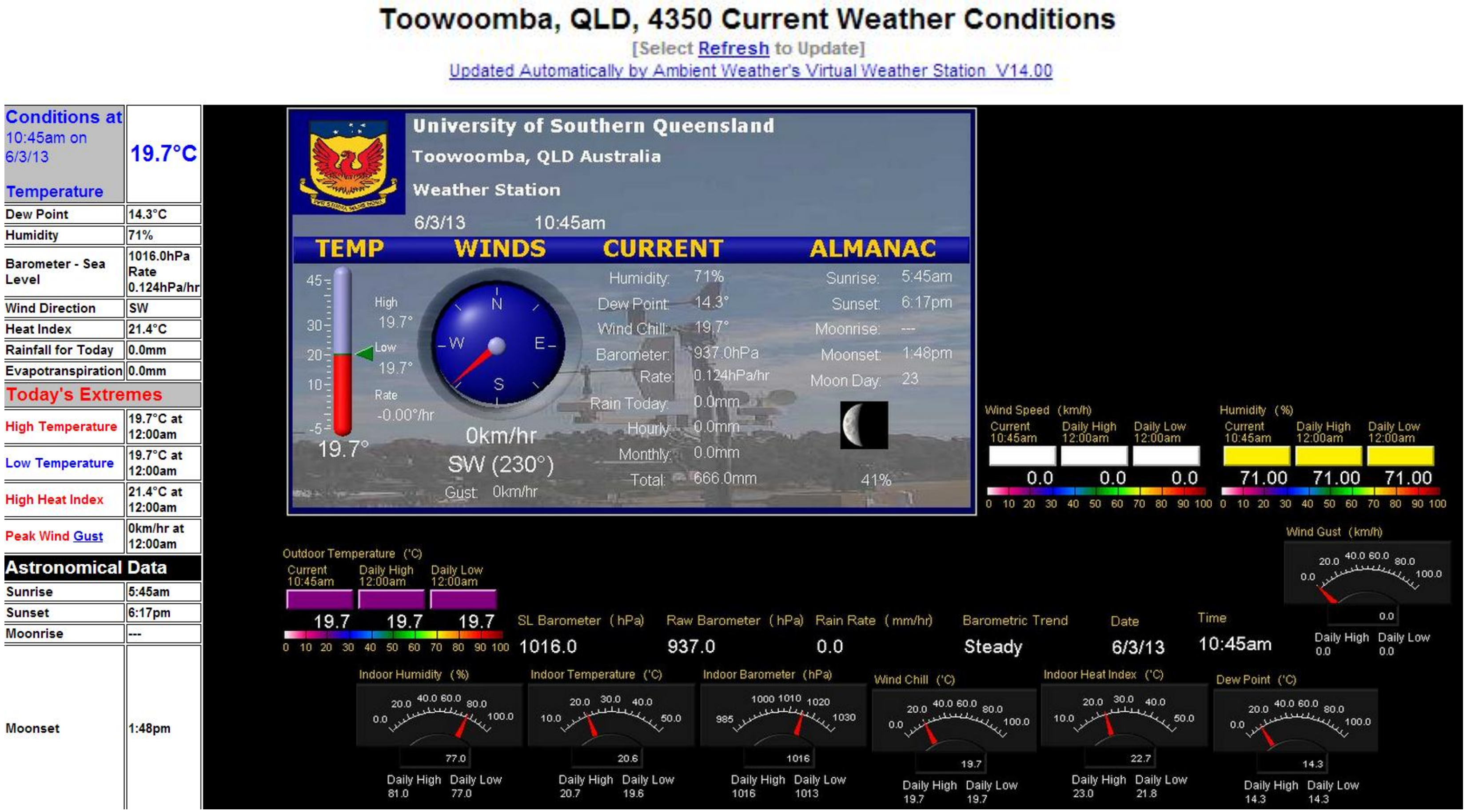

Toowoomba, QLD, 4350 Current Weather Conditions

[Select Refresh to Update]

Updated Automatically by Ambient Weather's Virtual Weather Station V14.00

Conditions at 10:45am on 6/3/13 Temperature	19.7°C
Dew Point	14.3°C
Humidity	71%
Barometer - Sea Level	1016.0hPa Rate 0.124hPa/hr
Wind Direction	SW
Heat Index	21.4°C
Rainfall for Today	0.0mm
Evapotranspiration	0.0mm
Today's Extremes	
High Temperature	19.7°C at 12:00am
Low Temperature	19.7°C at 12:00am
High Heat Index	21.4°C at 12:00am
Peak Wind Gust	0km/hr at 12:00am
Astronomical Data	
Sunrise	5:45am
Sunset	6:17pm
Moonrise	---
Moonset	1:48pm

University of Southern Queensland
Toowoomba, QLD Australia
Weather Station
6/3/13 10:45am

Figure B.11: Sample USQ weather report (USQ, 2013).

Appendix C

Experimental Setup and Ignition Testing

This appendix summarises more information about the combustion chamber setup and ignition testing. The ignition testing consisted of methane premixed combustion, methane non-premixed combustion and biogas combustion.

C.1 Overall Experimental Setup

The overall experimental setup consisting of a gas control panel, a combustion chamber and a data acquisition and measurement system can be seen in Figure C.1. It includes the data acquisition and measurement system control panel and data visual display for the real time monitoring for the thermocouples, pressure transducers, oxidant heating element and lambda sensor. The furnace gas supply piping was installed by a certified gas fitter.

C.2 Ignition Trial

In the experimental work, it was a great challenge to ignite and sustain the ignition for non-premixed, partially premixed and premixed flames. With the suction power of the exhaust extraction, the flow speed exceeded the blow-off velocity, therefore flame stabilisation could not occur. In this furnace system, when the flame ignited, the flame interlock system must sense the flame to provide feedback to the system that the flame was ignited properly. Otherwise the fuel gas supply will be shut off and the flame will blow-off immediately. All the ignition testing was repeated at least three times for each test condition to ensure the collected data were statistically stable. The ignition data for non-premixed, partially premixed and premixed flames are summarised in Table C.1.

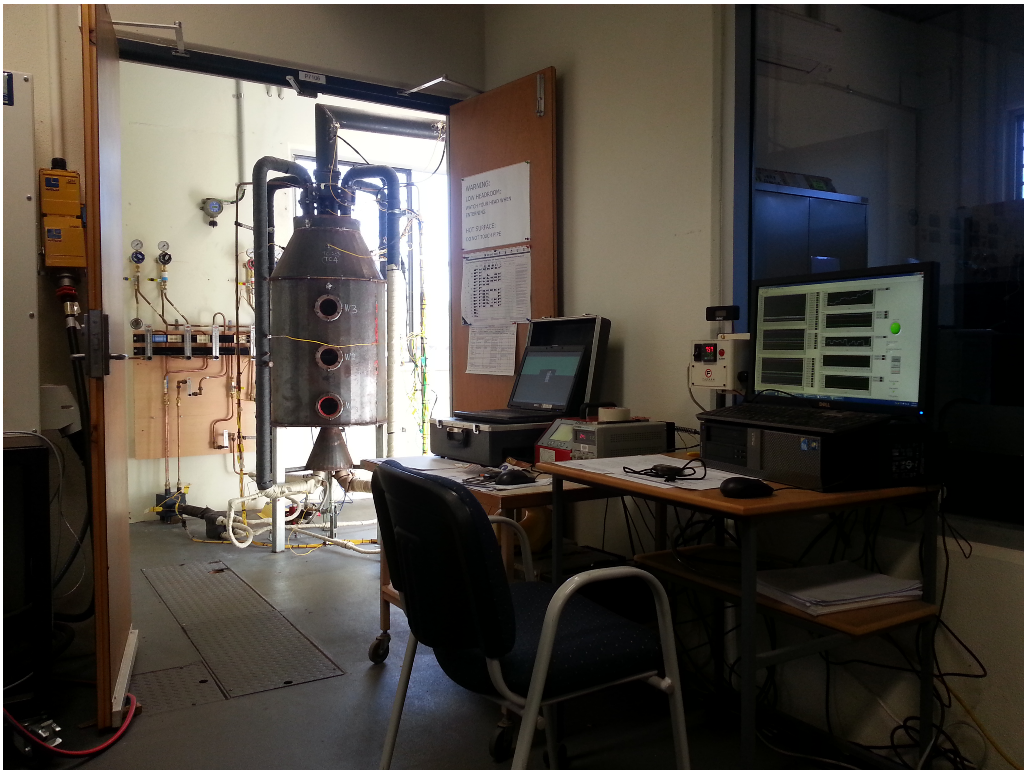

Figure C.1: Overall experimental setup with gas control panel, combustion chamber, data acquisition and measurement system.

.

Table C.1: Summary of ignition started for 15.30 L/min (20 kPa) methane with non-premixed, partially premixed and premixed flames (HY is pre-heating, HN is without preheating and SAN is without secondary air).

Case	**NPF HN**	**NPF HY**	**PPF HN**	**PPF HY**	**PF SAN**
Frame number	28	24	26	19	25
Ignited (sec)	0.93	0.80	0.87	0.63	0.83

C.2.1 Ignition of Non-Premixed Flame

The ignition for the non-premixed flame (NPF) is conducted for non-heated and heated 23.6 L/min secondary air. The non-premixed setting is when the primary air supply is totally closed and only fuel is injected through the central burner pipe. There is a methane supply of 15.30 L/min (20 kPa), zero primary air and 23.6 L/min of non heated secondary air (Figure C.2). The flame ignited at 0.93 seconds after the spark started (frame 28) and was fully steady at 30 seconds after spark started (frame 900). The highest flame height is 241.1 mm at 2.0 seconds after the spark started (frame 60) and the steady flame height at 30 seconds after the spark started (frame 900) is 198.2 mm. The flame experienced rich conditions at 3.0 seconds after the spark started (frame 90) and 5.0 seconds after the spark started (frame 150), the flame height was 192.9 and 208.9 mm respectively. The flame temperature for the steady flame was 1,616.7 K.

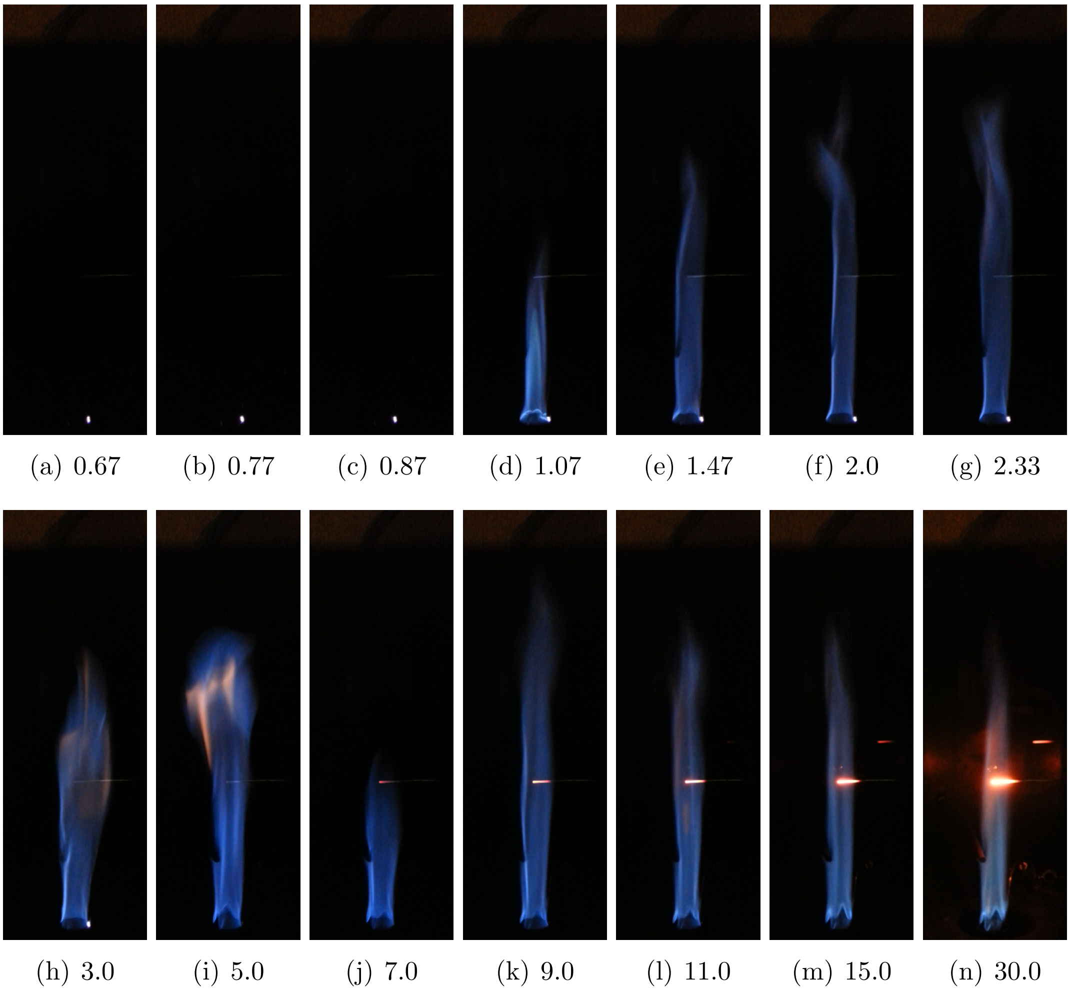
(a) 0.67 (b) 0.77 (c) 0.87 (d) 1.07 (e) 1.47 (f) 2.0 (g) 2.33

(h) 3.0 (i) 5.0 (j) 7.0 (k) 9.0 (l) 11.0 (m) 15.0 (n) 30.0

Figure C.2: Time (seconds) from the beginning of the test for 15.30 L/min (20 kPa) methane non-premixed flame with 23.6 L/min non-heated secondary air without primary air supply with 30 fps recording rate (image size is 100 mm × 300 mm).

The ignition for the non-premixed flame was tested for the methane supply of 15.30 L/min (20 kPa) and 23.6 L/min of heated secondary air flow rate (Figure C.3). Ignition started at 0.77 seconds after the spark started (frame 23) and was fully steady at 30 seconds of combustion (frame 900). As in the previous case, the yellow sooty flame occurred at 3.0 seconds (frame 90) and 5.0 seconds after the spark started (frame 150) when the combustion experienced the rich fuel condition. The highest flame height occurred at 3.0 seconds after the spark started (frame 90) with a height of 278.6 mm. the fully steady flame height at 30.0 seconds after the spark started (frame 900) was 192.8 mm.

The shortest flame height occurred at a similar time of 7.0 seconds after the spark ignited. The ignition of NPF with heated secondary air is quicker than NPF with non-heated secondary air. After the ignition process, during the flame propagation at 3.0 and 5.0 seconds after the spark started, the yellow sooty diffusion flame occurred at the locations where the mixture was rich. This condition occurred for both NPF with non-heated secondary air (Figure C.2) and NPF with heated

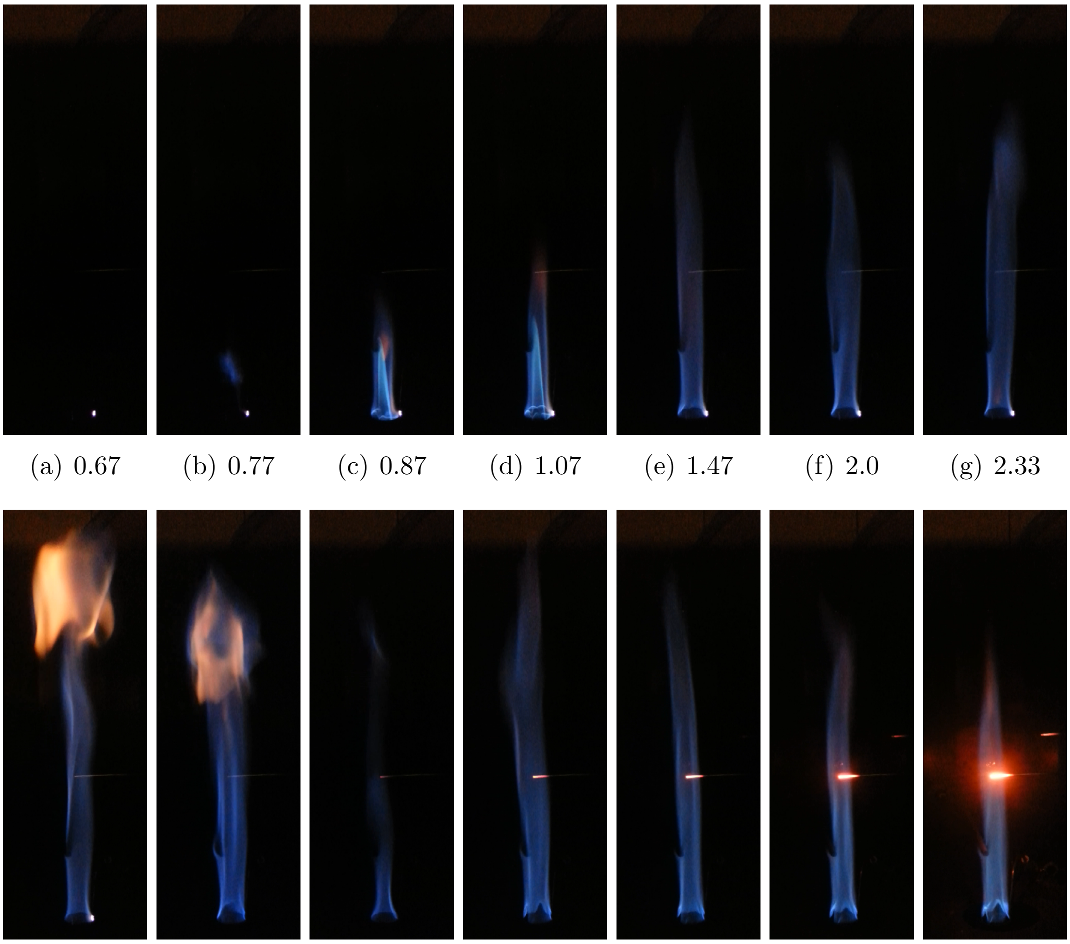

(a) 0.67 (b) 0.77 (c) 0.87 (d) 1.07 (e) 1.47 (f) 2.0 (g) 2.33

(h) 3.0 (i) 5.0 (j) 7.0 (k) 9.0 (l) 11.0 (m) 15.0 (n) 900

Figure C.3: Time (seconds) from the beginning of the test for 15.30 L/min (20 kPa) methane non-premixed flame with 23.6 L/min heated secondary air without primary air supply with 30 fps recording rate (image size is 100 mm × 300 mm).

secondary air (Figure C.3). Occurrence of the yellow sooty flame of NPF with heated secondary air is quicker than NPF with non-heated secondary air which was at 3.0 seconds and 5.0 seconds respectively.

C.2.2 Ignition of Partially Premixed Flame

The ignition for the partially premixed flame (PPF) was conducted for non-heated and heated secondary air and reported in the subsection below. The partially premixed setting means that the fuel and primary air are injected downstream of the fuel nozzle. The mixture was again mixed with secondary air at the burner nozzle just before the flame ignited. Methane at 15.30 L/min (20 kPa) was partially premixed with atmospheric air downstream of the fuel nozzle and mixed with non-heated secondary air at 23.6 L/min (Figure C.4). The flame was fully steady after 30 seconds of the ignition. The highest flame during the unstable flame propagation after the ignition was at 3.0 seconds after the spark ignited (frame 90) which is 241.1 mm. At 5.0 seconds (frame 150) and 7.0 seconds after the spark started (frame 210), the flame experienced the flame cut and lift-off. The fully steady flame at 45 seconds after the spark started (frame 1,350) is divided into two zones. The flame height for the primary zone is 42.9 mm and the secondary flame zone including the flame brush is 128.6 mm.

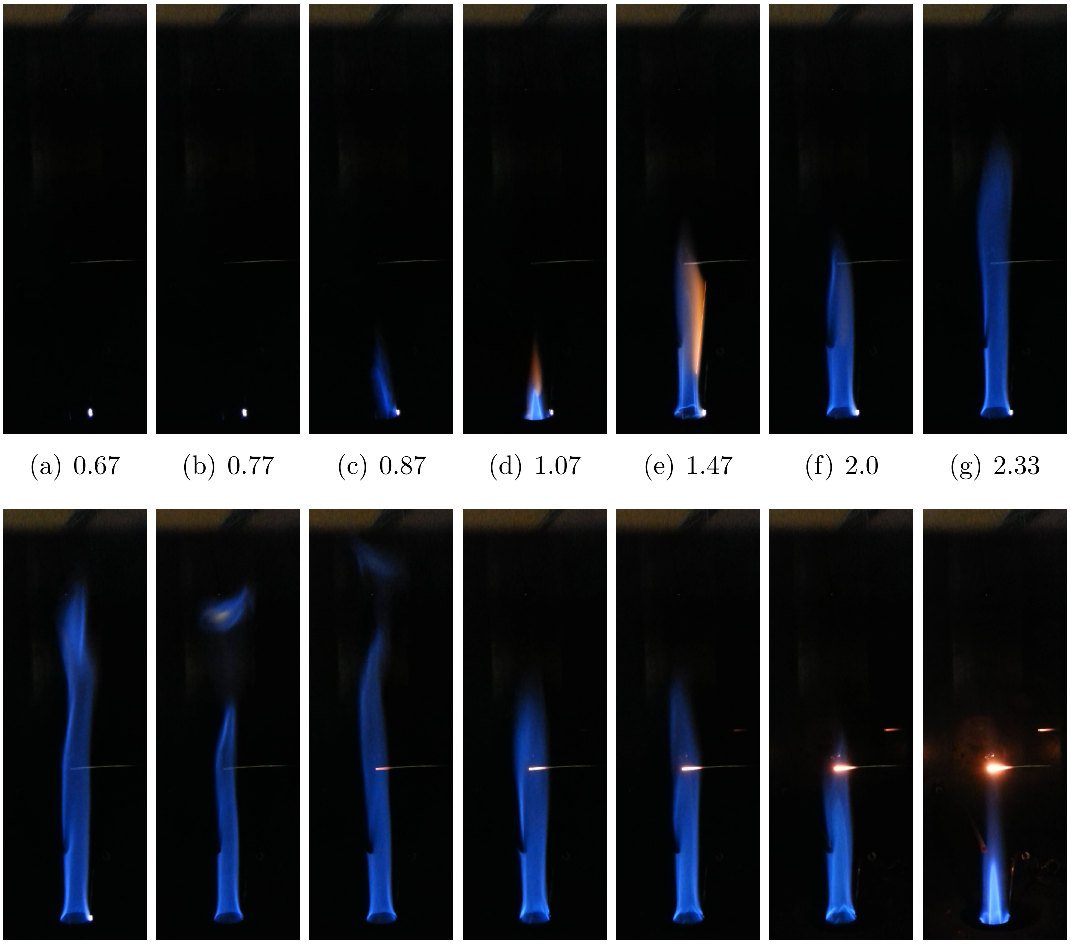
(a) 0.67 (b) 0.77 (c) 0.87 (d) 1.07 (e) 1.47 (f) 2.0 (g) 2.33

(h) 3.0 (i) 5.0 (j) 7.0 (k) 9.0 (l) 11.0 (m) 15.0 (n) 900

Figure C.4: Time (seconds) from the beginning of the test for 15.30 L/min (20 kPa) methane partially premixed flame with 23.6 L/min heated secondary air with 30 fps recording rate (image size is 100 mm × 300 mm).

Methane at 15.30 L/min (20 kPa) was partially premixed with atmospheric air downstream of the fuel nozzle and then mixed with secondary air at 47.2 L/min heated to 673 K (Figure C.5). The flame ignited at 0.63 seconds after the spark started (frame 19), was nearly steady at 30 seconds after the spark started (frame 900) and fully steady at 45 seconds after the spark started (frame 1,350). At 2.3 seconds (frame 70) and 5.0 seconds after the spark started (frame 150), the flame reached the fuel rich condition and created a yellow sooty flame. The highest flame occurred at 2.3 seconds after the spark started (frame 70) with a height of 262.5 mm. The steady flame had two zones with a blue cone and diffusion flame zone with height of 91.1 mm and 192.9 mm respectively.

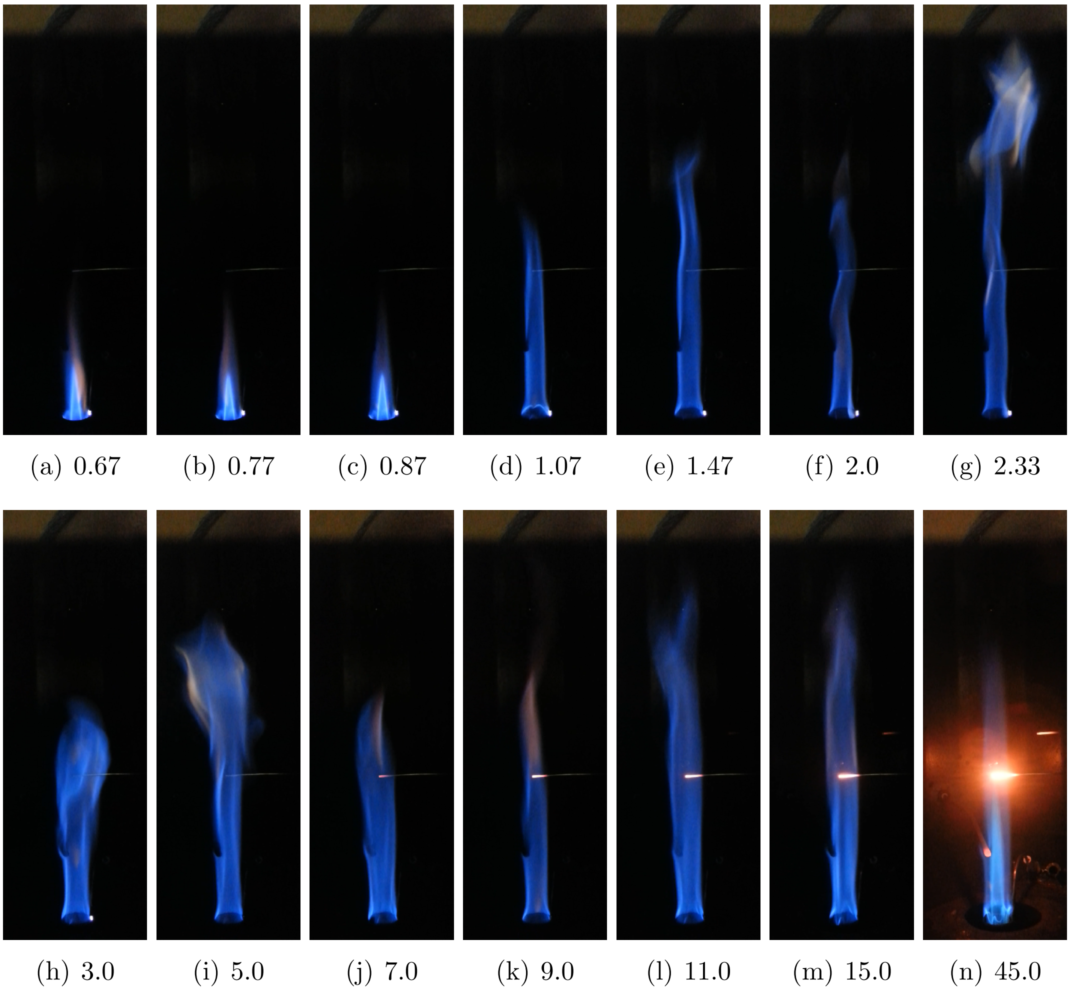

(a) 0.67 (b) 0.77 (c) 0.87 (d) 1.07 (e) 1.47 (f) 2.0 (g) 2.33

(h) 3.0 (i) 5.0 (j) 7.0 (k) 9.0 (l) 11.0 (m) 15.0 (n) 45.0

Figure C.5: Time (seconds) from beginning of the test for 15.30 L/min (20 kPa) methane partially premixed flame with 23.6 L/min heated secondary air with 30 fps recording rate (image size is 100 mm × 300 mm).

C.2.3 Ignition of Premixed Flame

The premixed flame (PF) ignition with step by step flame image can be seen in Figure C.6. Methane at 15.30 L/min (20 kPa) was premixed with atmospheric air downstream of the fuel nozzle without secondary air. The flame ignited 0.83 seconds after the spark started (frame 25) and was fully steady after 30 seconds of ignition. The highest flame during the unstable flame propagation after the ignition was at 2.0 seconds after the spark started (frame 60) which was 267.9 mm. The steady flame at 30 seconds after the flame ignited was divided into two zones. The flame height for the primary zone was 53.6 mm and the secondary flame zone including the flame brush was 91.1 mm. In the premixed flame, a yellow sooty flame did not occur because the mixture cannot become fuel rich.

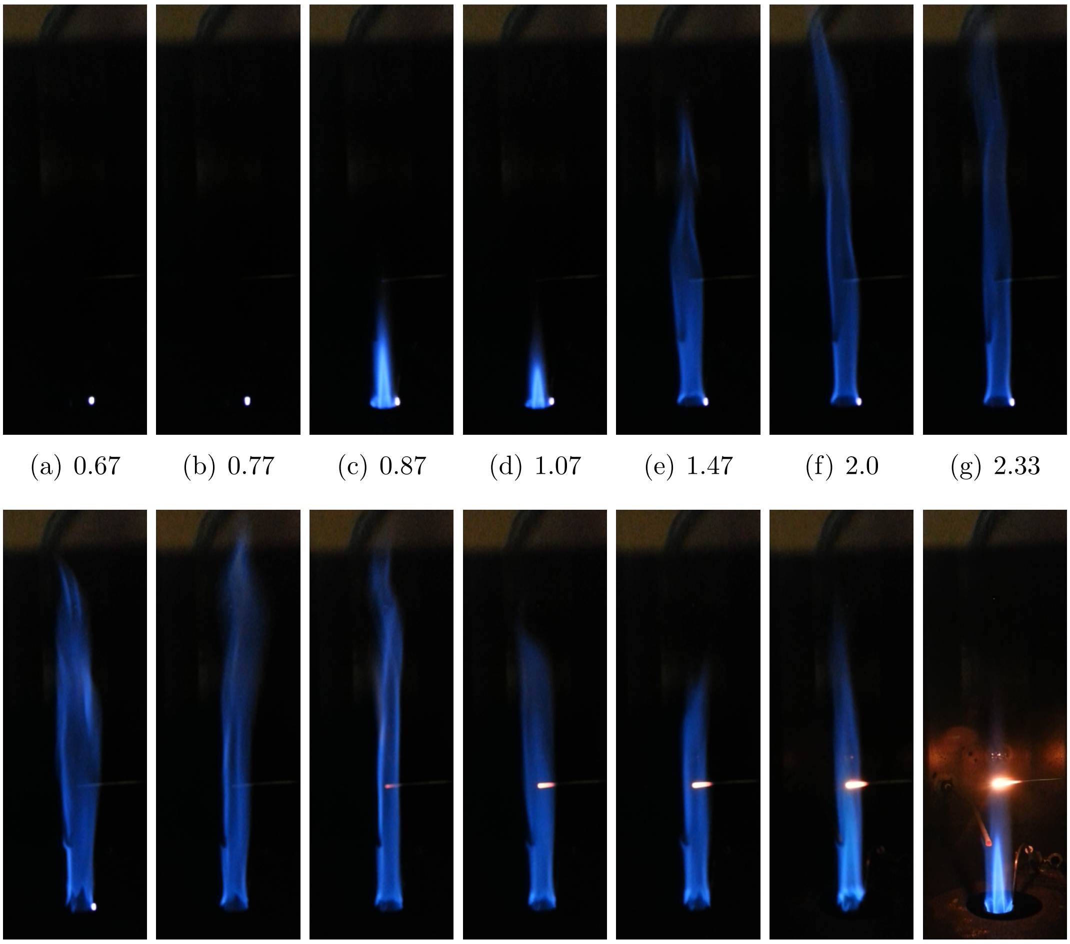
(a) 0.67 (b) 0.77 (c) 0.87 (d) 1.07 (e) 1.47 (f) 2.0 (g) 2.33

(h) 3.0 (i) 5.0 (j) 7.0 (k) 9.0 (l) 11.0 (m) 15.0 (n) 30.0

Figure C.6: Time (seconds) from beginning of the test for 15.30 L/min (20 kPa) methane premixed flame without secondary air with 30 fps recording rate (image size is 100 mm × 300 mm).

C.2.4 Ignition of Biogas Flame

The ignition of biogas is much harder than methane and it is easier to blow-off after the ignition spark is deactivated. Figure C.7 shows an example case of biogas ignition at 0.97 seconds after the spark started (frame 29) and blow-off at 4.87 seconds after the spark started (frame 146). This blow-off occurred due to the presence of carbon dioxide in the fuel stream. A second ignition trial was successful and is reported in Figure 5.14.

C.2.5 Ignition Without Exhaust Extraction Fan

The ignition test was conducted for the non-premixed flame without an exhaust fan. The exhaust fan gives the extraction pressure of 13.7 Pa in normal mode function. In addition, the extraction power from the exhaust fan helps to induce the air from the primary air supply. When this exhaust fan is in off mode and the primary air valve is closed the combustion depends on its air supply from

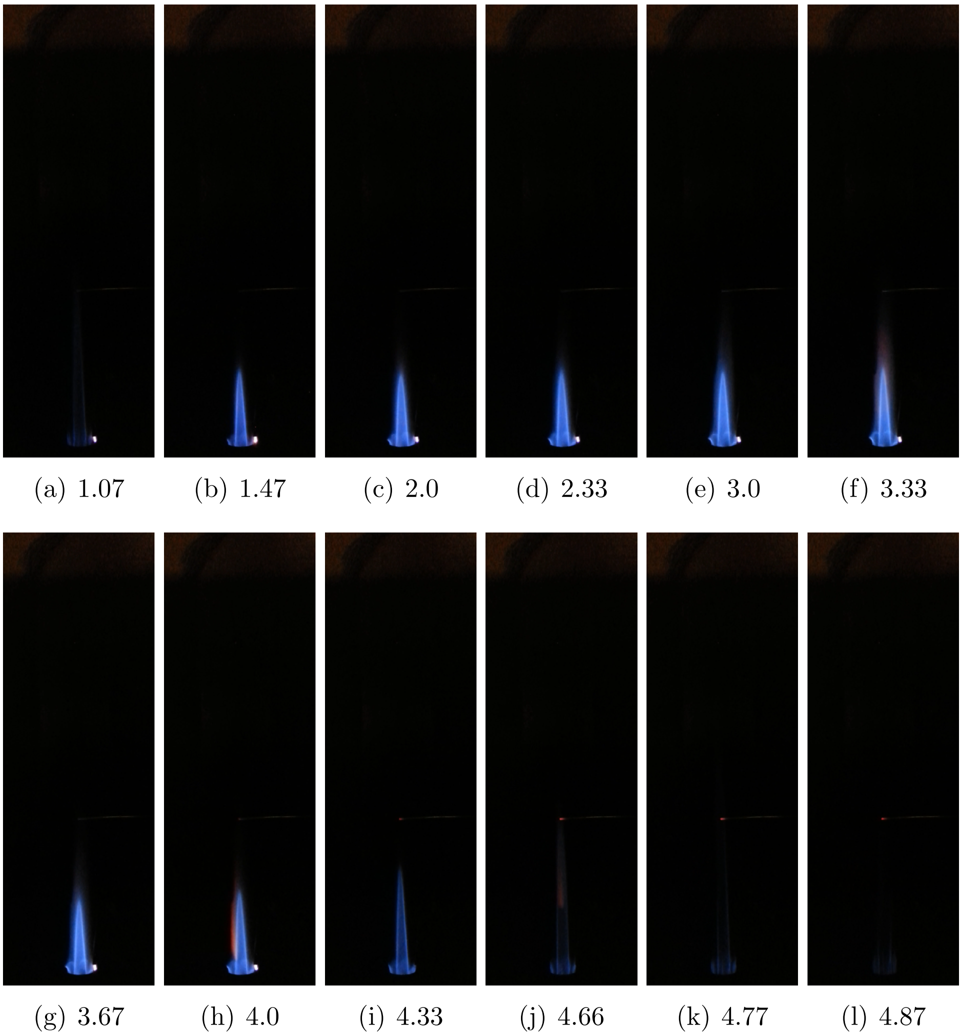
(a) 1.07 (b) 1.47 (c) 2.0 (d) 2.33 (e) 3.0 (f) 3.33

(g) 3.67 (h) 4.0 (i) 4.33 (j) 4.66 (k) 4.77 (l) 4.87

Figure C.7: Time (seconds) from beginning of the test for 15.30 L/min (20 kPa) Biogas non-premixed flame with 23.6 L/min secondary air with 30 fps recording rate (image size is 100 mm × 300 mm).

the secondary air. The ignition test was conducted with a methane supply at 10.82 L/min (10 kPa) with 11.8 L/min non heated secondary air. The ignition started at 2.7 seconds after the spark started (frame 80) and the flame blew out at 4.17 seconds after the spark started (frame 125) (Figure C.8). From frame 105 onward, the yellow sooty flame can be seen due to rich conditions and lack of oxygen to complete the combustion.

C.2.6 Unsuccessful Ignition

The ignition for non-premixed conditions was tested for the methane supply of 40 kPa and various air flow rates (Figure C.9). These tests were run consecutively with all the settings fixed and the air and fuel flow rates were stable after a few tests. The tests were repeated more than three times for all cases. The location of the igniter was fixed and the exhaust gas was purged and sucked-out

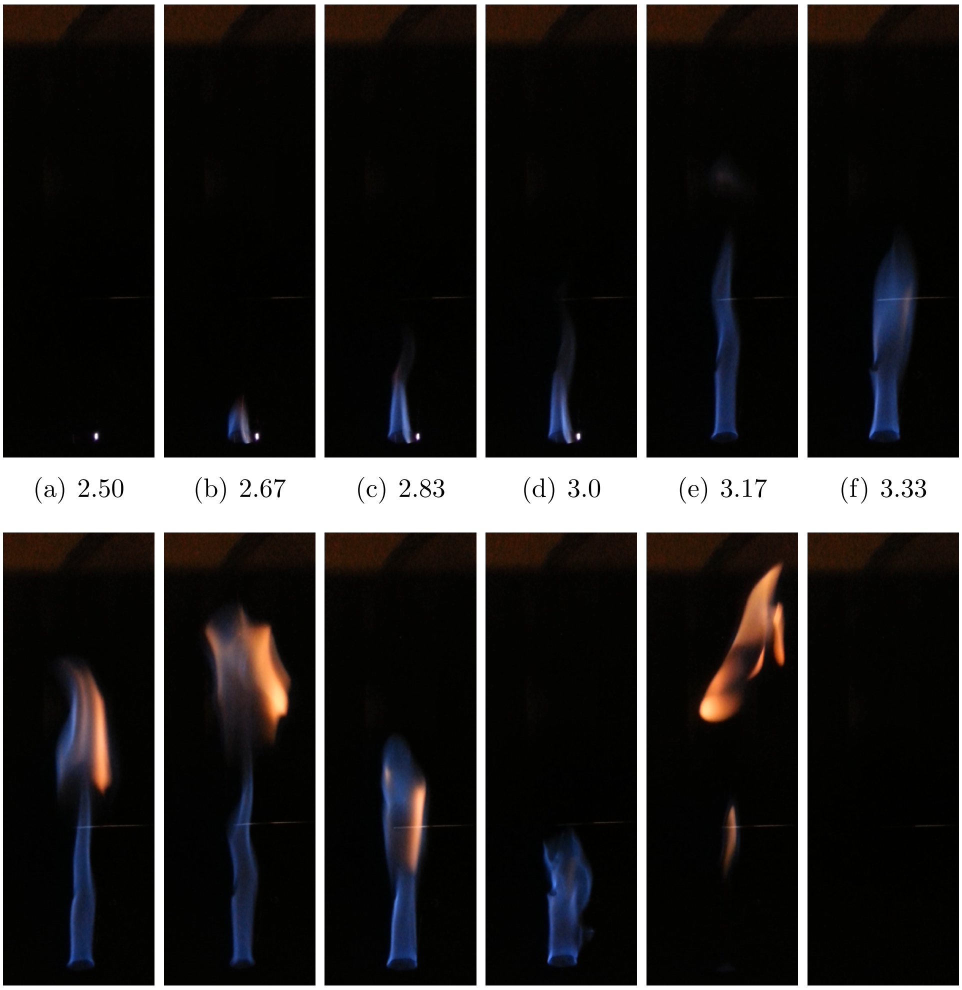
(a) 2.50 (b) 2.67 (c) 2.83 (d) 3.0 (e) 3.17 (f) 3.33

(g) 3.50 (h) 3.67 (i) 3.83 (j) 4.0 (k) 4.17 (l) 4.33

Figure C.8: Time (seconds) from beginning of the test for 10.82 L/min (10 kPa) methane non-premixed flame with 11.8 L/min non-heated secondary air without primary air supply and exhaust fan off with 30 fps recording rate (image size is 100 mm × 300 mm).

after each test. The air flow rates tested ranged from 35.4 L/min to 70.8 L/min. Figure C.9(a) shows the chamber's temperature recorded for the ignition testing and the flame ignition duration for all four air flow rates. The result shows that for the air flow rates of 70.8 L/min and 35.4 L/min, the flame ignited for 5 seconds but then was blown-off. These cases were unsuccessful because the ignited flame was blown-off by the supplied air, possibly due to an unstable air flow rate at the beginning of the test. After a few attempts, the ignited flames were sustained. For the air flow rates of 47.2 L/min and 59.0 L/min, the flame was ignited and blown-off after 36 and 40 seconds respectively. Further testing was done for the air supply in the range of 48.3 L/min to 141.5 L/min. The ignition was successful and sustained the flame for air supply of 35.4 L/min and 44.8 L/min for durations of 38 and 37 seconds respectively. The temperature record for the test can be seen in Figure C.9(b).

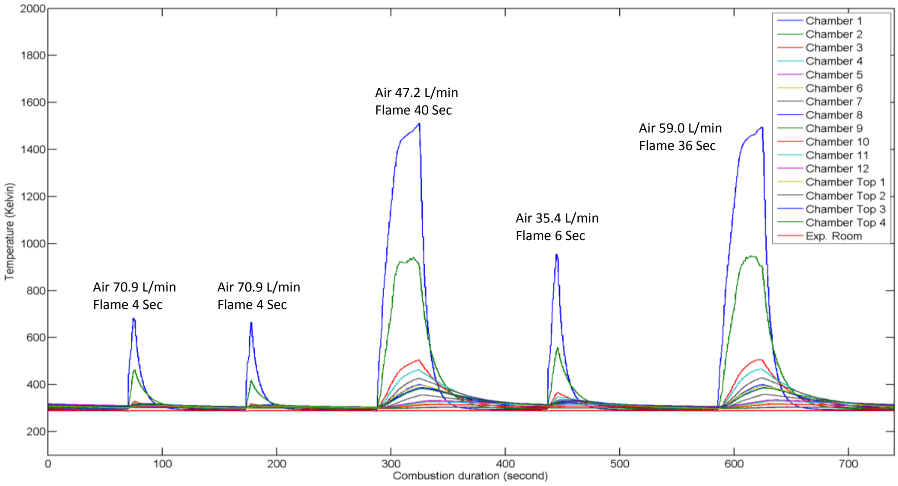

(a) First test.

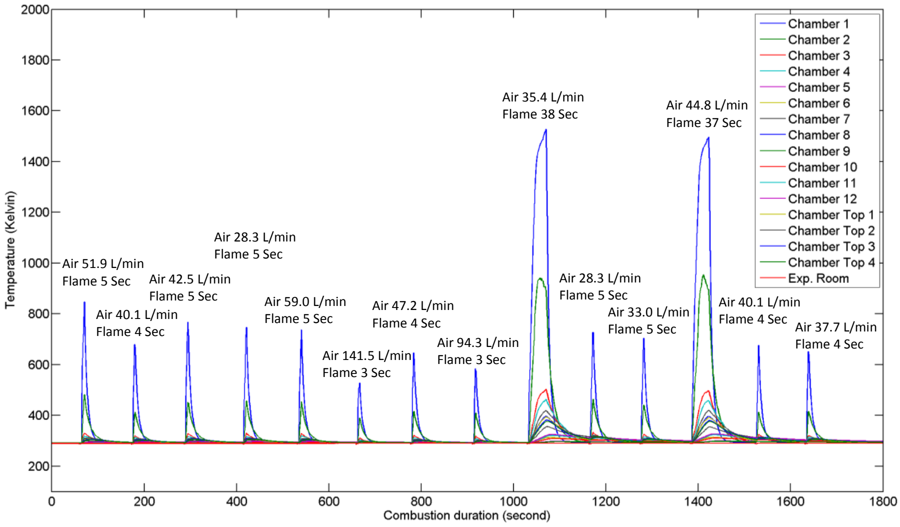

(b) Second test.

Figure C.9: Ignition testing for non-premixed flame for 24.2 L/min of methane flow rate.

.

Appendix D

Additional Numerical Results

This appendix summarises additional numerical results for methane and biogas flames. Both fuels were simulated at 10.82 L/min (10 kPa) with $\lambda = 3.81$. The details of the chamber temperature and exhaust combustion product are shown in the figures below.

D.1 Methane Flame

The numerical results for methane-air with λ of 3.81 are shown in Figures D.1 to D.3. The chamber temperature at full range and restricted range of 299 K to 500 K can be seen in Figure D.1. The flame temperature is 1,495 K and the wall temperature is about 320 K. Figure D.2 shows the combustion product of unburned hydrocarbon, oxygen, water vapour, oxide of nitrogen, carbon dioxide and carbon monoxide. The methane distribution in Figure D.2(a) shows that all fuel is consumed and left no trace of unburned hydrocarbon in the exhaust and EGR pipe. For oxygen in Figure D.2 (b), the excess oxygen in the exhaust pipe is 8.41 % and in the downstream of the EGR is 16.61 %. The oxygen in the supply air is diluted by the EGR by a factor of 20.94 %: from 21.01 % to 16.61 %. This is because the oxygen mole fraction in the EGR is much lower than the oxygen mole fraction in the secondary air supply. The oxygen mole fraction at the combustion (flame) zone is almost zero due to it being consumed by the combustion process in the chemical reaction with the methane.

Figure D.2(c) shows the contour of the water vapour for the combustion chamber. Except for the flame zone, the water vapour is in low concentration throughout the entire combustion chamber and EGR pipes. The water vapour is high at the flame area due to the intense chemical reaction that produces the water vapour. It is then distributed to other areas in the combustion chamber. Figure D.2(d) shows that the NO_x of the combustion chamber is high at the flame area due to the chemical reaction still being incomplete. When it is completed, the NO_x is detected as 1.0 ppm at the exhaust and EGR pipes. Figure D.2(e) shows the

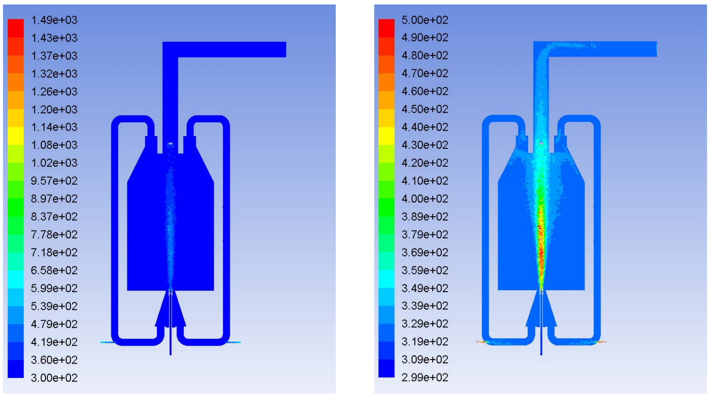

(a) Full range (b) 299–500K

Figure D.1: Temperature contour for combustion of 10.82 L/min (10 kPa) methane at λ 3.81.

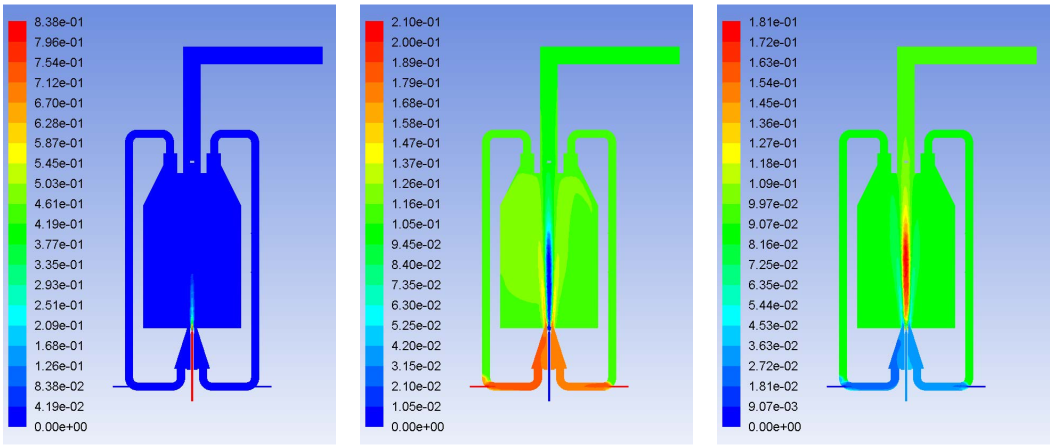

(a) CH_4 (b) O_2 (c) H_2O

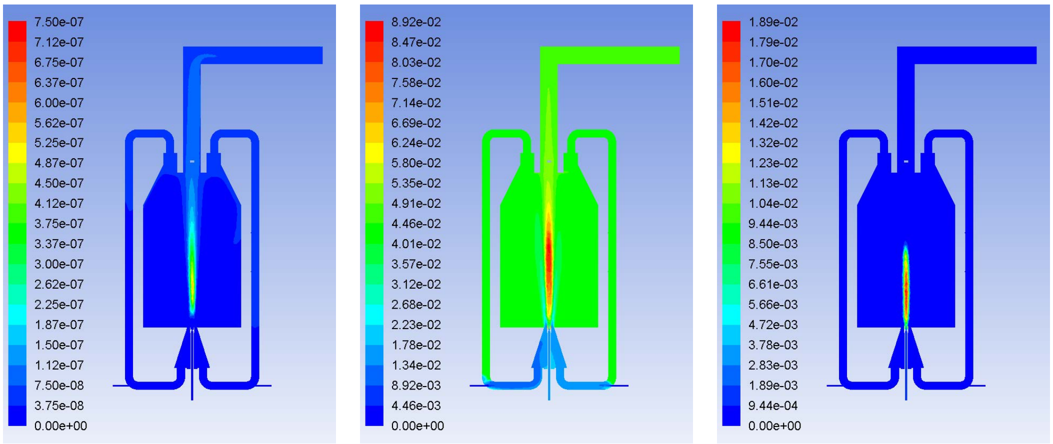

(d) NO_x (e) CO_2 (f) CO

Figure D.2: Combustion products for combustion of 10.82 L/min (10 kPa) methane at $\lambda = 3.81$.

contour of the carbon dioxide which has the same behaviour as the water vapour because it is produced in the same manner. Figure D.2(f) shows the contour of the carbon monoxide which is only detected at the flame area. This carbon monoxide was detected during the continuous chemical reactions (combustion process), but the reactions are quickly completed to produce carbon dioxide as a combustion product.

Figure D.3 shows the chamber density, velocity magnitude and pressure. Beside the flame and the location where the chemical reaction occurred, the chamber density is about 1.02–1.16 kg/m^3. The density is low at the location of the chemical reaction and high velocity stream. The maximum velocity of 22.33 m/s occurred at the air/fuel nozzle burner. The pressure distribution is uniformly distributed with a low level of pressure through out the combustion chamber. The pressure is slightly high at the air and fuel supply inlets, as can be seen in Figure D.3(c).

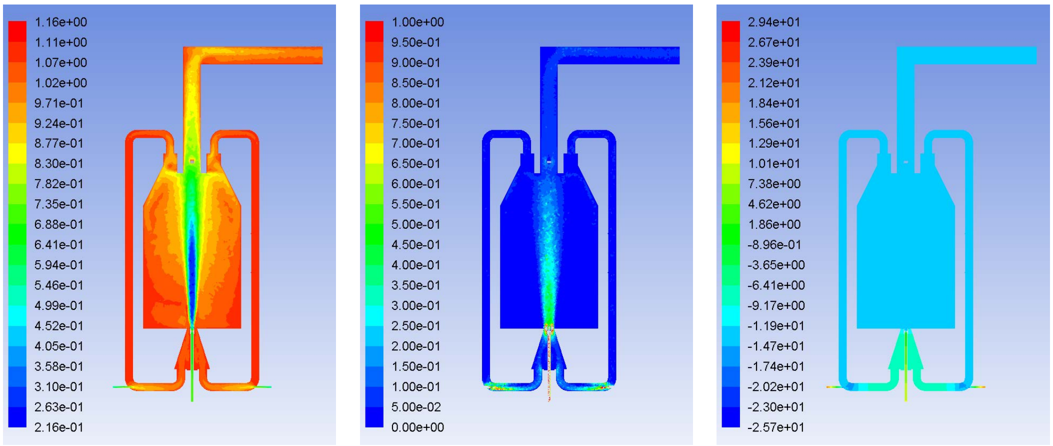

(a) Density (b) Velocity magnitude (c) Pressure

Figure D.3: Chamber density, velocity magnitude and gauge pressure for combustion of methane at $\lambda = 3.81$.

D.2 Biogas Flame

The numerical results for biogas-air with λ of 3.81 are shown in Figures D.4 to D.6. The chamber temperature at full range and restricted range of 299–500 K can be seen in Figure D.4. The flame temperature is 1,375 K and the wall temperature is about 319 K. Figure D.5 shows the species distribution for the numerical simulation. The methane distribution in Figure D.5(a) shows a similar result to methane (Figure D.2(a)). For oxygen in Figure D.5(b), the excess oxygen in the exhaust pipe is 9.80 % and in the downstream of the EGR is 16.60 %. The oxygen in the supply air is diluted by the EGR by a factor of 20.99 %: from 21.01 % to 16.60 %. Similar to the methane flame, the oxygen mole fraction in EGR is much lower than the oxygen mole fraction in the secondary air supply. The oxygen mole fraction at the flame zone is almost zero due to it being consumed by the combustion process in the chemical reaction with the methane.

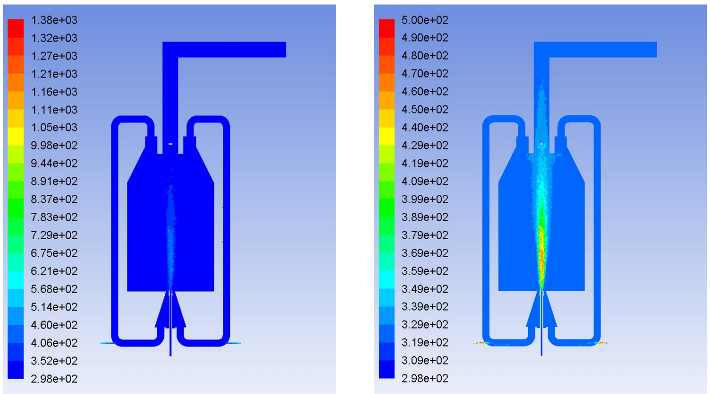

(a) Full range (b) 299–500K

Figure D.4: Temperature contour for combustion of biogas at $\lambda = 3.81$.

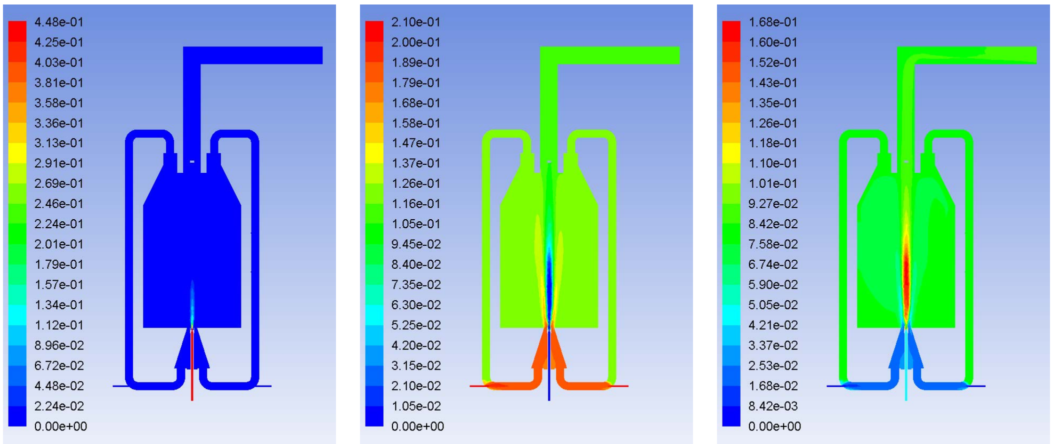

(a) CH_4 (b) O_2 (c) H_2O

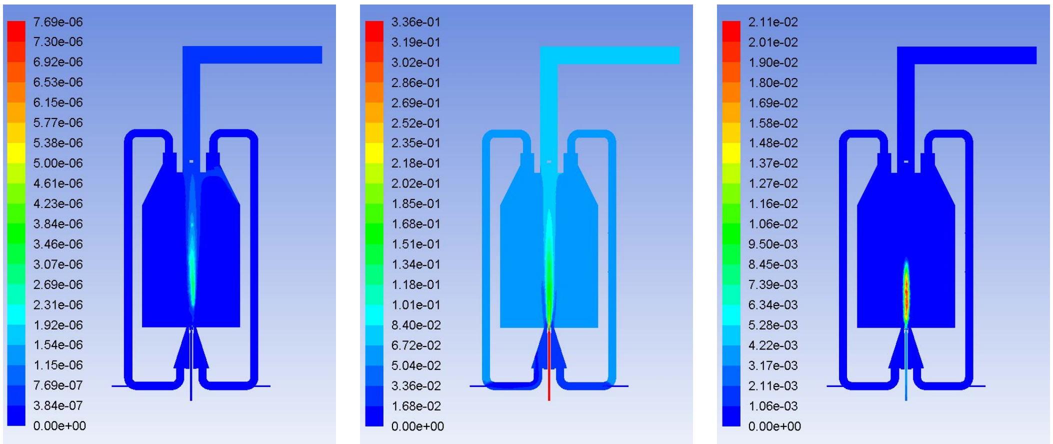

(d) NO_x (e) CO_2 (f) CO

Figure D.5: Combustion products for combustion of 10.82 L/min (10 kPa) biogas at $\lambda = 3.81$.

Figure D.5 shows the contour of unburned methane, excess oxygen, water vapour, oxide of nitrogen, carbon dioxide and carbon monoxide for the combustion chamber. Except for the carbon dioxide, all other contours show the a similar trend to

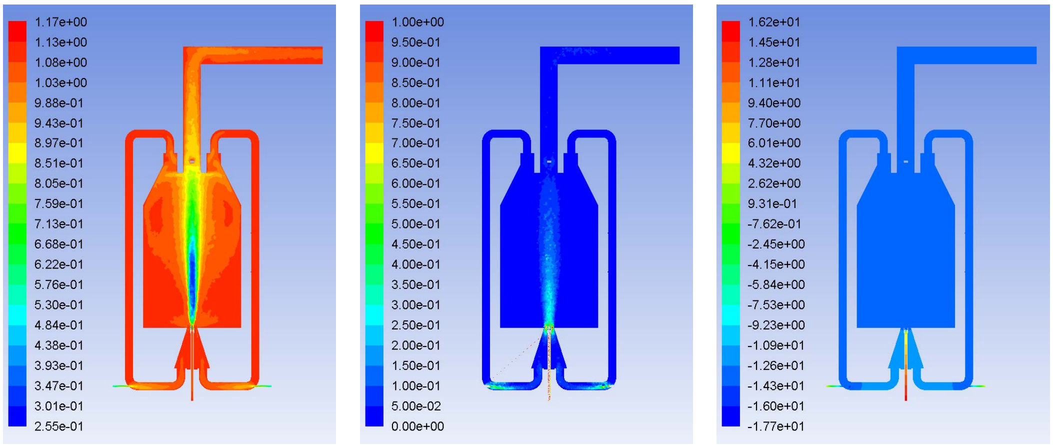

(a) Density (b) Velocity magnitude (c) Pressure

Figure D.6: Chamber density, velocity magnitude and gauge pressure for combustion of biogas at $\lambda = 3.81$.

the methane flame (Figure D.2). The carbon dioxide shows a higher concentration in the exhaust gas due to its presence in the biogas fuel, unlike the methane fuel. The carbon dioxide in the biogas fuel is not involved in the combustion and is released together with the exhaust gas. Figure D.6 shows the chamber density, velocity magnitude and pressure. Beside the flame and the location where the chemical reaction occurred, the chamber density is about 1.03–1.17 kg/m^3. The density is low at the location of the chemical reaction and high velocity stream. The maximum velocity of 13.60 m/s occurred at the air/fuel nozzle burner. The pressure distribution is uniformly distributed with a low level of pressure through out the combustion chamber. The pressure is slightly high at the air and fuel supply inlets, as can be seen in Figure D.6(c).

Appendix E

Detailed Experimental Work Procedure and Safety

This appendix discusses details about safety measures and standard operating procedures for the experimental work. The safety system includes a gas detection system, gas interlock system and room air ventilation. Step by step work procedures are detailed for pre-start-up procedure, combustion chamber air purging procedure, normal start-up and operating procedure, normal shut down procedure and emergency shut down procedure.

E.1 Commissioning of Test Equipment

Prior to experimental work procedures, all equipments and instrumentation was tested. The pre-startup procedure was carried out to initialise and start the equipment to be properly prepared for the experimental work. Before the flame temperature was recorded, the thermocouples were checked by reading at room temperature and were compared with an external thermometer. Room temperature was also monitored simultaneously throughout the experimental work using a K-type thermocouple (Table 4.6). The flame was ignited with spark ignition and reached a steady state before any measurement was taken. Before the measurement was started, the burner was run at low gas injection (1.0 m/s) for around five minutes to reach a steady state combustion flame. These practices are crucial to ensure the data collected was reliable at the stable flame propagations. Then all the measurements were for two minutes and monitored for readings stability. Immediately after this procedure was completed, the test procedures were executed.

E.2 Safety Measures

Safety measures include a gas detection system, automatic burner safety shut-off system, burner safety cover and experimental room air ventilation as listed below.

E.2.1 Gas Detection System

A gas leak from the pipe line or too much unburned gas from the burner itself is a hazard for unwanted burning at inappropriate locations outside the burner. Therefore a gas detection system was installed in the combustion laboratory (Figure E.1). The gas detection system will trigger and cut the gas supply from the gas cylinder when leaked gas is detected by the wall gas sensors (Figure E.1(a)) or the water drain gas detector (Figure E.1(b)). The gas supply will be cut off at the outside pipeline near to the gas cylinder.


(a) (b) (c)

Figure E.1: Gas detection system (a) wall gas detection sensor (b)water drain gas detector (c) gas detection system control panel.

The combustion laboratory was equipped with an air ventilation system to suck the air out of the room and replace it with fresh air. The room ventilation also acts as a safety measure: any combustible gases will be sucked out together with the air from the room.

E.2.2 Automatic Burner Safety Shut-off System

Solenoid valves were installed to cut the gas supply if the ignition failed to ignite the burner. The flame detection probe detected the flame (Figure 4.11).

E.3 Standard Operating Procedure

Safety is critical to the experimental work. A Standard Operating Procedure (SOP) for startup, normal operation, normal shut down and emergency shut down is summarised in the below subsections. In case of emergency, the emergency button is used to stop the gas supply.

E.3.1 Pre-Start-up Procedure

The start-up process must be carried out every time to start the experimental work to ensure it us safe. The Standard Operating Procedure (SOP) is as follows:

Step 1 Notify others as required (supervisor, lab manager or other students/researchers) prior to running the burner.
Step 2 Do not operate the burner after hours except with supervisor, other researcher or laboratory manager.
Step 3 Check the status of gas detection alarm (Figure E.1). Ensure the gas alarm is in normal mode.
Step 4 Turn ON air ventilation system and exhaust gas extraction fan, with the switches located in the Control Room. Confirm that they are running.
Step 5 Ensure the exhaust fan and room ventilation is ON. Both fans will give some air flow noise sound.
Step 6 Turn ON the secondary air supply, turn ON the air heating element (Figure 4.14) and check the air supply temperature to reach the desired level.
Step 7 Put on Personal Protective Equipment (PPE) (boots and eye protection glasses).
Step 8 Perform safety and pre-system checks on burner.
Step 9 Check gas control panel – all gas isolator valves must be CLOSED and ensure all gas flow-meters show zero flow rates.
Step 10 Combustion chamber – start purging to ensure no methane gas in the chamber. See procedure for Combustion Chamber Purging with Air.
Step 11 Confirm all needed guards are in places.
Step 12 Confirm there are no entanglement risks (sensor cabling is appropriately tied back).
Step 13 Ensure that 240 V AC power supply to the Igniter/Flame-out interlock is switched OFF.
Step 14 Turn ON the DAQ system and all power supply switches. Ensure all sensors in ready mode.

E.3.2 Combustion Chamber Air Purging Procedure

The purging process is important to ensure that there are no combustion products or unburned fuel remaining inside the combustion chamber. The purging process has to be done after every experiment and again at the end of the experiment before the burner shut-down.

Step 1 Check and ensure all gas isolator valves are CLOSED and all gas flow-meters shows zero flow rate.
Step 2 Conduct a visual inspection outside and inside the chamber to check any abnormalities.
Step 3 Adjust air pressure regulator (Figure E.2) to 6 bar.
Step 4 Start the air purge process by turning ON the air flow to maximum at the air flow-meter.
Step 5 Continue to purge for 15 seconds.

Figure E.2: Compressed air supply valves and flow-meter.

E.3.3 Normal Start-up and Operating Procedure

The experimental work will normally use this procedure and it will be repeated until the experimental work is completed for the day.

Step 1 Ensure that DAQ is ready to collect data.
Step 2 Turn ON gas isolator valves as shown in Figure 4.5.
Step 3 Set the flow rates of each gas (Figure 4.5) as required. This is to be done by adjusting the flow-meters for each gas. Methane flow rate to be adjusted last prior to light-up.
Step 4 Press the ignition power ON (power supply on the wall beside the gas interlock and ignition control box to start the combustion (Figure 4.11(a)).
Step 5 If the ignition has not occurred within a certain period, the ignition probe (Figure 4.11(b)) will send the signal to the control box and the gas interlock solenoid valve will automatically switch OFF the methane gas supply. Carry-out the combustion chamber air purging procedure to purge all the gas from the ignition chamber and repeat steps 2, 3 and 4.
Step 6 Let the burner run for about two to three minutes to warm up to operating temperature.
Step 7 Conduct data collection.

E.3.4 Normal Shutdown Procedure

After completing the experiment work, the normal shutdown process will take place. The purging process must be done to blow out the balance of combustion product or UHC from the combustion chamber.

Step 1 Turn OFF all the gas supplies by turning OFF all the gas isolator valves, beginning with methane.
Step 2 Switch OFF the 240 V AC power to the Igniter/Flame-out interlock (Figure 4.11(a)).

Step 3 Turn OFF the DAQ system.
Step 4 Start the purging procedure as detailed in section E.3.2 (Combustion Chamber Air Purging Procedure) to blow out the flue gas remaining in the combustion chamber.
Step 5 Turn OFF the ventilation system and exhaust gas extraction fan in the Control Room.
Step 6 Check to ensure the main power supply to the DAQ is OFF.

E.3.5 Emergency Shutdown Procedure

The emergency procedure is the preparation for the emergency stop for the experiment. The stop button will cut the methane gas supply.

Step 1 Turn OFF gas supply by pressing the gas supply emergency button.
Step 2 Call security on 2222 if someone has been injured, there is a fire emergency or there is a major escape of flammable gas or liquid posing a risk of explosion.
Step 3 If evacuation is necessary, sound the emergency alarm by air horn.
Step 4 Exit the building following the exit sign.
Step 5 Follow USQ emergency procedures.

Appendix F

Gas and Air Supply System

This appendix gives more detail about the experimental setup technical drawing, gas supply system, air supply system and gas control panel.

F.1 Detailed MILD Burner Drawing

The schematic drawing with detailed geometry for the combustion chamber was shown in Figure F.1. The drawing includes side and plan view, complete with detailed dimensions and all sensor locations. The total volume for the combustion chamber and EGR is $0.33\,\mathrm{m}^3$.

F.2 Gas Control Panel Supply System

The gas supply for the experiment was from the gas cylinder installed outside the combustion laboratory. For methane gas, the overall maximum gas cylinder pressure was 13.5 MPa. The pressure regulator was set to supply the gas pressure at 125 kPa at the gas cylinder and the pressure was further reduced to 100 kPa when the gas reached the control panel in the combustion room. In the experimental work by He (2008) , the gas supply was reduced to 55 kPa when it reached his combustion laboratory and further reduced to below 35 kPa for his experimental work. He then used the pressure range of 0.7–18.7 kPa and flow through OMEGA FL4511 rotameter to his 3.25 mm, 4.20 mm and 5.41 mm burner nozzles.

In this experiment, Dwyer RMA-21-SSV rotameters were used to measure the methane, carbon dioxide and oxygen flow rates. The calculation of the gas flow rate conversion factor can be seen in Figure F.2. The gas control panel designed for this research consists of five flow meters to measure and control the gas flow rates. Two gas plenum mounted at the bottom of the control panel were used to mix the gases. One mixer is for the fuel which mixed methane and carbon dioxide to produce biogas and the other mixer is for air or synthetic air (mixture of oxygen and nitrogen at required percentage).

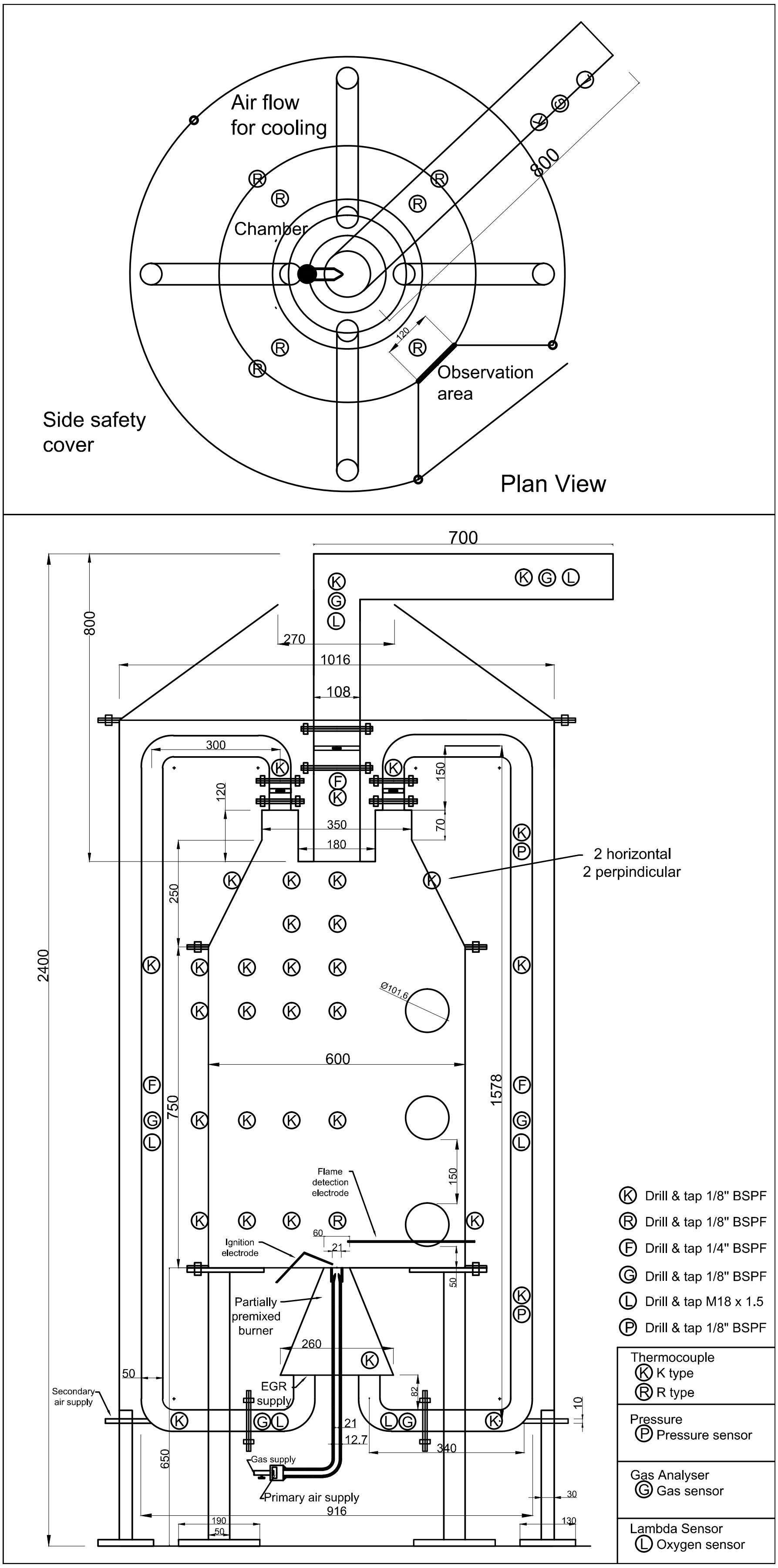

Figure F.1: Detailed MILD burner schematic diagram.

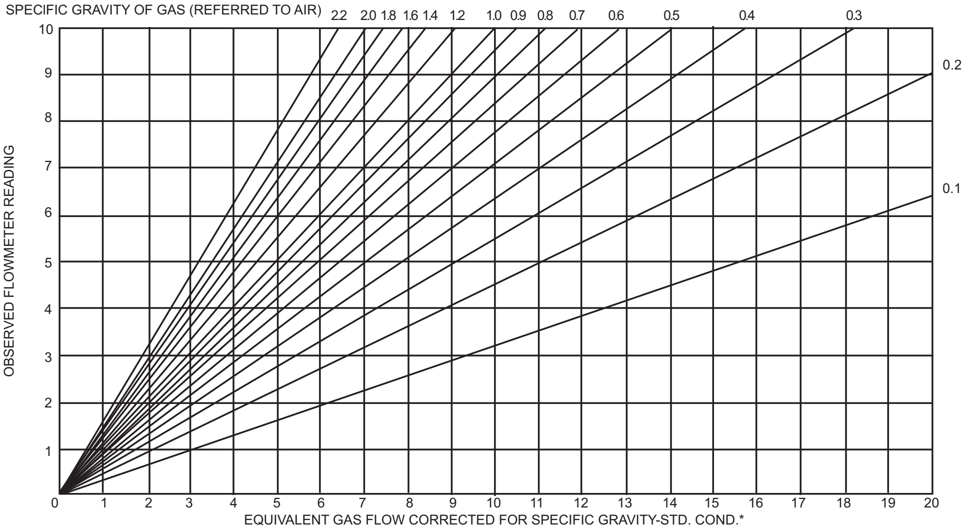

If more convenient, approximate correction factors may be determined using the following formulas.

A. Pressure: $Q_2 = Q_1 \times \sqrt{\frac{P_1 \times T_2}{P_2 \times T_1}}$

Where: Q_1 = Actual or Observed Flowmeter Reading
Q_2 = Standard Flow Corrected for Pressure and Temperature
P_1 = Actual Pressure (14.7 psia + Gage Pressure)
P_2 = Standard Pressure (14.7 psia, which is 0 psig)
T_1 = Actual Temperature (460 R + Temp °F)
T_2 = Standard Temperature (530 R, which is 70°F)

B. Specific Gravity: $Q_2 = Q_1 \times \sqrt{\frac{1}{S.G.}}$

Where: Q_1 = Observed Flowmeter Reading
Q_2 = Standard Flow Corrected for Specific Gravity
1 = Specific Gravity of Air or Water
S.G.= Specific gravity of media being used in flowmeter originally calibrated for air or water.

Note: The corrections shown in the curves and in the formulas are for variations in specific gravity and internal pressure* only. Further correction may be necessary for variations in viscosity and changes in type of flow from laminar to turbulent or vice versa. This is particularly true in the case of extremely low flows of the lighter gases. Nevertheless these charts and correction factors can be quite useful when dealing with small changes in pressure* and specific gravity.

*Measured at discharge on all but TMV units. Inlet pressure on TMV models.

Figure F.2: Dwyer flow meter gas correction factor.

F.3 Secondary Air Supply System

Normal air for the combustion was supplied by an air compressor. The idle air compressor shows the steady readings at gauge pressure of 700 kPa (7 bar). Air density at 20 °C is 1.205 kg/m^3 which produces a speed of 34.1 m/s. The secondary air supply to the combustion chamber is split into four inlets, with each pipe having a 10 mm diameter, providing a maximum possible air flow rate of 14.35 m^3/minute. For the experimental work, the air pressure was fixed at 500 kPa. This provides a maximum of 200 L/min, which is 0.2 m^3/min.